

THE CHARACTERIZATION OF THE INFRASONIC NOISE FIELD AND
ITS EFFECTS ON LEAST SQUARES ESTIMATION

A
THESIS

Presented to the Faculty
of the University of Alaska Fairbanks
in Partial Fulfillment of the Requirements
for the Degree of

DOCTOR OF PHILOSOPHY

By
Joseph Galbraith, B.S.

Fairbanks, Alaska

December 2007

UMI Number: 3302506

INFORMATION TO USERS

The quality of this reproduction is dependent upon the quality of the copy submitted. Broken or indistinct print, colored or poor quality illustrations and photographs, print bleed-through, substandard margins, and improper alignment can adversely affect reproduction.

In the unlikely event that the author did not send a complete manuscript and there are missing pages, these will be noted. Also, if unauthorized copyright material had to be removed, a note will indicate the deletion.

UMI[®]

UMI Microform 3302506

Copyright 2008 by ProQuest LLC.

All rights reserved. This microform edition is protected against unauthorized copying under Title 17, United States Code.

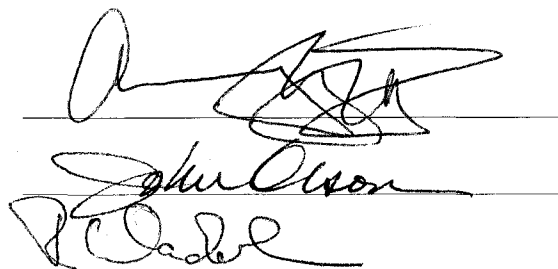
ProQuest LLC
789 E. Eisenhower Parkway
PO Box 1346
Ann Arbor, MI 48106-1346

THE CHARACTERIZATION OF THE INFRASONIC NOISE FIELD
AND ITS EFFECTS ON LEAST SQUARES ESTIMATION

By

Joseph Galbraith

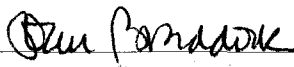
RECOMMENDED:

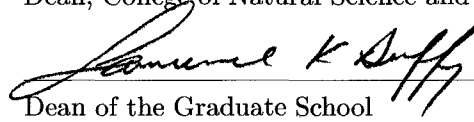


Advisory Committee Chair

John D. Craven
Chair, Department of Physics

APPROVED:


Dean, College of Natural Science and Mathematics


Dean of the Graduate School

10-10-07

Date

Abstract

Localization of the source of an acoustic wave propagating through the atmosphere is not a new problem. Location methods date back to World War I, when sound location was used to determine enemy artillery positions. Since the drafting of the Comprehensive Nuclear-Test-Ban Treaty in 1996 there has been increased interest in the accurate location of distant sources using infrasound. A standard method of acoustic source location is triangulation of the source from multi-array back azimuth estimates. For waves traveling long distances through the atmosphere, the most appropriate method of estimating the back azimuth is the least squares estimate (LSE). Under the assumption of an acoustic signal corrupted with additive Gaussian, white, uncorrelated noise the LSE is theoretically the minimum variance, unbiased estimate of the slowness vector.

The infrasonic noise field present at most arrays is known to violate the assumption of white, uncorrelated noise. The following work characterizes the noise field at two infrasound arrays operated by the University of Alaska Fairbanks. The power distribution and coherence of the noise fields was determined from atmospheric pressure measurements collected from 2003-2006. The estimated power distribution and coherence of the noise field were not the white, uncorrelated noise field assumed in the analytic derivation of the LSE of the slowness vector.

The performance of the LSE of azimuth and trace velocity with the empirically derived noise field was numerically compared to its performance under the standard noise assumptions. The effect of violating the correlation assumption was also investigated. The inclusion of clutter in the noise field introduced a dependence to the performance of the LSE on the relative signal amplitude. If the signal-to-clutter ratio was above 10 dB, the parameter estimates made with the correlated noise field were comparable to the estimates made with uncorrelated noise. From the results of these numerical studies, it was determined that the assumption of Gaussian, white, uncorrelated noise had little effect on the performance of the LSE at signal-to-noise ratios greater than 10 dB, but tended to over estimate the performance of the LSE at lower signal-to-noise ratios.

Table of Contents

	Page
Signature Page	i
Title Page.....	ii
Abstract	iii
Table of Contents.....	iv
List of Figures.....	vi
Chapter 1 Background	1
1.1 Acoustic Waves in the Atmosphere.....	4
1.2 Dispersion.....	8
1.3 Attenuation.....	16
Chapter 2 Digital Signal Processing & Array Processing	24
2.1 Random Vectors.....	27
2.1.1 Statistical Description of a Random Process.....	27
2.1.2 Frequency Domain Description of a Random Process.....	31
2.2 Arrays.....	34
2.3 Parameter Estimation.....	39
2.3.1 Estimation Background and Methods of Estimation.....	39
2.3.2 Classical Estimation and the MVU Estimate.....	41
2.4 Linear Least Squares Estimation.....	46
Chapter 3 Bias in LSE	52
3.1 Introduction.....	52
3.2 The Slowness Vector.....	52
3.3 Bias in the Estimates of Slowness Magnitude and Azimuth.....	54
3.3.1 Derivation of the pdf of the Slowness Vector.....	54
3.3.2 Bias in the Estimate of Slowness Vector Magnitude.....	58
3.4 Bias in the Estimate of Azimuth.....	73
3.4.1 Numerical Calculation of the Bias in the Azimuth Estimate.....	74
3.4.2 Effect of Array and Wave Parameters on the Bias in the Estimate of Azimuth.....	78
3.5 Conclusion.....	82

	Page
Chapter 4 Distribution of the Infrasonic Noise Field	85
4.1 Introduction.....	85
4.2 The Noise Field.....	86
4.2.1 Method.....	87
4.2.2 Results.....	91
4.3 Effects of Wind on the Noise Field.....	100
4.3.1 Method.....	101
4.3.2 Results.....	104
4.3.3 Application.....	108
4.4 Effect of the Infrasonic Noise Field on LSE.....	110
4.5 Conclusion.....	114
Chapter 5 Correlation of the Infrasonic Noise Field	117
5.1 Introduction.....	117
5.2 Correlation of the Noise Field.....	118
5.2.1 Method.....	119
5.2.2 Results.....	122
5.2.3 Discussion.....	133
5.3 Effects of Local Wind Speed on the Coherence Spectrum.....	141
5.3.1 Method.....	141
5.3.2 Results.....	142
5.3.3 Discussion	147
5.4 Effect of Correlated Noise on LSE of Azimuth and Trace Velocity.....	160
5.4.1 Method.....	161
5.4.2 Results.....	162
5.5 Conclusion.....	165
Chapter 6 Conclusions	169
6.1 Summary.....	169
6.2 Discussion.....	173
Bibliography	176
Appendix	182

List of Figures

	Page
Figure 1.1 Location of the IMS infrasound stations as of April 2007.....	3
Figure 1.2 Dispersion relation for atmospheric pressure waves. The atmosphere was assumed to be isothermal and the dispersion relations were derived in the long wave regime. Wave frequency is shown on the vertical axis and horizontal wave number is shown on the horizontal axis. Each line represents a different value of the vertical wave number m . The scale height of the atmosphere was set equal to unity to produce this plot. The blue lines are the acoustic waves, the red lines are the gravity waves, and the green line is the Lamb wave.....	13
Figure 1.3 Atmospheric pressure versus height for May 1986 at 60° N latitude. The data was taken from the National Space Science Data Center's COSPAR model atmosphere	15
Figure 1.4 Atmospheric temperature versus height for May 1986 at 60° N latitude. The data was taken from the National Space Science Data Center's COSPAR model atmosphere.....	16
Figure 1.5 Brunt-Vaisala and acoustic cut-off frequency for the model atmosphere on May 1986 at 60 N latitude. The solid line is the Brunt-Vaisala frequency and the dashed line is the acoustic cut-off frequency.....	17
Figure 1.6 The classic attenuation of an acoustic wave as a function of the wave frequency. The atmosphere is assumed to be homogeneous, isothermal, and dry. The relaxation time \sim equals 1.7×10^{-10} sec for 20°C.....	22
Figure 2.1 Example of a large amplitude signal and the background noise recorded at the Fairbanks array. The eight plots correspond to the output of the eight array elements. The y-axis displays the recorded pressure in Pascal and the x-axis is the time index.....	25
Figure 2.2 Example of a typical low amplitude far-field signal and the background noise recorded at the Fairbanks array. The eight plots correspond to the output of the eight array elements. The y-axis displays the recorded pressure in Pascal and the x-axis is the time index.....	26

Figure 2.3	The approximate array geometry of the Fairbanks and Windless Bight arrays. The pentagrams denote the location of the individual array elements.....	39
Figure 2.4	Graphical representation of the decision process to choose the general method of parameter estimation. The decision process starts in the top left corner of the figure. The process evolves by moving along the paths until a style of estimation is chosen or the determination of no estimation method available is reached.....	42
Figure 2.5	Flow chart illustrating the process of choosing a classical parameter estimator. The process starts in the upper left hand corner of the figure. The choices then evolve down and to the left until the most appropriate classical parameter estimate has been chosen.....	45
Figure 3.1	2-D geometric representation of the slowness magnitude bias. The solid ellipse is an arbitrary confidence limit of the slowness vector distribution. The dashed line is the contour of constant magnitude of the slowness vector, which divides the slowness vector distribution into high magnitude estimates and low magnitude estimates. The slowness vector representing a signal with a slowness magnitude of 3 s/km and an azimuth of 0 is represented by s_0 . For the reader's convenience a line tangent to the contour of constant slowness magnitude has been included in the figure.....	59
Figure 3.2	Bias in the estimate of the slowness vector magnitude for a range of magnitudes of the slowness vector. The aspect ratio of the ellipse was held constant at $\frac{1}{2}$. The area of the ellipse was held at a value of π and the azimuth was constant at 45 degrees. The dependence of the bias in the estimate on the slowness vector magnitude was modeled by a sum of exponentials.....	66

- Figure 3.3 Bias in estimate of the slowness vector magnitude when the slowness vector is aligned with the principal axes of the ellipse. The solid ellipse is an arbitrary confidence limit of the distribution of the slowness vector. The dashed line is the contour of constant slowness vector magnitude, which divides the distribution into high magnitude estimates and low magnitude estimates. The slowness vector representing a signal with a slowness magnitude of 3 s/km and an azimuth of 45 degrees is represented by s_o68
- Figure 3.4 Bias in the estimate of the slowness vector magnitude for wave azimuths ranging from -90 to 90 degrees. The contour of constant probability for the simulated pdf was a coordinate aligned ellipse with the semi-major axis aligned along the y-axis and the semi-minor axis along the x-axis. The ellipse was centered about a point with slowness magnitude s_o for each azimuth.....69
- Figure 3.5 Change in the bias of the estimate of the slowness vector magnitude as the area bounded by the contour of constant probability increases. The aspect ratio of the ellipse was held constant at $\frac{1}{2}$ and the area was increased from $\pi/2$ to 2π . The azimuth was held constant at 45 degrees and the magnitude of the slowness vector was constant at 3 s/km.....70
- Figure 3.6 The dependence of the bias in the estimate of the slowness vector magnitude on the aspect ratio of the ellipse. The area of the ellipse was held constant at π and the aspect ratio was decreased from 1 to 0.1. The azimuth was held constant at 45 degrees and the magnitude slowness was constant at 3 s/km.....72
- Figure 3.7 Setup for the calculation of the azimuthal estimate bias. The blue ellipse is an arbitrary contour of constant probability of the slowness pdf. Azimuth estimates made on the dashed red lines inside the ellipse will return estimates of $\pm \theta$. The dashed lines intersect the ellipse at $\pm a$ and $\pm b$75

- Figure 3.8 Bias in the azimuth estimates when the confidence ellipse is aligned with the principle axes of the array. The left hand plot shows the range of possible azimuth estimates in the arbitrary confidence ellipse. The right hand plot shows the difference between the line integral for the positive angle and the negative angle for the range of possible angles.....76
- Figure 3.9 Bias in the azimuth estimates when the confidence ellipse is not aligned with the principle axes of the array. The left hand plot shows the range of possible azimuth estimates in the arbitrary confidence ellipse. The right hand plot shows the difference between the line integral for the positive angle and the negative angle for the range of possible angles.....78
- Figure 3.10 Bias in the estimate of the azimuth versus the area of an arbitrary confidence ellipse. The blue + are the results of the numerical simulation for various ellipse areas. The red line is the linear curve fit of the numerical results.....79
- Figure 3.11 Bias in the estimate of the azimuth versus the aspect ratio of the confidence ellipse. The blue + are the results of the numerical simulation for various aspect ratios of the ellipse. The red line is the inverse power law curve fit of the numerical results.....80
- Figure 3.12 Bias in the estimate of the azimuth versus the slowness vector magnitude. The blue + are the results of the numerical simulation for slowness between 2 s/km and 4 s/km. The red line is a sum of exponentials curve fit of the numerical results.....81
- Figure 3.13 Bias in the estimate of the azimuth versus the azimuth of the center of the confidence ellipse. The blue + are the results of the numerical bias simulation for azimuths between +/- 90 degrees.....83
- Figure 4.1 Sunrise and sunset times for Fairbanks, AK during 2006. The black x are the local times of sunrise and the black + are the local sunset times. The dashed lines are the limits of the three hour block for sunrise and sunset.....90

- Figure 4.2 Median power spectra for the months of January-April 2006 measured at the Fairbanks array. The solid black line is the median power spectrum for the three hour time block centered about midnight, the solid magenta line is the median power spectrum during the noon time block, the solid red line is the median power spectrum during sunset, and the solid blue line is the power spectrum during sunrise. The black dashed lines indicate the 95% and 5% confidence limits of all the power spectra for the entire month.....92
- Figure 4.3 Median power spectra for the months of May-August 2006 measured at the Fairbanks array. The solid black line is the median power spectrum for the three hour time block centered about midnight, the solid magenta line is the median power spectrum during the noon time block, the solid red line is the median power spectrum during sunset, and the solid blue line is the power spectrum during sunrise. The black dashed lines indicate the 95% and 5% confidence limits of all the power spectra for the entire month.....93
- Figure 4.4 Median power spectra for the months of September-December 2006 measured at the Fairbanks array. The solid black line is the median power spectrum for the three hour time block centered about midnight, the solid magenta line is the median power spectrum during the noon time block, the solid red line is the median power spectrum during sunset, and the solid blue line is the power spectrum during sunrise. The black dashed lines indicate the 95% and 5% confidence limits of all the power spectra for the entire month.....94
- Figure 4.5 2006 seasonal noise power spectra measured at the Windless Bight array. The solid black line is the median power spectrum for the three hour time block centered about midnight, the solid magenta line is the median power spectrum during the noon time block, the solid red line is the median power spectrum during sunset, and the solid blue line is the power spectrum during sunrise. The black dashed lines indicate the 95% and 5% confidence limits of all the power spectra for the entire month.....96

- Figure 4.6 Digitizer temperature for both the Windless Bight and Fairbanks arrays. The + are the daily median digitizer temperature at Fairbanks and the • are the daily median temperatures at Windless Bight. The daily digitizer temperatures were calculated for the year of 2006.....100
- Figure 4.7 The increase in the noise field power as a function of local wind speed. The red dots represent the power measured at a frequency of 0.08 Hz and the green dots are the power estimates at 5 Hz. The solid black lines are the best-fit lines of the median power estimates at each of the measured wind speeds. Note the different rates of power increase for the two frequencies.....102
- Figure 4.8 The wind response of the Fairbanks and Windless Bight arrays. The top plot is the median power at 0.63 Hz at Fairbanks, with the wind response at the same frequency at Windless Bight on the bottom.....105
- Figure 4.9 Rate of power increase with local wind speed for the Windless Bight array. The 95% and 5% confidence limits are included with each value of b as vertical bars. The curve fit corresponding to a frequency of 0.16 Hz during the winter months failed the coefficient of determination test and was excluded from the final data set.....106
- Figure 4.10 Rate of power increase with local wind speed for the Fairbanks array. The 95% and 5% confidence limits are included with each value of b as vertical bars. The bottom left panel is blank due to the lack of wind data available during the spring at the Fairbanks array.....107
- Figure 4.11 Power spectra for high and low wind speeds at Windless Bight and Fairbanks. The top plot is for the Windless Bight array during the winter months of 2006. The red line is the median power spectrum for all estimates when the mean wind speed during the time window was 6 m/s and the blue line is the median power spectrum for a wind speed of 2 m/s. The bottom plot is for the winter months of 2005 at the Fairbanks array, this time the red line is for 1.5 m/s and the blue line is 0.3 m/s. At high wind speeds the noise power spectrum is deformed from the median noise field by the effects of the local wind.....109

Figure 4.12 Variance in the distribution of parameter estimates for assumed and empirical noise.

The data were filtered between 1 and 10 Hz before the parameter estimation was preformed. The blue + are the variance in the distribution when the empirical noise is used, the red + are the variances for white noise.....113

Figure 5.1 The sample spring noise field coherence spectrum at the Fairbanks array. The coherence spectrum for March 2005 was used as the representative spring noise field coherence spectrum at Fairbanks. The red curves depict the coherence spectra of the noise field for intersensor separations of approximately 200 meters, the small separations. The blue curves are the coherence spectra for intersensor separations on the order of a kilometer, the large separations. The sample time windows of midnight, sunrise, noon, and sunset are shown in the top left, top right, bottom left, and bottom right, respectively. The monthly median local wind speed is not shown on this plot due to a lack of wind data during the month of March.....123

Figure 5.2 The sample summer noise field coherence spectrum at the Fairbanks array. The red curves display the coherence spectra of the noise field for intersensor separations of approximately 200 meters, the small separations. The blue curves are the coherence spectra for intersensor separations on the order of a kilometer, the large separations. The sample time windows of midnight, sunrise, noon, and sunset are shown in the top left, top right, bottom left, and bottom right, respectively. The monthly median local wind speed for each time block is included with each coherence spectrum.....127

Figure 5.3 The sample winter noise field coherence spectrum at the Fairbanks array. The red curves depict the coherence spectra of the noise field for intersensor separations of approximately 200 meters, the small separations. The blue curves are the coherence spectra for intersensor separations on the order of a kilometer, the large separations. The sample time windows of midnight, sunrise, noon, and sunset are shown in the top left, top right, bottom left, and bottom right, respectively. The monthly median local wind speed for each time block is included with each coherence spectrum.....129

- Figure 5.4 The sample noise field coherence spectrum for the Windless Bight array. The red curves display the coherence spectra of the noise field for intersensor separations of approximately 200 meters, the small separations. The blue curves are the coherence spectra for intersensor separations on the order of a kilometer, the large separations. The sample time windows of midnight, sunrise, noon, and sunset are shown in the top left, top right, bottom left, and bottom right, respectively. The local wind speed recorded at Windless Bight were not used in the local wind speed study and are omitted from these plots.....130
- Figure 5.5 The direction of stratospheric and tropospheric wind arrival at the Fairbanks array during 2003. The stratospheric winds, 50 to 70 km, are shown with + and the tropospheric winds, 10 to 20 km, are plotted with •. The Julian day number for 2003 is plotted along the x-axis. The direction of arrival is shown on the y-axis. The y-axis is oriented in the mathematical sense, with 0 degrees pointing due east, 90 degrees pointing due north, and -90 degrees pointing due south.....138
- Figure 5.6 The median small separation noise field coherence spectrum estimated at the Fairbanks array versus the median local wind speed. The coherence spectra were estimated for the winter of 2005 at the Fairbanks array. The estimated coherence spectrum of the noise field for periods with local wind speeds of 0.1, 0.5, 1, and 1.5 m/s are shown in blue, red, green, and magenta, respectively. Notice that as the median local wind speed increases the estimated noise field coherence spectrum decreases across all estimated frequencies.....144
- Figure 5.7 The median small separation noise field coherence spectrum estimated at the Windless Bight array versus the median local wind speed. The coherence spectra were estimated for the winter of 2006 at the Windless Bight array. The estimated coherence spectrum of the noise field for periods with local wind speeds of 1, 2, 3, 4, 5, and 6 m/s are shown in blue, red, green, magenta, cyan, and black, respectively. Notice that as the median local wind speed increases the estimated noise field coherence spectrum decreases across all estimated frequencies. At high local wind speeds the coherence floor at Windless Bight approaches the expected value of 0.14.....146

- Figure 5.8 The wind response of the coherence estimates at the microbarom and neighboring frequencies. The frequencies most responsive to increases in the local wind speed are shown in the left hand panel. The right hand panel displays the frequencies less responsive to the local wind speed. In the left hand panel the coherence of the lower frequencies begin decreasing at lower wind speeds than the higher frequencies. Frequencies greater than or less than the microbaroms, 0.04, 0.63, and 1.25 Hz shown in the right hand panel, displayed a limited response to changes in the local wind speed.....150
- Figure 5.9 The frequency dependence of the rate of increase of the wind noise power for winter 2006 at Windless Bight, Antarctica. The b was found by fitting an exponential curve to the median power versus wind speed data. The red circle represents the point of maximum noise power increase with wind speed at 0.08 Hz. The green and cyan circles represent the rate of increase at 0.16 and 0.32 Hz, respectively. The bulk of the coherence microbarom energy at the Windless Bight array occurs between 0.08 and 0.32 Hz. The 5% and 95% confidence limits of the rates of increase are shown with vertical bars.....155
- Figure 5.10 The estimated noise field coherence spectrum for April 2005 at the Fairbanks array. The red curves display the coherence spectra of the noise field for intersensor separations of approximately 200 meters, the small separations. The blue curves are the coherence spectra for intersensor separations on the order of a kilometer, the large separations. The sample time windows of midnight, sunrise, noon, and sunset are shown in the top left, top right, bottom left, and bottom right, respectively. The median monthly local wind speed for each time block is included with each coherence spectrum.....157
- Figure 5.11 PSD of the Fairbanks array for the months of April and June. The median PSDs for midnight, sunrise, sunset, and noon are shown in black, blue, red, and magenta, respectively. The frequency range was chosen to focus attention on the microbarom frequencies. The top plot was made using the data collected during June 2005 and the bottom plot used the data collected during April 2005.....159

Figure 5.12	The effect of correlated noise on the least squares parameter estimates. The noise field correlation levels of 0.7, 0.5, 0.3, and uncorrelated are shown by +, x, *, and •, respectively. The upper plot shows the median azimuth estimates and the lower plot shows the median trace velocity estimates. The azimuth of the signal of interest was 113 degrees and the azimuth of the clutter signal was 23 degrees. The clutter trace velocity was 0.330 km/s and the signal of interest had a trace velocity of 0.350 km/s	163
Figure 6.1	The percentage of synthetic slowness vector pdfs that fail a chi-squared distribution test as a function of the signal-to-noise ratio.....	174

Chapter 1

Background

Infrasound is the study of acoustic energy with frequencies in the range below human hearing, 0.001 to 16 Hz.¹ Many natural events emit infrasound: storms at sea,^{2,3} earthquakes,⁴ meteors,^{5,6} volcanos,⁷ turbulent airflow over mountain ranges,^{8,9} and the aurora¹⁰ can all emit infrasonic waves. Turbulent wind flow can also create pressure fluctuations in the atmosphere with frequencies in the infrasonic range.^{11,12,13,14,15} Human activities such as explosions, airplanes, and rockets can produce infrasonic waves.¹ These low frequency waves can propagate through the atmosphere for thousands of kilometers without substantial attenuation. By monitoring infrasound, information about events many kilometers away can be gathered remotely.

One of the earliest recorded instances of infrasound was from the 1883 eruption of Krakatoa volcano in Indonesia. The explosive eruption emitted low frequency pressure waves that circled the globe several times and were recorded on barometers.^{7,16,17} Barometers also recorded infrasound from the meteor explosion above Tunguska, Russia in 1908.^{6,5} The infrasound generated by these two early events was recorded using barometers and mechanical pressure gauges. Barometers and mechanical pressure gauges generally operate at frequencies that are too low for use in the study of infrasound and lack the required sensitivity (D. Osborne, personal communication, September 2006). It wasn't until World War I that an electronic microphone designed for the low frequencies of infrasound was developed.

During WWI[†] both the French and German armies experimented with sound ranging to locate the positions of enemy artillery. The large artillery cannons produced both a shell wave and a report from the muzzle of the gun when fired. The explosion of the artillery shell upon impact produced another set of sound waves associated with the operation of the artillery cannons. Only the sound waves emitted from the muzzle report were used to locate the position of the opposing artillery. For sound ranging to be an effective method of gun position location, the gun report wave needed to be separated from the waves produced by the flight and explosion of the artillery shell. In 1916 Bragg and Tucker discovered

[†]The history of infrasound given in this section was adapted from a talk given by D. Osborne in September 2006 at the Infrasound Technology Workshop in Fairbanks, Alaska.

that the muzzle report produced a low frequency acoustic wave while the shell flight and explosion produced high frequency acoustic waves. This discovery allowed the separation of the muzzle report wave from the high frequency acoustic shell and detonation waves. In June of 1916 Bragg and Tucker produced a frequency selective hotwire microphone that could be tuned to the frequency of the gun report by using a Helmholtz resonator. The Tucker hotwire microphone was the first microphone designed specifically for the collection of infrasonic signals.

Interest in sound ranging waned during WWII. The WWII battle fronts moved too quickly to make sound ranging useful and the technique was little improved during the war. After WWII the nuclear test explosions of the Atomic Age produced a new source of infrasonic waves. The atmospheric nuclear test explosions of the early Cold War era were monitored using infrasound. The use of infrasound as a monitoring system of atmospheric nuclear test explosions decreased in the late 1960s as satellite technology improved and the atmospheric tests could be seen rather than heard. When the nuclear tests were conducted underground to avoid satellite observation, seismic data was used to monitor the test explosions. Interest in infrasound increased with the drafting of the Comprehensive Nuclear-Test-Ban Treaty in 1996.¹ The United Nations treaty called for the use of infrasound, among other technologies, to continuously monitor for nuclear test detonation.

To enforce the treaty the preparatory commission for the Comprehensive Nuclear-Test-Ban Treaty Organization (CTBTO) created the International Monitoring System (IMS), a network of geophysical sensor stations located around the world that monitor seismic signals, atmospheric radioactive material releases, hydroacoustic signals and infrasound. The locations of the current and proposed infrasound monitoring stations in the IMS¹ are shown in Figure 1.1. The exact geometry of each of the infrasound monitoring stations is variable, but each station has four to nine microphone elements and a mechanism to reduce the wind noise.¹⁸ In addition to monitoring compliance with the Comprehensive Test Ban Treaty, the IMS infrasound stations provide opportunities to explore low frequency atmospheric acoustics. The IMS infrasound stations have been used to locate geophysical sources, explore low frequency atmospheric turbulent pressure fluctuations, gather data on long distance propagation of sound through the atmosphere, and test the performance of atmospheric models.

Infrasound Network (60 Stations)

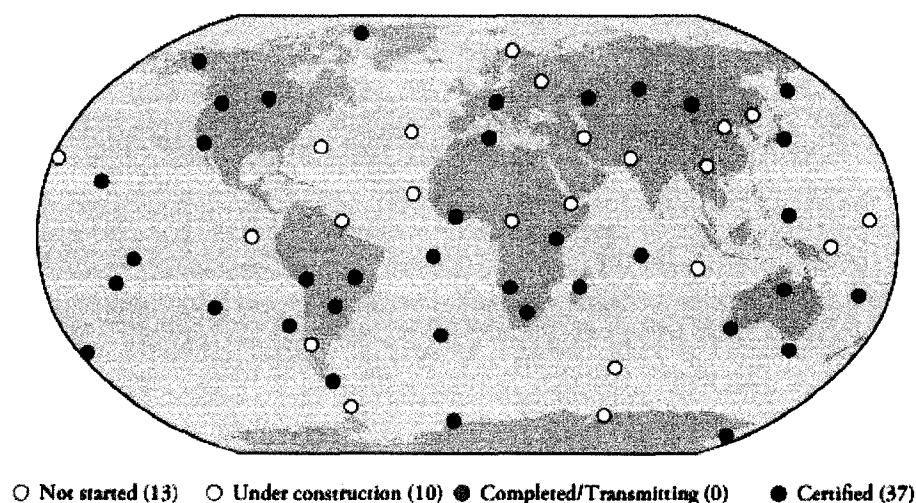


Figure 1.1. Location of the IMS infrasound stations as of April 2007.

One avenue of research provided by the pressure data collected by the IMS infrasound stations is the structure of the noise field present at the arrays. In the following work the validity of the common signal processing noise field assumptions (Gaussian, white, uncorrelated) will be tested. It has been proved¹⁹ that under the assumption of Gaussian, white, uncorrelated noise (GWU) the least squares estimate is the most efficient estimate of signal parameters; the derivation of this fundamental result will be recapitulated. Then the performance of the least squares estimate will be investigated with the GWU noise field. Next the effects of the physical noise field on the least square estimate will be investigated. To explore the effects of the noise field, the character of the noise field at two of the IMS infrasound arrays, IS55 in Windless Bight, Antarctica and IS53 in Fairbanks, Alaska, will be explored in detail. Synthetic noise data will then be generated to statistically study the effect of the noise on the performance of far-field source location using least squares parameter estimation. The performance of the least squares estimate in the measured physical noise field will then be compared with the performance of the estimate in the GWU noise field.

To aid in the study of the noise field and acoustic source location a basic understanding

of acoustic waves and atmospheric wave propagation is useful. This will provide a rudimentary knowledge of how acoustic waves are produced and how they propagate through the atmosphere. The non-acoustic waves that may arise in the atmosphere will also be introduced along with the frequencies at which each wave type can propagate. The attenuation of the atmospheric waves will also be explored to illustrate the utility of infrasonic waves in far-field source location and monitoring. An understanding of atmospheric acoustic waves will provide insight into what affects the propagation of a wave from its source to the array. Both the direction and speed of wave propagation are used in the source location problem, and information about anything that could alter the propagation parameters is useful.

1.1 Acoustic Waves in the Atmosphere

[‡] Acoustic waves are pressure disturbances that can propagate through any compressible fluid. These pressure disturbances are caused by changes in the mass density as small volume elements of the fluid move from their respective equilibrium positions. An acoustic wave is different from the familiar “wave in a string” in that it is a longitudinal wave formed by molecules moving back and forth in the same direction as the wave propagation.²² The more familiar waves are the transverse wave where the molecules move perpendicular to the direction of propagation.

Acoustic waves can be described as spherical waves propagating radially outward from a point source pressure disturbance in three dimensions. As the distance from the source increases, the curvature of the spherical wave front becomes smaller and the spherical wave effectively becomes a plane wave propagating through the medium.²⁴ The distance where the plane wave approximation is valid depends on the aperture size of the observing array and the sampling rate of the array.²⁵ Sources that are closer than ten times the array aperture, approximately 15 to 20 km for the IMS arrays, produce waves that can be discerned as spherical waves at the array.²⁵ The pressure waves produced by sources at greater distances than ten times the array aperture can be approximated as plane waves at the Fairbanks and Windless Bight arrays. This factor of ten is valid for the particular sampling rate used at IS53 and IS55. The exact source distance at which the pressure waves can be approximated

[‡]This material can be found in many standard texts.^{20,21,22,23} The formalism of L.E. Kinsler and A.R. Frey was principally employed in this section.

as plane waves is array and sample rate dependant and must be calculated separately for each individual array.²⁵

To derive the wave equation for an acoustic plane wave the displacement of a volume element of the fluid must be related to the change in mass density that must have occurred from the displacement of that fluid volume element. Consider the displacement of a volume element defined by the cross-sectional area S and the length $x - (x + dx) = dx$. The mass contained in this volume will be given by the equilibrium mass density of the fluid, ρ_o , multiplied by the volume Sdx . As the acoustic pressure wave passes through the volume element, assume that the plane originally at x is displaced a distance $\psi(x)$. The plane, originally at $x + dx$, will be displaced a distance $\psi(x) + \frac{\partial\psi(x)}{\partial x} dx$. The volume enclosed between the planes has been modified by the movements of the planes. The volume is now given by $Sdx(1 + \frac{\partial\psi(x)}{\partial x})$, which will be larger or smaller than Sdx depending on the sign of the partial derivative of the displacement. To satisfy conservation of mass the density inside the volume must change to offset the change in volume so that the mass enclosed inside the new volume remains constant. The conservation of mass equation can be used to relate the change in the density to the change in position,

$$\rho Sdx(1 + \frac{\partial\psi(x)}{\partial x}) = \rho_o Sdx. \quad (1.1)$$

Equation 1.1 can be simplified by defining the dimensionless condensation, $s = \frac{\rho - \rho_o}{\rho_o}$.²² Writing $\frac{\rho}{\rho_o}$ in terms of the condensation,

$$\begin{aligned} (1 + s) &= 1 + \frac{\rho - \rho_o}{\rho_o} \\ &= \frac{\rho_o + \rho - \rho_o}{\rho_o} \\ &= \frac{\rho}{\rho_o}, \end{aligned} \quad (1.2)$$

and substituting into Equation 1.1 results in a new form of the density equation,

$$(1 + s)(1 + \frac{\partial\psi(x)}{\partial x}) = 1. \quad (1.3)$$

Even for acoustic waves with amplitudes that are painful to the human ear, both the dimensionless condensation, s , and the partial derivative of the displacement, $\frac{\partial\psi(x)}{\partial x}$, do not exceed 10^{-4} and the quantity $s\frac{\partial\psi(x)}{\partial x}$ in Equation 1.3 can be neglected as vanishingly small.²²

Neglecting $s \frac{\partial \psi(x)}{\partial x}$ in Equation 1.3 leads to a form of the continuity equation in terms of the condensation and the partial derivative of the displacement

$$s = -\frac{\partial \psi(x)}{\partial x}. \quad (1.4)$$

The change in position can now be related to the change in pressure using Equation 1.4. Relating the change in pressure to the change in position is an essential step in the derivation of the acoustic wave equation. A knowledge of which thermodynamic process best describes the compression and expansion of the medium due to the motion of the planes is necessary in order to determine the relationship between the pressure and the density. The compression of a fluid requires the expenditure of work that is converted into heat energy. This heat energy will increase the temperature of the fluid in the volume being compressed unless the compression process is slow enough to allow the heat generated to flow into the surrounding fluid. When a fluid is transmitting acoustic waves the temperature gradients between adjacent compressed and expanded parts of the fluid are relatively small.²² Small temperature gradients allow a slow rate of heat transfer between the volume elements. The transfer of heat between volume elements occurs at a rate that is too low to change the temperature of surrounding volume elements before compression cycle on the volume element is completed and compression halts.²² Under these assumptions, the process of the acoustic wave propagating through the fluid may be considered an adiabatic process.^{¶22}

With the knowledge of thermodynamic process involved in the wave propagation the changes in density can be related to the changes in pressure. Without loss of generality, the adiabatic process compression process can be represented by the equation

$$dP = \left(\frac{dP}{d\rho}\right)_o d\rho, \quad (1.5)$$

where $\left(\frac{dP}{d\rho}\right)_o$ is the slope of the line measured at the coordinate point, (P_o, ρ_o) , of the adiabatic pressure versus density plot.²² The changes in pressure and density due to the acoustic waves are small by assumption. The assumption of small pressure and density changes allows the incremental pressure change dP to be replaced with the acoustic pressure^{||}

[¶]An adiabatic process is one for which no thermal energy enters or leaves the system. This can be achieved by thermally insulating the system or by performing the process rapidly.

^{||}Acoustic pressure is defined as the difference between the instantaneous total pressure and the pressure that would be present in the absence of the acoustic waves.²³

and the incremental density change $d\rho$ with the equilibrium density times the condensation, $\rho_o s$. Substituting these small variation approximations into Equation 1.5 results in a new form of the adiabatic process equation

$$p = \left(\frac{dP}{d\rho}\right)_o \rho_o s. \quad (1.6)$$

Defining the quantity $c_s^2 = \left(\frac{dP}{d\rho}\right)_o$ as the squared sound speed in the fluid allows further simplification of the equation for an adiabatic process,

$$p = \rho_o c_s^2 \frac{\partial \Psi(x)}{\partial x}, \quad (1.7)$$

where the condensation, s , has been replaced with $-\frac{\partial \psi(x)}{\partial x}$ according to Equation 1.4.

When a fluid is deformed in the manner described above the resulting pressures on the two faces of the volume element will be slightly different, resulting in a net force that will accelerate the fluid contained in the volume. The external force acting on each face of the volume element is equal to the product of the pressure on the face and the area of the face. The net force pushing the volume element Sdx in the positive x direction is

$$\begin{aligned} dF_x &= [p - (p + \frac{\partial p}{\partial x} ds)]S \\ &= -\frac{\partial p}{\partial x} dx S. \end{aligned} \quad (1.8)$$

According to Newton's 2nd Law, this force from the pressure difference is equal to the product of the mass contained in the volume element and acceleration of the volume element

$$-\frac{\partial p}{\partial x} dx S = \rho_o S dx \frac{\partial^2 \psi(x)}{\partial t^2}. \quad (1.9)$$

Canceling like terms in Equation 1.9 produces a simplified equation that relates changes in position to changes in the pressure

$$-\frac{\partial p}{\partial x} = \rho_o \frac{\partial^2 \psi(x)}{\partial t^2}. \quad (1.10)$$

Taking the derivative of Equation 1.7 and substituting the result into Equation 1.10 results in the acoustic wave equation

$$\frac{\partial^2 \psi(x)}{\partial t^2} = c_s^2 \frac{\partial^2 \psi(x)}{\partial x^2}. \quad (1.11)$$

Equation 1.11 can be extended to three dimensions, resulting in the three dimensional acoustic wave equation

$$\frac{\partial^2 p}{\partial t^2} = c_s^2 \nabla^2 p \quad (1.12)$$

where ∇^2 is the Laplacian operator.

1.2 Dispersion

** In the Section 1.1 the wave equation for pressure waves was derived in a fluid ignoring the effects of gravity on the fluid element and the rotation of the coordinates. When gravity is included in the equations governing waves in a fluid additional solutions to the wave equation arise in the form of gravity waves and the Lamb wave. The governing equations of waves in a fluid are the Mass Conservation Equation,

$$\frac{1}{\rho} \frac{d\rho}{dt} + \nabla \cdot \vec{u} = 0, \quad (1.13)$$

where ρ is the mass density of the fluid and \vec{u} is the velocity of the fluid. The Momentum Equation,

$$\frac{d\vec{u}}{dt} + 2\Omega \times \vec{u} = -\frac{1}{\rho} \nabla p - \vec{g} + \nu \nabla^2 \vec{u}, \quad (1.14)$$

where Ω is the angular frequency of the earth's rotation, p is the pressure, g is the acceleration due to gravity, \vec{u} is the fluid velocity, and ν is the frictional coefficient. Each term in Equation 1.14 represents a different force-like term that acts on the fluid element. From left to right the terms are: the inertia, the centrifugal force, the pressure gradient, the gravitational force, and the viscosity force.²¹ The final governing equation is the Equation of State,

$$\rho = \rho(p, q, \tilde{\theta}), \quad (1.15)$$

where ρ is the mass density, p is the pressure, q is the humidity, and $\tilde{\theta}$ is the potential temperature.^{††} To facilitate the derivation of the wave equation with the effects of gravity included it is common to make simplifying assumptions involving the governing equations. The term in the momentum equation that arises from the rotation of the earth can be

**The wave equation derivations of A.E. Gill are principally followed in this section. All work, unless otherwise specified, should be attributed to A.E. Gill.²¹

††The potential temperature is defined as the temperature that the fluid parcel would acquire if adiabatically brought to a standard reference pressure p_0 .²³

neglected if the time scale of the waves are much less than the time scale of rotation, that is $\omega \gg \Omega$.²⁰ The term introduced by friction may also be ignored if $\omega \gg \mu k^2$.²⁰ Finally, let $\vec{u} = (u, v, w)$ and assume that there is no motion in the y-direction so that $v = 0$.

To derive the wave equation including the effects of gravity consider small perturbations in pressure, p' , and density, ρ' , away from their respective equilibrium positions of p_o and ρ_o . Since the assumed perturbations are small, the governing equations can be linearized.^{††} The linearized conservation of mass equation is

$$\frac{\partial \rho'}{\partial t} + w \frac{\partial \rho_o}{\partial z} = -\rho_o \left(\frac{\partial u}{\partial x} + \frac{\partial w}{\partial z} \right), \quad (1.16)$$

where ρ' is the perturbation in mass density, ρ_o is the equilibrium mass density of the fluid, u is the velocity in the horizontal, and w is the velocity in the vertical. Separation of the momentum equation into vertical and horizontal components results in two momentum equations,

$$\frac{\partial u}{\partial t} = -\frac{1}{\rho_o} \frac{\partial p'}{\partial x} \quad (1.17)$$

for the horizontal momentum, and

$$\frac{\partial w}{\partial t} = -\frac{1}{\rho_o} \frac{\partial p'}{\partial z} - \frac{\rho'}{\rho_o} g \quad (1.18)$$

for the momentum in the vertical direction. The linearized equation of state is found by taking the total time derivative[†] of the equation of state under the assumption that the humidity (q) and the potential temperature (θ) are constants. Linearization of the equation of state will result, with the use of the hydrostatic equation $\frac{dp}{dz} = -g\rho$, in the equation

$$\frac{1}{(c_s)^2} \left(\frac{\partial p'}{\partial t} - \rho_o g w \right) = \frac{\partial \rho'}{\partial t} + w \frac{d\rho_o}{dz}, \quad (1.19)$$

where c_s is the wave speed in the fluid.

Combination of Equation 1.16 and Equation 1.19 results in the expression

$$\frac{1}{(c_s)^2} \left(\frac{\partial p'}{\partial t} - \rho_o g w \right) = -\rho_o \left(\frac{\partial u}{\partial x} + \frac{\partial w}{\partial z} \right). \quad (1.20)$$

The first wave equation governing waves in a fluid is found by combining the partial time derivative of Equation 1.20 and the partial derivative with respect to the x coordinate

^{††}To linearize replace a with $a + a'$ and ignore products of perturbations.²⁶

[†]The total time derivative is defined as $\frac{d}{dt} = \frac{\partial}{\partial t} + u \frac{\partial}{\partial x} + v \frac{\partial}{\partial y} + w \frac{\partial}{\partial z}$.

of Equation 1.17 into a single equation. By eliminating the terms containing u from the combined equation, the first wave equation for the fluid has been derived,

$$\frac{\partial^2 p'}{\partial x^2} - \frac{1}{(c_s)^2} \frac{\partial^2 p'}{\partial t^2} = \rho_o \frac{\partial^2 w}{\partial z \partial t} - \frac{\rho_o g}{c_s^2} \frac{\partial w}{\partial t}. \quad (1.21)$$

A second wave equation can be found by rewriting Equation 1.18 as

$$\rho' = \frac{\rho_o}{g} \frac{\partial w}{\partial t} + \frac{1}{g} \frac{\partial p'}{\partial z} \quad (1.22)$$

and take the partial time derivative. Equation 1.22 can be used to eliminate ρ' in Equation 1.19 resulting in the second wave equation for the fluid,

$$\frac{\partial^2 w}{\partial t^2} + N^2 w = -\frac{1}{\rho_o} \frac{\partial^2 p'}{\partial z \partial t} - \frac{g}{\rho_o c_s^2} \frac{\partial p'}{\partial t}, \quad (1.23)$$

where N^2 is an important quantity known as the Brunt-Väisälä frequency. The Brunt-Väisälä frequency is the frequency above which there is no propagating gravity wave solution. N^2 is defined by

$$N^2 = -\frac{g}{\rho_o} \frac{d\rho_o}{dz} - \frac{g^2}{c_s^2}. \quad (1.24)$$

Equation 1.23 and Equation 1.21 govern the waves that occur in a stratified, compressible atmosphere.[‡]

To explicitly solve Equation 1.23 and Equation 1.21 the form of the solutions to the wave equations must be assumed. The choice of harmonic waves as the form of the wave equation solutions results in

$$\begin{aligned} w &= \frac{A}{\sqrt{\rho_o}} e^{i(kx + mz - \omega t)} \\ p' &= B \sqrt{\rho_o} e^{i(kx + mz - \omega t)} \end{aligned} \quad (1.25)$$

as the solutions²¹ to the wave equations, where A and B are wave amplitudes, m is the vertical wave number, k is the horizontal wave number, and ω is the frequency of the wave. The solutions to the wave equations can now be used to obtain the dispersion relationship for pressure waves from Equation 1.21 and Equation 1.23. Substitution of the wave solutions, shown in Equations 1.25, into Equation 1.21 returns the equation

$$-k^2 p' - \frac{-\omega^2}{c_s^2} p' = \rho_o m \omega w + \frac{\rho_o g}{c_s^2} i \omega w. \quad (1.26)$$

[‡]The assumption of a stratified atmosphere is implicit in the hydrostatic equation.

Equation 1.23 yields

$$-\omega^2 w + N^2 w = \frac{-m\omega}{\rho_o} p' + \frac{ig\omega}{\rho_o c_s^2} p' \quad (1.27)$$

when the harmonic wave solutions are inserted into the equation.

There are now two equations, Equation 1.26 and Equation 1.27, for two unknowns, k and ω . To remove the dependence on the vertical velocity w Equation 1.27, solved for w , is substituted into Equation 1.26. The result is a quadratic equation in ω^2 ,

$$\omega^4 - [(mc_s)^2 + g^2 + (kc_s)^2 + N^2]\omega^2 + (c_s N k)^2 = 0, \quad (1.28)$$

which can be solved using the quadratic formula. The solution of Equation 1.28 is the dispersion relation for pressure waves in a compressible, stratified atmosphere,

$$\omega^2 = \frac{1}{2} \left((mc_s)^2 + g^2 + (kc_s)^2 + N^2 \pm \sqrt{[(mc_s)^2 + g^2 + (kc_s)^2 + N^2]^2 - 4(c_s N k)^2} \right). \quad (1.29)$$

It is now customary to look at the dispersion relation for the short waves and the long waves separately.^{21,23,27} The gravity and sound waves decouple in the dispersion relation for waves of small wavelength making it possible to ignore the effects of gravity on sound waves and the effects of compressibility on gravity waves. For long wavelength waves, like infrasound waves, the gravity waves and the sound waves are not decoupled and the assumption of an isothermal atmosphere is made to facilitate the analysis of the dispersion relation. In an isothermal atmosphere the change in the density is a constant given by the equation

$$\frac{1}{\rho_o} \frac{d\rho_o}{dz} = -\frac{1}{H_s}, \quad (1.30)$$

where H_s is the scale height of the atmosphere.²⁷ The scale height is the height at which the pressure has fallen to e^{-1} of the value at the Earth's surface. The scale height is given by the expression

$$H_s = \frac{RT_c}{g}, \quad (1.31)$$

where R is the gas constant and T_c is constant temperature.²⁷ From the surface of the earth to an altitude of 70 km the temperature is within fifteen percent of 250 K for the standard atmosphere.²¹ The stability of the lower atmospheric temperature about 250 K makes it the logical choice for the assumed T_c . The approximation of a constant temperature removes the

derivative from the Brunt-Väisälä frequency and leaves an expression for the Brunt-Väisälä frequency dependant on the wave speed in the fluid,

$$N^2 = \frac{g}{H_s} - \frac{g^2}{c_s^2}. \quad (1.32)$$

In the long wave regime the Brunt-Väisälä frequency serves as a separation point between the acoustic and gravity waves. Acoustic waves cannot propagate at frequencies below the Brunt-Väisälä frequency and gravity wave cannot propagate at frequencies above the Brunt-Väisälä frequency.

There is an additional solution to the wave equation whose energy falls off exponentially with height called the Lamb wave. In an isothermal atmosphere the Lamb wave has no vertical velocity.²⁷ The derivation of the dispersion relation for the Lamb wave exploits the lack of vertical velocity in the Lamb wave solution. To derive the Lamb wave dispersion relation the vertical velocity is set to zero, $w = 0$, in equation Equation 1.21 and Equation 1.23. There are two solutions for the dispersion relation in the case where the wave cannot propagate vertically,

$$\omega = kc_s,$$

and

$$\omega = 0,$$

the latter of which is not a pressure wave.

With equations defining the three dispersion relations, a plot of the wave frequency versus the horizontal wave number for various vertical wave numbers can be produced. There are distinct regions where gravity and acoustic waves can propagate, separated by the Brunt-Väisälä frequency, as shown in Figure 1.2. Acoustic waves, shown as the blue lines, cannot propagate at frequencies below the Brunt-Väisälä frequency and gravity waves, plotted as red lines, cannot propagate at frequencies above the Brunt-Väisälä frequency. Between the acoustic and gravity waves is the Lamb wave, plotted in green in Figure 1.2. The lowest acoustic frequency that can propagate in a given atmosphere is known as the acoustic cut-off frequency, which is given by

$$\omega_A = \frac{\gamma}{2\sqrt{\gamma-1}}N, \quad (1.33)$$

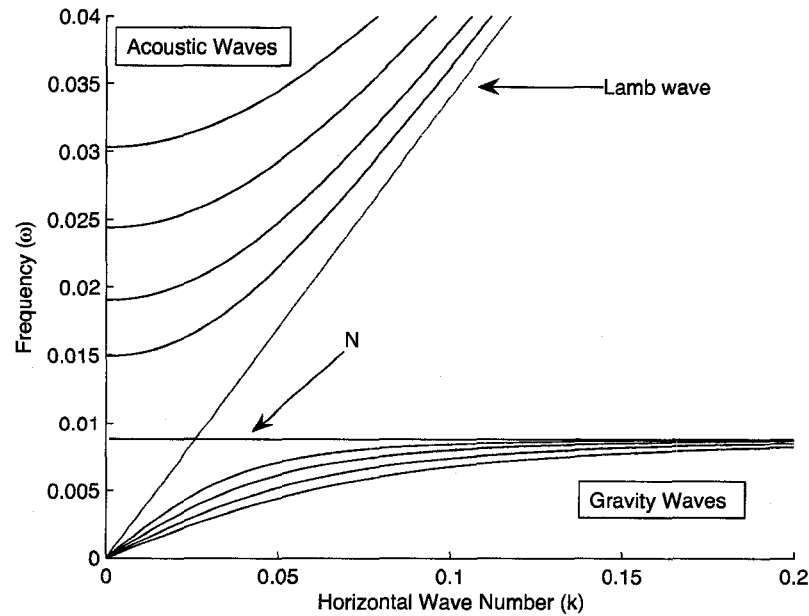


Figure 1.2. Dispersion relation for atmospheric pressure waves. The atmosphere was assumed to be isothermal and the dispersion relations were derived in the long wave regime. Wave frequency is shown on the vertical axis and the horizontal wave number is shown on the horizontal axis. Each line represents a different value of the vertical wave number m . The scale height of the atmosphere was set equal to unity to produce this plot. The blue lines represent the acoustic waves, the red lines are the gravity waves, and the green line is the Lamb wave.

where γ is the adiabatic index. The slope of each of the lines in Figure 1.2 is the speed at which pressure waves with different vertical wavenumbers propagate. The sound speed slows for all frequencies of acoustic waves as horizontal wave number approaches zero.

In the real atmosphere temperature, pressure, and density all vary with height. For this reason the atmosphere is divided into several regions based on the way the temperature changes with height in the region. The four regions that can easily support acoustic waves are the troposphere, stratosphere, mesosphere, and thermosphere.²¹ The troposphere is the closest atmospheric layer to the earth. The troposphere extends from the surface of the earth to an altitude of 12 km on average. It is in this layer that 80% of the mass and nearly all the water vapor in the atmosphere resides. Strong vertical mixing occurs in the troposphere due to solar heating. The strong vertical mixing causes the temperature to

decrease with height as a result of expansive cooling in the troposphere. The troposphere is capped by the tropopause, which marks the boundary between the troposphere and the stratosphere. The stratosphere is a very stable region of the atmosphere with little mixing that extends in altitude from 12 km to approximately 50 km. Due to the stability of the stratosphere the temperature increases with height in this region. Between the stratosphere and the mesosphere is the stratopause. Only 0.1% of the atmospheric mass lies above this boundary. From 50 km to 85 km lies the mesosphere in which the temperature decreases with height. Above the mesosphere, from 85 km to 640 km, is the thermosphere where temperatures rapidly increase with height to about 600 K in periods with little sun activity and to 2000 K for periods with an active sun.^{27,21}

The fact that the atmosphere is not isothermal directly contradicts a key assumption made in the derivation of the dispersion relation. To see how this will effect the results of the dispersion relation derivation, an atmospheric model can be used to calculate the Brunt-Väisälä frequency and the acoustic cut-off frequency as a function of altitude. The model used was the COSPAR International Reference Atmosphere (CIRA) provided by the National Space Science Data Center.²⁸ The CIRA atmospheric model is an empirical model of the temperatures and the densities gathered by ground and satellite observations. The CIRA was used to determine how the temperature and pressure vary with height. The Brunt-Väisälä frequency and acoustic cut-off frequency were calculated using the empirical temperature and pressure profiles from CIRA as a function of altitude. In order to calculate a realistic profile of the Brunt-Väisälä frequency an altitude dependent form of the equation must be found. Recasting Equation 1.24 in terms of the potential temperature, θ , results in an altitude dependent form of the Brunt-Väisälä frequency equation,²¹

$$N^2 = \frac{g}{\theta} \frac{d\theta}{dz}. \quad (1.34)$$

The potential temperature is given by the equation²⁷

$$\theta = \left[\frac{p_r}{p} \right]^\kappa T, \quad (1.35)$$

where p_r is some reference pressure and κ is $\frac{\gamma-1}{\gamma}$. The adiabatic index is defined as the ratio of the specific heats²⁷ which can be calculated using the equations

$$c_p = \frac{7}{2} R \left(1 - q + \frac{8q}{7\epsilon} \right)$$

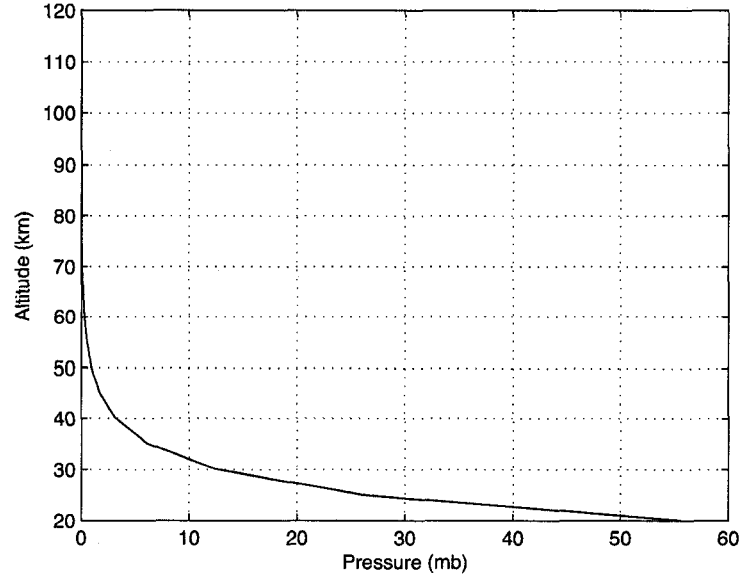


Figure 1.3. Atmospheric pressure versus height for May 1986 at 60°N latitude. The data was taken from the National Space Science Data Center's COSPAR model atmosphere.

and

$$c_v = \frac{5}{2}R(1 - q + \frac{6q}{5\epsilon}), \quad (1.36)$$

where q is the humidity of the atmosphere and ϵ is the ratio of the molecular mass of water to the molecular mass of air. Under the assumption of dry air²⁷ q will be zero and the adiabatic power is

$$\gamma = \frac{c_p}{c_v} = \frac{7}{5}.$$

Using the temperature and pressure data obtained from the CIRA model, shown in Figures 1.3 and 1.4, the acoustic cut-off frequency and the Brunt-Väisälä frequency were plotted as functions of height. In the model atmosphere the Brunt-Väisälä frequency varies with height, shown in Figure 1.5. The acoustic cut-off frequency is calculated using the Brunt-Väisälä frequency and it varies with altitude in the same manner. The acoustic frequency is greater than the Brunt-Väisälä frequency at all altitudes calculated in the stable model atmosphere. Since the acoustic cut-off frequency tracks the Brunt-Väisälä frequency at all altitudes, the Brunt-Väisälä frequency can still be used as a discriminator between

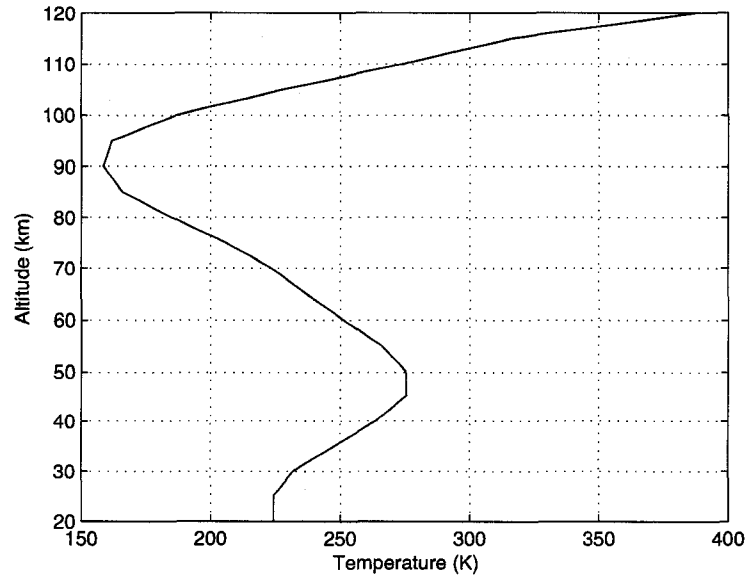


Figure 1.4. Atmospheric temperature versus height for May 1986 at 60°N latitude. The data was taken from the National Space Science Data Center's COSPAR model atmosphere.

gravity wave and acoustic wave frequencies even in a realistic atmosphere.

With the effects of gravity included there are three types of pressure waves that the atmosphere can support: acoustic, gravity, and Lamb waves. The infrasound waves belong to the acoustic wave set of atmospheric pressure waves. The frequencies at which the gravity and acoustic waves can propagate in the atmosphere are separate and distinct. Using the dispersion relations, the frequency band of the infrasound can be defined as the frequencies below 10 Hz but above the Brunt-Väisälä frequency.

1.3 Attenuation

As a pressure wave travels through the atmosphere the intensity of the wave decreases. The process of energy loss is known as attenuation. The rate of attenuation is dependent on the frequency of the pressure wave. Low frequency waves are attenuated less than high frequency waves over the same distance. It is because low frequency waves are not greatly attenuated that infrasonic waves can travel for long distances through the atmosphere.

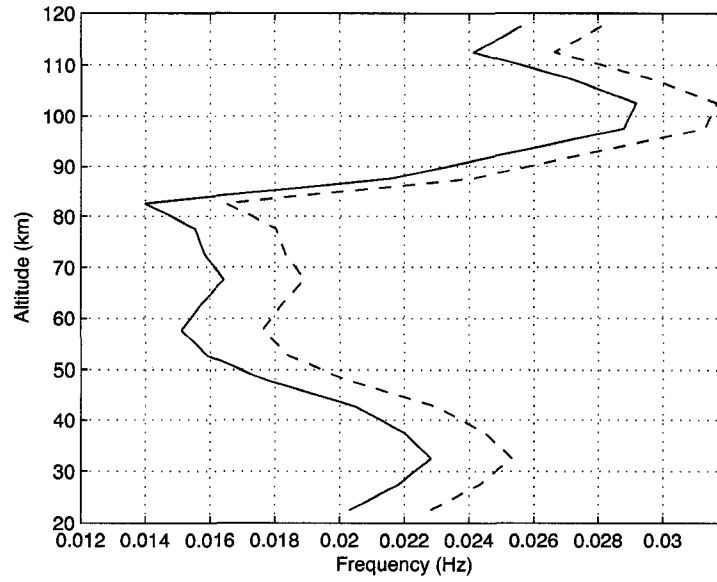


Figure 1.5. Brunt-Väisälä and acoustic cut-off frequency for the model atmosphere on May 1986 at 60N Latitude. The solid line is the Brunt-Väisälä frequency and the dashed line is the acoustic cut-off frequency.

There are several sources of pressure wave attenuation in the atmosphere. In this section the various mechanisms of attenuation will be explored.

The idealized acoustic wave is assumed to be spherically symmetric when it is generated at a point source.²³ The spherically symmetric pressure wave will expand radially outward from the source. The expanding acoustic wave can be represented as a sound field defined by the spatial and temporal dependent quantities of pressure and velocity.²³ To explore the attenuation an expression for the sound intensity as a function of space and time must be derived. For purposes of the derivation of sound intensity consider harmonic waves that oscillate with at a single frequency of ω . An acoustic wave is said to be harmonic if the time dependence of the sound pressure is given by a factor of $\cos(\phi - \omega t)$ where ϕ is a constant phase angle.²⁷

Under the assumption of harmonic waves the pressure of the wave is defined by

$$p = \text{Re}(p_c e^{-i\omega t}), \quad (1.37)$$

where p is the wave pressure, ω is the frequency of the wave, t is the time, p_c is the complex pressure, and Re indicates that the real part of the expression the wave pressure.²⁷ The velocity of the harmonic acoustic wave can be expressed as

$$\vec{u} = Re(\vec{u}_c e^{-i\omega t}), \quad (1.38)$$

where \vec{u}_c is the complex wave velocity, ω is the frequency of the wave, and t is the time. The complex quantities in Equation 1.37 and Equation 1.38 are defined as $p_c = p_r + ip_i$ and $\vec{u}_c = \vec{u}_r + i\vec{u}_i$ respectively.²⁷ Defining the acoustic intensity as $\vec{I} = p\vec{u}$ and using the definitions of the acoustic pressure and the acoustic velocity produces an expression for the intensity of the wavefield²⁷

$$\begin{aligned} \vec{I} &= Re[(p_r \cos \omega t + p_i \sin \omega t)(\vec{u}_r \cos \omega t + \vec{u}_i \sin \omega t)] \\ \vec{I} &= Re[p_r \vec{u}_r \cos^2(\omega t) + \frac{1}{2} p_r \vec{u}_i \sin(2\omega t) + \frac{1}{2} p_i \vec{u}_r \sin(2\omega t) + p_i \vec{u}_i \sin^2(\omega t)]. \end{aligned} \quad (1.39)$$

It would be useful to eliminate the explicit time dependence in Equation 1.39 in order to find the attenuation of the acoustic wave in terms of the average acoustic intensity. To eliminate the explicit time dependence take the time average of the acoustic intensity, in which case $\cos^2(\omega t)$ and $\sin^2(\omega t)$ are each replaced with $\frac{1}{2}$ and $\sin(2\omega t)$ goes to zero. The time average of Equation 1.39 produces the average acoustic intensity²⁷,

$$\begin{aligned} \vec{I}_{av} &= \frac{1}{2} p_r \vec{u}_r + \frac{1}{2} p_i \vec{u}_i \\ &= Re\left(\frac{1}{2} p_c^* \vec{u}_c\right). \end{aligned} \quad (1.40)$$

The average acoustic power emitted by the source can now be defined by integrating the average intensity of the acoustic wave over an arbitrary surface enclosing the source of the acoustic wave.²⁷ The average acoustic power is defined as

$$W_{av} = \int \int_{S_c} \vec{I}_{av} \cdot \vec{n} \, dS_c, \quad (1.41)$$

where \vec{n} is the outward unit normal vector to the surface, S_c , enclosing the source. The use of a spherical shell to enclose the acoustic source is appropriate under the assumption of a radially expanding acoustic wave. The integral in Equation 1.41 results in an average acoustic intensity of

$$I_{av} = \frac{W_{av}}{4\pi r^2}. \quad (1.42)$$

Notice that in Equation 1.42 the average power emitted by the source is divided by the square of the radial distance of the surface from the source. As the distance from the source increases the average acoustic intensity decays as the inverse square of the distance to the source. This decrease in the acoustic intensity is known as geometrical attenuation and only occurs for spherical waves.

In the plane wave approximation there is no attenuation of the acoustic waves during transit in the ideal atmosphere. The effects of atmospheric absorption, which have been ignored up to this point, introduce attenuation. There are three types of attenuation caused by atmospheric absorption: viscosity, thermal transfer, and molecular relaxation.

The first mechanism of wave attenuation is absorption of wave energy due to the viscosity of the air. The viscosity of the air attenuates the wave by reducing the velocity gradients of sound waves with small momentum transfers between fluid elements. To obtain a quantitative expression of the amount of attenuation expected from the viscosity it is necessary to once again derive the acoustic wave equation with a viscosity term included in the momentum equation. To simplify the derivation, work in one dimension and ignore the effects of gravity.²⁷ Including the viscosity term the one dimensional momentum equation becomes

$$\frac{\partial u}{\partial t} = -\frac{1}{\rho} \frac{\partial p'}{\partial x} + \nu \frac{\partial^2 u}{\partial x^2}, \quad (1.43)$$

where as before p' is the perturbed pressure, ρ is the mass density of the atmosphere, u is the horizontal velocity of the wave, and ν is the viscosity of the air. Following the method developed in Section 1.2, take the partial time derivative of Equation 1.43 and the spatial derivative of the conservation of mass equation to get the wave equation including the term from the viscosity,

$$\frac{\partial^2 u}{\partial t^2} = \frac{\partial^2 u}{\partial x^2} + \nu \frac{\partial^3 u}{\partial x^2 \partial t}. \quad (1.44)$$

To represent the attenuation assume that the solution to Equation 1.44 has complex wave numbers. Assume a solution of the form

$$u = Ae^{i(\omega t - k'x)}, \quad (1.45)$$

where

$$k' = k - i\alpha \quad (1.46)$$

is the complex wave number.²² Substitution of the complex wave number into Equation 1.45 results in a solution of to the acoustic wave equation,

$$u = Ae^{i(\omega t - kx)}e^{-\alpha x}, \quad (1.47)$$

that explicitly shows the effect of the attenuation in the term the exponential term $e^{-\alpha x}$.

To derive an expression for the attenuation coefficient the wave number must be related to frequency and sound speed through the familiar equation

$$k = \frac{\omega}{c_s}. \quad (1.48)$$

The use of a complex wavenumber in Equation 1.48 requires that the sound speed also be expressed as a complex number,

$$c'_s = c_s(1 + i\omega\tau)^{\frac{1}{2}}, \quad (1.49)$$

where τ is the relaxation time of air.²² The relaxation time is defined as the time it takes the perturbed pressure to relax to within $\frac{1}{e}$ of its equilibrium value.²² Using the complex forms of the wavenumber and the sound speed in Equation 1.48 results in a equation in terms of the real sound speed and wavenumber that also includes the attenuation coefficient²²

$$\omega = c_s(k - i\alpha)(1 + i\omega\tau)^{\frac{1}{2}}. \quad (1.50)$$

Either the wavenumber or the wave frequency may be eliminated by equating the real and imaginary parts of Equation 1.50. The real part of Equation 1.50 is

$$k^2 - \alpha^2 = \frac{\omega^2}{c_s^2(1 + \omega^2\tau^2)} \quad (1.51)$$

and the imaginary part is

$$2\alpha k = \frac{\alpha^3\tau}{c_s^2(1 + \omega^2\tau^2)}. \quad (1.52)$$

The attenuation coefficient²² can be expressed as

$$\alpha = \frac{\omega}{c_s\sqrt{2}} \left[\frac{1}{(1 + \omega^2\tau^2)^{\frac{1}{2}}} - \frac{1}{(1 + \omega^2\tau^2)} \right]^{\frac{1}{2}}. \quad (1.53)$$

For the vast majority of fluids the relaxation time is very short and $\omega\tau \ll 1$.²² Using the assumption of a small relaxation time Equation 1.53 is approximately equal to

$$\alpha \approx \frac{\omega^2\tau}{2c}. \quad (1.54)$$

The attenuation coefficient that occurs from the viscosity of the fluid is directly proportional to the square of the frequency. It follows that acoustic waves with higher frequencies will suffer from higher attenuation due to the viscosity of the atmosphere.

The thermal conduction of the air in the atmosphere is the second mechanism by which the atmosphere absorbs the energy of an acoustic wave. When the pressure wave compresses the fluid contained in a volume, the temperature is raised in the volume element according to the ideal gas law, $pV = nRT$.^{||} The increase in the temperature of the fluid in the volume causes a temperature gradient between the volume being compressed and the neighboring fluid volume elements which are less compressed. The temperature gradient results in a flow of heat. The attenuation caused by the transport of heat between the volumes is given by the expression²²

$$\alpha = \frac{\gamma - 1}{2c} \omega^2 \tau,$$

where γ is the power coefficient of the ratio of the specific heats of the air. The attenuation due to heat conduction is smaller than the attenuation due to the viscosity, but is of the same order of magnitude. The sum of the absorption due to the viscosity and thermal conduction is known as the classical attenuation.²²

The last source of absorption in the atmosphere is absorption due to molecular relaxation.²² Molecular relaxation is an effect of the diatomic molecules that are the primary constituents of the atmosphere.²¹ As an acoustic wave compresses a volume element of the fluid, the temperature in the volume element increases. The temperature increase raises the energy contained in the volume element according to the equation

$$\Delta E = c_v \Delta T. \quad (1.55)$$

When a diatomic gas is compressed the work done by the compression is not immediately distributed evenly to all the various degrees of freedom of the diatomic molecule. The delay in the energy distribution occurs as a result of the finite time required for molecular collisions to distribute any excess energy to the rotational and vibrational modes of the diatomic molecules. The delay attenuates the wave by causing the increase in the density of the molecules from the compression of the volume to lag behind the pressure increase

^{||} T is the temperature, p is the gas pressure, R is the universal gas constant, V is the volume and the number of moles is n in the ideal gas law.

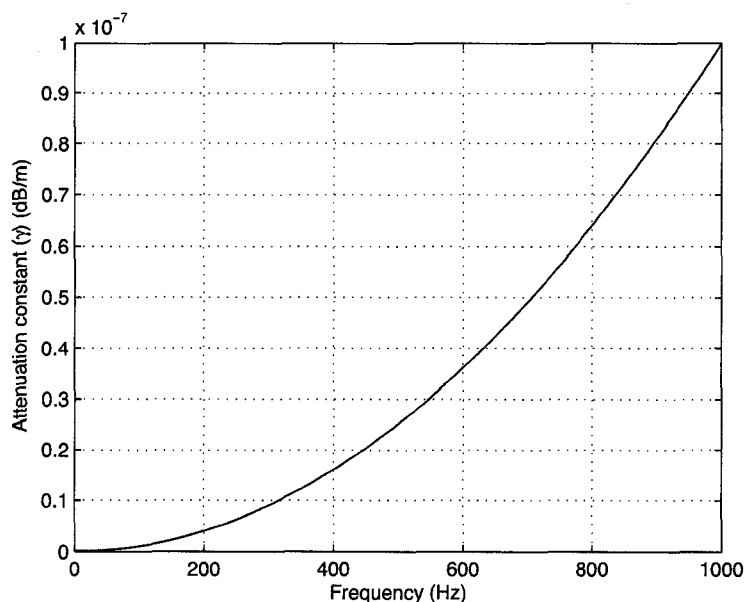


Figure 1.6. The classic attenuation of an acoustic wave as a function of the wave frequency. The atmosphere is assumed to be homogeneous, isothermal, and dry. The relaxation time τ equals 1.7×10^{-10} sec for 20°C.

in the volume due to the compression. The lag occurs because some of the translational energy of the molecules goes into exciting other states in the molecules instead of moving the molecules. Energy is then transferred back from the rotational and vibrational state to the translational state during the expansion part of the acoustic cycle, smoothing out the acoustic wave. The degree to which this process will attenuate the wave is dependent on the frequency of the wave.²¹ If the wave period is much longer than the molecular relaxation time, the molecules can transfer their energy between all states well within the period of the wave making the phase difference between the temperature and pressure changes small. If the wave period is much smaller than the molecular relaxation time the molecules do not have the time to interchange energy between states within the cycle of compression and expansion.

Figure 1.6 illustrates how the classic attenuation constant for the acoustic waves increase as the square of the frequency of the acoustic waves for dry air. Increasing the humidity of the air, q , increases the attenuation caused by the atmospheric absorption of energy

increases faster than the classical attenuation theory can explain. This excess absorption is explained by the absorption due to molecular excitation. As the humidity increases the number of collisions needed to excite the vibrational mode of oxygen is reduced. For dry air, the oxygen is not normally excited because the relaxation time of oxygen is of the order of several seconds.²¹ As the humidity increase the number of collisions need to excite the oxygen decreases. The decrease in the number of collisions required results in a shorter relaxation time for oxygen. With the decrease in the relaxation time of the oxygen molecules the attenuation due to molecular excitation greatly increases. The amount of absorption is still dependent on the proximity of the frequency of the acoustic wave to the relaxation time of the molecules and has a greater attenuating effect when the wave period is comparable to the relaxation time.²² The relaxation time of oxygen is between 0.01 and 1 ms depending on the relative humidity, and does not affect low frequency waves excessively.²⁷

With this knowledge of how a acoustic wave is produced and propagates through the atmosphere the source location problem can now be addressed. In Chapter 2 the statistical tools for describing an acoustic wave in the atmosphere will be developed. Procedures for the estimation of desired wave parameters from the pressure data gathered by an array of sensors will also be discussed in Chapter 2. The performance of the Least Squares estimate of the trace velocity (the speed at which the 3-D acoustic wave appears to traverse the 2-D array), and of the azimuth with the assumed GWU noise field will be explored in Chapter 3. The assumptions about the infrasonic noise field and the effects of the physical infrasonic noise field will be investigated in Chapters 4 and 5. Chapter 4 will address the assumption of Gaussian, white noise and Chapter 5 with the assumption of an uncorrelated noise field.

Chapter 2

Digital Signal Processing & Array Processing

Thus far acoustic waves traveling in the atmosphere have been modeled as deterministic signals, meaning the signal can be expressed by a mathematical formula. In real world situations the corruption of the signal with noise requires that the acoustic waves be treated as random signals. Two examples of pressure data recorded at IS53 are shown in Figures 2.1 and Figure 2.2, one where the signal is clearly visible and the more typical case where the signal is buried in the background noise. In Figure 2.1 an obvious signal can be seen near the center of all eight sensor output plots. The unknown signal in Figure 2.1 is a short duration, high frequency (1 – 10 Hz) signal. This signal is superimposed on a background fluctuating pressure field known as the noise. Due to the high signal-to-noise ratio of the data in Figure 2.1 the signal is clearly visible in the unfiltered raw pressure data. Figure 2.2 shows the more common case where the signal is not clearly separable from the background noise field due to a lower signal amplitude. The noisy data collected at the Fairbanks array was bandpass filtered to isolate the signal of interest from the clutter[†] in the noise field, which is a common practice in the infrasound community. Even though the data has been filtered to remove the effects of clutter, the signal is not clearly visible in the data due to a low signal-to-noise ratio. The lower signal-to-noise ratio reveals that the noise that appeared to be smoothly varying in Figure 2.1 is actually fluctuating rapidly in an apparently random fashion, which is typical for the infrasonic noise field at Fairbanks and Windless Bight. The particular signal in Figure 2.2 is a far-field volcanic signal from Mt. Augustine eruption in January 2006 recorded at the Fairbanks array, but the relation between the signal and noise amplitudes is typical for far-field infrasonic signals at IS53 and IS55. The corruption of the acoustic signals with random noise requires that the signals themselves be treated as random signals.²⁹

Since the signals are random it is only possible to talk about the statistical characteristics of the signals. The statistical description of the signals will provide a look at the average properties of the recorded signals.^{29,19} The necessary statistical tools for analyzing random signals recorded by an array of sensors are developed in this section. The statistical methods of describing the characteristics of random signals are first summarized. The

[†]Clutter are acoustic signals that are not of interest to the signal processor.

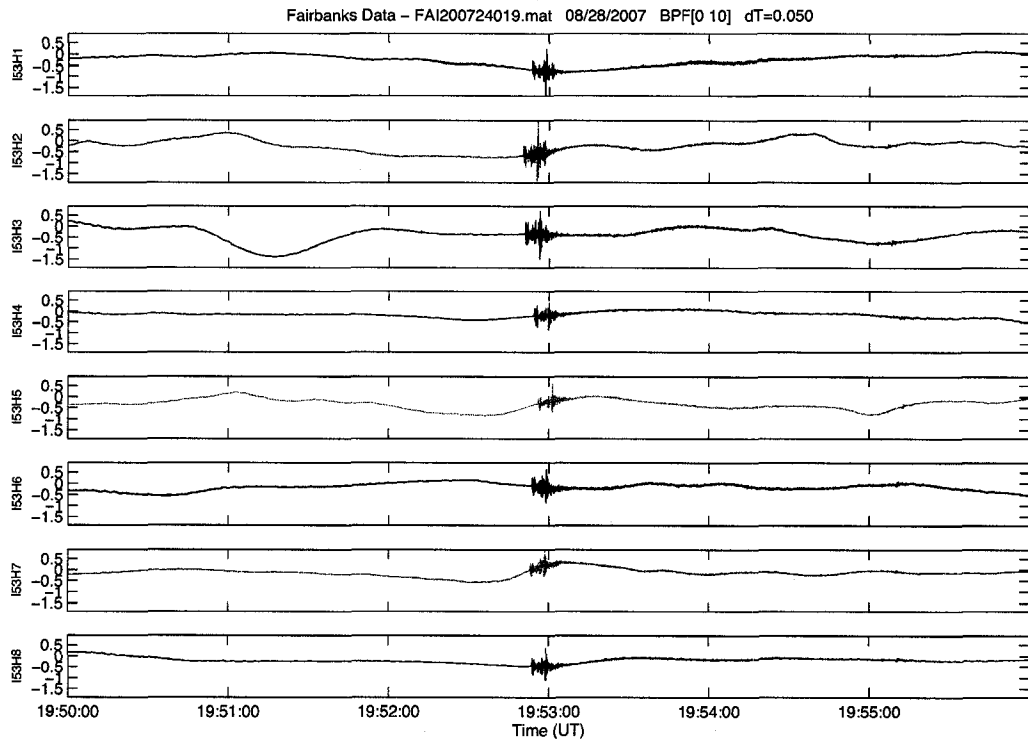


Figure 2.1. Example of a large amplitude signal and the background noise recorded at the Fairbanks (IS53) array. The eight plots correspond to the output of the eight array elements. The y-axis displays the recorded pressure in Pascal and the x-axis is the time index.

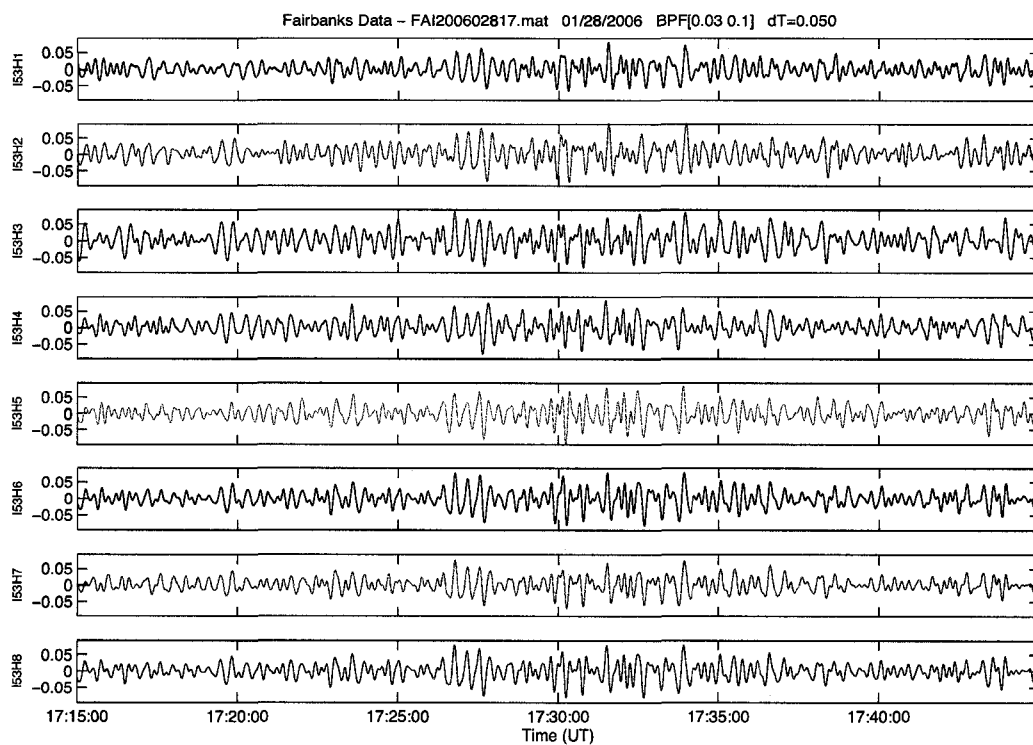


Figure 2.2. Example of a typical low amplitude far-field signal and the background noise recorded at the Fairbanks (IS53) array. The eight plots correspond to the output of the eight array elements. The y-axis displays the recorded pressure in Pascal and the x-axis is the time index.

details concerning the spatial sampling of the random signals, with an array of sensors, will then be presented. Finally, statistical methods of extracting desired information from recorded random signals, via parameter estimation, are summarized.

2.1 Random Vectors

2.1.1 Statistical Description of a Random Process

A compact way to represent a random signal is with a vector, where the elements of this random signal vector are samples of the signal taken at uniformly spaced times. The primary statistical tool used in describing a random signal is the distribution function.^{29,19} If the random signal is described as a random column vector,

$$\vec{x} = \begin{bmatrix} x_1 \\ x_2 \\ x_3 \\ \vdots \\ x_N \end{bmatrix},$$

the distribution function of the random signal vector is defined as

$$F_x(\vec{x}^o) = Pr[\vec{x} \leq \vec{x}^o],$$

where \vec{x}^o is some specific value for the vector and $Pr[]$ represents the probability that the elements of the random vector \vec{x} are less than or equal to the corresponding elements of the vector \vec{x}^o .²⁹ The distribution function is a discrete function of the specific value of the vector \vec{x}^o chosen and therefore is of little practical use in statistical signal processing.²⁹ A more useful quantity used to describe the random vector is the continuous probability density function (pdf). The two quantities are related by the expression

$$F_x(\vec{x}^o) = \int_{\vec{x}_{min}}^{\vec{x}^o} f_x(\vec{x}) d\vec{x}$$

or equivalently,

$$f_x(\vec{x}^o) = \frac{\partial}{\partial x_1} \frac{\partial}{\partial x_2} \cdots \frac{\partial}{\partial x_N} F_x(\vec{x})|_{\vec{x}=\vec{x}^o}. \quad (2.1)$$

The utility of the probability density function stems from the fact that if it is known, expectations can be calculated. The expectation of a quantity derived from the random

vector is the value that the quantity is expected to take on average.²⁹ Only expectations of quantities which can be derived from the random vector whose pdf is being used can be calculated.²⁹ The formula for calculating the expectation is

$$\mathcal{E}\{\Psi(\vec{x})\} = \int_{-\infty}^{\infty} \Psi(\vec{x}) f_x(\vec{x}) d\vec{x}, \quad (2.2)$$

where the pdf $f_x(\vec{x})$ is the pdf of the random vector from which $\Psi(\vec{x})$ is derived.

When $\Psi(\vec{x})$ involves products of the components of \vec{x} , the resulting expectations are referred to as moments of the pdf.^{29,19} For a Gaussian random process the first and second moments completely characterize the distribution.³⁰ The moments are useful in describing the pdf in situations where the pdf is not known and is too difficult to estimate from the available data. The first moment is the mean of the pdf and is given by the equation

$$\begin{aligned} \vec{m}_x &= \mathcal{E}\{x\} = \int_{-\infty}^{\infty} \vec{x} f_x(\vec{x}) d\vec{x} \\ &= \sum_i \frac{x_i}{N}, \end{aligned} \quad (2.3)$$

where N is the number of elements in the vector and \mathcal{E} is the expectation operator. The non-central second moments of the random vector \vec{x} are given by the correlation[†] matrix

$$R_x = \mathcal{E}\{\vec{x}\vec{x}^{*T}\}.$$

In general the correlation matrix for random signals has the form²⁹

$$R_x = \begin{bmatrix} \mathcal{E}\{|x_1|^2\} & \mathcal{E}\{x_1 x_2^*\} & \cdots & \mathcal{E}\{x_1 x_N^*\} \\ \mathcal{E}\{x_2 x_1^*\} & \mathcal{E}\{|x_2|^2\} & \cdots & \mathcal{E}\{x_2 x_N^*\} \\ \vdots & \vdots & \ddots & \vdots \\ \mathcal{E}\{x_N x_1^*\} & \mathcal{E}\{x_N x_2^*\} & \cdots & \mathcal{E}\{|x_N|^2\} \end{bmatrix}. \quad (2.4)$$

The covariance matrix contains the set of central second moments

$$C_x = \mathcal{E}\{(\vec{x} - m_x)(\vec{x} - m_x)^{*T}\} \quad (2.5)$$

and is related to the correlation matrix by the equation

$$R_x = C_x + m_x m_x^{*T}. \quad (2.6)$$

[†]Random variables are said to be correlated if knowledge about one of the variables provides some information about the other random variable.³⁰

The diagonal elements of the covariance matrix have the form of the variance of the individual variables,

$$\sigma^2 = \sum_i (x_i - m_x)^2, \quad (2.7)$$

while the off-diagonal elements are the covariances, which measure how strongly the two measurements are related to each other.³⁰ Most infrasound data is collected experimentally by discrete sampling of the continuous pressure field present in the atmosphere. The sampling results in the collection of discrete random signals. With discrete random signals it is necessary to use the discrete form for the mean,

$$m_x[n] = \mathcal{E}\{x[n]\}, \quad (2.8)$$

and for the correlation matrix,

$$R_x[n_1, n_0] = \mathcal{E}\{x[n_1]x^*[n_0]\}, \quad (2.9)$$

where n is the sample number.

For a stationary random process[†] the pdf is only a function of the spacing between the elements of the random vector.²⁹ The mean and correlation of a stationary random process will depend only on the spacing between the sample points. By the definition of a stationary process the mean is a constant,

$$m_x[n] = m_x. \quad (2.10)$$

By defining the difference between the two sample points as the lag²⁹, the correlation becomes a function of only the lag,

$$R_x[n_1, n_0] = R_x[l] = \mathcal{E}\{x[n]x^*[n-l]\} \quad (2.11)$$

where l is the lag between the two sample points. By the same token, the covariance is also a function of the lag and it is given by

$$C_x[n_1, n_0] = C_x[l] = \mathcal{E}\{(x[n] - m_x)(x[n-l] - m_x)^*\}. \quad (2.12)$$

The interrelation between the covariance and the correlation in terms of the lag becomes

$$R_x[l] = C_x[l] + |m_x|^2. \quad (2.13)$$

[†]A random process is said to be stationary if its statistical description is not a strong function of time.^{29,19}

When the lag equals zero some useful quantities are given by the correlation and the covariance. The average power of the random process is given by the correlation at zero lag and the variance of the random process is given by the covariance at zero lag²⁹

$$\begin{aligned} C_x[0] &= \mathcal{E}\{|x[n] - m_x|^2\} \\ &= \sigma_x^2. \end{aligned} \quad (2.14)$$

If a quantity is a function of two random vectors – a multivariate process – the joint probability density function must be used in the calculation of the expectation of any quantities derived from the multivariate process.²⁹ The joint pdf is defined by a joint distribution function. The joint distribution function gives the probability of the joint event $\vec{x} \leq \vec{x}^o$ and $\vec{y} \leq \vec{y}^o$. The joint pdf is related to the joint distribution function by

$$f_{x,y}(\vec{x}^o, \vec{y}^o) = \frac{\partial}{\partial x_1} \frac{\partial}{\partial x_2} \cdots \frac{\partial}{\partial x_N} \frac{\partial}{\partial y_1} \frac{\partial}{\partial y_2} \cdots \frac{\partial}{\partial y_N} F_{x,y} |_{\vec{x}=\vec{x}^o, \vec{y}=\vec{y}^o}. \quad (2.15)$$

The expectation of a multivariate process is defined by

$$\mathcal{E}\{\Psi(\vec{x}, \vec{y})\} = \int_{-\infty}^{\infty} \int_{-\infty}^{\infty} \Psi(\vec{x}, \vec{y}) f_{x,y}(\vec{x}, \vec{y}) d\vec{x} d\vec{y}. \quad (2.16)$$

The dependence of a process on two random vectors does not change the first moments at all, but it will effect the second moments. The correlation matrix becomes the cross-correlation matrix,

$$R_{xy} = \mathcal{E}\{\vec{x}\vec{y}^{*T}\}, \quad (2.17)$$

and the covariance matrix becomes the cross-covariance matrix,

$$C_{xy} = \mathcal{E}\{(\vec{x} - m_x)(\vec{y} - m_y)^{*T}\}. \quad (2.18)$$

The discrete form of the multivariate mean is the same as the discrete form the one variable mean. The discrete form of the correlation matrix can be extended to accommodate two random processes. If the two processes are jointly stationary the cross-correlation matrix is given by

$$R_{xy}[n_1, n_0] = \mathcal{E}\{x[n]y^*[n-l]\}. \quad (2.19)$$

The cross-covariance matrix is calculated according to the equation

$$C_x[n_1, n_0] = C_x[l] = \mathcal{E}\{(x[n] - m_x)(y[n-l] - m_y)^*\} \quad (2.20)$$

with the appropriate means for the x and y processes. The relation between the covariance and the correlation is given by

$$R_{xy}[l] = C_{xy}[l] + m_x m_y^*. \quad (2.21)$$

Using the definitions of the second moments for two random processes, the definitions can be expressed in terms of the cross-correlation and cross-covariance. The random vectors are uncorrelated if the cross-covariance is equal to zero.²⁹ The vectors are orthogonal if the cross-correlation is zero.²⁹

2.1.2 Frequency Domain Description of a Random Process

The first and second moments of a random process are calculated in the time domain of the random process. A useful tool in the analysis of deterministic sequences contained in the random time series is the frequency domain description of a random process.^{29,19,31,32} The frequency domain is the Fourier transform of the time domain. Two frequency domain quantities will be used extensively in this thesis and will be introduced in this section: the power spectral density function (PSD) and the magnitude squared coherence spectrum (MSC) of a time series.

The power spectral density function is the Fourier transform of the correlation function of the random process. The power spectral density function is estimated by taking the discrete Fourier transform of the correlation function²⁹,

$$S_x(e^{i\omega}) = \sum_{l=-\infty}^{\infty} R_x[l] e^{-i\omega l}, \quad (2.22)$$

where ω is the signal frequency, l is the lag, and R_x is the correlation function. The power spectral density represents an estimate of the power contained in the random process at each frequency.

The cross-power density function can be found by taking the discrete Fourier transform of the cross-correlation function,

$$S_{xy}(e^{i\omega}) = \sum_{l=-\infty}^{\infty} R_{xy}[l] e^{-i\omega l}. \quad (2.23)$$

The cross-power spectrum is a plot of the cross-power density plotted against the frequency. The cross-power spectrum can be interpreted as a measure of the correlation between the

two random processes, x and y , at a given frequency.³¹ The square of the normalized cross-spectrum is called the magnitude squared coherence (MSC) which is the cross-power spectrum normalized by the square root of the individual power spectral densities. The MSC is given by the formula

$$|\Gamma_{xy}|^2 = \frac{|S_{xy}(e^{i\omega})|^2}{S_x(e^{i\omega})S_y(e^{i\omega})}. \quad (2.24)$$

The value of the MSC can range between 0, when the two processes are absolutely uncorrelated, and 1, when the processes are perfectly correlated.²⁹

The PSD and the MSC are generally not known and must be inferred from the measured data. The process of inferring desired quantities from measured data is known as estimation.¹⁹ There are two common methods for estimation of the power spectrum, the correlogram and the periodogram.^{29,19} The correlogram uses an estimate for the correlation function and Equation 2.22 to estimate the PSD. The estimate of the correlation function is given by²⁹

$$\hat{R}_x[l] = \frac{1}{N_s} \sum_{n=0}^{N_s-1-l} x[n+l]x^*[n], \quad (2.25)$$

where N_s is the total number of data samples, l is the lag, and $x^*[n]$ is the complex conjugate of the sequence x . The periodogram is given by the formula²⁹

$$\hat{P}_x(e^{i\omega}) = \frac{1}{N_s} |X(e^{i\omega})|^2, \quad (2.26)$$

where $X(e^{i\omega})$ is the Fourier transform of the sequence x . The periodogram is more convenient to compute than the correlogram.²⁹

Assuming that the underlying process is stationary, there are several methods to decrease the variance of the PSD estimate and improve the performance of the basic periodogram or correlogram PSD estimate. The first method is to average a number of different PSD estimates. The statistical properties of the periodogram do not improve with greater lengths of data.^{29,33} A more efficient use of long data segments is break the data into smaller segments and average the resulting PSD estimates.³³ The method of averaging several PSD estimates is known as the Bartlett procedure. When employing the Bartlett procedure the variance of the PSD estimate is decreased by a factor equal to the inverse of the number of data sub-segments if the sub-segments of the data are uncorrelated.²⁹ The variance of the

PSD estimate can also be decreased by smoothing the correlation function estimate with a window before Fourier transformation. The decrease in variance when using the Blackman-Tukey procedure is dependent on the window size and shape.³⁴ It has been argued that when the transformed window is narrow compared to the variations in the spectrum, and the half length of the window is much smaller than the data length, the variance in the PSD estimate is reduced by

$$\frac{1}{N_s} \sum_{l=-L+1}^{L-1} w^2[l], \quad (2.27)$$

where N_s is the number of data samples, L is the half length of the smoothing window, and the sequence w is the smoothing window.³⁵ The final method of reducing the variance of the PSD estimate is the Welch method.³⁶ The Welch method, which is used extensively in the following work, combines smoothing windows and averaging the PSD estimates. The decrease in the PSD estimate variance when using the Welch method is approximately the same as the Bartlett method.²⁹

The Bartlett and Welch procedures both segment the data in order to decrease the variance of the PSD estimate. The objective is to estimate the power spectrum of the data with high fidelity and high stability.³¹ High fidelity is obtained when the bias in the estimated spectrum is small. A spectral estimate with high stability has a small estimate variance. The data segment chosen when estimating a smoothed spectrum must be large enough to allow estimation of the low frequency components of the data set, but short enough to allow for averaging to improve the stability. There exists no set procedure to determine the optimal data segment length when estimating the power spectrum. The process for determining the segment length while balancing the fidelity and the stability is known as the window closing procedure.³¹ The technique of window closing involves estimating a smoothed spectral estimate with a large frequency space window and then estimating the spectrum using progressively smaller frequency space windows until an acceptable spectral estimate has been produced.³¹ Generally, a compromise between fidelity and stability suitable for the desired application must be found during the window closing process.

2.2 Arrays

Sensors are used to convert the propagating atmospheric wave energy into electric signals that can be measured and recorded. The recorded electric signals result in a timeseries that represents the response of the instrument to the physical signal propagating past the sensor. Pressure waves vary in both space and time and any measurement device used should be able to sample the propagating wave spatially and temporally. There are two general kinds of sensors used to sample the field, directional and omnidirectional.²⁴ Directional sensors gather the energy propagating from a specific direction and spatially integrate the energy in order to focus the sensor on the desired propagation direction. Omnidirectional sensors have no preferred direction of propagation and simply sample the environment at the location of the sensor. A group of individual sensors that are used to spatially sample the environment is called an array.²⁴

The sampling process used by an array converts a wave field that is continuous in both space and time into a discrete time and space series. According to the Sampling Theorem,³⁷ under certain conditions, a discrete sample of a function can be used to represent the complete set of function values without any loss of information. Since the function is sampled in both space and time, there will be two separate but similar conditions for the validity of sampling theorem. The condition for the sampling theorem to be valid for both the temporal sampling and the spatial sampling is that the function be “bandlimited” in the temporal domain and the spatial domain respectively. The function is bandlimited in the temporal domain if the Fourier transform of the function is zero for temporal frequencies greater than some maximum temporal frequency, f_{\max} .³⁷ The sampled function must also be bandlimited in the spatial domain and can not have spatial frequencies, wavenumbers, greater than some maximum spatial frequency, k_{\max} .²⁴

The sampling theorem allows the representation of a continuous function with a discrete series sampled from the function.³⁷ Due to physical limitations of computer memory it is desirable to sample the function as infrequently as possible to limit computer file sizes. The limiting factor on how few samples are needed to reconstruct the function accurately is dependent on the bandwidth of the function.³⁷ Due to the sampling of the continuous function, the Fourier transform of the sampled function is composed of replications of the Fourier transform of the continuous function. As long as the sample frequency is sufficiently

high, the replications do not overlap and the Fourier transform of the continuous function can be estimated using the Fourier transform of the sampled function.³⁷ When the sampling frequency is not sufficiently high, the replications of the continuous Fourier transform overlap and it is no longer possible to accurately estimate the continuous Fourier transform from the Fourier transform of the sampled function. The overlap of the replications of the continuous Fourier transform is known as aliasing. To avoid aliasing the sample frequency must be at least twice the upper edge of the continuous function bandwidth; this is known as the Nyquist frequency.³⁷ The need to avoid aliasing dictates the minimum temporal sample rate for an array.

The maximum distance between sensors in an array is also dictated by the need to avoid spatial aliasing. Spatial aliasing of the wavefunction can be avoided by using the minimum spatial sample rate, which is given by

$$k_{\text{sample}} = 2 k_{\text{max}}. \quad (2.28)$$

The maximum distance between the elements of the array can be found by recalling that the wavelength is the inverse of the spatial frequency, giving

$$d = \frac{1}{2 k_{\text{max}}} \quad (2.29)$$

as the maximum distance between the elements of the array.²⁴ For certain applications it is desirable to have the maximum allowable distance between elements of an array. The source localization problem is one of the applications that benefit by placing the array element at maximum inter-element distance. Placing the array elements at the maximum allowable distance from each other maximizes the time it takes an acoustic wave to travel between the elements of the array. The maximization of the time delays between the array elements improves the accuracy of the time of flight calculated from the recorded data. A large spatial separation also reduces the effects of noise on estimations of the time of flight between the array elements made using the collected data due to the spatial decoherence of the noise. (This will be discussed in more detail in Chapter 5.)

The minimum temporal sampling frequency is given by³⁷

$$f_s = 2 f_{\text{max}} \quad (2.30)$$

and, by using the relation between the frequency and period, the minimum temporal sample spacing is found to be

$$T_s = \frac{1}{2 f_{\max}}. \quad (2.31)$$

A relation between bandlimiting in time domain and spatial domain is given by the formula for the propagation speed of a wave. If the function is bandlimited in the time domain with temporal frequencies less than f_{\max} , then using the formula for the propagation speed of a wave,

$$c = \frac{2\pi f}{k}, \quad (2.32)$$

the function can have no wavenumber greater than $\frac{2\pi f}{c}$. The anti-aliasing requirements stated in Equation 2.29 and Equation 2.31 can be combined to produce a relationship between the minimum time domain and the minimum spatial domain sampling rates,

$$d = \frac{c T_s}{2\pi}. \quad (2.33)$$

The placement of sensors in the array determines the spatial sampling rate and, in general, cannot be easily moved once deployed. The temporal sampling rate is determined by electronics and can be adjusted according to Equation 2.33. Arrays can be designed to increase the sensitivity to bandwidths of the waves of interest. A consequence of the dependence of the bandwidths on the wave is that different array geometries are responsive to waves with different frequencies. An array with a large aperture will detect low frequency waves better than an array with a small aperture, just as a small aperture array will be superior at detecting high frequency waves.²⁴

The aperture of an array acts as a spatial window through which the wavefield is observed.²⁴ The observed spectrum of the wavefield is convolved with the Fourier transform of the aperture window. Define the output of the sensor as

$$z(\vec{x}, t) = w(\vec{x}) f(\vec{x}, t), \quad (2.34)$$

where $w(\vec{x})$ is an array aperture weighting function and $f(\vec{x}, t)$ is the space-time signal.²⁴ To obtain the spectrum of the sensor output take the space-time Fourier transform of the sensor output

$$Z(\vec{k}, f) = \frac{1}{(2\pi)^3} \int_{-\infty}^{\infty} W(\vec{k} - \vec{l}) F(\vec{l}, f) d\vec{l}. \quad (2.35)$$

Notice that the spectrum of the sensor output is a convolution over wavenumber between the space-time signal and the aperture smoothing function, $W(\vec{k})$.²⁴ The convolution between the two functions smooths the spectrum of the wavefield with the transform of the aperture window.³⁷ The aperture weighting function of an array is a discrete function represented in the time domain by w_m . For instance, if the spatially sampled wavefield is sampled every d meters, the wavefield can be represented by $y_m(t) = f(md, t)$. The smoothed sensor output²⁴ is

$$z_m(t) = w_m y_m(t) \quad (2.36)$$

and the frequency-wavenumber spectrum is given by the convolution

$$Z(k, f) = \frac{d}{2\pi} \int_{-\frac{\pi}{d}}^{\frac{\pi}{d}} Y(l, f) W(k - l) dl, \quad (2.37)$$

where

$$W(k) = \sum_m w_m e^{ikmd}. \quad (2.38)$$

The aperture smoothing function alters the wavenumber-frequency spectrum of the sampled wavefield.²⁴ This alteration affects the power spectrum and coherence spectrum estimated from the data collected with an array. The Fourier transform of the correlation function of a random signal is the power spectral density function of the random signal.^{29,19} The cross-correlation function of jointly stationary random processes is defined as

$$R_{xy}[l] = \mathcal{E} \{x[n]y^*[n - l]\}. \quad (2.39)$$

In an array of sensors the wavefield is sampled at discrete locations and the output of the N sensors can be treated as N different random signals. Since the wavefield is only sampled at specific locations in space, the output of the m^{th} sensor is the product of the continuous wavefield and a spatial weighting function,

$$y_m(t) = w_m f(\vec{x}_m, t). \quad (2.40)$$

The $(m_i, m_j)^{th}$ entry in the spatiotemporal cross-correlation matrix is given by

$$\begin{aligned} \mathbf{R}_{m_i, m_j}(\tau) &= [w_{m_i} f(\vec{x}_{m_i}, t_i)] [w_{m_j} f(\vec{x}_{m_j}, t_j)]^* \\ &= w_{m_i} w_{m_j}^* R_f(\vec{x}_{m_i} - \vec{x}_{m_j}, \tau). \end{aligned} \quad (2.41)$$

Notice that the spatiotemporal correlation matrix is just the correlation function of the wavefield sampled by the array at a point in space. The correlation function of the wavefield is sampled by the product of $w_{m_i}w_{m_j}^*$, which is an element of the co-array.²⁴ The co-array is defined as the sum of $w_{m_i}w_{m_j}^*$ over indices of equal baselines

$$c(\vec{\chi}) = \sum_{(m_i, m_j) \in \vartheta(\vec{\chi})} w_{m_i}w_{m_j}^*, \quad (2.42)$$

where $\vartheta(\vec{\chi})$ represents the set of indices for which $\vec{x}_{m_i} - \vec{x}_{m_j} = \vec{\chi}$.²⁴ For an array with unit weighting the co-array is the matrix of inter-sensor separations. To avoid aliasing in the spatial frequency domain the co-array sample spacing must be smaller than half the wavelength corresponding to the wavefield's shortest wavelength, which is the main result of the Nyquist theorem.²⁴

The results of any study done with an array of sensors are dependent on the geometry of the particular array used to perform the measurement. The arrays at Fairbanks (IS53), and Windless Bight, Antarctica (IS55), both have identical transducer geometries; but the actual realizations in the field have slight differences[§]. Both arrays are digital microphone arrays that use a digitizer to passively sample the pressure field at a sampling frequency of 20 samples per second. The arrays are comprised of eight Model 5 Chaparral microphones with Geotech digitizers (D. Osborne, personal communication, January 2007).

The arrays are both eight sensor arrays arranged in an outer pentagon and an inner triangle as shown in Figure 2.3. The outer pentagon sensors are about one kilometer from the center of the array and the inner triangle sensors are approximately one hundred meters from the center of the array. The Windless Bight array (WBA) is located on the Ross ice shelf, 77.7416 degrees South latitude and 167.5820 degrees East longitude, about 30 kilometers from McMurdo station. The terrain WBA is situated in is a level, perpetually snow-covered sheet of ice with no vegetation. The Fairbanks array is located on the campus of the University of Alaska Fairbanks, 64.8671 degrees North latitude and 147.8559 degrees West longitude, on a hillside that is covered by a boreal forest consisting mainly of black spruce trees.

[§]Additional information about the arrangement of the arrays and the terrain surrounding the arrays can be found on the UAF infrasound website.³⁸

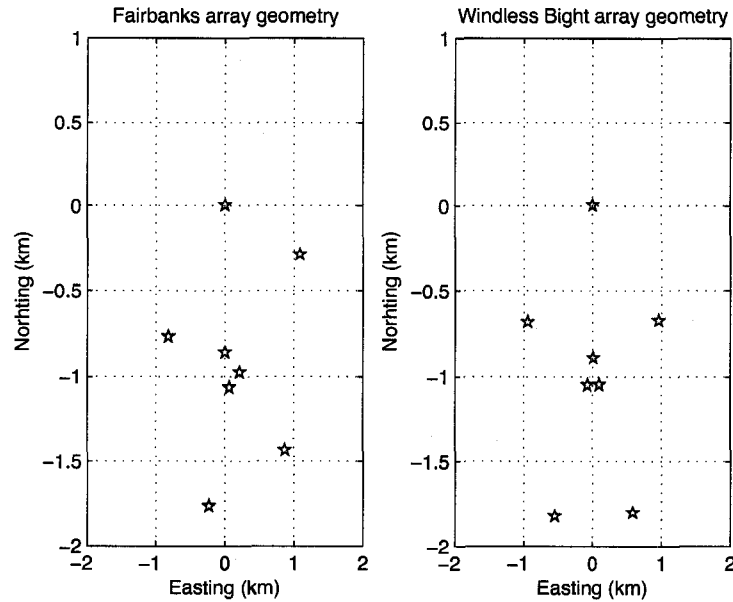


Figure 2.3. The approximate array geometry of the Fairbanks (IS53) and Windless Bight (IS55) arrays. The pentagrams denote the location of the individual array elements.

2.3 Parameter Estimation

2.3.1 Estimation Background and Methods of Estimation

To estimate useful quantities from the raw recorded data, estimation theory must be employed.^{29,19,31} An estimated parameter will be a function of the observed data since the estimate of the parameter is derived from the observed data. The estimated quantity will therefore take on the properties of the data used to derive the estimate. If the variable is derived from a random signal, the estimate of the variable will be a random variable.¹⁹ To reflect this explicit dependence on the observations, the estimate of the variable is written as

$$\hat{\theta}_N = \hat{\theta}_N(x), \quad (2.43)$$

where N is the number of observations and x is the recorded data.

Comparison of one method of estimation with another involves several qualities of the estimate. One of the most important statistical quantities used to compare the effectiveness of different estimates is the bias of the estimate.^{29,19} An estimate of a random variable, θ , is

unbiased if the expectation value of the estimate is equal to the true value of the variable,

$$\mathcal{E}\{\hat{\theta}_N\} = \theta. \quad (2.44)$$

If the expectation value of the estimated variable does not equal the true value of the variable,

$$\mathcal{E}\{\hat{\theta}_N\} = \theta + b(\theta), \quad (2.45)$$

the estimate is said to be biased by the quantity $b(\theta)$. It is possible that an estimate is only unbiased if the number of observations, N , is very large. This is known as an asymptotically unbiased estimate and is represented by the expression

$$\lim_{N \rightarrow \infty} \mathcal{E}\{\hat{\theta}_N\} = \theta. \quad (2.46)$$

The Cramér-Rao lower bound is also used to describe the performance of an estimate. The Cramér-Rao lower bound states that the variance of any unbiased estimate is given by

$$\text{Var}[\hat{\theta}] \geq \frac{1}{\mathcal{E}\left\{\left(\frac{\partial \ln f_x(x;\theta)}{\partial \theta}\right)^2\right\}}, \quad (2.47)$$

where $\left(\frac{\partial \ln f_x(x;\theta)}{\partial \theta}\right)$ is the partial derivative of the log likelihood function. The likelihood function is defined as the density function taken as a function of θ for fixed values of the observations.²⁹ An estimate is said to be most efficient when the estimate satisfies the Cramér-Rao lower bound with equality.¹⁹

There are many different schemes for estimating variables from data collected. All the different estimation methods fall into two basic approaches to parameter estimation.^{||} The first method of parameter estimation assumes that the parameter vector, $(\vec{\theta})$, is a deterministic constant. Methods of estimation that use this assumption are called classical approaches to the estimation problem. In the classical approach the information contained in the data is summarized by a pdf that is determined from the data collected. The pdf is functionally dependent on the parameter vector in the classical estimation method.¹⁹ The second method of estimation assumes that the parameter vector is a realization of a random vector. Methods making use of this assumption are known as Bayesian approaches. Bayesian approaches make use of a pdf that describes any knowledge of the parameter vector

^{||} This material can be found in the book by S.M. Kay, Chapter 14.¹⁹

before any data is collected. In Bayesian approaches there must be some prior knowledge about the pdf of the parameter vector, $(\text{pdf}(\vec{\theta}))$, while the classical approach requires no prior knowledge of the parameter vector.

There are some general rules to assist in deciding between the two approaches to parameter estimation.¹⁹ The flow chart pictured in Figure 2.4 illustrates the process for choosing between the approaches to the estimation problem.[†] Given a signal processing problem the first step shown in Figure 2.4 is to determine if dimensionality is a problem in the desired parameter estimate. A dimensionality problem occurs when the number of data points is not sufficiently larger than the number of parameters being estimated causing a lack of averaging.¹⁹ Regardless of the answer to the question of dimensionality, the next step is to determine if there is prior knowledge about the parameters available. If prior knowledge is available the Bayesian approach to estimation should be used regardless of the question of dimensionality. If dimensionality is not a problem and no prior knowledge about the parameters is available then the classical approach should be used. The last possible path through the flow chart leads to the last choice, find a new data model or take more data. If it is not possible to either take more data or try a different data model then there is no estimation method available. With more data or a new data model the classical approach should be employed. For the specific case of acoustic source localization the classical approach is the most appropriate, because there should be no prior knowledge of the location of the source available, making it impossible to use the Bayesian approach to estimate the parameters.

2.3.2 Classical Estimators and the MVU Estimate

Although the choice of a particular classical estimator is dependent on many considerations, the data model is the main factor in choosing an estimator.¹⁹ The data model should be complex enough to describe the important features of the data, yet simple enough to allow the best estimator to be used. The different estimators are based on different assumptions about the data and process models. Out of all the estimators that can be used to estimate the parameters the “best” possible estimator is the unbiased estimator with the smallest variance for all values of the parameters. This estimator is called the minimum variance

[†]This flow chart has been adapted from Chapter 14 of S.M. Kay's book.¹⁹

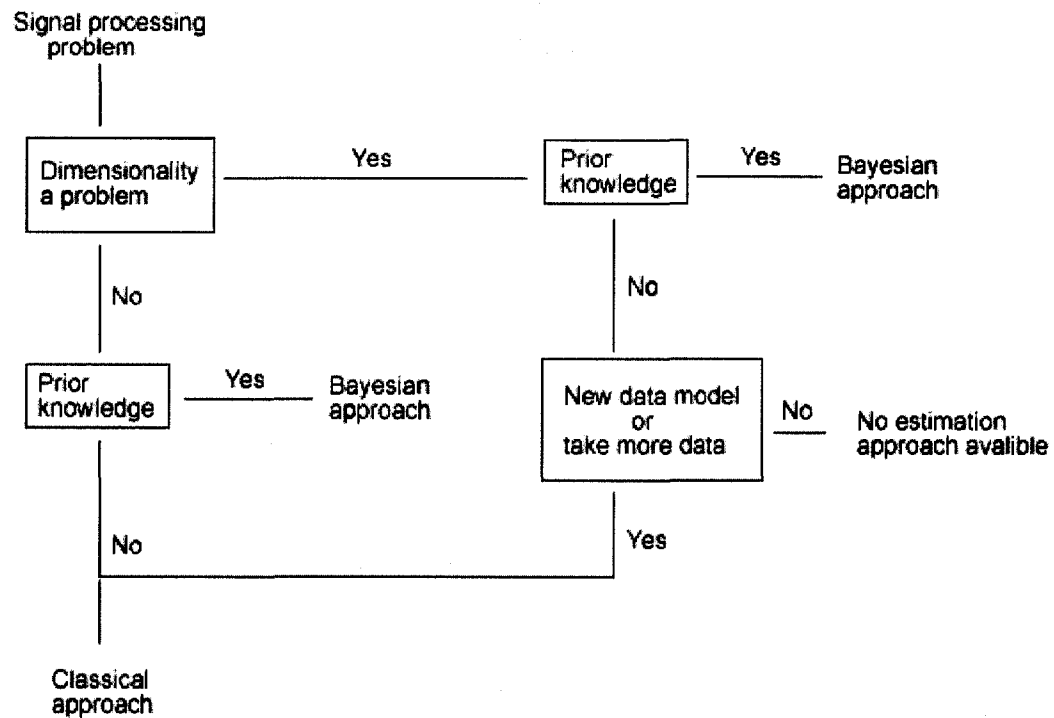


Figure 2.4. Graphical representation of the decision process to choose the general method of parameter estimation. The decision process starts in the top left corner of the figure. The process evolves by moving along the paths until a style of estimation is chosen or the determination of no estimation method available is reached.

unbiased estimator (MVU). There is no guarantee that the MVU estimator exists, and there is no standard method for finding the MVU when it does exist.¹⁹ The common classical estimators will be briefly described along with the data model assumptions.

There are three classical estimators that do not make use of a data model, but require that the pdf that describes the data is known. The Cramer-Rao lower bound is satisfied with equality when

$$\frac{\partial \ln p(\vec{x}; \vec{\theta})}{\partial \vec{\theta}} = I(\vec{\theta})(\vec{g}(\vec{x}) - \vec{\theta}), \quad (2.48)$$

where $I(\vec{\theta})$ is a matrix dependent on the parameter vector $\vec{\theta}$ and $\vec{g}(\vec{x})$ is a function of the data \vec{x} . If the equality condition of the Cramér-Rao lower bound is satisfied, the Cramér-Rao lower bound can be used to estimate parameters from the data and the estimator is $\vec{g}(\vec{x})$. If it exists this estimator will be the MVU estimator.¹⁹

The next estimator that only requires knowledge of the pdf is the Rao-Blackwell-Lehmann-Scheffe estimator. If the pdf can be factored, then

$$f(\vec{x}; \vec{\theta}) = g(\vec{T}(\vec{x}), \vec{\theta})h(\vec{x}), \quad (2.49)$$

where $h(\vec{x})$ is a function of only \vec{x} , and a complete, sufficient statistic exists. Then, if the expectation value of \vec{T} is $\vec{\theta}$, the estimator is just \vec{T} . If the expectation value of \vec{T} is not the parameter vector, a function of \vec{T} whose expectation value is $\vec{\theta}$ must be found and the function of \vec{T} will be the estimate. If this estimate exists it will be the MVU estimate, but this method will fail if a sufficient statistic does not exist.¹⁹

The final classical estimator that only requires a knowledge of the pdf of the data is the Maximum Likelihood Estimator (MLE). The MLE is defined as the value of $\vec{\theta}$ that maximizes the log of the likelihood function when \vec{x} is replaced by the observed data. The likelihood function is the density function of the data when it is viewed as a function of the parameter θ . The MLE is defined²⁹ as

$$\hat{\theta}_{ml} = \operatorname{argmax}_{\theta} f_{\vec{x}; \theta}. \quad (2.50)$$

If the MVU exists, then the MLE will produce the MVU estimate.¹⁹

The remaining common classical estimators make use of data models, but do not require a knowledge of the pdf of the data. The Best Linear Unbiased Estimator (BLUE) makes

the assumption that the data is linear and of the form

$$\vec{x} = H\vec{\theta} + \vec{w}, \quad (2.51)$$

where H is a known matrix and the expectation of \vec{w} is zero. The BLUE is given by

$$\hat{\vec{\theta}} = (H^T C^{-1} H)^{-1} H^T C^{-1} \vec{x} \quad (2.52)$$

where C is the covariance matrix of the data. The BLUE has the minimum variance of all estimators that are linear in \vec{x} and will be the MVU if \vec{w} is a Gaussian random vector.¹⁹

The second classical estimator that is data model dependent is the Least Squares Estimator (LSE). The LSE assumes that the data is composed of a signal that depends explicitly on the unknown parameters and an additive noise vector,

$$\vec{x} = s(\vec{\theta}) + \vec{w}. \quad (2.53)$$

The method for determining the LSE will be discussed in great detail in Section 2.4. If the noise vector, \vec{w} , is a Gaussian random vector the LSE is equivalent to the MLE estimate.¹⁹

The final common classical estimator is the Method of Moments. The assumption necessary to implement the Method of Moments estimator is that there are p known moments of the data that depend on the parameter vector in a known way. If the moments are expressed as

$$\vec{\mu} = \vec{h}(\vec{\theta}), \quad (2.54)$$

where \vec{h} is an invertible function of the parameter vector, then the estimator is

$$\hat{\vec{\theta}} = \vec{h}^{-1}(\hat{\vec{\mu}}), \quad (2.55)$$

where $\hat{\vec{\mu}}$ is the vector of estimates of the moments. The Method of Moments estimator is not, in general, the best estimator, but it is usually the most straightforward estimator to implement.¹⁹

There are some general rules to help choose an estimator for a given parameter estimation problem.¹⁹ The flow chart in Figure 2.5 illustrated the method used to choose a classical parameter estimate.[†] To start the process of choosing a classical estimate the knowledge

[†]This flow chart has been adapted from Chapter 14 of S.M. Kay's book.¹⁹

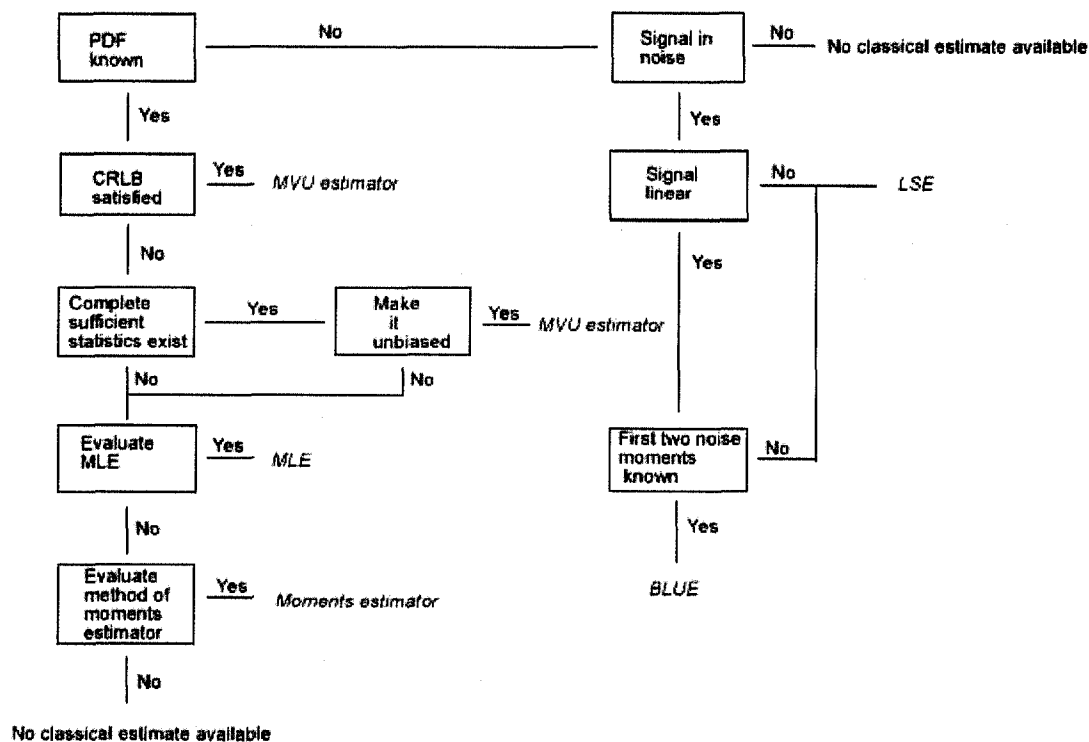


Figure 2.5. Flow chart illustrating the process of choosing a classical parameter estimator. The process starts in the upper left hand corner of the figure. The choices then evolve down and to the left until the most appropriate classical parameter estimate has been chosen.

of the pdf of the data must be taken into account. If the pdf is known, travel down the “yes” decision track in Figure 2.5 to the Cramér-Rao lower bound. If the Cramér-Rao lower bound is satisfied with equality use the Cramér-Rao lower bound estimator. If the Cramér-Rao lower bound is not satisfied with equality the next step is to determine if the complete sufficient statistic exists. If the statistic exists and it can be made unbiased, the estimator to use is the Rao-Blackwell-Lehmann-Schette estimator. If the statistic does not exist or cannot be made unbiased the next step is to evaluate the Maximum Likelihood Estimator. If the MLE can be evaluated it is the estimator to use, otherwise evaluate the Method of Moments Estimator. In the event that the Method of Moments cannot be evaluated there is no classical estimate available for the signal processing problem being attempted. The other major leg of the choice flow chart in Figure 2.5 is for the situation where the pdf of the data is not known. The data model being used is the first choice on this path of the choice chart. If the data cannot be modeled as a signal in noise no classical estimator is available. If the data can be modeled as a signal in noise and is not assumed to be linear then the Least Squares Estimator must be used to estimate the parameters. If the data is assumed to be linear and the first two moments of the noise are known then the Best Linear Unbiased Estimator can be used, if the first two noise moments are not known then the Least Squares Estimator must be employed to determine the parameters.

2.4 Linear Least Squares Estimation

The most appropriate method of classical estimation in the source location problem is Least Squares Estimation. In the process of determining the source location it is not assumed that the pdf of the desired parameters is available, nor is it assumed that the first two moments of the noise are known. As can be seen in Figure 2.5 the most appropriate estimation method in this particular case is the Least Squares Estimator. The estimate made using Least Squares Estimation involves the solution of linear equations and a knowledge of the first and second moments of the pdf of the random variable, but not knowledge of the moments of the noise. Since the Least Squares Estimator involves linear equations it is sometimes known as “linear mean-square” estimation.^{19,39}

To formally develop the method of linear mean-square estimation, consider an estimate

of the quantity y with the form

$$\hat{y} = ax + b, \quad (2.56)$$

where the constants a and b are parameters that will be chosen in order to minimize the expectation of the square of the difference between y and the estimate \hat{y} .¹⁹ Define the mean-square error as

$$\varepsilon = \mathcal{E}\{(y - \hat{y})^2\}, \quad (2.57)$$

where the error is defined to be $\epsilon = y - \hat{y}$. Equation 2.57 has the form of the second moment of the error, ϵ , and may be replaced with the known result for the second moment,

$$\varepsilon = m_\epsilon^2 + \sigma_\epsilon^2, \quad (2.58)$$

where m_ϵ is the mean of the error and σ_ϵ^2 is the variance of the error.¹⁹ Equation 2.58 will only be minimized if the mean of the error is set to zero. The mean, unlike the variance, can always be set to zero by detrending the recorded data.¹⁹ With the mean of the error set to zero, one of the free parameters in Equation 2.56 can now be eliminated,

$$\begin{aligned} m_\epsilon &= 0 \\ \mathcal{E}\{y - \hat{y}\} &= 0 \\ \mathcal{E}\{y - ax - b\} &= 0 \\ \mathcal{E}\{y\} - a\mathcal{E}\{x\} - \mathcal{E}\{b\} &= 0. \end{aligned} \quad (2.59)$$

The expectation value of the constant b is equal to b . The expectation values of y and x are the mean of y , m_y , and the mean of x , m_x .²⁹ The form of b that will minimize the square error can now be determined,

$$\begin{aligned} 0 &= m_y - am_x - b \\ b &= m_y - am_x. \end{aligned} \quad (2.60)$$

The estimate of y is written in terms of only one free parameter, a , by substituting Equation 2.60 into Equation 2.56

$$\hat{y} = a(x - m_x) + m_y. \quad (2.61)$$

Using Equation 2.61 in the expression for the mean-square error (Equation 2.57), results in the mean-square error also being in terms of the one free parameter a ¹⁹,

$$\begin{aligned}\mathcal{E}\{(y - [a(x - m_x) + m_y])^2\} &= \mathcal{E}\{[(y - m_y) - a(x - m_x)]^2\} \\ &= \mathcal{E}\{(y - m_y)^2 - 2a(x - m_x)(y - m_y) + a^2(x - m_x)^2\} \\ &= \mathcal{E}\{(y - m_y)^2\} - 2a\mathcal{E}\{(x - m_x)(y - m_y)\} + a^2\mathcal{E}\{(x - m_x)^2\}.\end{aligned}\quad (2.62)$$

Recall that the variance in y is given by $\mathcal{E}\{(y - m_y)^2\}$ and $\mathcal{E}\{(x - m_x)^2\}$ gives the variance in x . The last term in Equation 2.62, $\mathcal{E}\{(x - m_x)(y - m_y)\}$, is the cross-covariance of x and y . Writing the mean-square error in terms of the first and second moments of the pdf results in the equation

$$\mathcal{E}\{(y - \hat{y})^2\} = \sigma_y^2 - 2ac_{xy} + a^2\sigma_x^2. \quad (2.63)$$

The mean-square error can be minimized by determining the value of the last free parameter, a , that will minimize the mean-square error. The mean-square error will be the minimum if the derivative of the mean-square error with respect to a is zero,

$$\begin{aligned}\frac{d\mathcal{E}_{\text{ms}}}{da} &= 0 \\ -2c_{xy} + 2a\sigma_x^2 &= 0 \\ a &= \frac{c_{xy}}{\sigma_x^2}.\end{aligned}\quad (2.64)$$

The final form of the estimate is found by replacing the free parameters b and a with Equation 2.60 and Equation 2.64 respectively,

$$\hat{y} = \frac{c_{xy}}{\sigma_x^2}x + (m_y - \frac{c_{xy}}{\sigma_x^2}m_x). \quad (2.65)$$

To apply linear mean-square estimation, the general estimate given by Equation 2.65 must be tailored to the specific problem.¹⁹ The location of the source of acoustic plane waves using measurements taken across an array of microphones is the specific problem of interest. In order to determine the location of the source of the acoustic plane waves, the speed of the wave and the direction of arrival of the wave must be estimated from the recorded data. The most direct measurement that contains the desired information is the time it takes the wave front to travel between two known sensor locations in the array.

For an arbitrary two dimensional coordinate system the wave front will make an unknown angle, θ , with the y -axis and travel with an unknown speed of v . Define the vector $\vec{d}_{m,n}$ as the displacement from the m^{th} sensor to the n^{th} sensor; the distance between those sensors is $d_{m,n} = |\vec{d}_{m,n}|$. The time taken to travel between those two sensor locations can be related to the distance between those two sensor locations by the simple equation

$$d_{m,n} = v_{\parallel} \times \tau_{m,n}, \quad (2.66)$$

Here $\tau_{m,n}$ is the time it takes the wave to travel between the m^{th} and n^{th} sensors, and v_{\parallel} is the component of the wavefront vector velocity parallel to the displacement between those two sensors, because the direction of arrival of the wave is not guaranteed to be aligned to $\vec{d}_{m,n}$. Solving Equation 2.66 for time and inserting the components of both $d_{m,n}$ and \vec{v} results in the general time of flight equation

$$\tau_{m,n} = \frac{x_m - x_n}{v \sin(\theta_{m,n})} + \frac{y_m - y_n}{v \cos(\theta_{m,n})}. \quad (2.67)$$

For an N sensor array, there are $M = \frac{(N-1)N}{2}$ possible unique intersensor separations which will produce M different time delay equations. With only two unknowns, the azimuthal angle θ and trace velocity v , only two of the M equations are necessary to find a solution. The use of only two of the M equations would disregard the information contained in the remaining $M - 2$ equations. An analogy here is to the process of fitting a line: the more data points that are used, the more accurate the solution for the unknowns will be. All M equations can be used to find the two unknowns if, instead of writing M separate equations, Equation 2.67 is written conceptually in matrix form

$$\vec{\tau} = \frac{\mathcal{X}}{\vec{v}}, \quad (2.68)$$

where the matrix of intersensor separations is given by

$$\mathcal{X} = \begin{bmatrix} x_1 & y_1 \\ x_2 & y_2 \\ \vdots & \vdots \\ x_N & y_N \end{bmatrix}. \quad (2.69)$$

It is not possible to solve Equation 2.68 in the current form since no operation exists to divide by a vector. To circumvent this problem, replace the vector of the velocity with a

new quantity called the slowness vector.³⁹ The components of the velocity vector are related to the components of the slowness vector by the conformal map³⁹

$$s_x = \frac{v_x}{v_x^2 + v_y^2} \quad (2.70)$$

$$s_y = \frac{v_y}{v_x^2 + v_y^2}. \quad (2.71)$$

Replacing the velocity vector with the slowness vector in Equation 2.68 results in a new equation for the time delays

$$\vec{\tau} = \mathcal{K} \vec{s}. \quad (2.72)$$

To make use of all the information recorded by the array, linear mean-square error estimation is used solve for the slowness vector. The only quantity that is being directly measured is the set of the time delays between sensors. The set of time delays is estimated from the data by determining the lags that maximize the cross-correlation functions between unique sensor pairs. When the presence of error in the time measurements is included explicitly, Equation 2.72 takes the form

$$\vec{\tau} = \mathcal{K} \vec{s} + \vec{\epsilon}, \quad (2.73)$$

where $\vec{\epsilon}$ is the set of errors in the measurement of time delays. To use the method of mean-square error to estimate the slowness vector, an expression for the error is required. An expression for the error is obtained by solving Equation 2.73 for the error,

$$\vec{\epsilon} = \vec{\tau} - \mathcal{K} \vec{s}. \quad (2.74)$$

Notice that, similar to Equation 2.56, the error is in terms of a free parameter, in this case \vec{s} . Next form the mean-square error $E = \vec{\epsilon}^\dagger \vec{\epsilon}$,

$$\begin{aligned} \vec{\epsilon}^\dagger &= (\vec{\tau}^\dagger) - \mathcal{K}^\dagger (\vec{s}^\dagger) \\ E &= (\vec{\tau}^\dagger) \vec{\tau} - (\vec{\tau}^\dagger) \mathcal{K} \vec{s} - \mathcal{K}^\dagger (\vec{s}^\dagger) \vec{\tau} + \mathcal{K}^\dagger (\vec{s}^\dagger) \mathcal{K} (\vec{s}^\dagger). \end{aligned} \quad (2.75)$$

Since the only free parameter is \vec{s} the next step is to set the derivative of the mean-square error with respect to \vec{s} equal to zero

$$\vec{\nabla}_s (\vec{\epsilon}^\dagger) \vec{\epsilon} = 0$$

$$\begin{aligned}
\vec{\nabla}_s(\vec{\epsilon}^\dagger)\vec{\epsilon} &= \vec{\epsilon} \\
\vec{\epsilon} &= 0 \\
\vec{\tau} - \mathcal{X}\vec{s} &= 0 \\
\hat{\vec{s}} &= \mathcal{X}^{-1}\vec{\tau}.
\end{aligned} \tag{2.76}$$

Equation 2.76 is the Least Squares estimate of the slowness, but there is still a potential problem in the application of the estimate. The matrix of the intersensor separations is generally not a square matrix. Only square matrices can have an inverse.⁴⁰ To solve this problem, form the pseudo inverse of the matrix \mathcal{X} by multiplying from the left by \mathcal{X}^\dagger ^{39,40},

$$\mathcal{X}^\dagger\vec{\tau} - \mathcal{X}^\dagger\mathcal{X}\vec{s} = 0. \tag{2.77}$$

Since $\mathcal{X}^\dagger\mathcal{X}$ must be Hermitian, and since it can be shown that its determinant is non-zero, it is possible to find its inverse and solve Equation 2.77 for the Least Squares slowness estimate,

$$\hat{\vec{s}} = (\mathcal{X}^\dagger\mathcal{X})^{-1}\mathcal{X}^\dagger\vec{\tau}. \tag{2.78}$$

The azimuth and trace velocity of the plane wave are reconstructed from the estimated slowness vector. Estimates of the azimuth and trace velocity can be calculated once the slowness vector has been estimated using Equation 2.78. The azimuth estimate from multiple arrays can then be employed to localize the source of the acoustic wave using triangulation.^{41,42} The source is located in the region where the multiple azimuth estimates, plus or minus the uncertainty in the estimates,⁴³ intersect. More accurate estimates of azimuth produce source locations with less uncertainty. A greater understanding of what affects the error sources in the least squares estimate of the slowness vector leads to an improved understanding of what affects the uncertainty in the far-field localization of an acoustic source.

Chapter 3

Bias in LSE

3.1 Introduction

Estimation theory is used to estimate desired signal parameters from the sampled fluctuations in the pressure field. To accurately estimate signal parameters from the recorded data it is necessary to determine if the estimate used to obtain the signal parameter has any systematic error. In this chapter the bias of the least squares estimate of the magnitude of the slowness vector and of the azimuth is explored. When possible an analytic expression for the bias in the estimate is determined, followed by a numerical simulation to determine any dependence of the estimate bias on wave or array parameters. The chapter concludes with a numerical simulation to determine the quantitative magnitude of the bias in both the estimate of the slowness vector magnitude and the estimate of azimuth for the IS53 and IS55 arrays. The magnitude of the bias in the estimates is then compared with the uncertainties in the estimates of the signal parameters for the respective arrays.

3.2 The Slowness Vector

To locate the source of an acoustic wave that traverses an array, the direction of arrival (azimuth) of the wave and the magnitude of the wave velocity must be estimated from the recorded data.^{39,41,44} The slowness vector is used to reconstruct both the magnitude of the wave velocity and the azimuth. An estimate of the slowness vector can be used to form estimates of the magnitude of the wave velocity and azimuth. The estimate of the magnitude of the wave velocity³⁹ is

$$\hat{v} = \frac{1}{\sqrt{\hat{s}_x^2 + \hat{s}_y^2}} \quad (3.1)$$

and the estimate of the azimuth is given by

$$\hat{\theta} = \tan^{-1}\left(\frac{\hat{s}_x}{\hat{s}_y}\right). \quad (3.2)$$

Notice that the estimate for the magnitude of the wave velocity is the inverse of the estimate of the magnitude of the slowness vector. For the purposes of determining the statistical properties of the estimate of the magnitude of the wave velocity, the estimate of the magnitude of the slowness vector can be used instead of the estimate of the magnitude of the wave velocity.

The mean-square error of the least squares estimate of the slowness vector was found in Section 2.4. The least squares estimate of the slowness vector is formed³ by substituting $\vec{\tau} = \mathcal{X}\vec{s} + \vec{\epsilon}$ into Equation 2.78,

$$\begin{aligned}\hat{\vec{s}} &= (\mathcal{X}^\dagger \mathcal{X})^{-1} \mathcal{X}^\dagger (\mathcal{X}\vec{s} + \vec{\epsilon}) \\ \hat{\vec{s}} &= \vec{s} + (\mathcal{X}^\dagger \mathcal{X})^{-1} \mathcal{X}^\dagger \vec{\epsilon}.\end{aligned}\tag{3.3}$$

The expectation value of the least squares estimate of the slowness vector, shown in Equation 3.3, must be calculated to determine if the estimate is biased,

$$\mathcal{E}\{\hat{\vec{s}}\} = \mathcal{E}\{\vec{s}\} + (\mathcal{X}^T \mathcal{X})^{-1} \mathcal{X}^\dagger \mathcal{E}\{\vec{\epsilon}\}.\tag{3.4}$$

The expectation value of the slowness vector estimate is

$$\mathcal{E}\{\vec{s}\} = \vec{s}$$

and the expectation of the vector of timing errors is

$$\mathcal{E}\{\vec{\epsilon}\} = m_\epsilon,$$

where the mean of the timing errors, m_ϵ , is zero by assumption.³⁹ The least squares estimate of the slowness vector is unbiased by definition,^{29,19}

$$\mathcal{E}\{\hat{\vec{s}}\} = \vec{s}.$$

3.3 Bias in the Estimates of Slowness Magnitude and Azimuth

The least squares estimate of the vector slowness is an unbiased estimate. The fact that the estimate of the slowness vector is unbiased does not mean the estimates of the magnitude of the slowness vector and azimuth, which are derived from the slowness vector, are unbiased. The expectation value for both the estimate of slowness vector magnitude and the estimate of azimuth must be calculated to determine if the estimates are unbiased.

To calculate the expectation value of the estimates of slowness vector magnitude and azimuth it is first necessary to determine the probability density function of the slowness vector. Recall that the expectation value of any quantity derived from a random vector is given by the integral of the product of the quantity and the pdf of the random vector.²⁹ The

estimate of the magnitude of the slowness vector and the azimuth estimate are derived from the estimate of the slowness vector. The pdf of the slowness vector is needed to analytically calculate the expectation values of the slowness vector magnitude and azimuth estimates. It has been shown that the pdf of the vector slowness is distributed as a d -dimensional Gaussian in slowness space.⁴³

3.3.1 Derivation of the pdf of the Slowness Vector

Two methods are available for deriving the pdf of the slowness vector. The first method, which is summarized in this section, requires that assumptions be made about the distribution of the error in the measurement of the time delay.⁴³ An alternative method to making assumptions about the measurement error is to use the principles of entropy optimization⁴⁵ to derive the pdf of the slowness vector. Both methods result in a Gaussian slowness vector pdf. Since the first method relies on physical arguments more than mathematical principles, it will be used as the primary means of deriving the slowness vector pdf. The derivation of the slowness vector pdf using the principles of entropy optimization is shown in Appendix A.

To derive the pdf of the slowness vector, assume that errors in measurement of the time delays between sensors are distributed normally about a central time delay that represents the signal.⁴³ The assumption can be justified empirically by contaminating a synthetic time series with Gaussian white noise and observing the distribution of intersensor time delays produced by the contaminated time series. The pdf of the normally distributed time delays can be represented as^{29,43}

$$f(\vec{\tau}) = \frac{1}{(2\pi)^{\frac{N}{2}} |\mathcal{C}_{\tau}|^{\frac{1}{2}}} e^{-\frac{1}{2}[(\vec{\tau}^{\dagger} - \vec{\tau}_o^{\dagger})\mathcal{C}_{\tau}^{-1}(\vec{\tau} - \vec{\tau}_o)]}, \quad (3.5)$$

where \mathcal{C}_{τ} is the covariance matrix of the time delays, N is the number of unique intersensor separations, and $\vec{\tau}_o$ is the time delay vector that represents the signal. In addition to the assumption that the errors in measuring the time delays are normally distributed about $\vec{\tau}_o$, it is also assumed that the covariances of the time delays are uncorrelated.⁴³ The assumption of uncorrelated covariances of the time delays allows the covariance matrix of the time delays to be written as the diagonal matrix

$$\mathcal{C}_{\tau} = \sigma_{\tau}^2 \mathcal{I}, \quad (3.6)$$

where σ_τ is the variance in the time delay vector and \mathcal{I} is the identity matrix. A completely uncorrelated noise field is rarely realized in physical situations, but the assumption seems to hold in studies done with impulsive signals moving across the IS53 array at University of Alaska Fairbanks.⁴³

Replacing the covariance matrix in Equation 3.5 with Equation 3.6 results in a simpler form for the pdf of the time delay vector

$$f(\vec{\tau}) = \frac{1}{(2\pi\sigma_\tau^2)^{\frac{N}{2}}} e^{-\frac{\sigma_\tau^2}{2}[(\vec{\tau}^\dagger - \vec{\tau}_o^\dagger)\mathcal{I}(\vec{\tau} - \vec{\tau}_o)]}. \quad (3.7)$$

The vector of time delays is related to the slowness vector through the familiar distance equals time multiplied by velocity equation,

$$\vec{\tau} = \mathcal{X}\vec{s}, \quad (3.8)$$

where \mathcal{X} is a matrix of intersensor separations, $\vec{\tau}$ is a vector of intersensor flight times, and \vec{s} is the vector slowness. Substituting Equation 3.8 into Equation 3.7 produces the pdf for the slowness vector,

$$f[\vec{s}] = \kappa e^{-\frac{\sigma_\tau^2}{2}[(\vec{s}^\dagger \mathcal{X}^\dagger - \vec{s}_o^\dagger \mathcal{X}^\dagger)(\mathcal{X}\vec{s} - \mathcal{X}\vec{s}_o)]}, \quad (3.9)$$

to within a (insignificant) normalization constant κ .⁴³

Both the pdf of the time delay vector and the pdf of the vector slowness have the form of a Gaussian distribution. The pdf of the time delays is an N -dimensional Gaussian distribution centered on $\vec{\tau}_o$. When the pdf of the time delay vector was transformed into the pdf of the slowness vector, the M -dimensional Gaussian was mapped into a d -dimensional Gaussian distribution centered on \vec{s}_o .⁴³ An effect of transforming the pdf of the time delays into the pdf of the slowness vector is the reduction of the dimension of the problem from M , the dimension of the time delay vector, to d , the dimension of both the vector slowness and the array used in the problem. To simplify the pdf of the vector slowness it is convenient to define residual slowness as the difference of the measured slowness and the actual slowness of the signal,

$$\tilde{\vec{s}} = \vec{s} - \vec{s}_o. \quad (3.10)$$

Further simplification of the slowness vector pdf is achieved by collecting the factor of \mathcal{X}^\dagger in the first term in the argument of the exponent in Equation 3.9 and the factor of \mathcal{X} from

the second term. Equation 3.9 can now be written in the compact form

$$f[\vec{s}] = \kappa e^{-\frac{\sigma_s^2}{2} [\vec{s} \mathcal{C} \vec{s}]}, \quad (3.11)$$

where $\mathcal{C} = \mathcal{X}^\dagger \mathcal{X}$ is the covariance matrix of the intersensor separations.⁴³

The covariance matrix has the form of a d dimensional Hermitian matrix whose elements are determined by the geometry of the array. Working with a generalized two dimensional array ($d = 2$), the covariance matrix has the form

$$\mathcal{C} = \begin{bmatrix} C_{11} & C_{12} \\ C_{21} & C_{22} \end{bmatrix}. \quad (3.12)$$

The covariance matrix in Equation 3.12 can be simplified by using the Hermitian symmetric property shared by all covariance matrices²⁹,

$$C_{xy} = C_{yx}^\dagger. \quad (3.13)$$

The matrix elements of Equation 3.12 are real numbers and $C_{12} = C_{21}$. In general the covariance matrix of the intersensor separations is not diagonal and the d -dimensional Gaussian pdf of the vector slowness cannot be separated into the product of d one dimensional Gaussian distributions. When the argument of the exponent in Equation 3.11 is expanded,

$$\vec{s} \mathcal{C} \vec{s} = C_{11} s_x^2 + 2C_{12} s_x s_y + C_{22} s_y^2, \quad (3.14)$$

it is clear that the cross term will foil any attempt to separate the pdf of the slowness vector. Physically, the cross term in Equation 3.14 indicates that the components of the slowness vector are correlated in the chosen coordinate system. While a correlation between the components of the slowness vector does not violate any of the assumptions made in the derivation of the slowness vector pdf or any physical laws, it greatly complicates any calculations done with the pdf and makes many of the necessary integrals intractable.

To remove any correlation between the vector components of the slowness, the covariance matrix can be diagonalized via the eigenvalue equations. The operation that diagonalizes the covariance matrix is equivalent to a rotation of the coordinate axes into alignment with the principal axes of the covariance matrix.^{29,43} If the matrix \mathcal{D} is the d -dimensional diagonal matrix of the eigenvalues of the covariance matrix and \mathcal{E} is the matrix of eigenvectors of

the covariance matrix, then the covariance matrix can be diagonalized using the eigenvalue equations

$$\begin{aligned}\mathcal{D} &= \mathcal{E}^\dagger \mathcal{C} \mathcal{E} \\ \mathcal{C} &= \mathcal{E} \mathcal{D} \mathcal{E}^\dagger.\end{aligned}\tag{3.15}$$

Defining the product of the eigenvector matrix and the residual slowness as a new variable, $\hat{\vec{s}}$, and substituting Equation 3.15 into Equation 3.11 produces a Gaussian density function with components that are uncorrelated in the rotated coordinate system,

$$f[\vec{s}] = \kappa e^{-\frac{\sigma^2}{2} (\hat{\vec{s}}^\dagger \mathcal{D} \hat{\vec{s}})}.\tag{3.16}$$

With the uncorrelated components of the slowness vector, the d -dimensional Gaussian density function separates into the product of d one-dimensional Gaussian distributions.

The pdf of the vector slowness can be plotted as contours of constant probability in slowness space.⁴³ The contours of constant probability in slowness space are defined by the relation $f[\vec{s}] = \text{constant}$. The pdf of the vector slowness is a function of the components of the slowness vector, and a contour of constant probability will be a curve on which the density function remains constant as the components of the slowness vector vary. The components of the slowness vector are contained in the argument of the exponent in the slowness vector pdf. The contours of constant probability are found by setting the argument of the exponent equal to a constant.⁴³

The surfaces of constant probability for the Gaussian pdf of the slowness vector are d -dimensional ellipsoids.^{43,46} Under the assumption that the noise corrupting the signal is a Gaussian random vector distributed as

$$\vec{w} \sim N(0, \sigma^2 \mathcal{I}),$$

the least squares estimate is equivalent to the maximum likelihood estimate.¹⁹ The maximum likelihood estimate is given by maximizing the likelihood function

$$P \propto \prod_i^N \{e^{-\frac{1}{2}(\frac{y_i - y(x_i)}{\sigma_i})^2} \Delta y\}.\tag{3.17}$$

If each data point (x_i, y_i) has its own standard deviation in y , σ_i , then the maximum likelihood estimate of the parameters is equivalently given by minimizing the quantity

$$\chi^2 = \sum_{i=1}^N \left(\frac{y_i - y(x_i; a_1 \cdots a_m)}{\sigma_i} \right)^2$$

known as the “chi-square” minimization.⁴⁶ When the method used to estimate the parameters is a chi-square minimization, the natural choice for the confidence region of the estimate is a region where χ^2 increases by no more than a set amount $\Delta\chi^2$.^{19,46,47} For a chi-squared distribution with ν degrees of freedom and a confidence level of p , the equation of the ellipse[†] becomes

$$\Delta\chi^2_{\nu|p} = \sum_{i=1}^d \frac{\hat{s}_i^2}{\sigma_{\hat{s}_i}^2}. \quad (3.18)$$

The ellipse in Equation 3.18 ensures that p percent of the data points in the distribution will be enclosed by the ellipse. Notice that the axes of the ellipsoid in Equation 3.18 have lengths that are proportional to the variances in the components of the slowness vector. The magnitudes of the variances are dependent on the uncertainty in the measurement of the time delays and on the array geometry according to the equation

$$\sigma_{\hat{s}_i} = \sqrt{\frac{\sigma_\tau^2}{D_{ii}}}, \quad (3.19)$$

where σ_τ^2 is the variance in the time measurements and the array geometry is included through the term D_{ii} which is the diagonalized covariance matrix of the co-array.⁴³

3.3.2 Bias in the Estimate of Slowness Vector Magnitude

Geometric Illustration of the Bias in the Slowness Vector Magnitude

A geometric exploration of the bias in the estimate of the magnitude of the slowness vector can be made using the contours of constant probability.⁴³ In Figure 3.1, a generalized ellipse represents a contour of constant probability for an arbitrary pdf of the slowness vector. Not shown in the figure is density of estimates for each point inside the ellipse. The derived Gaussian pdf of the slowness vector is a symmetric distribution of estimates about s_o . Since the distribution of estimates about s_o is symmetric in s_y and s_x the exact heights are not qualitatively important to the general geometric argument. The dashed line indicates the curve where the magnitude of the slowness vector is constant. The pdf of the slowness is centered on the slowness representing the signal, and the curve of constant slowness vector magnitude will pass through the center of the contour of constant probability. The correct slowness vector is shown as s_o in Figure 3.1.

[†]The general coordinate-aligned equation of an ellipsoid is $\frac{x^2}{a^2} + \frac{y^2}{b^2} + \dots = 1$.

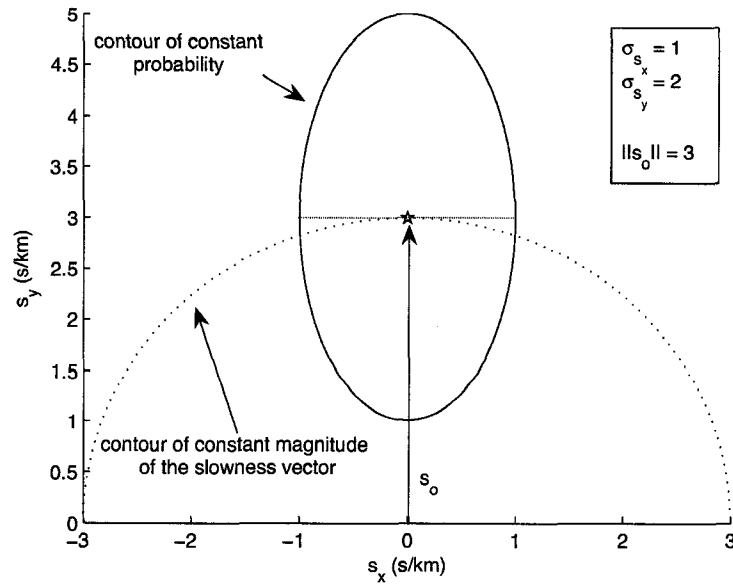


Figure 3.1. 2-D Geometric representation of the bias in the estimate of the slowness magnitude. The solid ellipse is an arbitrary confidence limit of the slowness vector distribution. The dashed line is the contour of constant magnitude of the slowness vector which divides the slowness vector distribution into high magnitude estimates and low magnitude estimates. The slowness vector representing a signal with a slowness magnitude of $3 \frac{s}{km}$ and an azimuth of 0° is represented by s_0 . For the reader's convenience a line tangent to the contour of constant slowness magnitude that divides the slowness distribution in half has been included in the figure.

The curve of constant slowness vector magnitude in Figure 3.1 divides the pdf of the slowness vector into two separate regions, one of high magnitude estimates and one of low magnitude estimates. The volume above the curve of constant slowness vector magnitude will produce estimates of the slowness vector magnitude that are high; the volume below the curve yields magnitude estimates that are lower than the true value. Only estimates that are found on the curve of constant slowness vector magnitude will correctly return the slowness vector magnitude as 3 s/km. For the estimate of the slowness vector magnitude to be unbiased the volume above the curve of constant slowness vector magnitude must equal the volume below the curve of constant slowness vector magnitude. The dotted line in Figure 3.1 is tangent to the curve of constant slowness vector magnitude and cuts the

ellipse in half. The volume below the curve of constant slowness vector magnitude is less than the volume above by the volume contained in the region between the two lines and so there must be a bias in the estimate of the magnitude of the slowness vector.

The volume between the two lines gives a rough idea of the size of the bias and how the bias reacts to a change in parameters. There are four independent parameters that affect the magnitude of the bias in the estimate of the slowness vector magnitude. These parameters are: the slowness vector magnitude, the wave direction of arrival, the area of the ellipse representing an arbitrary confidence limit, and the aspect ratio of the ellipse. The first two parameters, slowness and azimuth, are determined by the wave impinging on the array and are out of the control of the array operator. The area of the ellipse is determined by the size of the uncertainties in the components of the slowness vector, which are controlled by the array geometry and the error in the time measurements. The aspect ratio of an arbitrary confidence ellipse is completely dependent on the geometry of the array and is a constant once the array is deployed. The relation between the ellipse parameters and the bias in the estimate of the slowness vector magnitude can be explored using computer simulation; see Subsection 3.3.2.

Analytic Derivation of the Estimate Bias

In two dimensions the density function of the vector slowness is a normal distribution of the form,

$$f[\vec{s}] = \frac{1}{2\pi\sigma_{s_x}\sigma_{s_y}} e^{-\left[\frac{(s_x-s_{x_0})^2}{2\sigma_{s_x}^2} + \frac{(s_y-s_{y_0})^2}{2\sigma_{s_y}^2}\right]}, \quad (3.20)$$

where the x -axis and y -axis are assumed to be aligned with the principal axes of the array.^{43,45} The magnitude of the slowness vector is found according to the equation,

$$\begin{aligned} ||s|| &= \sqrt{\vec{s}^\dagger \vec{s}} \\ &= \sqrt{s_x^2 + s_y^2}, \end{aligned} \quad (3.21)$$

where s_x is the slowness vector component in the x direction and s_y is the slowness vector component in the y direction.

Since the estimate of the magnitude of the slowness vector is derived from the slowness vector, its pdf can be used to calculate the expectation value.²⁹ Direct application of the

expectation value definition results in the integral

$$\mathcal{E}\{|s|\} = \frac{1}{2\pi\sigma_{s_x}\sigma_{s_y}} \int_{-\infty}^{\infty} \int_{-\infty}^{\infty} \sqrt{s_x^2 + s_y^2} e^{-[\frac{(s_x-s_{x0})^2}{2\sigma_{s_x}^2} + \frac{(s_y-s_{y0})^2}{2\sigma_{s_y}^2}]} ds_x ds_y. \quad (3.22)$$

The integral is intractable, but it is possible to circumvent the integral by using the formula for standard deviation of the slowness magnitude. All authors agree that the formula for the standard deviation is,

$$\Delta|s| = \sqrt{\langle||s|^2\rangle - (\langle||s|\rangle)^2}, \quad (3.23)$$

where $\langle||s|^2\rangle$ is the expectation of the magnitude of the slowness vector squared and $(\langle||s|\rangle)^2$ is the square of the expectation of the magnitude of the slowness vector.³⁰ Solving Equation 3.23 for the expectation of the magnitude of the slowness vector yields,

$$\langle||s|\rangle = \sqrt{\langle||s|^2\rangle - (\Delta|s|)^2}, \quad (3.24)$$

in terms of the expectation of the magnitude of the slowness vector squared and the variance in the magnitude of the slowness vector.

The expectation of the magnitude of the slowness vector squared can now be calculated using the pdf of the vector slowness. The expectation of the magnitude of the slowness vector squared is given by the equation

$$\begin{aligned} \mathcal{E}\{|s|^2\} &= \int_{-\infty}^{\infty} \int_{-\infty}^{\infty} |s|^2 f[\vec{s}] ds_x ds_y \\ &= \frac{1}{2\pi\sigma_{s_x}\sigma_{s_y}} \int_{-\infty}^{\infty} \int_{-\infty}^{\infty} (s_x^2 + s_y^2) e^{-[\frac{(s_x-s_{x0})^2}{2\sigma_{s_x}^2} + \frac{(s_y-s_{y0})^2}{2\sigma_{s_y}^2}]} ds_x ds_y. \end{aligned} \quad (3.25)$$

Rotating the coordinate system into the principle axes decorrelates the components of the covariance matrix and so the vector slowness pdf is the product of two one-dimensional Gaussian distributions. The expectation of the magnitude of the slowness vector squared is calculated by breaking the integral into the sum of two integrals,

$$I_1 = \int_{-\infty}^{\infty} \int_{-\infty}^{\infty} s_x^2 e^{-[\frac{(s_x-s_{x0})^2}{2\sigma_{s_x}^2}]} e^{-[\frac{(s_y-s_{y0})^2}{2\sigma_{s_y}^2}]} ds_x ds_y \quad (3.26)$$

and

$$I_2 = \int_{-\infty}^{\infty} \int_{-\infty}^{\infty} s_y^2 e^{-[\frac{(s_x-s_{x0})^2}{2\sigma_{s_x}^2}]} e^{-[\frac{(s_y-s_{y0})^2}{2\sigma_{s_y}^2}]} ds_x ds_y. \quad (3.27)$$

These integrals are recast into the form of standard Gaussian integrals which can be found in integral tables.

The integral with respect to s_y in Equation 3.26 was already in a form that can be found in standard integral tables. Integration with respect to s_y yields

$$I_1 = \sqrt{2\pi\sigma_{s_y}^2} \int_{-\infty}^{\infty} s_x^2 e^{-\left[\frac{(s_x - s_{x_o})^2}{2\sigma_{s_x}^2}\right]} ds_x. \quad (3.28)$$

Some manipulation of the remaining integral with respect to s_x is required in order to obtain the desired form of a Gaussian integral. A change of variables produces the desired form of the integrand. Let

$$u = s_x - s_{x_o} \quad \text{and} \quad du = ds_x,$$

then

$$s_x = u + s_{x_o} \Rightarrow s_x^2 = u^2 + s_{x_o}^2 + 2us_{x_o}.$$

Substituting the new variables into the integral with respect to s_x produces a sum of three integrals that are all in standard Gaussian form. The integrals are

$$\begin{aligned} \int_{-\infty}^{\infty} u^2 e^{-\frac{u^2}{2\sigma_{s_x}^2}} du + s_{x_o}^2 \int_{-\infty}^{\infty} e^{-\frac{u^2}{2\sigma_{s_x}^2}} du + 2s_{x_o} \int_{-\infty}^{\infty} u e^{-\frac{u^2}{2\sigma_{s_x}^2}} du \\ = \frac{1}{2} \sqrt{\pi(2\sigma_{s_x}^2)^3} + s_{x_o}^2 \sqrt{2\pi\sigma_{s_x}^2}. \end{aligned} \quad (3.29)$$

Combining result shown in Equation 3.29 with Equation 3.28 gives

$$I_1 = 2\pi\sigma_{s_x}\sigma_{s_y}(\sigma_{s_x}^2 + s_{x_o}^2)$$

as the result for Equation 3.26. Repeating the procedure used to evaluate Equation 3.26 with Equation 3.27 produces

$$I_2 = 2\pi\sigma_{s_x}\sigma_{s_y}(\sigma_{s_y}^2 + s_{y_o}^2) \quad (3.30)$$

as the result of the integration.

Combination of Equation 3.3.2 and Equation 3.30 with the normalization constant for the pdf of the slowness vector results in the expression

$$\begin{aligned} \mathcal{E}\{|s|^2\} &= \frac{1}{2\pi\sigma_{s_x}\sigma_{s_y}} 2\pi\sigma_{s_x}\sigma_{s_y}[\sigma_{s_x}^2 + s_{x_o}^2 + \sigma_{s_y}^2 + s_{y_o}^2] \\ &= (\sigma_{s_x}^2 + \sigma_{s_y}^2) + \|s_o\|^2 \end{aligned} \quad (3.31)$$

for the expectation value of the magnitude of the slowness squared where $\|s_o\|^2 = (s_{x_o}^2 + s_{y_o}^2)$. Replacing $\langle \|s\|^2 \rangle$ in Equation 3.24 with Equation 3.31 yields the formula

$$\mathcal{E}\{\|s\|\} = \sqrt{(\sigma_{s_x}^2 + \sigma_{s_y}^2) + \|s_o\|^2 - (\Delta\|s\|)^2} \quad (3.32)$$

for the expectation value of the magnitude of the slowness vector. Notice that if $(\sigma_{s_x}^2 + \sigma_{s_y}^2)$ is equal to $(\Delta\|s\|)^2$ the expectation value of the estimate of the magnitude of the slowness vector will equal $\|s_o\|$ and the estimate will be unbiased.

An expression relating the magnitudes of $(\Delta\|s\|)^2$ and $(\sigma_{s_x}^2 + \sigma_{s_y}^2)$ is required to determine if the least squares estimate of the magnitude of the slowness vector is a biased estimate. In Equation 3.24 $\Delta\|s\|$ is defined as the standard deviation of the magnitude of the slowness vector, making $(\Delta\|s\|)^2$ the variance of the magnitude of the slowness vector. The variances of the slowness vector magnitude and the sum of the variances in the components of the slowness must be calculated in order to compare the quantities and determine the bias in the least squares estimate of the slowness vector magnitude. The definition of variance was used to calculate the variance of the slowness vector magnitude,

$$\begin{aligned} \sigma_s^2 &= \frac{1}{n-1} \sum_i (s_i - \bar{s})^2 \\ &= \frac{1}{n-1} \sum_i [\sqrt{s_{x_i}^2 + s_{y_i}^2} - \sqrt{\bar{s}_x^2 + \bar{s}_y^2}]^2, \end{aligned} \quad (3.33)$$

where \bar{s}_x and \bar{s}_y are the means of s_x and s_y , respectively, and n is number of elements in the sample. To facilitate the comparison of the sum of the variances in the components of the slowness vector and the variance of the magnitude of the slowness vector, the square in Equation 3.33 is expanded as

$$\sigma_s^2 = \frac{1}{n-1} \sum_i (s_{x_i}^2 + s_{y_i}^2 + \bar{s}_x^2 + \bar{s}_y^2 - 2\sqrt{s_{x_i}^2 \bar{s}_x^2 + s_{x_i}^2 \bar{s}_y^2 + s_{y_i}^2 \bar{s}_x^2 + s_{y_i}^2 \bar{s}_y^2}). \quad (3.34)$$

The variances of the x and y -components of the slowness vector are found to be

$$\sigma_{s_x}^2 = \frac{1}{n-1} \sum_i (s_{x_i} - \bar{s}_x)^2 \quad (3.35)$$

and

$$\sigma_{s_y}^2 = \frac{1}{n-1} \sum_i (s_{y_i} - \bar{s}_y)^2, \quad (3.36)$$

respectively. Summing the variance of s_x and s_y and expanding the square gave the sum of the variances in the components of the slowness vector,

$$\sigma_{s_x}^2 + \sigma_{s_y}^2 = \frac{1}{n-1} \left[\sum_i s_{x_i}^2 + \bar{s}_x^2 + s_{y_i}^2 + \bar{s}_y^2 - 2s_{x_i}\bar{s}_x - 2s_{y_i}\bar{s}_y \right]. \quad (3.37)$$

Note that both the variance of the slowness vector magnitude and the sum of the variances of the components of the slowness vector have many common terms. The only terms that are not common between the two quantities are the cross terms picked up when the squares in Equation 3.33 were expanded,

$$\sqrt{s_{x_i}^2 \bar{s}_x^2 + s_{x_i}^2 \bar{s}_y^2 + s_{y_i}^2 \bar{s}_x^2 + s_{y_i}^2 \bar{s}_y^2}, \quad (3.38)$$

and

$$s_{x_i}\bar{s}_x + s_{y_i}\bar{s}_y \quad (3.39)$$

in the sum of the variances of the components of the slowness vector. The relative magnitudes of the terms which are not in common must be determined to relate magnitudes of the variance of the magnitude of the slowness vector and the sum of the variances of the components of the slowness vector. To eliminate the square root in Equation 3.38 the squares of Equation 3.39 and Equation 3.38 are compared instead of the original quantities.

The inequality

$$\sqrt{s_{x_i}^2 \bar{s}_x^2 + s_{x_i}^2 \bar{s}_y^2 + s_{y_i}^2 \bar{s}_x^2 + s_{y_i}^2 \bar{s}_y^2} \geq |(s_{x_i}\bar{s}_x + s_{y_i}\bar{s}_y)| \quad (3.40)$$

must be proven to complete the comparison of the variance in the slowness magnitude and the sum of the variance in the components of the slowness vector. Notice that the right-hand term is the magnitude of Equation 3.39. Proving the inequality in Equation 3.40 is sufficient to prove that terms in Equation 3.39 is less than or equal to the terms in Equation 3.38. If the magnitude of quantity Equation 3.39 is less than Equation 3.38, the sign of Equation 3.39 will not change that fact. To simplify the algebra, the squares of the quantities in Equation 3.40 were compared,

$$s_{x_i}^2 \bar{s}_x^2 + s_{x_i}^2 \bar{s}_y^2 + s_{y_i}^2 \bar{s}_x^2 + s_{y_i}^2 \bar{s}_y^2 \geq s_{x_i}^2 \bar{s}_x^2 + s_{y_i}^2 \bar{s}_y^2 + 2s_{x_i}\bar{s}_x s_{y_i}\bar{s}_y. \quad (3.41)$$

The terms on the right hand side of the inequality in Equation 3.41 are moved to the left by subtraction,

$$s_{x_i}^2 \bar{s}_y^2 + s_{y_i}^2 \bar{s}_x^2 - 2s_{x_i}\bar{s}_y s_{y_i}\bar{s}_x \geq 0.$$

The right hand side of the resulting inequality is rewritten as a perfect square,

$$(s_{x_i} \bar{s}_y - s_{y_i} \bar{s}_x)^2 \geq 0. \quad (3.42)$$

Since any real number squared is positive, semidefinite, the inequality is proved and Equation 3.38 is shown to be greater than or equal to Equation 3.39. It follows from this result that

$$\sigma_s^2 \leq (\sigma_{s_x}^2 + \sigma_{s_y}^2). \quad (3.43)$$

With the equation relating magnitudes of the variances known, it becomes apparent that there is a bias in the least squares estimate of the magnitude of the slowness vector. The estimate of the magnitude of the slowness vector will be unbiased if the expectation of the estimate returns $\|s_o\|$. According to Equation 3.32, the least squares estimate of the slowness vector magnitude will be unbiased when $(\sigma_{s_x}^2 + \sigma_{s_y}^2) = \sigma_s^2$, which occurs as $\|s_o\|$ goes toward infinity. A slowness magnitude of infinity corresponds to a trace velocity of zero. For magnitudes of the slowness vector less than infinity, $(\sigma_{s_x}^2 + \sigma_{s_y}^2) > \sigma_s^2$ and the estimate of the magnitude of the vector slowness is biased high,

$$\mathcal{E}\{\|s\|\} \geq \|s_o\|. \quad (3.44)$$

Effect of Array and Wave Parameters on the Bias in the Estimate of Slowness Vector Magnitude

The slowness vector magnitude is related to the speed at which the plane wave traverses the array. The slowness vector magnitude will affect the curvature of the contour of constant slowness vector magnitude, the dashed line in Figure 3.1. As the magnitude of the slowness increases, the curvature of the contour of constant slowness magnitude decreases and the bias in the estimate of slowness magnitude, represented by the volume between the lines, also decreases. In the limit that the magnitude of the slowness approaches infinity, the estimate of the slowness vector magnitude becomes unbiased, due to the curvature of the contour of constant slowness vector magnitude approaching a straight line. The disappearance of the bias in the limit of infinite slowness magnitude can be verified with the analytic solution by taking the limit of s_o going toward infinity in Equation 3.32.

The dependence of the bias in the estimate of slowness magnitude on the slowness vector magnitude was explored using a Monte Carlo-like computer simulation. The simulation

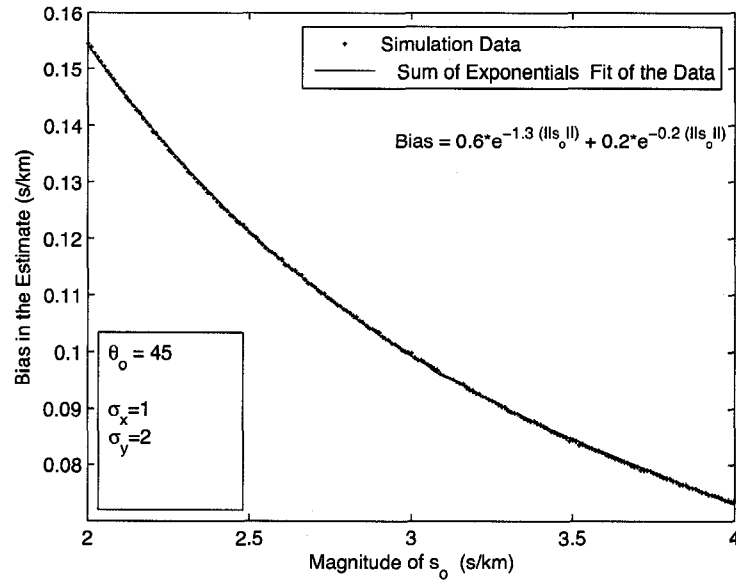


Figure 3.2. Bias in the least squares estimate of the slowness vector magnitude for a range of slowness vector magnitudes. The aspect ratio of the ellipse was held constant at $\frac{1}{2}$. The area of the ellipse was held at a value of π , and the azimuth was constant at 45° . The dependence of the bias in the estimate on the slowness vector magnitude was modeled by a sum of exponentials (equation shown in the figure).

consisted of producing simulated slowness vector pdfs for a range of slowness magnitudes. The other three parameters were held constant as the slowness magnitude was varied to ensure that any change in the bias of the estimate was due solely to the change in the slowness magnitude. The least squares estimate of the slowness vector magnitude was then calculated for each point in the simulated slowness vector pdf and the bias in the estimate determined using the definition of bias.

The results of the bias test using simulated slowness magnitude estimates are shown in Figure 3.2. In this simulation the shape of the ellipse was unchanged as the slowness vector magnitude was varied. The slowness vector magnitude was varied between 2 s/km and 4 s/km; acoustic waves generally have a slowness magnitude of approximately 3 s/km. The area of the ellipse was a constant value of π and the aspect ratio was held at one half. The wave was launched from the same arbitrarily chosen azimuth of 45° for all trials in the

simulation. Figure 3.2 showed that the magnitude of the bias in the estimate of slowness vector magnitude increases as the slowness vector magnitude decreases. An increase in the slowness vector magnitude corresponds to a decrease in the magnitude of the wave velocity. Physically, the slower the encroaching wave, the less the bias in the estimate of the magnitude of the velocity of the wave.

The relation between the slowness vector magnitude and the bias in the estimate was not a linear relationship. The relationship between the slowness magnitude and the bias in the estimate of the slowness magnitude was modeled as a sum of exponentials. The model sum of exponentials curve was chosen because the sum of exponentials had the correct behavior as the magnitude of the slowness approaches infinity, since the bias predicted by the fit model approaches zero. The equation of the model curve was

$$\hat{b} = 0.6 e^{-1.3 \|s_o\|} + 0.2 e^{-0.2 \|s_o\|},$$

where \hat{b} is the bias and $\|s_o\|$ is the slowness magnitude. The reliability of the curve fits was measured with a goodness of fit test to quantitatively compare the accuracy of the curve fits. To test the goodness of fit, the coefficient of determination was used to quantitatively measure how well the data was fit by the model.⁴⁷ The coefficient of determination is defined by the quotient of the sum of squares of regression to the total sum of squares. The sum of squares of regression is defined by

$$SSR = \sum_{i=1}^n w_i (\hat{y}_i - \bar{y})^2, \quad (3.45)$$

where \hat{y}_i is the curve fit data, w_i are the weights for the data points, and \bar{y} is the mean of the experimental data. The total sum of errors is given by the expression

$$SSE = \sum_{i=1}^n w_i (y_i - \bar{y})^2, \quad (3.46)$$

where y is the experimental data. The closer the coefficient of determination is to a value of one, the more the variance in the data is accounted for by the model. The coefficient of determination calculated for the model curve fit to the experimental data was one to within four significant figures, meaning that the curve fit model accounted for virtually all the variance in the data.

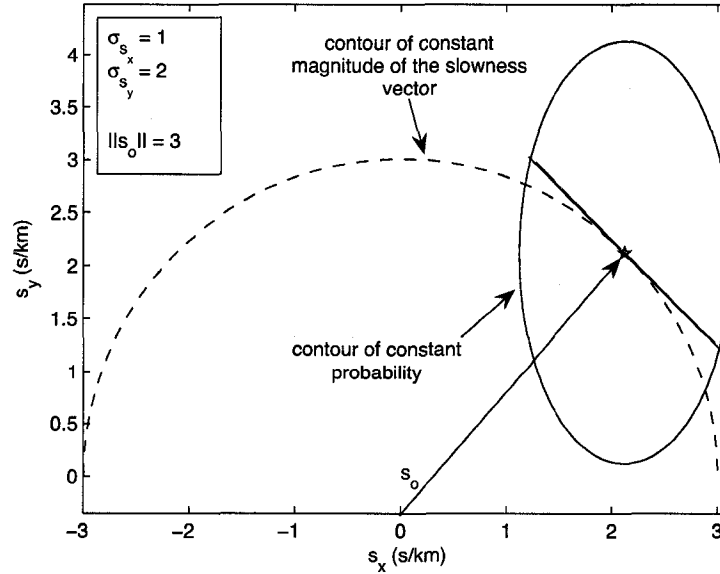


Figure 3.3. Bias in estimate of the slowness vector magnitude when the slowness vector is not aligned with the principal axes of the ellipse. The solid ellipse is an arbitrary confidence limit of the distribution of the slowness vector. The dashed line is the contour of constant slowness vector magnitude which divides the slowness vector distribution into high magnitude estimates and low magnitude estimates. The slowness vector representing a signal with a slowness magnitude of $3 \frac{s}{km}$ and an azimuth of 45° is represented by s_o . For the reader's convenience a line dividing the slowness distribution in half has been included in the figure.

The magnitude of the bias in the estimate of the slowness vector magnitude is also dependent on the angle of arrival of the wave. Figure 3.3 geometrically illustrates the bias in the estimate of the slowness vector magnitude for an azimuth of 45° instead of the azimuth of 0° shown in Figure 3.1. Notice that the bias in the estimate of the slowness vector magnitude has apparently been increased by simply changing the direction the wave impinges on the array. Figure 3.4 displays the resulting numerically calculated bias in the slowness vector magnitude estimates for azimuths ranging from -90° to 90° . The bias in the estimate was minimized when the slowness vector was aligned with the semi-major axis of the ellipse, an angle of 0° , and maximized when the slowness vector is aligned with the semi-minor axis, an angle of $\pm 90^\circ$. The estimate of the slowness vector magnitude was

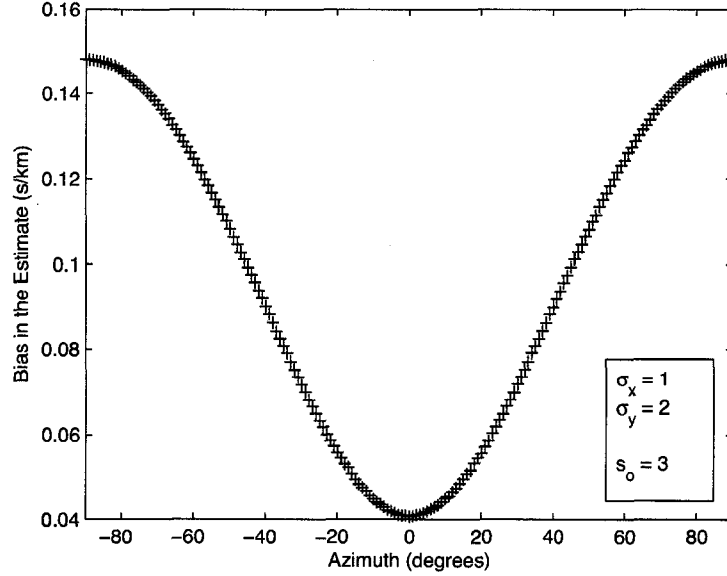


Figure 3.4. Bias in estimate of the slowness vector magnitude for wave azimuths ranging from -90° to 90° . The contour of constant probability for the simulated pdf was a coordinate aligned ellipse with the semi-major axis equal to σ_y and the semi-minor axis equal to σ_x . The ellipse was centered about a point with slowness magnitude s_o for each azimuth.

biased at all azimuths estimated. The bias in the estimate of the slowness vector magnitude was always biased high, resulting in a positive bias value for all estimated azimuths.

The last two ellipse parameters are, at least in part, determined by the geometry of the array and are pseudo-constants once the array is deployed. The shape of an arbitrary confidence ellipse can change in two distinct ways, the area of the ellipse can change or the aspect ratio of the ellipse can be varied. Physically, changing the area of the ellipse corresponds to changing the confidence limits. An increase in the area of the ellipse will cause increases in the variances of the components of the slowness vector, $\sigma_{s_y}^2$ and $\sigma_{s_x}^2$, and an increase in the variance of the slowness magnitude, σ_s^2 . The effect of increasing the area of the ellipse on the bias in the estimate of the slowness vector magnitude depends on the rate at which $\sigma_{s_x}^2 + \sigma_{s_y}^2$ and σ_s^2 increase. Figure 3.5 shows the results of a numerical simulation exploring how the magnitude of the bias in the estimate of slowness vector magnitude reacted to an expanding ellipse with a constant aspect ratio and at a constant

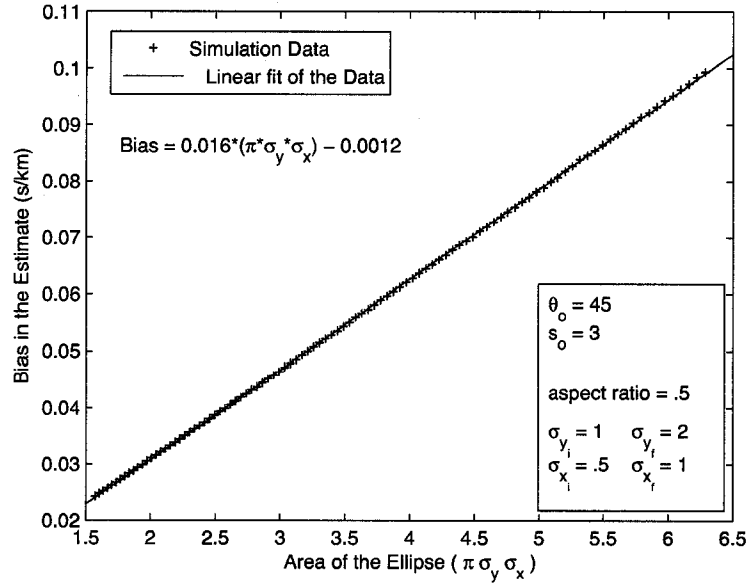


Figure 3.5. Change in the bias of the estimate of the slowness vector magnitude as the area bounded by the contour of constant probability increases. The aspect ratio of the ellipse was held constant at 0.5 and the area was increased from $\pi/2$ to 2π . The azimuth was held constant at 45° and the magnitude of the “true” slowness vector (s_o) was constant at $3 \frac{s}{km}$.

slowness magnitude and azimuth.

As the area of the ellipse increases from $\pi/2$ to 2π , the magnitude of the bias in the estimate increased linearly. The relationship between the bias in the estimate of the slowness vector magnitude and the area of the ellipse was modeled by a straight line,

$$\hat{b} = 0.02 (\pi * \sigma_x * \sigma_y) - 0.001,$$

where σ_x and σ_y are the semi-major and semi-minor axes of the ellipse of constant probability. The coefficient of determination for the linear fit was 1 to within four significant figures. The linear relationship indicated that, as the area of the ellipse increased the magnitude of the bias in the estimate of the slowness vector magnitude increased proportionately. The area of the ellipse can be altered once the array has been deployed through changes in the time measurement errors. The magnitude of the semi-major and semi-minor axes of the ellipse are proportional to the magnitude of the errors in the time measurements.⁴³

The dependence of the area of the ellipse on the errors in the time measurements can be seen analytically by using Equation 3.19 to find the uncertainties in the components of the slowness vector. Recall that the uncertainties in the components of the slowness vector are proportional to the semi-major/minor axes of the ellipse. Substituting the uncertainties into the equation for the area of an ellipse the dependence of the ellipse area on the time measurement errors is explicitly shown,

$$\begin{aligned} \text{Area} &= \pi \sigma_{s_x} \sigma_{s_y} \\ &= \frac{\pi \sigma_\tau^2}{\sqrt{D_{xx} D_{yy}}}. \end{aligned} \quad (3.47)$$

The array operator has some control over the magnitude of the uncertainties in the time measurements through the choice of the temporal sample rate.^{29,19,24} For impulsive signals the uncertainty in the time measurement, σ_τ can be approximated by $\sigma_\tau \approx \frac{1}{f_s}$.⁴³ Therefore, Equation 3.47 has an inverse squared dependence on the temporal sample rate. As the sample rate increases, the variances in the components of the slowness vector decrease and the area of the ellipse decreases as well. A smaller ellipse area corresponds to a smaller bias according to Figure 3.5. An increase in the temporal sample rate will decrease the bias in the estimate of the slowness vector magnitude.

The aspect ratio of the ellipse is entirely dependant on the geometry of the array. By combining the equation for the aspect ratio of ellipse with Equation 3.19 the dependence of the bias in the estimate of slowness vector magnitude on array geometry can be analytically proven. When the two equations are combined,

$$\begin{aligned} \text{aspect ratio} &= \frac{\sigma_{s_y}}{\sigma_{s_x}} \\ &= \frac{\sigma_\tau \sqrt{D_{xx}}}{\sigma_\tau \sqrt{D_{yy}}} \\ &= \sqrt{\frac{D_{xx}}{D_{yy}}}, \end{aligned} \quad (3.48)$$

the dependence on the errors in the time measurement drops out leaving only a dependence on the array geometry, represented by the diagonalized covariance matrix elements D_{ii} , in the aspect ratio. The exclusive dependence on the array geometry means that the aspect ratio of an arbitrary confidence ellipse will be a constant once the array is deployed.

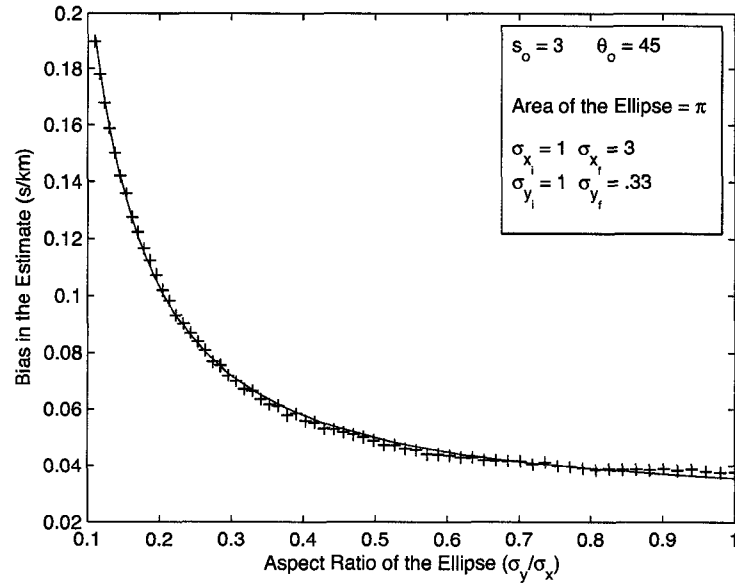


Figure 3.6. The dependence of the bias in the estimate of the slowness vector magnitude on the aspect ratio of the ellipse. The area of the ellipse was held constant at π and the aspect ratio was decreased from 1 to 0.1. The azimuth was held constant at 45° and the magnitude of the “true” slowness vector (s_o) was constant at $3 \frac{s}{km}$.

The aspect ratio amplifies the bias caused by varying the azimuth of the wave. The more eccentric the ellipse, the larger the range in the magnitude of the bias of the estimate of the slowness vector magnitude as the azimuth of the wave is varied around the circle. An ellipse with an aspect ratio equal to one (*i.e.* a circle) would no longer have any angular dependence in the bias of the estimate of the slowness vector magnitude.

The dependence of the bias in the estimate of the slowness vector magnitude on the aspect ratio is shown in Figure 3.6 for an azimuth of 45° . The azimuth, slowness magnitude, and ellipse area were held constant as the aspect ratio of the ellipse was varied. By convention the aspect ratio of the ellipse is calculated in such a way that the aspect ratio is less than or equal to one.²⁶ The bias in the estimate was at a minimum when the aspect ratio of the ellipse was equal to one. The bias in the estimate of slowness vector magnitude was estimated to have an inverse power law dependence on the aspect ratio of the ellipse based on the coefficient of determination for all the different curve fits of the data attempted. The

equation of the inverse power law was estimated as

$$\hat{b} = 0.001 \frac{\sigma_y^{-1.3}}{\sigma_x} + 0.03. \quad (3.49)$$

The coefficient of determination for the inverse power law fit to the data is 1 to four significant figures. The value of the coefficients in the power law fit, the power and the constants, varied depending on the wave azimuth, but the dependence of the bias on the aspect ratio was always found to be an inverse power law. An aspect ratio of one results in the smallest bias in the estimate of the slowness vector magnitude for all azimuths.

3.4 Bias in the Estimate of the Azimuth

Like the slowness magnitude, the azimuth is contained in the slowness vector and the pdf of the slowness vector can be used to obtain the expectation value of the azimuth. Continuing to work in two dimensions, the expectation value of the azimuth is obtained by solving the equation

$$\mathcal{E}\{\hat{\theta}\} = \int_{-\infty}^{\infty} \int_{-\infty}^{\infty} \hat{\theta} \frac{1}{2\pi\sigma_{s_x}\sigma_{s_y}} e^{-\left[\frac{(s_x-s_{x0})^2}{2\sigma_{s_x}^2} + \frac{(s_y-s_{y0})^2}{2\sigma_{s_y}^2}\right]} ds_x ds_y. \quad (3.50)$$

The azimuth can be expressed in terms of the components of the slowness vector using trigonometry,

$$\hat{\theta} = \tan^{-1} \left(\frac{s_y}{s_x} \right),$$

and then inserted into Equation 3.50, giving the intractable integral

$$\mathcal{E}\{\hat{\theta}\} = \int_{-\infty}^{\infty} \int_{-\infty}^{\infty} \tan^{-1} \left(\frac{s_y}{s_x} \right) \frac{1}{2\pi\sigma_{s_x}\sigma_{s_y}} e^{-\left[\frac{(s_x-s_{x0})^2}{2\sigma_{s_x}^2} + \frac{(s_y-s_{y0})^2}{2\sigma_{s_y}^2}\right]} ds_x ds_y. \quad (3.51)$$

A transformation of the problem into polar coordinates did not make the analytic integration of the pdf of the slowness vector and the azimuth possible.

The only way to calculate the expectation value of the least squares azimuth estimate was through numerical evaluation of the integral in Equation 3.51. Direct numerical integration of Equation 3.51 would produce results for the expectation value of the azimuth estimate, but there is a method for evaluation of the expectation of the azimuth estimate that produces more intuitive results than direct numerical integration. This second method makes use of the contours of constant probability of the slowness vector pdf and numerical evaluation of line integrals.

3.4.1 Numerical Calculation of the Bias in the Azimuth Estimate

Instead of attempting an analytic solution of the expectation value of the azimuth estimate, the sources of the bias in the least squares estimate of the azimuth can be identified using contours of constant probability. It can be argued geometrically that the bias in the estimate of azimuth will be determined by the volume of the ellipse on either side of a line drawn from the origin through the true azimuth at the center of the ellipse. If there is more volume on one side of this dividing line than on the other side of the dividing line the estimate of the azimuth will be biased toward the side with more volume enclosed. The task now becomes determining how much volume is on either side of the dividing line.

In order to determine the amount of volume on either side of the dividing line, first investigate the area under two slices at $+\theta$ and $-\theta$. Azimuth estimates occurring on these lines will return an azimuth estimate of $\pm\theta$. To calculate the volume on either side of the dividing line, the area under the $\pm\theta$ lines will be compared for a range of the estimates of the azimuth within an arbitrary confidence ellipse. Figure 3.7 illustrates the setup for the derivation of the bias in the estimate of the azimuth.

In Figure 3.7 the lines of constant azimuth estimates are shown as dashed lines. The lines are defined by $s_y = \tan(\pm\theta)s_x$ and intersect the ellipse at four points, $\pm a$ and $\pm b$. These intersection points define the range of integration for the one dimensional slowness pdf integrals. The results of the one-dimensional integrals are the areas under the $+\theta$ and $-\theta$ lines. Substituting the expression for s_y in terms of s_x and θ into the probability density function produces a one dimensional density function,

$$f[\vec{s}] = \frac{1}{2\pi\sigma_{s_x}\sigma_{s_y}} e^{-\left[\left(\frac{1}{2\sigma_{s_x}^2} + \frac{\tan^2(\theta)}{2\sigma_{s_y}^2}\right)s_x^2 - \left(\frac{s_x s_\theta}{\sigma_{s_x}^2} + \frac{s_y s_\theta \tan(\theta)}{\sigma_{s_y}^2}\right)s_x + \left(\frac{s_x^2 s_\theta^2}{2\sigma_{s_x}^2} + \frac{s_y^2 s_\theta^2}{2\sigma_{s_y}^2}\right)\right]}. \quad (3.52)$$

For the generalized case the slowness vector is not aligned with the principal axes of the array and the range of integration will be different for the $\pm\theta$ integrals. The integration of the slowness pdf along the $\pm\theta$ lines must be done when the lines are inside the confidence ellipse. An azimuth-dependent expression determining the intersection points of the lines and the ellipse must be found to ensure the proper limits of integration. The only points on the ellipse where $s_y = \tan(\theta)s_x$ are the points where the line and ellipse intersect. If the

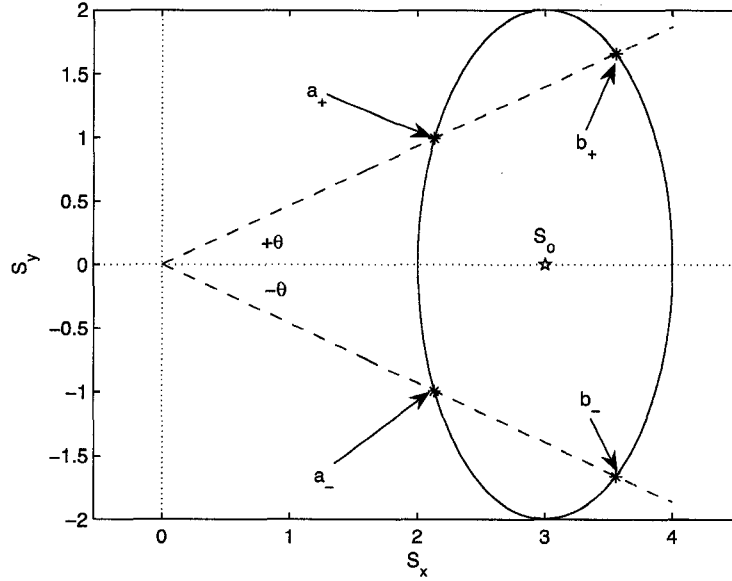


Figure 3.7. Setup for the calculation of the azimuthal estimate bias. The blue ellipse is a arbitrary contour of constant probability of the slowness pdf. Azimuth estimates made on the dashed red lines inside of the ellipse will return estimates of $+\theta$ and $-\theta$. The dashed lines intersect the ellipse at $\pm a$ and $\pm b$.

equation of the line is substituted into the equation of the ellipse,

$$\frac{(s_x - s_{x_o})^2}{\sigma_{s_x}^2} + \frac{(\tan(\theta)s_x - s_{y_o})^2}{\sigma_{s_y}^2} = 1, \quad (3.53)$$

the result is the equation[†] of the ellipse in terms of only one variable, s_x . Expanding the squares and gathering the terms of like power together gives an equation in a form that can be solved using the quadratic formula. The solutions to the equation

$$\left[\frac{1}{\sigma_{s_x}^2} + \frac{\tan(\theta)^2}{\sigma_{s_y}^2} \right] s_x^2 - 2 \left[\frac{s_{x_o}}{\sigma_{s_x}^2} + \frac{\tan(\theta)s_{y_o}}{\sigma_{s_y}^2} \right] s_x + \left[\frac{s_{x_o}^2}{\sigma_{s_x}^2} + \frac{s_{y_o}^2}{\sigma_{s_y}^2} - 1 \right] = 0 \quad (3.54)$$

are the points at which the line and the ellipse intersect.

The solutions of the one dimensional pdf integrals are error functions and must be evaluated numerically. A robust and accurate method for numerically evaluating integrals

[†] θ is the angle of incidence, plus or minus the angle of deviation from the dividing line.

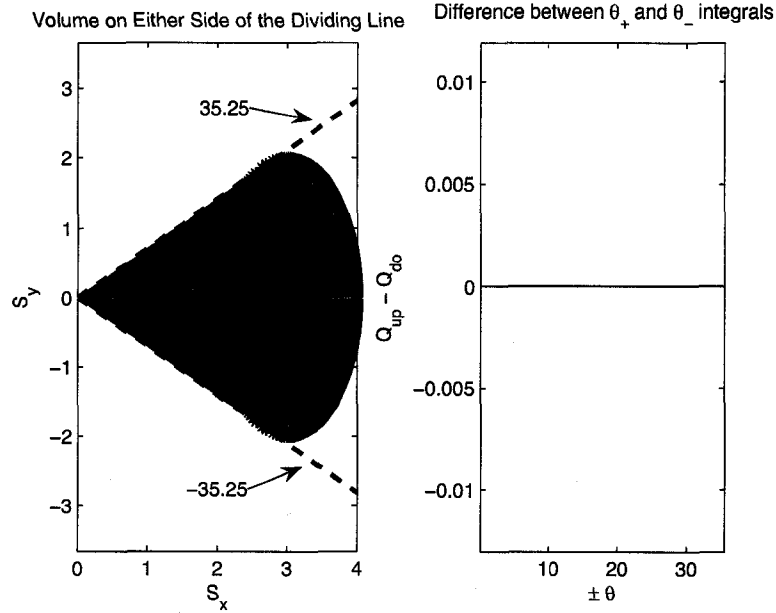


Figure 3.8. Bias in the azimuth estimates when the confidence ellipse is aligned with the principle axes of the array. The left hand plot shows the range of possible azimuth estimates in the arbitrary confidence ellipse. The right hand plot shows the difference between the line integral for the positive angle, Q_{up} , and the negative angle, Q_{do} , for the range of possible angles.

is the method of quadrature.⁴⁶ Using the built-in Matlab function “quadl.m”, the integrals were evaluated using adaptive Lobatto quadrature.⁴⁶

The bias in the estimate of the azimuth was determined by calculating the $\pm\theta$ integrals for a range of possible azimuth estimates inside the confidence ellipse. The $\pm\theta$ integrals were calculated in angle steps of 0.1° from the true azimuth to the positive and negative limit of possible azimuth estimates. The bias in the azimuth estimate for the special case where the slowness vector is aligned with the principal axes of the array was first considered. The method was then extended to the general case where the slowness vector was not aligned with the principle axes of the array.

When the slowness vector is aligned with the principle axes there will be no bias in the least squares estimate of azimuth. To illustrate that the azimuth estimate is unbiased in this special case, a range of $\pm\theta$ lines was plotted in Figure 3.8 for an arbitrary ellipse. The

left-hand plot in Figure 3.8 shows the range of $\pm\theta$ lines for an ellipse with semi-major axis of 2 and semi-minor axis of 1. The slowness vector magnitude is 3 s/km and the slowness vector has an azimuth of zero, which aligns the slowness vector with the principal axes of the ellipse. Note that in the case where the slowness vector is aligned with the principal axes of the ellipse, the range of possible $\pm\theta$ angles are the same on either side of the dividing line. The right hand plot shows the difference between the line integral for the positive angle, Q_{up} , and the negative angle, Q_{do} , for the range of possible angles. The difference between the two line integrals is zero for all angles calculated, meaning that the volume above the dividing line is equal to the volume below the dividing line resulting in an unbiased estimate of azimuth.

The estimate of the azimuth is unbiased if the slowness vector is aligned with one of the principal axes of the distribution ellipse, but becomes biased as the slowness vector moves away from a principal axis. Azimuths resulting in an unbiased azimuthal estimate are rare, occurring only at four of an infinite set of azimuths. The more common case is one for which the slowness vector is not aligned with the principal axes of the ellipse. A set of plots similar to the plots shown in Figure 3.8 was produced for an azimuth of 45° degrees. The estimate of the azimuth is biased for this azimuth. The range of possible azimuthal estimates was different for the region above and the region below the dividing line. The possible azimuth estimates above the dividing line could not exceed 23.5° , however the angles below the dividing line could take values greater than 23.5° . Due to the asymmetric range of possible angles, there were some low azimuth estimates that were not balanced out by high azimuth estimates.

The unbalanced range in the possible azimuth estimates does not, in of itself, prove that the least squares estimate of the azimuth is biased. The volume above the line could be much greater than the volume below the line and balance out the low estimates that have no high counterparts. The right hand plot in Figure 3.9 shows that this is not the case. The right hand plot shows the difference between value of the line integral for $+\theta$ and the line integral for $-\theta$. The difference between the results of the numerical integration is not zero for all angles calculated. In this biased case, the $-\theta$ line integral is always greater than the $+\theta$ line integral, making the volume below the dividing line greater than the volume above the dividing line for all the common angles. The difference in the volumes introduces

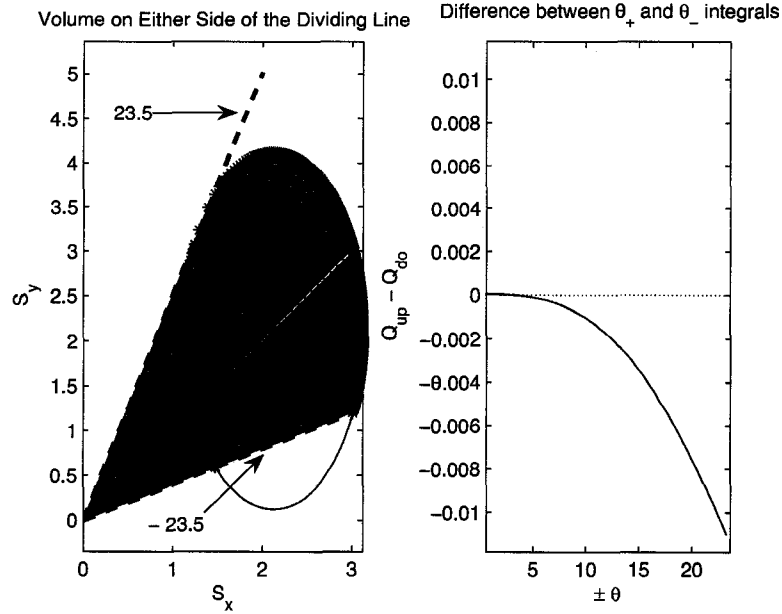


Figure 3.9. Bias in the azimuth estimates when the confidence ellipse is not aligned with the principle axes of the array. The left hand plot shows the range of possible azimuth estimates in the confidence ellipse. The right hand plot shows the difference between the line integral for the positive angle, Q_{up} , and the negative angle, Q_{do} , for the range of possible angles.

a bias toward low azimuth estimates at 45° , compounded by the fact there are more low estimates possible than high estimates.

3.4.2 Effect of Array and Wave Parameters on the Bias in the Estimate of Azimuth

The azimuth and slowness vector magnitude estimates are both derived from the estimate of the slowness vector. Since both estimates are derived from the same pdf the same four parameters that influenced the bias in the slowness vector magnitude estimate affect the bias in the estimate of azimuth. The parameters affecting the bias in the azimuth estimate are: area of the ellipse that encloses some fraction of the distribution, the aspect ratio of the ellipse, the slowness vector magnitude where the ellipse is centered, and the azimuth at which the ellipse is centered. The effects of these parameters on the bias in the estimate of azimuth were similar to the effects the parameters had on the estimate of the slowness

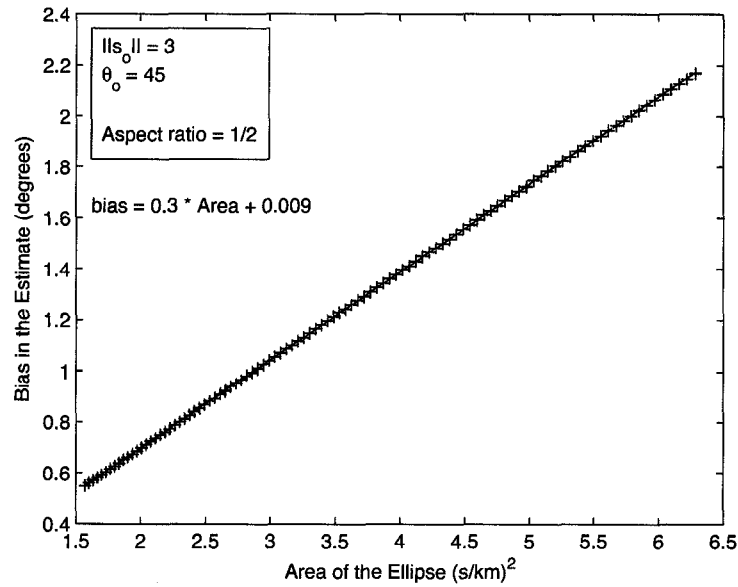


Figure 3.10. Bias in the estimate of the azimuth versus the area of an arbitrary confidence ellipse. The blue + are the results of the numerical simulation for various ellipse areas. The red line is the linear curve fit of the numerical results.

vector magnitude. The dependence of the bias in the azimuth estimate on wave and array parameters was explored using a numerical simulation in the same manner as the exploration of the bias in the slowness vector magnitude estimates.

The effect of the area of the confidence ellipse on the magnitude of the bias in the azimuth estimate was similar to the area effect for the estimate of the slowness vector magnitude. A linear relationship between the ellipse area and the magnitude of the bias in the azimuth estimate was observed in the numerical results of the azimuth bias versus the ellipse area test. The linear relation between the ellipse area and the bias in the azimuth estimate is shown in Figure 3.10. The aspect ratio of the confidence ellipse was held constant at 1/2 during the variation of the area. The slowness magnitude and the azimuth were also held constant during the simulation at 3 s/km and 45°, respectively. The blue + are the results of the numerical simulation for each ellipse area. The red line is a linear curve fit of the simulation results. The coefficient of determination for the linear fit was 1. The bias in the azimuth estimate increased proportionally with increases in the area of the confidence

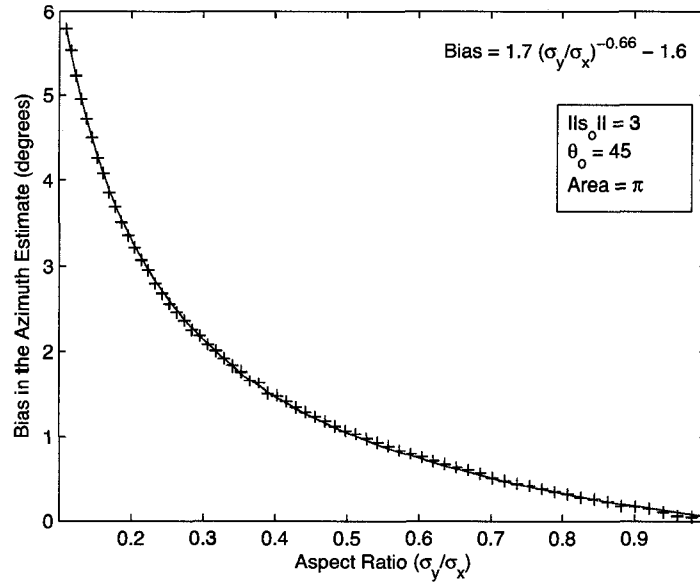


Figure 3.11. Bias in the estimate of the azimuth versus the aspect ratio of the confidence ellipse. The blue + are the results of the numerical simulation for various aspect ratios of the ellipse. The red line is the inverse power law curve fit of the numerical results.

ellipse.

The bias in the estimate of the azimuth displayed an inverse power law dependence on the aspect ratio of the confidence ellipse. The estimate of the azimuth was unbiased when the aspect ratio is 1. The magnitude of the bias in the azimuth estimate increased as the eccentricity of the confidence ellipse is increased. The area of the ellipse was held constant at π as the aspect ratio was varied between 1 and 0.1. The slowness vector magnitude was a constant equal to 3 s/km and the azimuth was constant at 45° . An inverse power law curve, shown by the red line in Figure 3.11, was fit to the results of the numerical simulation exploring the effects of the aspect ratio on the bias in the azimuth estimate. The inverse power law curve,

$$\hat{b} = 1.7 \left(\frac{\sigma_y}{\sigma_x} \right)^{-0.7} - 1.6, \quad (3.55)$$

fit the numerical results with a coefficient of determination of 1 to within four significant figures.

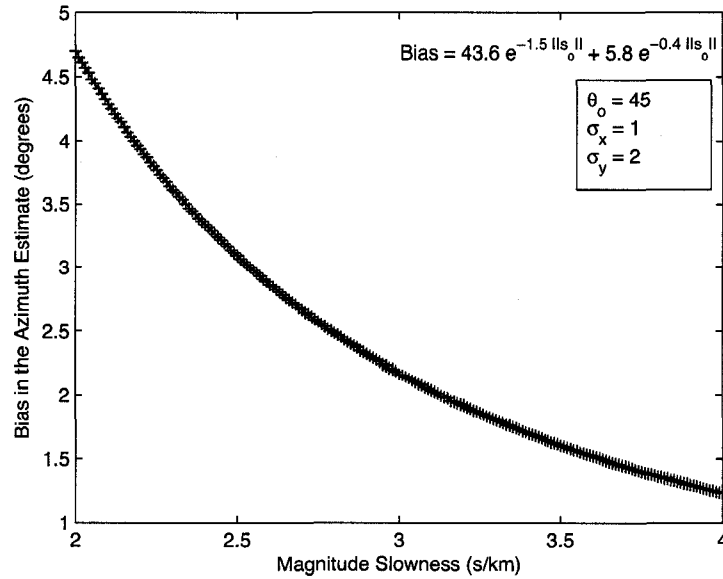


Figure 3.12. Bias in the estimate of the azimuth versus the slowness vector magnitude. The blue + are the results of the numerical simulation for slowness magnitudes between 2 s/km and 4 s/km. The red line is a sum of exponentials curve fit of the numerical results.

A circularly-symmetric array has a confidence ellipse with an aspect ratio of one. The bias in the azimuth estimate of a circularly symmetric array predicted by the fit curve was 0.052° . Unlike the estimate of the slowness vector magnitude, the theoretic bias in the azimuth estimate is zero for circularly symmetric array. The non-zero bias predicted by the curve fit is due to error in the curve fit. The bias in the least squares estimate of azimuth was minimized by a circularly symmetric array. Like the effect of the aspect ratio on the bias in the slowness magnitude estimate, a more eccentric aspect ratio of the confidence ellipse amplifies the angular dependence of the bias in the estimate of azimuth.

Similar to the effect of the slowness vector magnitude on the bias in the estimate of the slowness vector magnitude, the bias in the azimuth estimate decreased as the slowness vector magnitude is increased. The numerically simulated bias in the least squares azimuth estimate approached zero as the slowness vector magnitude increased toward infinity as expected. The blue + in Figure 3.12 are the results of the numerical simulation for slowness magnitudes varying between 2 s/km and 4 s/km. The numerical results were fit with a sum

of exponentials curve due to the asymptotic behavior of the azimuth bias as the slowness magnitude goes toward infinity,

$$\hat{b} = 43.6e^{-1.5||s_o||} + 5.8e^{-0.41||s_o||}.$$

The simulated bias data was fit with this model to ensure that the behavior of the azimuth bias had the correct behavior as the slowness vector magnitude increased toward infinity. The red line shows the sum of exponentials curve fit to the numerical results for the bias in the azimuth estimate. The coefficient of determination was equal to 1 to within four significant figures, indicating that the variance in the data was accounted for by the curve model. The decrease in the azimuth estimate bias as the slowness magnitude increased can also be seen geometrically. As the confidence ellipse moves toward infinity the angle subtended from the origin by the ellipse decreases and the difference between the two volumes of the ellipse decreases toward zero.

The last of the four parameters affecting the bias in the azimuth estimate is the azimuth of the center of the confidence ellipse. Figure 3.13 shows a harmonic dependence of the bias in the azimuth estimate on the wave azimuth. Unlike the azimuth dependence of the estimate of the slowness vector magnitude, the bias in the estimate of the azimuth took on both positive and negative numbers depending on the angle of the ellipse center. The estimate of the azimuth was unbiased when the slowness vector was aligned with one of the principle axes of the array, as was expected from the numerical derivation of the bias. The characteristic of being unbiased at finite slowness vector magnitudes separates the azimuth estimate from the estimate of the slowness vector magnitude.

3.5 Conclusion

The least squares estimates of the slowness vector magnitude and of the azimuth are biased estimates. The bias in the parameter estimates represents a systematic error in the source location process. The bias in the least squares estimate of the slowness vector was analytically derived from the pdf of the slowness vector.⁴³ The analytic expression of the bias in the slowness vector magnitude estimate showed that the estimate is always biased high for finite magnitudes of the slowness vector. The integrals required to analytically derive the bias in the least squares estimate of azimuth were intractable. A modified numerical integration scheme involving the curves of constant probability and one-dimensional numerical

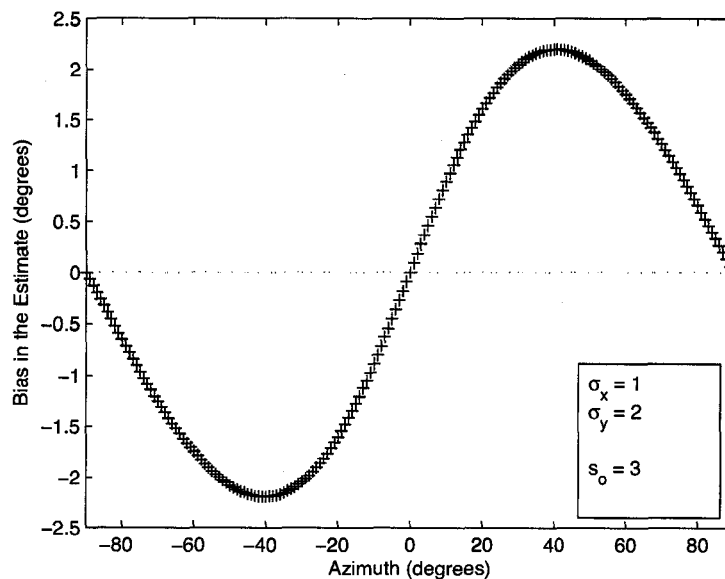


Figure 3.13. Bias in the estimate of the azimuth versus the azimuth of the center of the confidence ellipse. The blue + are the results of the numerical bias simulation for azimuths between ± 90 degrees.

integrals was used to determine that the azimuth estimate was biased. The bias in the least squares estimate of azimuth could be unbiased, biased high, or biased low depending on the wave and array parameters.

Numerical simulations were used to determine the effect of wave and array parameters on the magnitude of the bias in the estimates. The magnitude of the bias in both of the estimates was influenced by the wave parameters (the trace velocity of the wave and the wave azimuth) and the array parameters (the aspect ratio and area of the confidence ellipse). Since both estimates were derived from the same slowness vector pdf, the effects of the array and wave parameters on the bias in the estimates were similar for the two estimates. The bias in both the azimuth and slowness vector magnitude estimates due to the aspect ratio of the ellipse and due to the azimuth of the confidence ellipse is minimized for a circularly symmetric array. The azimuth estimate is unbiased for a circularly symmetric array. The bias in both estimates tended toward zero as the trace velocity of the acoustic wave approached zero. A linear dependence of the magnitude of the bias on the ellipse area

was observed for both the azimuth and slowness magnitude estimates.

The magnitude of the bias in the least squares estimates of trace velocity and azimuth is at least an order of magnitude less than the uncertainty in the estimates. The uncertainty in the least squares estimate of azimuth is geometrically found by the angle subtended from the origin by the confidence ellipse and the uncertainty in the estimate of the slowness vector magnitude is given by the difference in the extremal distances for the origin of the ellipse.⁴³ A numerical investigation of the magnitude of the bias in the parameter estimates for the Fairbanks and Windless Bight arrays revealed that the bias is negligible compared to the uncertainty in the estimate. For signal-to-noise ratios of approximately 10 dB and a slowness vector magnitude of approximately 3 s/km, the measured variances associated with the numerically simulated slowness vector were of the order 10^{-1} s/km for trace velocity and 1 degree for azimuth estimates. The bias in the estimates of the slowness vector magnitude and azimuth were at least an order of magnitude smaller than the uncertainty in the estimate of the slowness vector magnitude and azimuth for all azimuths estimated. While the effects of the bias on the estimates are not noticeable in practical situations, the bias in the least squares estimate of slowness vector magnitude and azimuth still represents a systematic error in the acoustic source location process.

Even with the assumed GWU noise corrupting a signal the least squares estimates of azimuth and trace velocity are not unbiased and, consequently, are not the MVU estimate. It is a widely accepted fact that the infrasonic noise field is not white, uncorrelated noise. The effects of the physical noise field could introduce a further degradation of the least squares estimates of azimuth and trace velocity. In the following chapters the infrasonic noise field at IS53 and IS55 will be characterized, and the effects of the infrasonic noise field on the estimation of the azimuth and trace velocity will be determined.

Chapter 4

Distribution of the Infrasonic Noise Field

4.1 Introduction

In the previous chapters the pressure data collected at an array of sensors was used to estimate velocity parameters of an acoustic wave traversing the array. In the process of estimating the wave parameters, data recorded by the sensors was modeled as a deterministic signal corrupted by an additive, random noise field. Due to the random nature of the noise field, the exact form of the noise field is generally not known in the source location problem. The standard assumption made about the characteristics of the noise field is that it is Gaussian, white, uncorrelated (GWU) noise. The GWU noise field is an idealization of the actual noise field present at the location of data collection. The deviation of the infrasonic noise field from this idealization could affect the accuracy of the least squares parameter estimation. By exploring the physical noise field present at the point of data collection it can be realistically modeled and the effects on the performance of the parameter estimation can be determined.

A statistical study was conducted to determine the form of the noise field at the Fairbanks and Windless Bight arrays. The results of this study revealed that the infrasonic noise field at the arrays was a composite field made up clutter and turbulent pressure fluctuations produced by convective ground heating and turbulent wind flow. The clutter elements of the noise field varied seasonally at the two array locations. A diurnal variation in the noise field power spectrum was also observed at the Fairbanks array in the summer months. The source of the diurnal cycle observed in the noise field power spectral density (PSD) is plausibly due to convective heating of the air by ground heated by solar insolation.

The effect of the local wind flow on the noise field at the Fairbanks and Windless Bight arrays was examined using the estimated power spectra. The noise power estimated from the data increased as the measured local wind speed increased. The increase in noise power with local wind speed did not occur equally across all frequencies for which the power was estimated. The frequency dependence of the noise power on local wind speed at both arrays was determined for the four seasons of the year. The effects of local terrain on the rate at which noise power increases with respect to local wind speed were inferred from the frequency-dependent data produced from the estimated power spectra.

The empirical noise field was then used to determine the effects of the discrepancy between the GWU and actual noise fields on least squares parameter estimation. Synthetic noise data, with a qualitatively similar power distribution to the actual noise field, was generated using the results of the statistical noise field study. With the synthetic noise data, the effects of the empirical noise field could be determined with numerical simulations. The effectiveness of bandpass filtering the raw data to reduce the negative effects of the empirical noise field was also explored. When the data with the empirical noise is bandpass filtered, the performance of the least squares parameter estimate is comparable to the estimate performance with GWU noise, although at a lower signal-to-noise ratio.

4.2 The Noise Field

In order to explore the nature of the noise field, a definition of noise must be presented. No single definition of noise exists, but it is common practice to define noise as everything that is not a signal.⁴⁸ This definition leads to an ambiguity in what exactly constitutes infrasonic noise. The definition of a signal is dependent on the application, and so, the definition of noise will be different for different applications. Without a well-defined way to identify noise it is difficult to explore the nature of the infrasonic noise field at Fairbanks and Windless Bight. In an attempt to more universally define what qualifies as noise, a new definition of the noise is proposed. In this application, noise is defined as the median, stationary fluctuating pressure field present at the point of data collection and a signal as a deviation away from this median, stationary fluctuating pressure field. The proposed definition is just a refinement of the common definition that noise is everything that is not a signal[†].

The proposed definition of noise requires the determination of the median, stationary fluctuating pressure field at an array. The infrasonic noise field is a composite field and it is not a simple matter to determine form of its components. There are two main components of the infrasonic noise field: clutter, and turbulent pressure fluctuations. Clutter is defined as omnipresent pressure waves created by geophysical or man-made sources. Microbaroms⁴⁹ are a known source of a persistent clutter that affect infrasound measurements worldwide. Turbulent pressure fluctuations are caused by turbulent wind flows^{12,13,14,15,50,51} and con-

[†]Or rather that signal is everything that isn't noise.

vective heating of the air by ground heated by solar insolation.⁵² The magnitude of the effects of the clutter and turbulent pressure fluctuations on the noise field is highly dependent on the location of data collection. Due to the dependence of the noise field on the location of the array, the noise field must be estimated for each array independently. In this study the noise field was estimated for the CTBTO arrays located at Fairbanks, Alaska (IS53) and Windless Bight, Antarctica (IS55).

4.2.1 Method

The noise field is a nondeterministic field and must be characterized using statistical methods. A method of determining the infrasonic noise field statistically was employed by Bowmann *et al.*⁴⁸ In their work, the recorded data were segmented, power spectra were estimated for each of the data segments, and the resulting power spectra were averaged together to characterize the noise field. A modified version of this basic method will be used to characterize the noise field at the Fairbanks and Windless Bight arrays. The major modifications to the method of Bowmann *et al.* will not be to the basic method, but to the application of the method to the data.

The first step in the process is to segment the data recorded at the arrays. There exists no analytic method to determine the optimal length of the data set, and the segment length must be determined empirically using the method of window closing.³¹ Although no exact rules exist to determine when to stop the window closing procedure, physical considerations can help guide the length of the data segment. For example, estimation of the power in frequencies lower than the Brunt-Väisälä frequency is not necessary since acoustic waves cannot propagate at frequencies lower than the Brunt-Väisälä frequency.

The length of the data segments used to estimate the power spectrum was chosen to be three minutes. This data segment length was chosen for several reasons. First, the PSD of a data segment of three minutes had only two frequency estimates that were lower than the Brunt-Väisälä frequency which contained no information on propagating acoustic waves. Second, the density of the frequency estimates in the frequency band of the microbaroms was high enough to produce a PSD with a fidelity that allowed for the analysis of the noise features caused by the microbaroms. Finally, a three minute data segment allowed a direct comparison of the results at the Fairbanks and Windless Bight arrays with the results of

the work done by Bowmann *et al.*⁴⁸ The resulting characterizations of the infrasonic noise fields produced by this method are insensitive to the choice of data segment length.

The stability of the estimated noise field PSD was enhanced by using the Welch method of spectral estimation;³⁶ the three minute data segments were further segmented into four subwindows that were 1024 samples long and the PSD of each subwindow was calculated. The resulting power spectra for the subwindows were averaged to produce the Welch estimate of the PSD for the three minute data segment. The number of samples in the subwindows was chosen to optimize the calculation speed of the periodograms. The subwindows were overlapped by 515 samples to minimize the number of data samples omitted at the end of the data segment and give an overlap of approximately fifty percent. The analog pressure data collected at both of the arrays was sampled at a rate of twenty samples per second, resulting in a Nyquist frequency of 10 Hz. The data digitizer employs an analog anti-aliasing filter that filters out any frequency greater than 10 Hz prior to digitization so the power spectra estimates did not include any frequency estimates above the Nyquist frequency.

The data used to create the power spectra were not pre-processed to exclude data segments that contain signals from geophysical or man-made sources. In addition to the possible presence of signals in the calculated power spectra, the wind speed and diurnal cycle have an effect on the fluctuating pressure field. To filter out the effects of signals and determine the median, stationary fluctuating pressure field, the statistics of the noise field can be built by grouping many of the raw power spectra together to form a statistical ensemble. It is possible that the fidelity of the resulting characterization of the noise field will be decreased in the process of building the statistics of the noise field. If the underlying processes that produce the key features of the noise field, such as the microbaroms and the diurnal cycle, change too much during the time period being averaged, the fidelity of the characterization of the noise field will be decreased and the structure of the key features of the noise field will be altered. The microbaroms and the diurnal cycle vary seasonally and the noise field will also vary throughout the year. The expected seasonal variation of the noise field must be taken into account when choosing which power spectra are included in the statistical ensemble.

To determine how many of the raw power spectra can be collected into the ensemble

the principles guiding window closing can be employed. The window closing process begins with the separate power spectra produced for each of the eight sensors. The power spectra of the eight sensors were qualitatively compared during random time periods at both array locations. The characteristics of the noise field power spectra were similar enough to suggest that the inclusion of all eight of the power spectra in the ensemble would not result in a loss of fidelity in the estimated noise power spectrum. The window closing process was repeated for each of the three minute data segments within the same hour. The key features of the noise power spectra for the three minute windows were similar, and all twenty of the power spectra for one hour were included in the ensemble to improve stability. At this point in the window closing process the ensemble of power spectra estimates includes the estimates from all eight sensors for a time period of one hour.

The number of hours included in the ensemble was influenced by the diurnal cycle of the power spectra. The diurnal cycle in the atmospheric boundary layer is driven by solar heating.⁵² Each day was broken into four blocks to determine the effect of the atmospheric diurnal cycle on the noise field. The time blocks for both arrays were centered on the hours of sunrise, sunset, noon, and midnight. The time of sunrise and sunset varies significantly throughout the year at the location of both arrays. The sunrise and sunset times at Fairbanks during the year 2006 are shown in Figure 4.1. Note that the largest time block that can be used at Fairbanks without sunrise and sunset overlapping is three hours, one hour before sunrise/sunset and one hour after sunrise/sunset. Using three hour blocks will lead to overlap of the noon, sunrise, and sunset time blocks for a week during the month of December, and of the midnight, sunrise, and sunset time blocks for a week during the month of June where all times refer to the local solar time. To avoid potential mixing of different atmospheric effects, these overlap weeks will be excluded from the averaging when the three hour block power spectra are created. The array at Windless Bight is at a higher latitude than the array at Fairbanks and during large portions of the year the sun is either always up or down. The sun never sets at Windless Bight from 24 October to 19 February and never rises from 25 April to 19 August. During these two periods the three hour time blocks were centered at 6:00 a.m., 12:00 a.m., 6:00 p.m., and 12:00 p.m., local solar time. The noon or midnight blocks overlap with the sunrise and sunset blocks at Windless Bight for the ten days preceeding and following the austral summer and winter. The days where

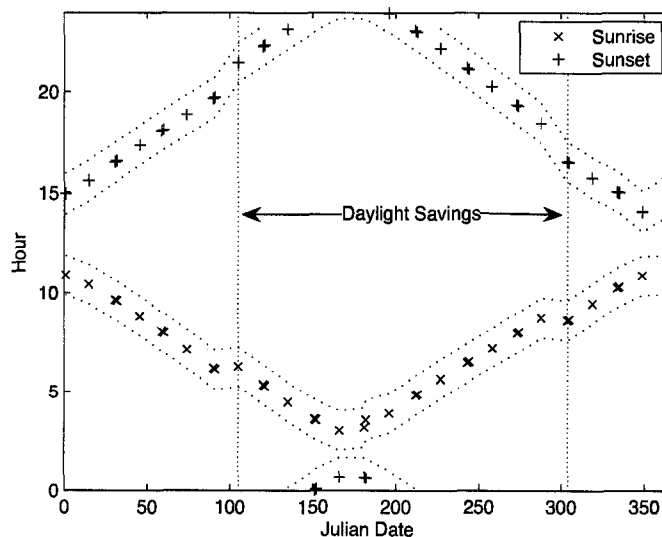


Figure 4.1. Sunrise and sunset times for Fairbanks, AK during 2006. The black \times are the local times of sunrise and the black $+$ are the local sunset times. The dashed lines are the limits of the three hour block for sunrise and sunset.

the overlap occurred were omitted from the ensemble of the Windless Bight data. For the rest of the year the time blocks were centered in the same manner as the Fairbanks data. The result of this grouping of power spectra into four separate time bins is a potentially different noise field for the four times of day. Without the binning, the effects of the local atmospheric diurnal cycle on the infrasonic noise field could not have been resolved.

The building of the noise field statistics through window closing continued with the grouping of days, weeks, and months. At a time scale on the order of months the characteristics of the microbaroms begin to vary at both array locations. The variation of the microbaroms must be considered while continuing to build the statistical ensembles. At the month-long time scale the ensembles for each of the four time periods consist of approximately 14,400 realizations of the fluctuating pressure field. Bowmann et al. further combined the monthly noise fields into seasonal representations of the noise field.⁴⁸ The grouping of the monthly noise power spectra into a seasonal noise field representation will improve the statistics of the noise power spectra, but at the cost of fidelity. The combi-

nation of the monthly noise fields must be done with care so as to not combine months in a manner that will sacrifice the fidelity of the microbaroms or the diurnal cycle observed in the noise field power spectrum estimate. The combination of months with dissimilar features averages the noise field features toward each other, resulting in a loss of resolution of the features. The grouping of months into seasonal groups must be dictated by the character of the microbaroms and the diurnal cycle during each month. The loss of fidelity resulting from seasonal groupings made seasonal groupings unattractive at the Fairbanks array. Simple four-season groupings of the monthly noise fields for Windless Bight did not suffer from this loss of fidelity and were used to improve the stability of the noise field power spectrum estimate.

4.2.2 Results

The median noise field power spectra, estimated from the separate statistical ensemble of the four time blocks, were plotted together on monthly log plots. The resulting noise fields estimated from the data collected at the Fairbanks array during 2006 are shown in Figure 4.2 to Figure 4.4. These median noise field power spectra were found by calculating the median value of the power estimate at each frequency estimated in the monthly ensemble of power spectra. The noise field for each of the time blocks is plotted in a different color: midnight in black, noon in magenta, sunrise in blue, and sunset in red. The 5% and 95% confidence limits of the noise field power spectra ensembles were included on each of the monthly plots. The confidence limits indicate the power amplitude where 95% or 5% of the ensemble PSD estimates were less than the limit. The variance of each of the monthly time block PSD estimates is on the order of 4.17×10^{-6} , under the assumption that the data in the time block ensemble is stationary.³¹ The layout of the plots was held constant across all the monthly ensembles produced from the data.

Microbaroms are acoustic signals associated with severe weather in the ocean and the high ocean surface waves caused by the severe weather.² Microbaroms are observed worldwide with coherent and incoherent energy between 0.1 and 1 Hz with a maximum energy at 0.2 Hz for open-ocean swells.^{53,3} The seasonal variation of the microbaroms was clearly illustrated in the plots of the monthly noise fields. During the month of January the microbarom peak, at approximately 0.2 Hz, was prominent. The prominence of the microbarom

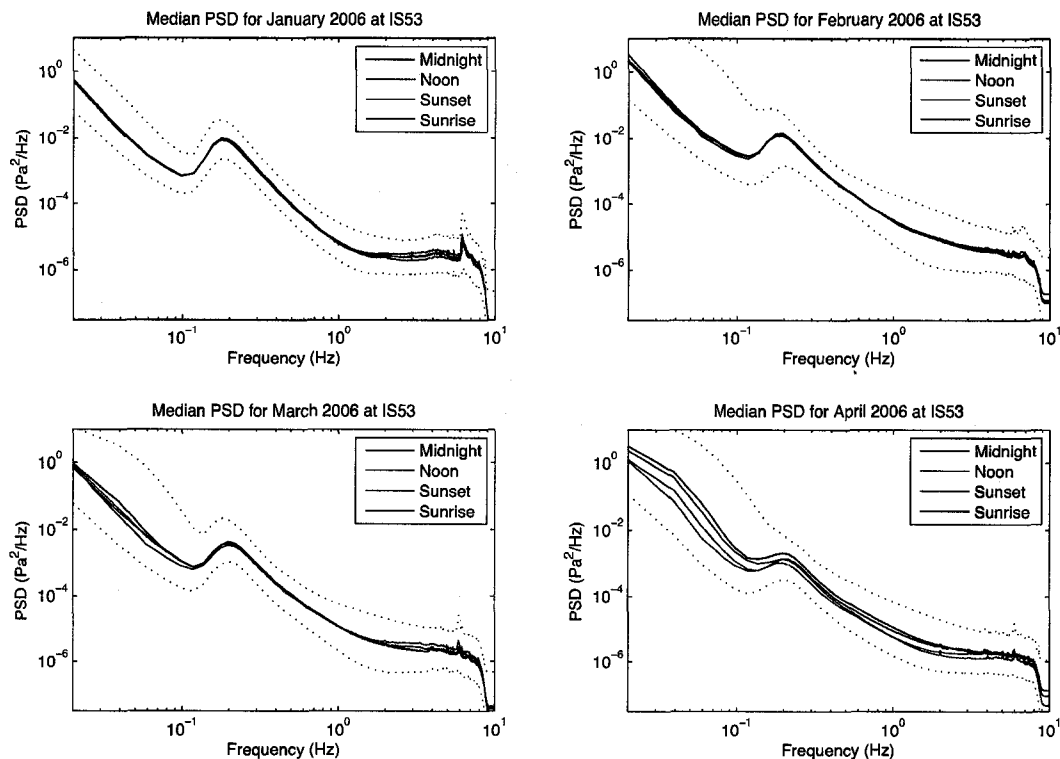


Figure 4.2. Median power spectra for the months of January-April 2006 measured at the Fairbanks array. The solid black line is the median power spectrum for the three hour time block centered about midnight, the solid magenta line is the median power spectrum during the noon time block, the solid red line is the power spectrum during sunset, and the solid blue line is the power spectrum during sunrise. The black dashed lines indicate the 95% and 5% confidence limits of all the power spectra for the entire month.

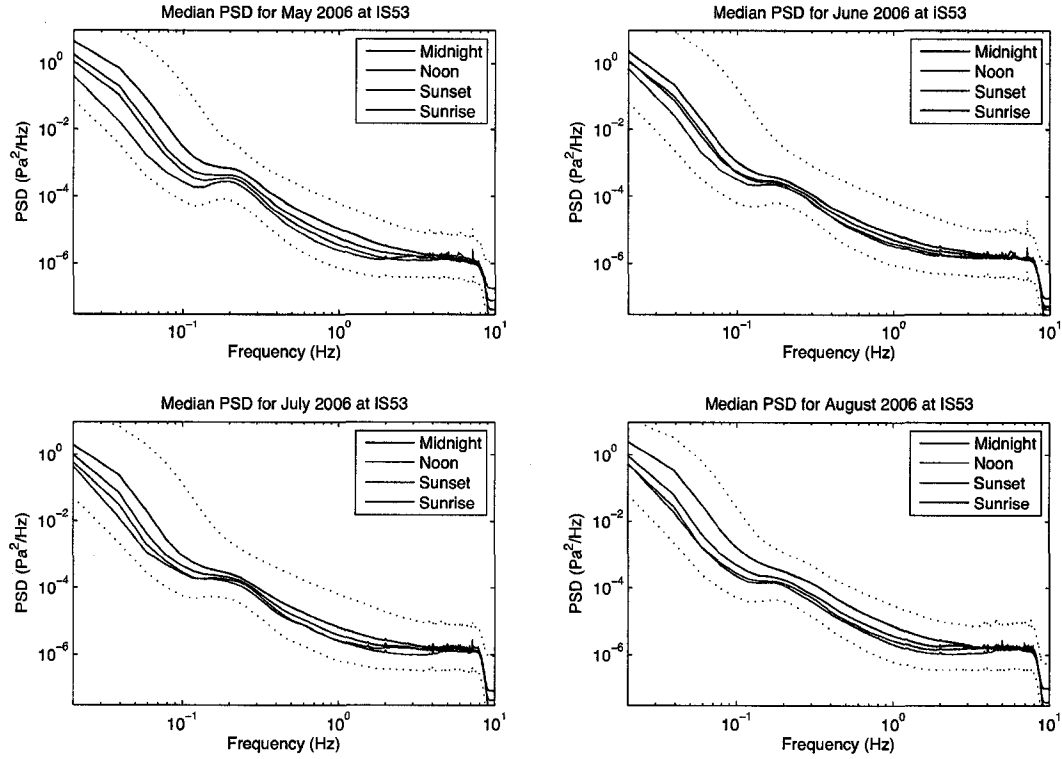


Figure 4.3. Median power spectra for the months of May-August 2006 measured at the Fairbanks array. The solid black line is the median power spectrum for the three-hour time block centered about midnight, the solid magenta line is the median power spectrum during the noon-time block, the solid red line is the power spectrum during sunset, and the solid blue line is the power spectrum during sunrise. The black dashed lines indicate the 95% and 5% confidence limits of all the power spectra for the entire month.

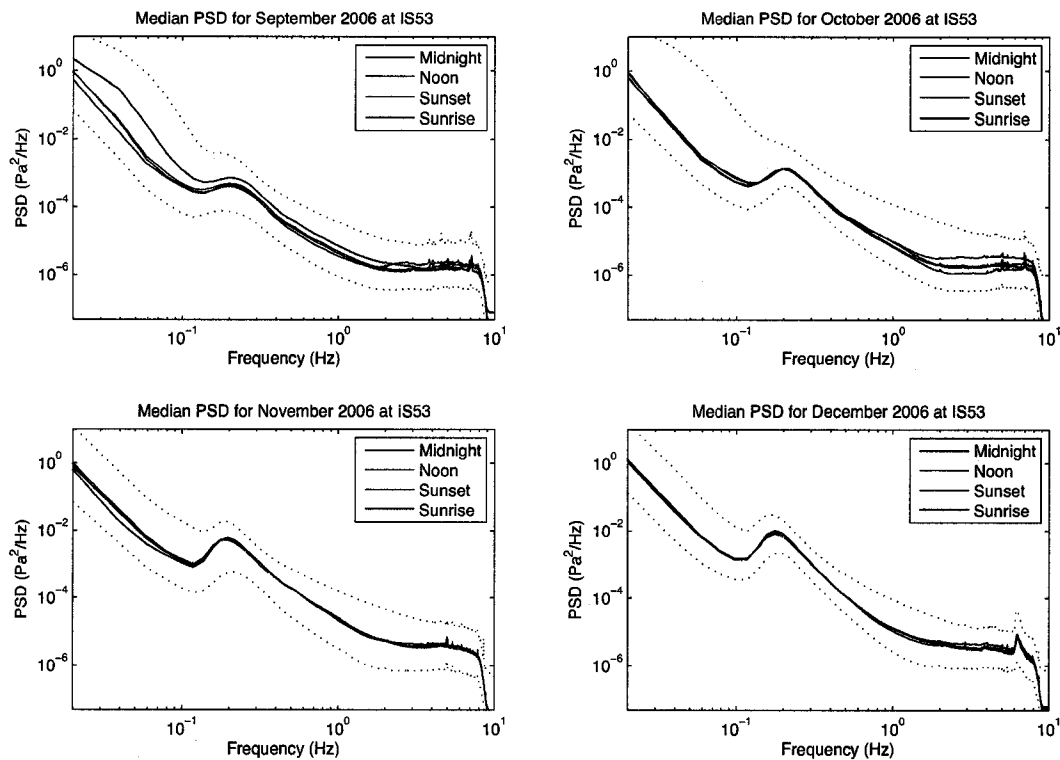


Figure 4.4. Median power spectra for the months of September-December 2006 measured at the Fairbanks array. The solid black line is the median power spectrum for the three-hour time block centered about midnight, the solid magenta line is the median power spectrum during the noon-time block, the solid red line is the power spectrum during sunset, and the solid blue line is the power spectrum during sunrise. The black dashed lines indicate the 95% and 5% confidence limits of all the power spectra for the entire month.

peak diminished during the spring and reached a minimum during the month of August. The microbarom peak increased during the fall and reached prominence again during the winter months.

A seasonal dependence of the diurnal cycle was also visible in the plots of the median noise field power spectra. The diurnal cycle was not observed at the Fairbanks array during the months of January, February, and March. The diurnal cycle emerged during the spring and summer. The diurnal cycle began to decay during September and was again absent during the months of October, November, and December. To ensure that the seasonal variations in the microbaroms and the diurnal cycle observed during the year of 2006 were consistent between years, the noise fields were also calculated for 2005 at the Fairbanks array. The microbaroms and the diurnal cycle showed qualitatively similar seasonal variations during the year 2005.

The seasonal variations of the estimated microbarom power were less pronounced at the Windless Bight array during 2006. The seasonal infrasonic noise field power spectra estimated at Windless Bight, shown in Figure 4.5, displayed a complete lack of any diurnal cycle. The smaller seasonal variation at Windless Bight allowed the statistics of the estimated noise field power spectra to be improved further by grouping the monthly power spectra into seasonal representations of the noise field power spectrum. The microbarom peak estimated at Windless Bight was most prominent during the austral fall and winter. During the summer season at Windless Bight the microbarom peak decreased slightly in amplitude, but remained the dominant feature of the infrasonic noise field. The dominance of the microbarom peak in the estimated noise field power spectra was reduced during the austral spring. During the spring season the estimated microbarom peak was similar in character to the microbarom peaks estimated at Fairbanks from May to August.

Meteorology

The variation in diurnal cycle observed at Fairbanks might be explained by boundary layer meteorology.⁵² The infrasonic noise field at the Fairbanks array was made up of pressure fluctuations from clutter and turbulence. The sources producing clutter do not vary according to the time of day during the months when the diurnal cycle was observed (D. Lee, personal communication, February 2007). It follows that the diurnal cycle in the infrasonic

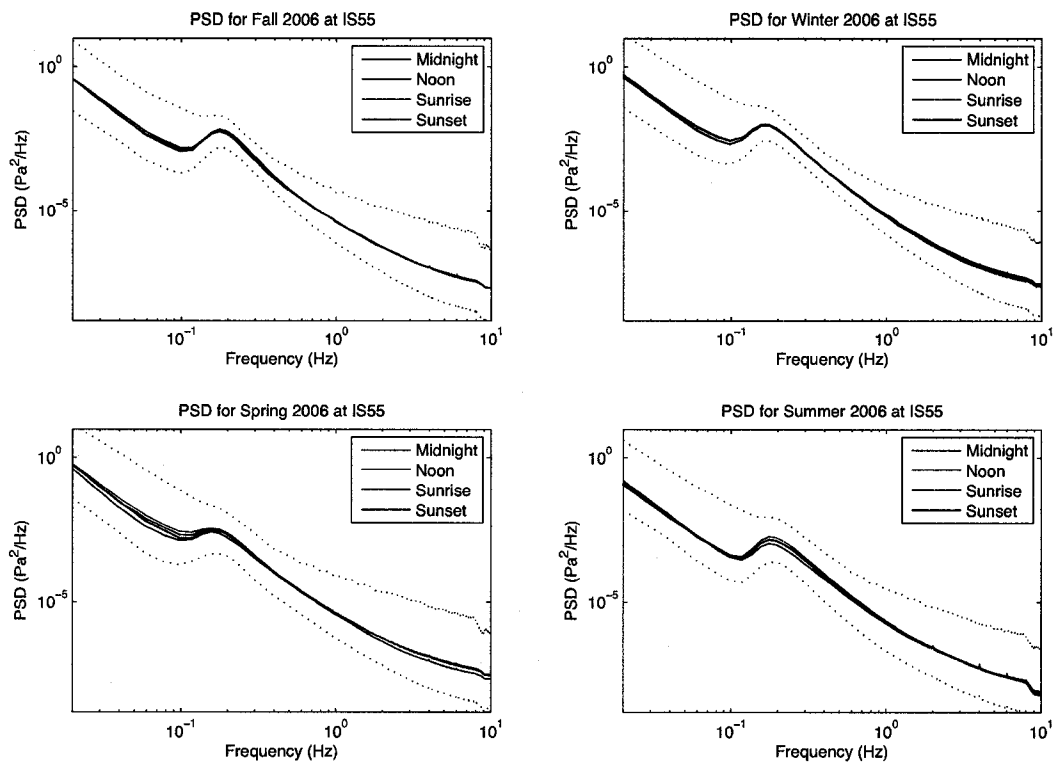


Figure 4.5. 2006 seasonal noise power spectra estimated at the Windless Bight array. The solid black line is the median power spectrum for the three-hour time block centered about midnight, the solid magenta line is the median power spectrum during the noon-time block, the solid red line is the power spectrum during sunset, and the solid blue line is the power spectrum during sunrise. The black dashed lines indicate the 95% and 5% confidence limits of all the power spectra for the entire month.

noise PSD was an effect of the turbulent pressure fluctuations, and not an effect of changes in the sources producing the clutter. The daily evolution of the turbulent mixing layer of the atmospheric boundary layer is summarized in general terms by Stull.⁵² The turbulent mixing layer is generally formed by convective heating, but is sometimes formed by strong winds. The local winds during the time blocks used to estimate the noise field power spectrum have an effect on the estimated noise power and will be explored in Section 4.3. For now it is simply noted that the pattern in the mean winds within the time blocks during the periods when the diurnal cycle was observed did not correspond to the pattern observed in the estimated noise field PSD.

There are two main sources of convective atmospheric heating.⁵² These two sources are: heat transfer from the warm ground to the air directly above it, and radiative cooling for the top of the cloud layer. The heat transfer from the ground to the air immediately above the surface causes thermals of warm air to rise from the ground, while cooling from the top of the cloud layer causes thermals of cool air to sink back toward the ground. Generally, the sun imparts energy to the ground during the day and the ground radiates this heat into the air above the ground. The heated air turbulently mixes with the cooler air above it, and produces turbulent pressure fluctuations.

The convective heating from the ground could drive the diurnal cycle observed in the noise field PSD. The assertion that the ground heating is critical to the formation of the diurnal cycle is supported by the correlation between the lack of a diurnal cycle and snow cover on the ground around the array. In Fairbanks the ground is typically covered by snow by October and remains covered until early April. The diurnal cycle in the noise field power spectrum estimates was absent in the power spectra from October through March at the Fairbanks array. When the ground surrounding the array at Fairbanks was covered by snow the diurnal cycle in the infrasonic noise field PSD was absent, and when the snow melted the diurnal cycle returned. Further support is given by the lack of a diurnal cycle at Windless Bight. At Windless Bight the surface underneath the array is a perpetually snow covered ice shelf. Even when the sun is up twenty four hours a day during the austral summer there, one expects a lack of a diurnal cycle in the noise field PSD because the surface surrounding the array cannot efficiently absorb and re-radiate the energy of the sun.

The effects of the diurnal cycle observed at Fairbanks display general trends in the noise fields for limited frequency bands. When the diurnal cycle is observed, the noise power is greatest during the sunrise time block from very low frequencies up to approximately 2 Hz. The power contained in the sunset time block is minimal from the lowest frequencies up to about 0.1 Hz for the months of observation. Details of the evolution of the boundary layer provided by Stull⁵² could explain why the sunrise block contains the most power and the sunset block the least. The turbulence created by the convective ground heating forms large thermals cells that mix heated air with the cooler air above the ground. This mixing happens in a shallow layer called the entrainment zone, whose location increases in altitude during the course of the day. The energy exchange between warm and cool air in the entrainment zone causes energetic turbulent cells to form. The turbulent air that is left underneath the entrainment zone as it increases in altitude is called the mixed layer. About half an hour before sunset the thermals cease to form and the turbulence in the mixed layer decays. During the night the air near the ground, at the arrays, becomes stable but the winds higher in the boundary layer may form nocturnal jets where the winds may accelerate to supergeostrophic speeds [†]. The net effect of the stable air near the ground and the nocturnal jets is short bursts of intense turbulence near the ground during the night. About thirty minutes after the sun has risen thermals once again start to form and the evolution of the boundary layer is repeated. The observed trends in the effects of the diurnal cycle on the noise field correspond to events in the evolution of the boundary layer. When the entrainment zone is near the ground, just after sunrise, the turbulence around the array is very intense and the noise power is greater in the majority of the frequency band. When the thermals cease to form, about one half hour before sunset, the noise power is at a minimum due to a lack of energy being added to the system.

Man-Made Clutter

In addition to the features of the infrasonic noise field that were natural in origin there was also man-made clutter present in the estimated noise power spectra. A “noise floor” was observed in the estimated noise field power spectra at Fairbanks and the summer noise field power spectra at Windless Bight. The electronic noise floor of the Model 5

[†]Supergeostrophic speeds are defined as speeds greater than required by the pressure gradient.⁵²

Chaparral microphones has been measured at approximately 10^{-8} Pascal.(D. Marriott, personal communication, February 2007) The analog data were filtered by the anti-aliasing filter, whose effect was visible in the estimated PSD as roll off in the spectra to an operational zero[‡] at 10 Hz. The noise field power spectra estimated for Windless Bight smoothly decrease to this operational zero value, with the exception of the summer months. The power spectra estimated from the data collected at Fairbanks become constant at about 1 Hz and then rapidly converge to the operational zero value at 10 Hz.

The exact origin of this noise floor is unclear, but several possible causes have been ruled out as its source. The ambient air temperature during the winter months at Fairbanks during the years included in the study was comparable to the temperature during the spring and fall at Windless Bight, yet the noise floor was not observed in the noise field PSD estimates during the spring or fall months at Windless Bight. The temperature of the data digitizer, shown in Figure 4.6, was also excluded as the source of the noise floor. In Figure 4.6 the daily median temperature of the data digitizer was plotted for both the Fairbanks array, the black +, and Windless Bight array, the black ·, during the year of 2006. If the noise floor was caused by the digitizer temperature then, according to the plot, spring at Windless Bight would have a higher noise floor since the digitizer temperature during the spring at Windless Bight was comparable to the digitizer temperature during the winter at Fairbanks. Rather, the Windless Bight data has a significantly lower noise floor in the estimated PSDs during the spring. The effects of wind speed on the noise field are investigated in the next section, but were also ruled out as a cause of the noise field. With all other obvious sources of the noise floor excluded it seems likely that human activity was responsible for the observed noise floor in the Fairbanks and summer time Windless Bight noise field PSD estimates. Human activity at Windless Bight is generally most intense during the summer months and almost non-existent during the rest of the year. The period of maximum human activity corresponded to the only time period where the noise floor was observed at Windless Bight and so we operationally conclude that the elevated noise floor is due to fundamentally anthropological residual transient sources.

The data digitizer creates electronic clutter in the high frequencies of the noise field at both Fairbanks and Windless Bight. The digitizer clutter was seen as small, narrow

[‡]Operational zero is a value on the order of 10^{-8} Pascal.

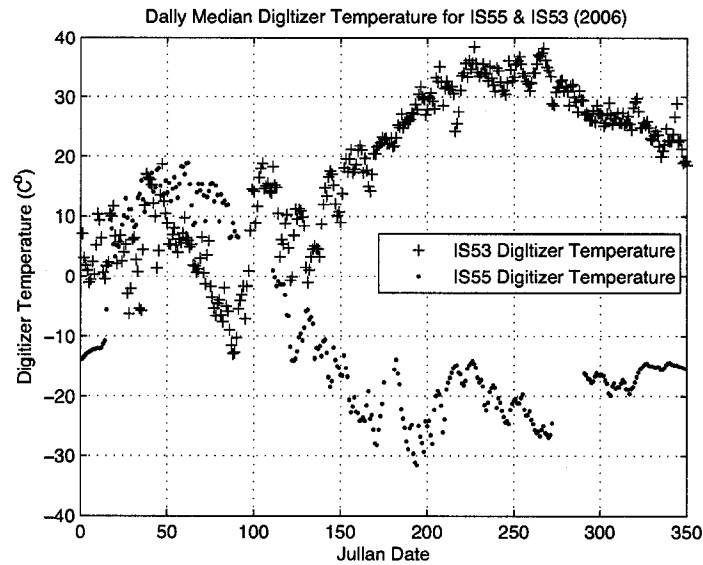


Figure 4.6. Digitizer temperature for both the Windless Bight and Fairbanks arrays. The + are the daily median digitizer temperatures at Fairbanks and the · are the daily median temperature at Windless Bight. The daily digitizer temperatures were calculated for the year of 2006.

peaks located at 2, 4, 6, and 8 Hz in the estimated noise field power spectra. Members of Chaparral Physics (J. Helmericks, personal communication, March 2007) explained that the data digitizer introduces this clutter when the collected data is transmitted from the digitizer every half second. The period of data transmission corresponds to a principle frequency of 2 Hz. The other peaks are the harmonics of this principle digitizer data transmission frequency.

4.3 Effects of Wind on the Noise Field

A large body of work^{12,13,14,15,50,51} has been dedicated to the problem of understanding pressure fluctuations resulting from turbulent air flows. Laboratory experiments and analytic derivations contained within these studies found that the mean-square amplitude of the pressure fluctuations is proportional to the mean-square velocity of the fluid flow. The power contained in the pressure fluctuations is proportional to the square of the amplitude

of the pressure fluctuations. It follows from the relationship between wind speed and pressure amplitude that an increase in the local wind speed at an array results in an increase in the noise power observed at that array. Field surveys of the pressure fluctuations reveal a rudimentary frequency dependence in the rate at which the noise power increases with wind speed.¹² The theoretical relationship between mean-square amplitude of the pressure fluctuations and the bulk wind speed does not provide a method to explore this frequency dependence in the rate of noise power increase. The shape of the noise power spectra will vary as the wind speeds vary due to the difference in the rate of increase of power across different frequencies. By exploring the different rates at which the power changes as a function of frequency, the general effects of the wind on the noise field were determined.

4.3.1 Method

The effects of the wind on the noise power spectrum were investigated by determining the frequency dependent rate of power increase for nine log-spaced frequencies. Each realization of the estimated power, in the manner described in Section 4.2.1, was plotted against the median wind speed. An example, Figure 4.7, shows the distribution of more than 34,000 power estimates, taken from the power spectra, plotted on a semilog plot against the mean wind speed for two of the frequencies estimated from the data collected at the Fairbanks array during a three-month period starting in May 2006. The red and green distributions are the noise power estimated at 0.08 Hz and 5 Hz respectively. The solid black lines are the best fit lines of the median power estimated at each of the measured wind speeds. The process of determining the best fit line for the median power estimate is discussed below. The median power was used to fit the lines instead of the mean power to minimize the effect of outliers in the distribution caused by the presence of signals in the data set.

The power appears to be increasing exponentially with wind speed since the black line through the median powers for each wind speed was linearly increasing on a semilog plot. The median estimated powers were fit with an exponential curve of the form

$$f(x) = a e^{bx}, \quad (4.1)$$

where $f(x)$ is the median power, x is the mean wind speed, and b is the exponential power which determines the slope of the linear line on a semilog plot. The fitting parameter a

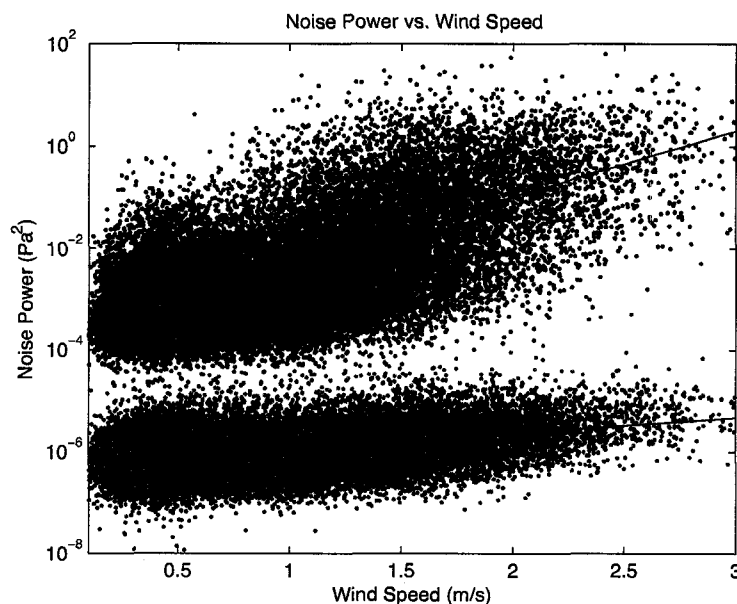


Figure 4.7. The increase in the noise field power as a function of local wind speed. The red dots represent the power measured at a frequency of 0.08 Hz and the green dots are the power estimates at 5 Hz. The solid black lines are the best fit lines of the median power estimates at each of the measured wind speeds. Note the different rates of power increase for the two frequencies.

determines the power at a wind speed of zero and was not used in the following analysis. Once the curve parameters were determined, the exponential power, b , for each one of the nine frequencies was plotted against the frequencies corresponding to the exponential power. The resulting plot revealed the frequency response of the rate at which the noise power increases with wind speed. The effects of the local wind speed on the noise power spectra can be inferred from the frequency dependence of b . The 95% confidence limit of the coefficient of determination for an ensemble of exponential curve fits, of the form shown in Equation 4.1, of normally distributed random noise is 0.045. Such a small coefficient of determination is expected for two unrelated curves.⁴⁷ A curve fit of the median estimated power versus local wind speed data that results in a coefficient of determination that is less than or equal to the 95% confidence limit of the coefficient of determination of the noise curve fit was excluded from the final analysis.

To build the statistics of the median estimated power at the measured local wind speeds, several months of power spectrum estimates were combined into statistical ensembles. The combination of the power spectrum estimates into the ensembles was guided by window closing principles. The magnitude of the median noise power during the period of data collection used to produce the noise power versus wind speed plot had an effect on the b found when performing the curve fitting on this data. If the power in the noise field is modeled as a composite of the power provided by the wind and the ambient power from the clutter and thermals, the power in the noise field is given by

$$S_{xy}(\exp i\omega) = \sum_{l=-\infty}^{\infty} R_{xy}[l]e^{-i\omega l} \quad (4.2)$$

where ω is the frequency, l is the lag, and R_{xy} is the cross-correlation function.²⁹ It can be shown²⁹ that the cross-correlation is bounded by the average powers of the two processes being correlated,

$$|R_{xy}[l]| \leq \frac{1}{2}(R_x[0] + R_y[0]). \quad (4.3)$$

The total noise power must be less than or equal to one half the average power contained in the wind noise and ambient noise. Letting $R_x[0]$ be the ambient power and $R_y[0]$ be the wind power, it can be verified that the smaller the ambient noise is with respect to the wind power, the more sensitive the total power is to increases in the wind power as the wind speed increase. The dependence of the rate of power increase (b) on the ambient power present during the time of power spectrum estimation limits the number of months that are grouped together to produce the noise power versus wind speed plots.

Months with high ambient noise will have a lower power increase with wind speed than months with lower ambient noise levels. The effect of a mismatch in the starting ambient noise power levels between the months was an averaging of the rates of noise power increase and, while not desirable, is not a critical flaw. To balance the desire for a large range of wind speeds with the desire to avoid the loss of too much resolution in the value of b , the data will be grouped into seasonal blocks when making the median power versus wind speed data sets. This grouping also allows the exploration of any seasonal changes in the frequency dependence of the growth rate.

4.3.2 Results

The terrain in which an array is located affects the rate of noise power increase with wind speed. Figure 4.8 shows the median power for a frequency of 0.63 Hz at both the Fairbanks and Windless Bight arrays. The vertical power scale is the same for both plots. At the Fairbanks array, the median noise power increased by approximately 1×10^{-5} Pascal as the wind speeds increased from 0.1 m/s to 1 m/s. At wind speeds greater than 1 m/s the median noise power began to rapidly increase, increasing to six times the median power at 1 m/s for a wind speed of 2 m/s. At the Windless Bight array the median noise power did not increase by 1×10^{-5} Pascal until the local wind speed was approximately 3.5 m/s. The noticeable difference in the rate at which the median noise power increases with wind speed was due to the different terrain in which the arrays are situated. The trees of the boreal forest surrounding the Fairbanks array caused the wind flow to become turbulent at lower wind speeds than the snow covered ice shelf at Windless Bight. The formation of turbulent flows at lower wind speeds at Fairbanks caused pressure fluctuations that raise the level of the median noise power at lower local wind speeds.

The rate of noise power increase with local wind speed is plotted in Figure 4.9 against the frequency for the four seasons at the Windless Bight array. The b versus frequency plots at the Fairbanks array, shown in Figure 4.10, were only produced for three seasons. A faulty wind sensor at Fairbanks meant that no wind speed data was collected for either spring 2006 or spring 2005. Three of the seasons at the Windless Bight array returned data that passed the goodness of fit test, described above, for all measured frequencies. The curve fit at a frequency of 0.32 Hz failed the goodness of fit test during the fall season at Windless Bight and was excluded from the final data set. The goodness of fit for the remaining eight frequencies calculated for the fall season pass the goodness of fit test with a coefficient of determination of at least 0.8 for all curves fit.

The Windless Bight b versus frequency plots, shown in Figure 4.9, do not display a uniform increase with increasing frequency of the rate of growth of the noise power with wind speed. The most sensitive frequency to increases in the mean local wind speed was a low frequency, 0.08 Hz, but it was not the lowest frequency estimated. The rate of increase of the median power decreased for the frequency estimates lower than the local maximum at 0.08 Hz. Moving away from this local maximum toward higher frequencies, the rate of

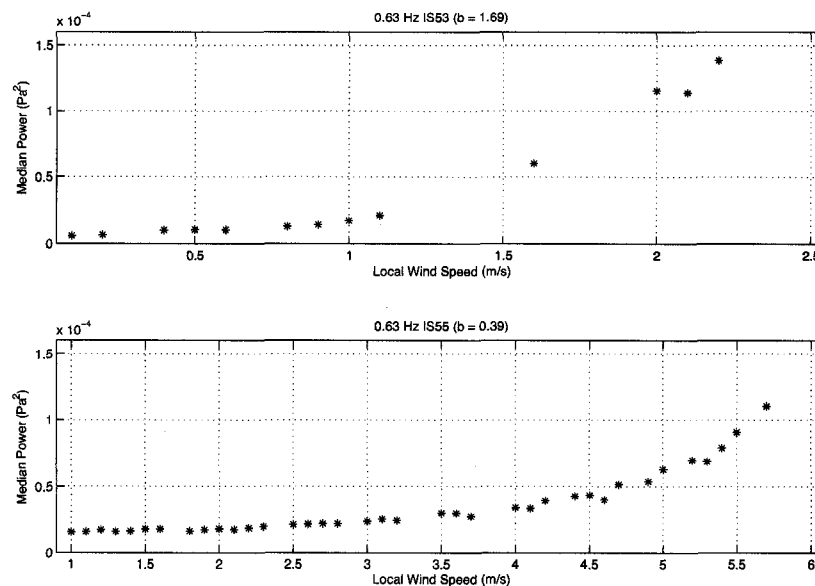


Figure 4.8. The wind response of the Fairbanks and Windless Bight arrays. The top plot is the median power at 0.63 Hz at Fairbanks, with Windless Bight at the bottom.

increase quickly decreased to a minimum in the frequency neighborhood of 0.32 Hz and then began to slowly increase for frequencies higher than the local minimum. The rate of increase for the summer period was different from the other seasons at Windless Bight, decreasing after 1 Hz instead of continuing to increase.

The high frequency behavior of noise power growth rate at Windless Bight during the summer can be explained by looking at the seasonal noise power spectra estimated for Windless Bight, shown in Figure 4.5. At high frequencies the noise floor was present during the summer months, but not during the other seasons. Recalling that the ambient power present affects the rate of increase of the noise power with local wind speed, it follows that the noise floor will affect the rate of increase. The noise floor raises the ambient noise level at high frequencies and the rate of increase in the median noise power is decreased.

The frequency dependence of b for the Fairbanks array, shown in Figure 4.10, is similar to the frequency dependence during the summer season at the Windless Bight array. The curve fit corresponding to a frequency of 0.16 Hz during the winter months failed the coefficient of

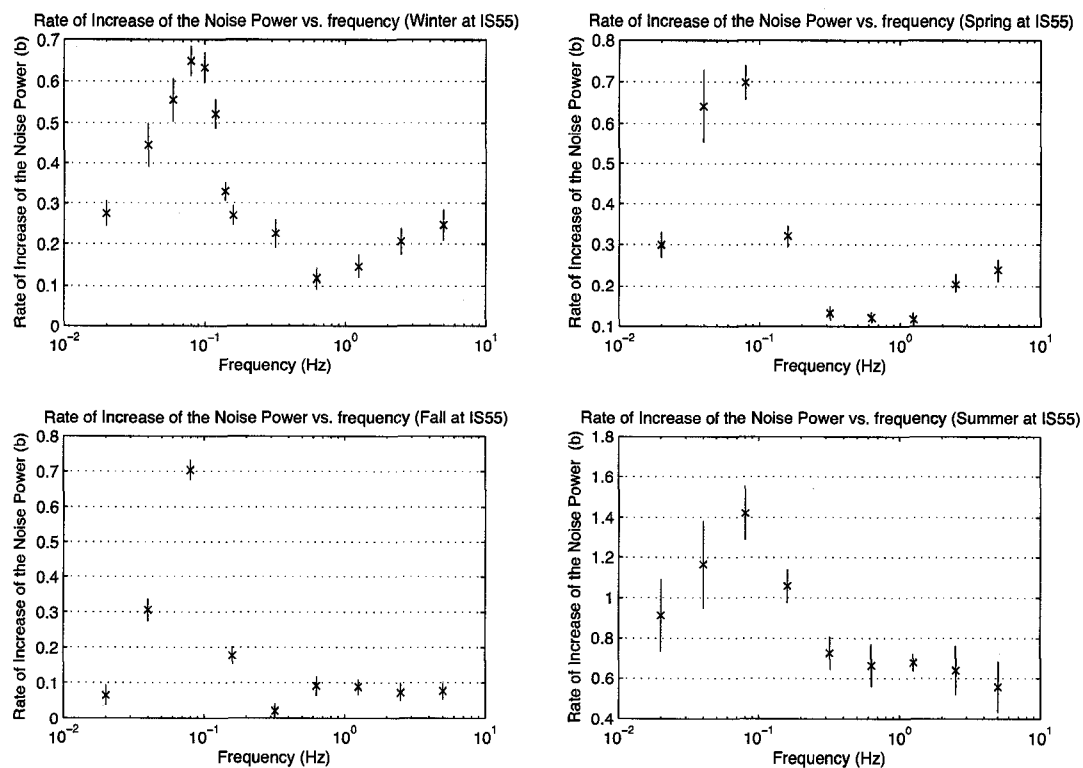


Figure 4.9. Rate of power increase with local wind speed for the Windless Bight array. The 95% and 5% confidence limits are included with each value of b as vertical bars. The curve fit corresponding to a frequency of 0.16 Hz during the winter months failed the coefficient of determination test and was excluded from the final data set.

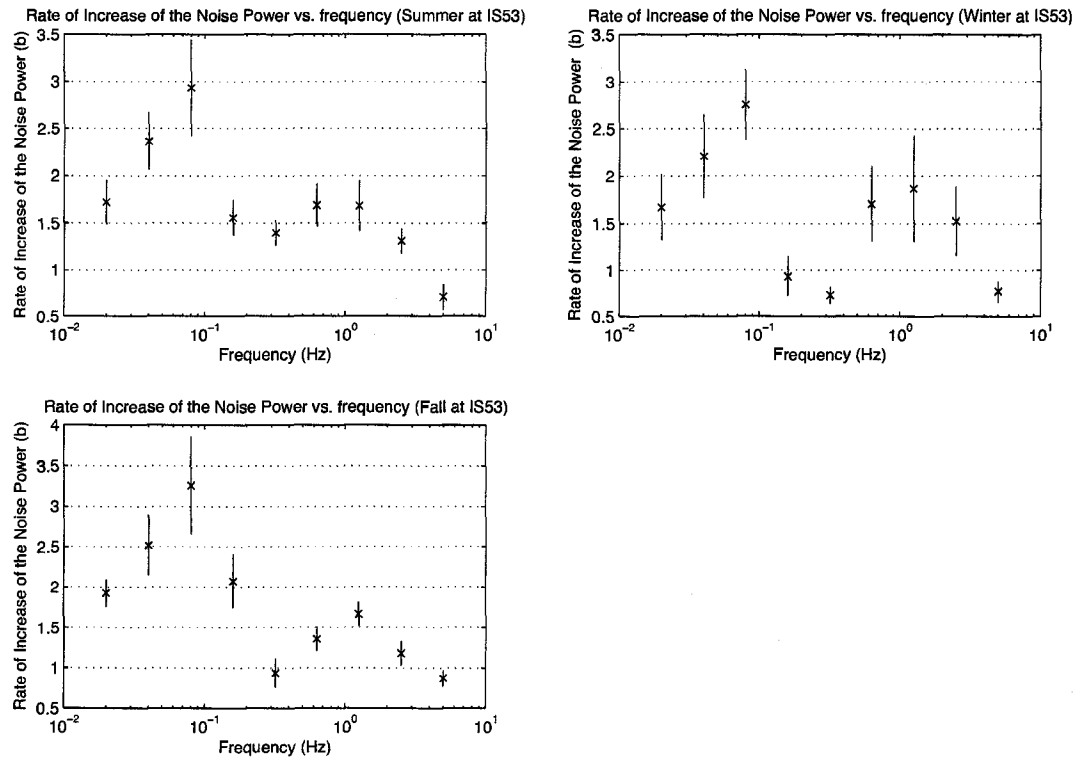


Figure 4.10. Rate of power increase with local wind speed for the Fairbanks array. The 95% and 5% confidence limits are included with each value of b as vertical bars. The bottom left panel is blank due to a lack of wind data available during the spring at the Fairbanks array.

determination test and was excluded from the final data set. The high frequency behavior of the data collected at the Fairbanks array was influenced by the noise floor present during all seasons. The rate of increase observed at frequencies higher than 1 Hz decreased for all estimated seasons at the Fairbanks array. As at Windless Bight, the most sensitive frequency to variations in wind speed was 0.08 Hz and the minimum response was still in the neighborhood of 0.32 Hz. The behavior of the rate of increase at the frequencies lower than 0.08 Hz was also similar to the behavior in the Windless Bight data.

The magnitudes of the frequency-dependent rates of increase were consistently lower at Windless Bight than at Fairbanks. The estimated ambient noise levels at Windless Bight were lower than those at the Fairbanks array throughout the year. Considering the ambient noise levels, one would expect the median noise power rates of increase to be greater at Windless Bight than Fairbanks. The seeming contradiction is explained by consideration of the terrain at each location. The boreal forest surrounding the Fairbanks array is apparently more efficient at creating turbulent wind flow than the smooth terrain at Windless Bight. The efficiency of the Fairbanks terrain at creating turbulence results in a faster noise power rate of increase. Although the magnitudes of the rates of increase were different for the different seasons and locations, the general shape of b versus frequency plot remained the same, particularly for the frequencies below 0.32 Hz. The trends in the higher frequencies remained consistent as well once the data was grouped to reflect the presence or lack of the noise floor. The noise power contained in the mid-range frequencies at both locations is the least affected by increases in the local wind speed.

4.3.3 Application

The frequency dependence of the rate of increase affects the estimated noise power spectra. Noise fields during days with higher than average wind speeds will be altered in character from the median noise field by the frequency dependent rate of noise power increase with local wind speed. To empirically demonstrate this deformation, the power spectra estimated from the data collected at the Windless Bight during the winter months of 2006 were sorted according to local wind speed. The top plot in Figure 4.11 is of the median power spectrum for a high and low wind speed during the winter months of 2006 at the Windless Bight array. The blue line, corresponding to the median power spectrum when the mean wind

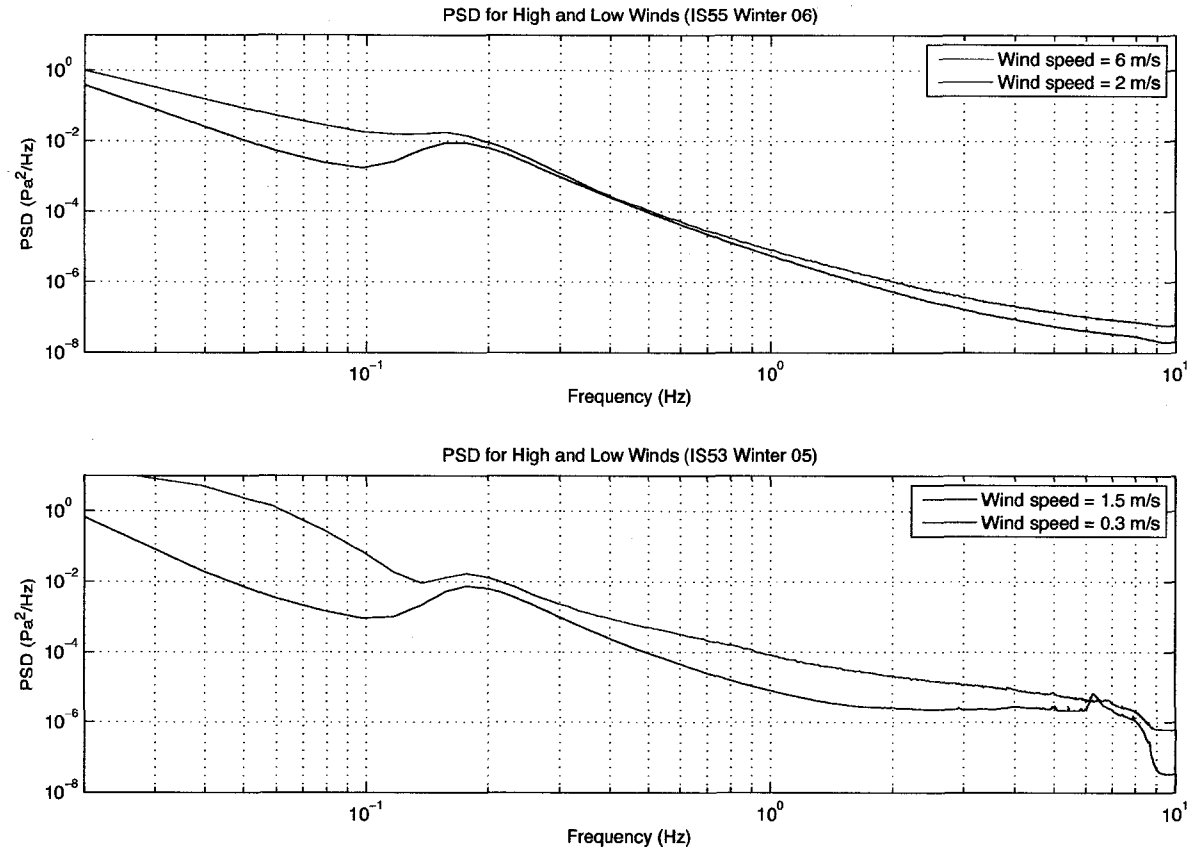


Figure 4.11. Power spectra for high and low wind speeds at the Windless Bight and Fairbanks arrays. The top plot is for the Windless Bight array during the winter months of 2006. The red line is the median power spectrum for all estimates when the mean wind speed during the time window was 6 m/s and the blue line is the median power spectrum for a wind speed of 2 m/s. The bottom plot is for the winter months of 2005 at the Fairbanks array, this time the red line is for 1.5 m/s and the blue line is 0.3 m/s. At high wind speeds the noise power spectrum is deformed from the median noise field.

speed was 2 m/s, shows the noise power spectrum at low wind speeds where a well-defined microbarom peak and some sensor clutter can be seen in the estimated noise field power spectrum. The median Windless Bight power spectrum estimated during periods of 6 m/s mean wind speed is shown by the solid red line. The changes in the median estimated noise field power spectrum from the low wind speeds to the high wind speed illustrate the frequency dependence of the rate of increase of the noise power with local wind speed. A large increase of the power level estimated in the lowest and highest frequencies was observed while the power level of the noise increased by a small amount in the mid-range frequencies. These changes in the noise power levels agree with the b versus frequency plots discussed above. The bottom plot of Figure 4.11 shows the high and low wind speed median power spectrum estimated at the Fairbanks array. The changes in the noise power levels between the high and low wind spectra echoed the rates of increase shown in Figure 4.10. The noise power in the lowest frequencies increased the most between the low and high wind examples. The noise power increase in the highest frequencies began to decrease as the frequency increased past 1 Hz. The noise power contained in the mid-range frequencies also increased noticeably, showing the greater rates of power increase present at Fairbanks. Finally, note that the clutter in the high frequencies was not present for the high wind speed median power spectra. It will be useful for the upcoming correlation study to note that the clutter disappeared at higher local wind speeds, indicating that the local wind can mask the clutter.

4.4 Effect of the Infrasonic Noise Field on LSE

A survey of the data recorded at Windless Bight and Fairbanks revealed that the amplitude distribution of the infrasonic noise field passed a Chi-squared distribution test at a rate comparable to GWU noise at all temporal window lengths. Although the infrasonic noise field was Gaussian, the noise estimated at both the Fairbanks and Windless Bight arrays was not white noise in the frequencies recorded by the instruments. The empirical form of the noise field affects the performance of least squares estimates of trace velocity and azimuth. A statistical study was undertaken to compare the effect of the empirical noise on the performance of the estimator by qualitatively exploring both noise regimes using synthetic data. It is common practice in the infrasound community to bandpass filter the

infrasound data before performing the least squares estimate to limit the effects of the empirical noise field. The effectiveness of the practice of bandpass filtering the infrasound data before performing a least squares estimate of the azimuth and trace velocity was also considered in this statistical study.

To qualitatively explore the effect of the empirical noise field on the least squares parameter estimates of azimuth and trace velocity, synthetic data was produced by propagating a chosen waveform at a known speed and azimuth across an array. A 0.5 Hz windowed sine wave was chosen as the surrogate signal waveform. The surrogate signal had a duration of 20 seconds and was windowed with a Hanning window.²⁹ A different waveform choice resulted in the same qualitative changes in the performance of the least square estimates though the changes were slightly different quantitatively due to the difficulty of ensuring an identical signal-to-noise ratio between different signal types. The geometry of the Windless Bight array was used during the generation of the synthetic data. The trace velocity was set to acoustic velocity, 0.343 km/s, and an arbitrary azimuth of 54 degrees, measured clockwise from due north, was chosen as the direction of arrival of the waveform. The effects of the azimuth and trace velocity on the performance of the least squares estimator have been discussed previously in this work and had little qualitative effect on the results of the present study.

The frequency bands used to filter the infrasound data are empirically determined by the person performing the data analysis. Considerations such as frequency location of clutter and previous knowledge of the frequency content of the signal of interest influence the choice of the passbands in the filtering process. The frequency bands used in this study were set to isolate the microbaroms in one frequency band. The broadband data was separated into three frequency bands. A low-frequency band, 0.015 to 0.1 Hz, a high-frequency band, 1 to 10 Hz, and the microbarom-frequency band, 0.1 to 1 Hz.

The estimator performance was evaluated by creating two synthetic data sets, one with empirical noise and one with GWU noise. The empirical noise set was created in a manner so that the PSD of the empirical noise was qualitatively similar to the PSD estimate during the winter months at Windless Bight. The data sets were then bandpass filtered and the azimuth and trace velocity were estimated using least squares estimation. The process was repeated 1000 times to build the statistics of the parameter distributions. The signal-to-noise ratio

was then altered and the process repeated to create ensembles of parameter variances and biases versus signal-to-noise ratio. By comparing the variance in the parameter distributions and the bias in the estimates at the various signal-to-noise ratios, the effect of the empirical noise was determined.

As the signal-to-noise ratio decreased, the least squares estimate of the trace velocity and azimuth began to fail at some critical signal-to-noise ratio. The first indication that the critical signal-to-noise ratio has been reached was an increase in the variance of the distribution of the estimated parameters. The bias in the estimate also began to increase rapidly after the critical signal-to-noise ratio has been exceeded. The effect of the empirical noise type on the performance of the least squares estimator was to increase the magnitude of the critical signal-to-noise ratio where the estimate began to fail. Physically, an increase in the magnitude of the critical signal-to-noise ratio translates into a higher required signal power for accurate parameter estimation.

The qualitative effects of the empirical noise on the least squares parameter estimates are the same for all three of the passbands used in this study. Quantitatively, the magnitude of the variance increase and the critical signal-to-noise were dependent on the frequency band used to filter the data. The largest variance increase was in the microbarom band, and the smallest increase was in the high-frequency band. The effects of the empirical noise were qualitatively similar for both the trace velocity and azimuth estimates. Figure 4.12 is an example of the variances in the distribution of trace velocity estimates in the high-frequency band for varying signal-to-noise ratios. The variance with the empirical noise was plotted with blue +; the variance for GWU noise estimation is shown with red +. The signal-to-noise ratio present when the parameter estimation was calculated is shown along the x -axis of the plot. The variance curve for the empirical noise distribution is similar to the variance curve of the GWU noise distribution, the former being shifted toward higher signal-to-noise ratios.

The performance of the least squares estimator with the empirical noise field was similar to the performance of the estimator with GWU noise, but at lower signal-to-noise ratios. For this reason the assumption of GWU noise is a valid assumption for the noise field, if the frequency band is separated to isolate the effects of the microbaroms. If data is not bandpass filtered, the performance of the least squares estimate was greatly reduced and

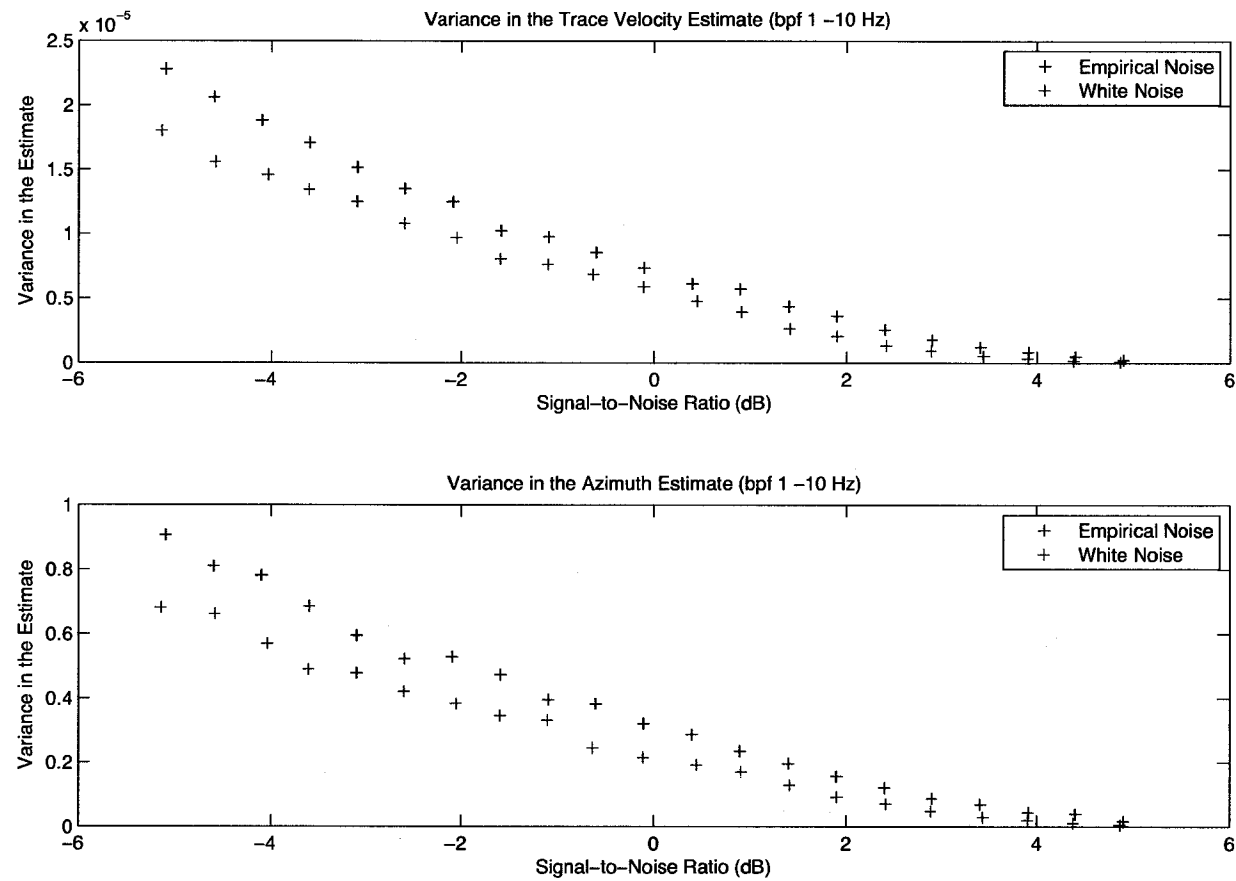


Figure 4.12. Variance in the distribution of parameter estimates for assumed and empirical noise. The data were filtered between 1 and 10 Hz before the parameter estimation was preformed. The blue + are the variance in the distribution when the empirical noise is used, the red + are the variances for white noise.

the assumption of GWU noise is violated.

4.5 Conclusion

The infrasonic noise field is composed of man-made and geophysical clutter and turbulent pressure fluctuations. The clutter contained in the infrasonic noise field of an array is dependent on the location of that array. The infrasonic noise field was estimated for the Fairbanks and Windless Bight arrays. There were differences between the infrasonic noise field at Fairbanks and Windless Bight. The infrasonic noise field at Fairbanks consists of microbarom clutter along with high-frequency, man-made clutter from nearby buildings on the UAF campus. The infrasonic noise field estimated at Fairbanks varied seasonally and diurnally. The Windless Bight noise field did not contain the high-frequency man-made clutter due to the remote location of the array. The noise field at Windless Bight was dominated by the microbarom clutter signal. The Windless Bight infrasonic noise field varied seasonally, but lacked a noticeable diurnal fluctuation in the estimated noise field power spectra. It is difficult to compare the results of the infrasonic noise field estimation at the Fairbanks and Windless Bight arrays with the results of Bowmann *et al.* due to the different array locations.⁴⁸ The infrasonic noise fields estimated at Fairbanks and Windless Bight were qualitatively similar to those shown by Bowmann *et al.* Both sets of noise fields had similar frequency distributions of the noise power and distinctive microbarom peaks in the PSD estimates. The seasonal and diurnal variations in the noise field PSD are markedly different between the Bowmann *et al.* results and the results from the Fairbanks and Windless Bight arrays. The difference in the seasonal and diurnal variations of the infrasonic noise field was not unexpected due to the drastically different latitudes of the Fairbanks and Windless Bight arrays relative to the Bowmann *et al.* array located in Bolivia. The difference in the diurnal variation maybe compounded by the different methods of choosing the temporal location of the sample windows.

Convective ground heating is suggested as a possible mechanism responsible for the much observed diurnal fluctuation of the noise field power spectra at the Fairbanks array. The magnitude of the diurnal variation of the infrasonic noise field was influenced by the ground cover around the array location. If the ground is covered by a reflective material, such as snow, the solar heating of the ground is inhibited and the diurnal cycle will not be

present in the noise field. The influence of the ground cover on the magnitude of the diurnal noise field variations can be seen in the Fairbanks noise field estimations. The character of the infrasonic noise field at the Fairbanks array did not vary diurnally in the winter. During the summer months a diurnal cycle in the noise field was observed. The emergence of a diurnal cycle corresponded to the annual melting of the snow cover in Fairbanks. The influence of the ground cover on the diurnal cycle was further supported by the lack of a diurnal cycle at Windless Bight, where the snow cover is persistent.

The turbulent pressure fluctuations caused by wind flow can change the shape of the noise power spectrum in a non-trivial manner. The rate at which power contained in the noise field increases with wind speed is dependent on the frequency of the pressure fluctuations. Both arrays displayed qualitatively similar frequency dependence in the rate of increase of the noise power with local wind speed. The noise power increased most rapidly at frequencies in the neighborhood of 0.08 Hz at both the Fairbanks and Windless Bight arrays. A local minimum was observed in the noise power rate of increase at the arrays for a frequency of approximately 0.32 Hz. The high frequency behavior of the noise power rate of increase differed between the Fairbanks and Windless Bight arrays. The rate of increase of noise power with local wind speed decreased for frequencies higher than 1 Hz for all seasons at Fairbanks and during the summer months at Windless Bight. The remaining three seasons at Windless Bight exhibited a continuing increase in the noise power rate of increase for frequencies greater than 0.32 Hz. The magnitude of increase with frequency of the noise power is influenced by the terrain at the location of the array. The noise power growth rate at Fairbanks was consistently greater than the growth rate at Windless Bight. The difference in the noise power rate of increase suggests that the terrain in which the Fairbanks array is situated is more efficient at converting the wind flow into turbulent pressure fluctuations. The frequency dependence of the noise power rate of increase with local wind speed will prove to be an important feature of the noise field affecting not only the shape of the noise power spectrum at different wind speeds, but also the frequency characteristics of the coherence spectrum of the noise field.

The infrasonic noise field estimated at both the Fairbanks and Windless Bight arrays did not possess the idealized white noise power spectrum. While the infrasonic noise field was found to violate the GWU noise model, the performance of the least squares parameter

estimate was not confounded if the data was bandpass filtered prior to estimation of the parameters. A study of the effects of the empirical noise field found that the effect of the empirical noise field on the performance of the least squares parameter estimate was analogous to the effects of decreasing the signal-to-noise ratio of the data when the data was first bandpass filtered. If the data was not first bandpass filtered, the empirical noise field greatly reduced the performance of the least squares parameter estimate for signal-to-noise ratios less than 5 dB. The study done on the effects of the empirical noise assumed uncorrelated noise. The presence of clutter in the infrasonic noise field suggests that the noise field could be correlated. In the next chapter the correlation of the infrasonic noise field will be explored for both array locations.

Chapter 5

Correlation of the Infrasonic Noise Field

5.1 Introduction

The infrasonic noise field is commonly assumed to be uncorrelated at the spatial separations of the IS53 and IS55 array elements, on the order of 100 m.^{39,43,41} Under the assumption of Gaussian, white, uncorrelated (GWU) noise, the least squares parameter estimate is the minimum variance unbiased parameter estimate.¹⁹ The infrasonic noise fields estimated at the Fairbanks and Windless Bight arrays were not white noise. The effects of the empirical infrasonic noise field on the least squares estimate were explored in Section 4.4. The assumption of an uncorrelated noise field and the effects of a correlated noise field on the least squares estimate of azimuth and trace velocity are explored in this chapter.

The accuracy of the least squares estimation of azimuth and trace velocity is dependent on the accuracy of the estimation of the lag vector from the recorded pressure data. When the infrasonic noise field is uncorrelated, the lag vector calculated by cross-correlation corresponds to the signal of interest at sufficiently high signal-to-noise ratios. The inclusion of correlated clutter in the infrasonic noise field changes the model of the sensor input from the assumed signal of interest plus additive uncorrelated noise^{29,19} to

$$y[n] = s_{interest}[n] + \sum_{i=1}^N s_i[n] + w[n], \quad (5.1)$$

where $s_{interest}$ is the signal of interest, s_i is the i^{th} clutter signal, and w is the additive uncorrelated noise. With this new sensor input model the lag returned by the cross-correlation function is dependent on the relative signal strengths of the signal of interest and the clutter signals.

The clutter observed in the infrasonic noise field at Fairbanks and Windless Bight are correlated signals across at least part of the arrays.^{3,9,10} To determine the effects of a correlated noise field on the least squares estimate of azimuth and trace velocity, the coherence spectrum of the noise field present at Windless Bight and Fairbanks was estimated from the recorded data. The coherence spectrum of the infrasonic noise field allowed for the identification of correlated clutter sources. A sense of the typical coherence level of the various clutter signals in infrasonic noise field was constructed by examining the estimated coherence spectra. Seasonal and diurnal fluctuations in the coherence spectrum were ex-

plored and the sources of the variation identified to provide a better understanding of the correlation of the noise field as a function of time. The result of the estimation of the infrasonic noise field coherence spectrum was an qualitative sense of the typical coherence spectrum at both array locations for each season and time of day.

In Section 4.3.3, it was found that the power contained in the 6 Hz clutter decreased at high local wind speeds. The power decrease of the clutter signal indicated that the turbulent pressure fluctuations produced by the local wind flow affected the ability to detect the clutter signal by decreasing the signal-to-noise ratio. A decrease in the signal-to-noise ratio of the clutter signal will result in a decrease of the clutter correlation level. The effect of the local wind on the estimated infrasonic noise coherence spectrum was investigated for both array locations. Knowledge of the effect of the local wind on coherence further improved the understanding of the sources and behavior of the coherent power in the noise field.

With a knowledge of the qualitative nature of the coherence spectrum at IS53 and IS55, a numerical simulation was performed to determine the effects of coherent noise on least squares estimates of azimuth and trace velocity. The estimated infrasonic noise field coherence spectra were used to produce surrogate, correlated noise data. The surrogate noise data was then used to corrupt a synthetic signal with a known azimuth and trace velocity. The azimuth and trace velocity were estimated from synthetic data at a range of signal-to-noise ratios and noise field correlation levels. The performance of the least squares estimates with correlated noise was then compared to the performance of the minimum variance unbiased estimate, the least squares estimate with GWU noise.

5.2 Correlation of the Noise Field

In Chapter 4 the noise fields present at IS53 and IS55 were found to be composed of two elements, clutter and turbulent pressure fluctuations from wind and convective heating. The most prominent clutter at both arrays was in the microbarom frequency band. Previous work done with microbaroms^{2,3,54,53} has shown that the signals can be coherent across arrays with sensor separations comparable to the separations of the inner triangle of microphones at the Fairbanks and Windless Bight arrays. Other clutter present in the infrasonic noise field at the arrays may also be correlated between the array elements. The level of clutter coherence must be determined in order to produce synthetic, correlated data to use in

numerically determining the effect of correlated noise on the least squares estimates of azimuth and trace velocity.

5.2.1 Method

The similarity of the data recorded at two sensor locations can be estimated in the time domain with the cross-correlation of the two data sets or, in the frequency domain, with the coherence function. The time and frequency domains are equivalent in time series analysis.³¹ Either the cross-correlation or the coherence can be used to determine the level of similarity of the noise field at two spatially separated locations in the array. The frequency domain measurement has several advantages over the time domain measurement. The cross-correlation function has the disadvantage that it is calculated without regard to frequency, and correlated energy at any frequency results in a high correlation value. The usage of the cross-correlation function to measure the similarity of the data would require that the data be bandpass filtered to isolate the correlated microbaroms. The coherence describes the correlation of the two data segments as a function of frequency.³¹ The coherence spectrum of the noise field can be used to identify the frequencies of the correlated energy contained in the infrasonic noise field. Since the coherence spectrum estimates the correlation of the noise field at a range of frequencies, no bandpass filtering is required to isolate the highly-correlated clutter. The value returned by the cross-correlation function is also dependent on the chosen data window length, which introduces an additional parameter in the estimation of the noise field correlation. The coherence function has the additional advantage that it is insensitive to the choice of the data window length. A possible disadvantage of using coherence to estimate the correlation of the noise field is that most of the previous work done concerning the correlation of the noise field has been done in the time domain. The coherence of the noise field was investigated instead of the correlation of the noise field to take advantage of desirable properties of the coherence function.

The magnitude square coherence (MSC) is estimated by

$$C_{xy}(f) = \frac{|P_{xy}(f)|^2}{P_x(f)P_y(f)}, \quad (5.2)$$

where $P_{xy}(f)$ is the cross power spectrum of the time series x and y , $P_x(f)$ is the power spectrum of x , $P_y(f)$ is the power spectrum of y , and f is the frequency.³¹ The power

spectra used to calculate the coherence were calculated using the Welch method of spectral estimation.³⁶ The data recorded at Fairbanks and Windless Bight were segmented into three minute data segments. Window closing techniques³¹ were used to determine the optimal data window length for the raw data. The effect of different window lengths was to make small changes in the fidelity and stability of the estimate of the coherence spectrum. A data segment length of three minutes produced stable estimates of the coherence spectra that correspond to the noise power spectra previously calculated. Three minute data segments were chosen to maximize the stability of the power spectrum estimate while preserving the fidelity of the estimated PSD. During the application of the Welch method of spectral estimation, the three minute data segments were further segmented into four subwindows that were 1024 samples long. The number of samples in the subwindows was chosen to optimize the calculation speed of the periodograms. The subwindows were overlapped by 515 samples to minimize the number of data samples omitted at the end of the data segment and give an overlap of approximately fifty percent. The magnitude square coherence of the three minute windows was then estimated using the resulting PSDs and Equation 5.2. Statistical methods were used to determine the coherence of the noise field present at both the Fairbanks and Windless Bight arrays. To improve the statistics of the coherence of the noise field and to filter out the effects of signals, an ensemble of coherence spectra was produced. The data were segmented into three minute data subsets and the coherence spectrum was then calculated for each three minute data segment for each of the 28 unique microphone pairs.

To improve the statistics of the noise coherence estimate, the 28 estimates of the coherence (each a unique intersensor vector separation) were combined into ensembles of coherence spectra. It has been empirically shown that the coherence of a signal decreases as the spatial distances between of sensors recording the signal is increased.^{12,55} Qualitative comparison of 28 coherence spectra estimates revealed that the coherence of data sets with small intersensor distances, approximately 200 m, could be combined into an ensemble without a loss of fidelity. Three of the 28 sensor pairs had this small intersensor distance and were combined into a “small” separation ensemble. The coherence spectra of the remaining 25 sensor pairs, with intersensor distances of approximately 1 km (a range from 0.8 km to a maximum of 2 km with an average intersensor distance of 1 km), were combined into a

“large” separation ensemble. The statistics of the noise field coherence spectrum were further improved by including all the coherence spectra estimates for an hour time block into the small or large separation ensembles, depending on the particular intersensor separation.

The number of hours that could be included together in the ensembles at the Fairbanks array was dictated by the observed diurnal cycle in the noise power spectra. To investigate whether or not the pressure fluctuations produced by the convective heating causing the diurnal cycle observed in the noise field power spectra estimates are coherent, the coherence spectra produced from the data for three hour time blocks were combined into ensembles centered on sunrise, sunset, noon, and midnight local time. The three hour time blocks were chosen to maximize the number of days that could be included in the ensembles without the time blocks overlapping and mixing the potential effects of the diurnal cycle on the coherence spectra. The local times of sunrise and sunset for Fairbanks were shown in Figure 4.1. When the time blocks overlapped the coherence spectra for those days were excluded from the coherence spectra ensembles. June 18-25 and December 18-25 for the Fairbanks and February 1-20, April 24 - 30, August 1-18, and October 16-31 for Windless Bight were excluded from the ensembles. More days were excluded at Windless Bight due to its higher latitude. This temporal grouping is identical to the groupings used in the noise field power spectra chapter.

The window closing continued with the grouping of days, weeks, and months to improve the statistics of the noise field coherence spectra. The character of the microbaroms vary between months at both array locations. The microbaroms are known to be coherent and the variation of the microbaroms must be considered while continuing to build the statistical ensemble. The small separation monthly ensembles of coherence spectra for each of the four time periods consist of approximately 5,400 realizations of the small separation noise coherence spectrum. The monthly large separation ensemble contained over 40,000 realizations of the large separation noise coherence spectrum. The size of the ensembles can be increased by combining the months seasonally, but the loss of fidelity in the estimate of the coherence spectrum makes this grouping undesirable at Fairbanks. The character of the microbaroms does not vary as much at Windless Bight and seasonal groupings were used for the noise coherence there to improve the stability of the estimate of the coherence spectrum.

5.2.2 Results

Monthly representations of the noise field coherence spectrum at both the Fairbanks and Windless Bight arrays were produced for the years of 2005 and 2006 using the described method. The noise field coherence spectra at Fairbanks exhibited seasonal and daily variations in both the small and large separation ensembles. Seasonal similarities were observed in the qualitative characteristics of the monthly coherence spectra at the Fairbanks array. In the interests of clarity and compactness, sample coherence spectrum plots from each of the seasons will be shown instead of the coherence plots for each month.

IS53 Coherence Spectra Results

The 2005 and 2006 noise field coherence spectra were qualitatively similar during the months of March and April at the Fairbanks array. The coherence spectrum for March 2005, shown in Figure 5.1, was used as the representative noise field coherence spectrum for the spring coherence spectrum at the Fairbanks array. The variance in the coherence spectrum was on the order of 0.01 for both the small and large separation estimates. The small and large separation coherence spectra for each of the four time blocks for the month of March are shown Figure 5.1. The coherence spectra for the three hours centered on local midnight are shown in the top left panel of Figure 5.1. The coherence spectra for sunrise, noon, and sunset are shown in the top right, bottom left, and bottom right panels of Figure 5.1 respectively. The red curves in each panel of the figure denote the noise field coherence spectra for the small separation sensors during the three hour time blocks. The blue lines correspond to the coherence spectra for the large separations sensor during the time blocks. By design, the magnitude square coherence, shown on the y -axis, varies between a value of zero and one.^{29,31} A MSC of one indicates the power contained at the frequency is perfectly correlated. The expected MSC value for GWU noise was estimated to be 0.14 using numerical simulation techniques and will be discussed in Section 5.2.3. The estimated frequencies, shown with a log scale along the x -axis, vary between 0.02 and 10 Hz.

Two distinct coherence peaks were observed at low frequencies in the large separation noise field coherence spectra for the spring season at the Fairbanks array. The higher frequency peak, which is present during all four time blocks, was produced by coherent

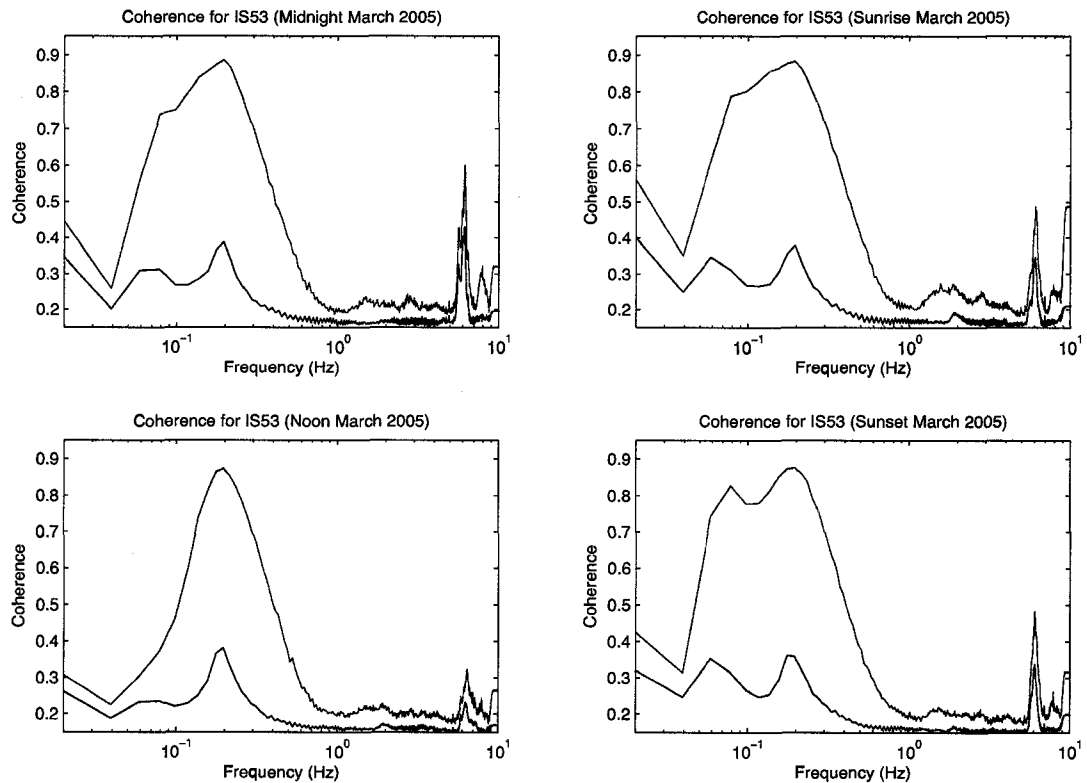


Figure 5.1. The sample spring noise field coherence spectrum at the Fairbanks array. The coherence spectrum for March 2005 was used as the representative spring noise field coherence spectrum at Fairbanks. The red curves depict the coherence spectra of the noise field for intersensor separations of approximately 200 meters, the small separations. The blue curves are the coherence spectra for intersensor separations on the order of a kilometer, the large separations. The sample time windows of midnight, sunrise, noon, and sunset are shown in the top left, the top right, the bottom left, and the bottom right, respectively. The monthly median local wind speed is not shown on this plot due to a lack of wind data during the month of March.

microbarom signals propagating across the array. The coherence of the microbaroms signals peaked around a frequency of 0.2 Hz for this study. Typical microbarom frequencies observed at the Fairbanks array range from 0.125 to 0.3 Hz,³ so the frequency location of the microbarom coherence peak estimated for the large sensor separations fell within the observed microbarom frequency range.

Coherent mountain associated waves⁹ (MAW) and high trace velocity events¹⁰ (HTV) produce the lower frequency coherence peak observed in the large separation coherence spectra. Both MAW and HTV are low frequency waves, with frequencies typically ranging from 0.014 to 0.05 Hz.^{8,9} The maximum coherence of the second peak in Figure 5.1 occurred around 0.06 Hz. The center of the estimated lower frequency coherence peak occurred at a higher frequency than expected for MAW or HTV. The frequency position of the second peak is due to the sparsity of the coherence estimates at low frequencies. Estimating the coherence spectrum following the method described above resulted in a gap in the frequency estimates at the expected frequency of maximum coherence of MAW/HTV waves. The coherence estimates closest in frequency space to the expected maximum for MAW/HTV were the coherence estimates at 0.0586 and 0.0391 Hz. Consequently, the apparent coherence peak of MAW occurred at a higher-than-expected frequency. Additionally, the height of the large separation MAW/HTV coherence peak varied between the noon time block and the other time blocks. The height of the MAW/HTV peak estimated during the midnight, sunrise, and sunset time blocks was comparable to the height of the microbarom coherence peak. The MAW/HTV coherence peak observed during the March noon block was noticeably smaller than the noon microbarom coherence peak.

At large separations the microbaroms and MAW/HTV coherence peaks were distinct during the month of March at Fairbanks. The two distinct large separation low frequency coherence peaks merge into a broad coherence peak for the small separation coherence spectra. The maximum of the coherence peak for small separations corresponded to the frequency of the microbarom peak seen in the large separation coherence spectra. The high coherence level, just under 0.9, of the microbaroms at small separations caused the width of the microbarom coherence peak to increase. The MAW/HTV coherence peak was not visible in the noon small separation spectrum due to the much greater coherence of the microbaroms. Since the noon MAW/HTV signal had a significantly lower coherence

level than the microbarom signal, the side lobes of the noon microbarom peak were able to completely mask the smaller MAW/HTV coherence peak. The width of the microbarom peak also made it difficult to determine the exact frequency location of the small separation MAW/HTV peak during the noon, midnight, and sunrise blocks. The apparent frequency location of the MAW/HTV peak in the sunset block appeared to shift toward a higher frequency in the small separation coherence spectrum. When the MAW/HTV peak was clearly visible in the spring coherence spectra, the apparent frequency location of the peak was consistently shifted toward higher frequencies. The apparent frequency shift of the small separation MAW/HTV peak was most likely due to highly correlated elements of the MAW/HTV signal with less power than at frequencies around 0.06 Hz. The decrease in the coherence with increasing intersensor separations was expected from previous studies conducted on the correlation of acoustic signals.^{12,55} The lower power of the highly correlated elements of the MAW/HTV signals meant the random pressure fluctuations cause a greater decrease in the correlation value at in the highly correlated elements than at 0.06 Hz. A separate signal that is coherent only at the small separations seems unlikely due to the fact that the 0.08 Hz small separation coherence peak was never observed when the MAW/HTV coherence peak was absent from the large separation coherence spectrum.

A high frequency coherence peak was observed at approximately 6 Hz in the small and large separation spring coherence spectra. This high frequency peak was produced by a near field signal from a building located near the array on the UAF campus (K. Arnoult, personal communication, September 2006). The peak was present during all four of the time blocks shown in Figure 5.1. The differences in the coherence of the 6 Hz signal between the time blocks were caused by difference in the local wind speeds and will be discussed in Section 5.3.2. Other high frequency coherence peaks were observed in the spring time small separation coherence spectra. The additional high frequency coherence peaks were not as well defined at the 6 Hz peak and absent in the large separation coherence spectra. The small coherence hump at approximately 2 Hz, while not clear in Figure 5.1, was persistent in the spring small separation coherence spectra. The level of coherence for the human activity coherence peaks was approximately equal to the background coherence observed at the Fairbanks array, with the exception of the coherence peak at 8 Hz which is of unknown origin.

The character of the noise field coherence spectrum changed markedly during the months of May, June, and July. The coherence spectra estimated from the data collected during June 2005, shown in Figure 5.2, were used as the representative summer noise field coherence spectra. The layout of the summer coherence spectrum plot was kept consistent with Figure 5.1. The frequency and coherence scales were also kept consistent with the spring coherence spectrum plot to facilitate direct comparison. The coherence of the low frequency peaks was generally less during the summer months than in the spring months. The MAW/HTV coherence peak was completely absent from the estimated summer coherence spectrum for the noon block. The large separation coherence spectra for the other time blocks had a coherence peak at frequencies corresponding to MAW/HTV signals. The microbarom coherence peak was not clearly observed in the large separation coherence spectra for the midnight, sunrise, and sunset time blocks during the summer months. A small microbarom coherence peak was seen in the estimated large separation coherence spectrum during the noon block.

The small separation microbarom coherence peaks seen during the summer season were smaller than the small separation microbarom coherence peaks seen during the spring season. The less coherent microbarom signals resulted in a coherence peak that was restricted in width. The summer small separation microbarom coherence peak estimated during the noon time block was particularly suppressed from the coherence level observed during the spring. The same frequency location shift of the small separation MAW/HTV seen in the spring occurred during the summer. No clear pattern of variation in the high frequency coherence peaks was observed between summer and spring.

The coherence plots for August and September[†] were qualitatively similar to the coherence plots for spring. In the interest of compactness, a separate fall coherence plot is not shown. The final representative Fairbanks array coherence plot illustrates the qualitative behavior of the coherence spectrum during the winter months of November, December, and January. The months of February and October show qualitatively similar behavior to the winter months, but the level of coherence is less than November, December and January. The coherence spectra for December 2005, shown in Figure 5.3, will be a representative winter plot due to the qualitatively similar behavior of the winter months. The daily vari-

[†]Spring and fall are the shoulder seasons of winter, which runs from October to March in Fairbanks.

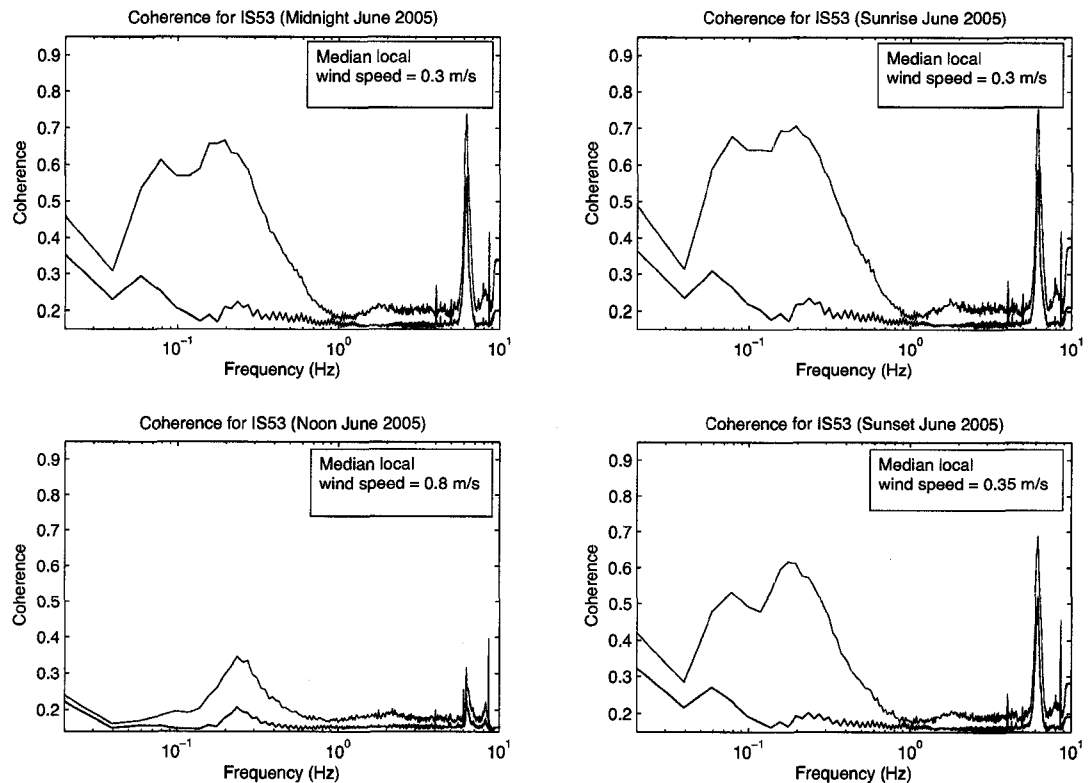


Figure 5.2. Sample summer noise field coherence spectrum for the Fairbanks array. The red curves display the coherence spectra of the noise field for intersensor separations of approximately 200 meters, the small separations. The blue curves are the coherence spectra for intersensor separations on the order of a kilometer, the large separations. The sample time windows of midnight, sunrise, noon, and sunset are shown in the top left, the top right, the bottom left, and the bottom right, respectively. The median monthly local wind speed for each time block is included with each coherence spectrum.

ation observed in the coherence spectra estimated during spring, summer, and fall was absent during the winter months. The coherence of the microbaroms and MAW/HTV was greater during the winter months than in any other season. The small separation coherence maximum was again located at the expected frequency of the microbarom signals. The coherence of the microbaroms estimated during the winter months was slightly greater than 0.9 for all time blocks. The exact value of the MAW/HTV coherence cannot be determined for the small separation coherence spectra due to the width of the microbarom coherence peak at small separations. A crude estimate of the frequency location of the small separation MAW/HTV appeared to continue the trend of the peak location of the MAW/HTV shifting toward higher frequencies. At large separations the coherence of the MAW/HTV was estimated at more than 0.4 for all time blocks. The coherence of the MAW/HTV and microbarom signals was comparable for the large separation ensemble during the winter. The high frequency coherence peaks varied only slightly between the times of day during the winter. The diurnal variation in the high-frequency peaks observed during the winter was the less than the summer, spring, and fall seasons.

IS55 Coherence Spectra Results

No obvious seasonal variation in the noise field coherence spectrum estimated at the Windless Bight array was observed. Since the estimated noise field coherence spectrum did not qualitatively vary seasonally, only the coherence of the noise field during the austral winter of 2006, shown in Figure 5.4, was used to represent the coherence of the noise field at Windless Bight. Since the sun is always down during the winter at Windless Bight the time blocks are centered at 6:00 a.m., 12:00 a.m., 6:00 p.m., and 12:00 p.m. local time. The layout and scale of Figure 5.4 is identical to the noise field coherence spectrum plots of the Fairbanks array data. The local median wind speeds during the four time blocks were not included in Figure 5.4, for the reason discussed in Section 5.3.2.

The large separation microbarom and MAW/HTV peaks at Windless Bight were not as distinct as those in Fairbanks during the spring, winter, and fall. The low coherence of the large separation microbarom signals and MAW/HTV signals coupled with the breadth of the coherence peaks made it difficult to identify well-defined peaks corresponding to the MAW/HTV and microbaroms at Windless Bight. The microbarom coherence peaks,

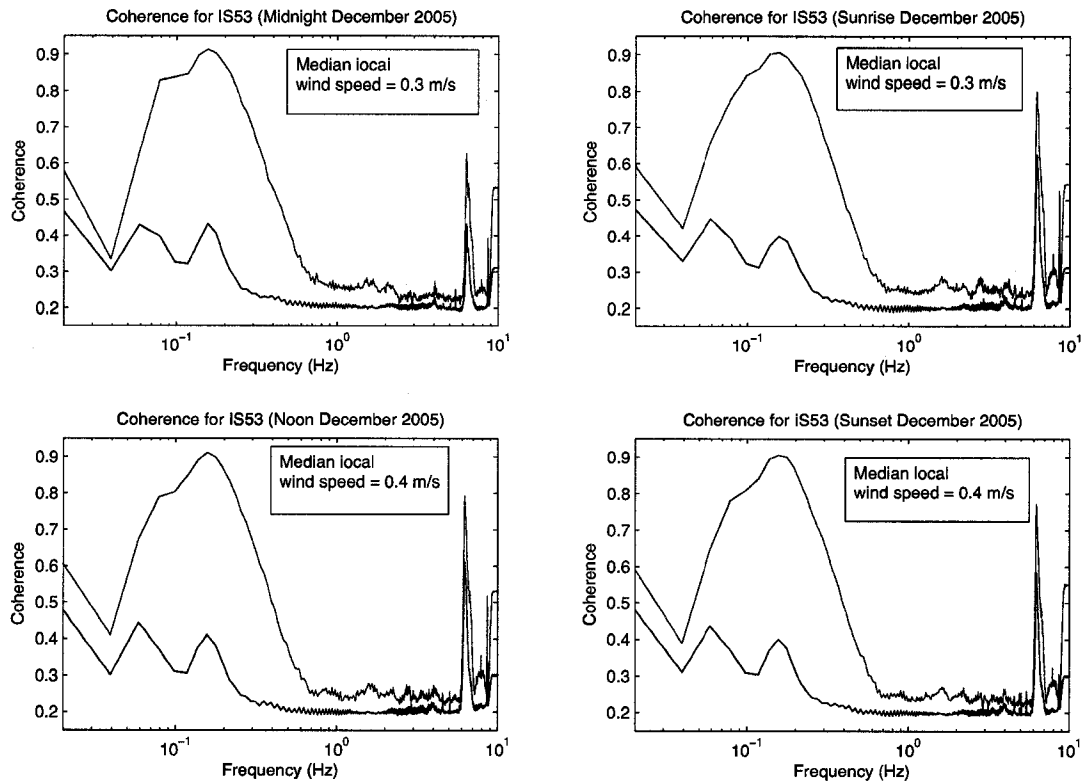


Figure 5.3. Sample winter noise field coherence spectrum for the Fairbanks array. The red curves depict the coherence spectra of the noise field for intersensor separations of approximately 200 meters, the small separations. The blue curves are the coherence spectra for intersensor separations on the order of a kilometer, the large separations. The sample time windows of midnight, sunrise, noon, and sunset are shown in the top left, the top right, the bottom left, and the bottom right, respectively. The median monthly local wind speed for each time block is included with each coherence spectrum.

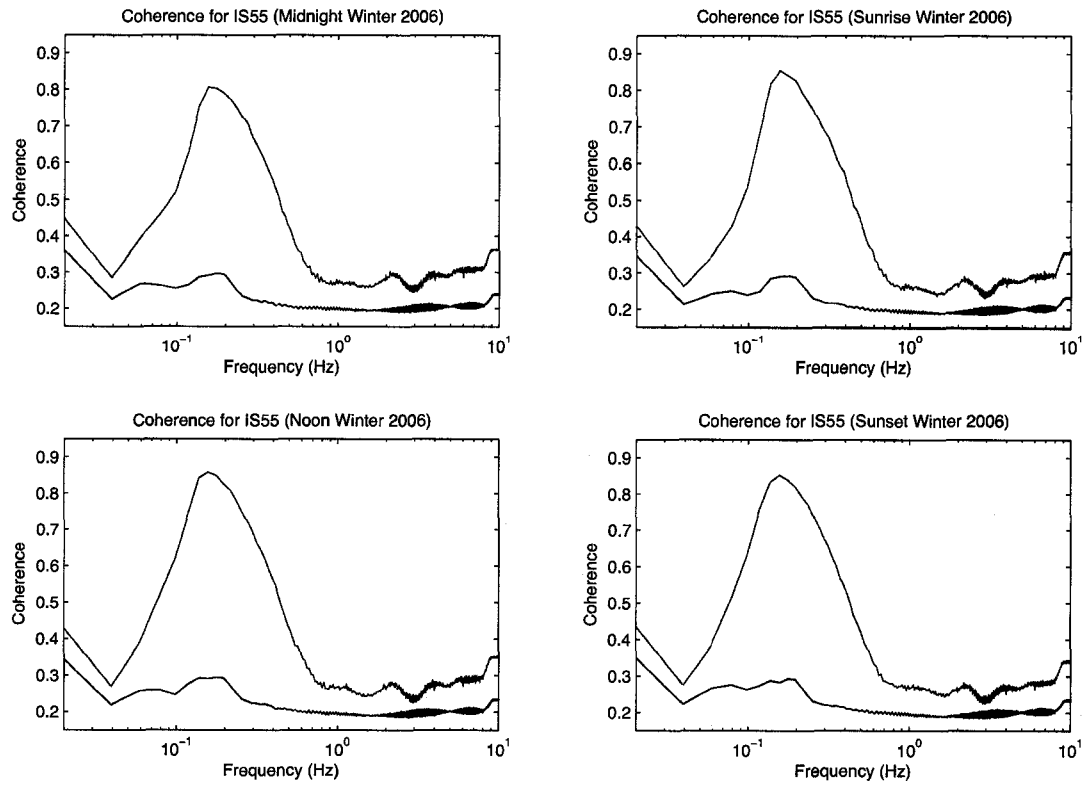


Figure 5.4. Sample noise field coherence spectrum for the Windless Bight array. The red curves display the coherence spectra of the noise field for intersensor separations of approximately 200 meters, the small separations. The blue curves are the coherence spectra for intersensor separations on the order of a kilometer, the large separations. The sample time windows of midnight, sunrise, noon, and sunset are shown in the top left, the top right, the bottom left, and the bottom right, respectively. The local wind speeds recorded at Windless Bight were not used in the local wind speed study and are omitted from these plots.

shown in Figure 5.4, occurred at frequencies between approximately 0.15 and 0.2 Hz. The frequency location of the microbarom coherence peaks estimated at Windless Bight were within the expected frequency band of the microbarom signals. The MAW/HTV peak was not distinct in any of the estimated coherence spectra. The estimated coherence of the MAW/HTV was always slightly less than the coherence of the microbarom peak for all time blocks. Determining the exact location of the peak coherence of the MAW/HTV was complicated due to the overlap of the peaks, but the peak coherence appeared to occur at a frequency between 0.06 and 0.08 Hz. The location of the large separation MAW/HTV coherence peak was similar to the Fairbanks peak.

A single large coherence peak was observed in the small separation noise field coherence spectrum estimated for the Windless Bight array. This large coherence peak was located at a frequency between 0.16 and 0.2 Hz. The frequency of the coherence peak corresponds to the expected frequencies of microbarom signals.³ The shape of the coherence curve seen at Windless Bight was qualitatively similar to the curves observed at the Fairbanks array when the coherence peak of the large separation MAW/HTV signals was small or not observed. The maximum coherence level of the data recorded was approximately 0.85. The maximum coherence level estimated was less than the maximal coherence during the winter months at Fairbanks.

A persistent 2 Hz coherence peak was observed at the Windless Bight array. This high frequency bump was persistent across all time blocks and all seasons at the Windless Bight array. This small 2 Hz coherence bump was also observed during the winter, spring, and fall months at the Fairbanks array, although not as clearly as at Windless Bight. The height of the 2 Hz coherence peak observed at the Windless Bight array was much less than the previously discussed coherence peaks at the Windless Bight and Fairbanks arrays. To determine if such a small coherence peak is statistically relevant, the variance of the coherence spectrum estimates must be taken into account. The variance of the magnitude square coherence spectral estimate is given by

$$\sigma_{coherence}^2 = \frac{I}{2T}, \quad (5.3)$$

where

$$I = \int_{-\infty}^{\infty} w(n)^2 dn, \quad (5.4)$$

T is the total length of the data record, and $w(n)$ is the smoothing window used in the estimation.³¹ The window used in the estimation of the coherence spectrum was a Hamming window, defined as

$$w(n) = 0.54 - 0.46 \cos \left(2\pi \frac{n}{L-1} \right), \quad (5.5)$$

where $0 \leq n \leq L-1$ and L is the length of the smoothing window.²⁹ Using Equation 5.3, the variance of the coherence spectral estimate was calculated to be 0.01. A variation in the coherence of less than the variance is not statistically significant and must be ignored. The height of the 2 Hz coherence peak above the surrounding local coherence level was larger than the variance of the coherence estimate. The 2 Hz coherence peak was therefore a statistically significant feature of the Windless Bight noise field coherence spectrum.

The source of the 2 Hz coherence bump remains unclear. The breadth of the 2 Hz frequency bump points toward an acoustic source rather than an electronic source of the coherent energy since the peaks produced by electronics are generally very sharp in frequency space. At the Windless Bight array a coherent signal from human activity was unlikely during the winter months due to the remote location of the array. The generator that charges the batteries used to run the electronics of the array is located near the inner triangle of the Windless Bight array. An acoustic wave produced by the generator was also excluded as the source of the coherent energy at the small separation Windless Bight sensors. Estimates of the noise field coherence spectrum were made with data collected during the times the generator was in operation and the times when the generator was not in operation. The 2 Hz coherence peak remained unaltered between the generator on and generator off data ensembles. A lee wave produced by the building housing the generator was investigated as a possible source of the 2 Hz coherence peak. If the coherence bump were caused by a correlated lee wave, changes in the median local wind speed should result in alterations in the 2 Hz frequency bump. The coherence bump remained constant between periods with different local wind speeds. The final possible source of the 2 Hz coherence bump investigated was the wind reducing pipe array. The wind reducing pipe array was also excluded as the source of the coherence bump. The bump was observed at both the Fairbanks and the Windless Bight arrays. The wind reducing arrays used at the two locations have different geometries. Any coherent signal produced by the geometry of one of the wind reducing arrays should not be produced by the other wind reducing array.

Although the source of the 2-Hz coherence bump remains unknown, the coherence level of the signal is very low. The effect of such a low coherence on the least squares estimate of the azimuth and trace velocity of signal of interest will be explored in Section 5.4.

5.2.3 Discussion

Seasonal and Daily Variation in the Low-Frequency Coherence

The estimated noise field coherence spectrum was observed to vary seasonally at the Fairbanks array. During spring, summer, and fall the noise field coherence spectrum also varied as a function of the time of day for which the estimate was made. The seasonal and daily variation was observed in both the microbarom and the MAW/HTV coherence peaks. The near-field coherent signal, at 6 Hz, did not vary seasonally at the Fairbanks array. To explore the variation in the microbarom and MAW/HTV coherence peaks it was necessary to be able to clearly identify the separate coherence peaks. To this end, the analysis of the MAW/HTV variation was done with the large separation coherence spectrum estimates. The microbarom coherence peak was distinguishable in both the small separation and large separation coherence spectrum estimates. The observed seasonal variations in the microbarom coherence peak were greater in the small separation coherence spectrum estimates. To assist in the analysis of the seasonal variations of the microbarom coherence peaks, the small sensor separations estimates of the microbarom coherence were used.

The MAW/HTV coherence peak was observed in the large separation coherence spectrum estimates during every month of the year at the Fairbanks array. The prevalence of the MAW/HTV coherence peak varied both seasonally and diurnally at the Fairbanks array. During the winter months a qualitatively similar MAW/HTV coherence peak was present during all times of the day with only slight differences in the quantitative coherence level. The estimated coherence of the MAW/HTV signals during spring displayed a general decrease in the level of coherence for all estimated daily time blocks. A diurnal variation in the coherence of the MAW/HTV signals was also observed during the spring months at the Fairbanks array. The MAW/HTV coherence peak estimated during the noon time block of March was noticeably smaller than the MAW/HTV coherence peak estimated during the other daily time blocks. As the year progressed, the height of MAW/HTV coherence peak

estimated during all time blocks continued to decrease, reaching a minimum coherence value during the month of June. The estimated MAW/HTV coherence peaks at all time blocks remained near the minimal coherence level until August. The much lower MAW/HTV coherence peak estimated for the spring noon time blocks disappeared for the noon time coherence spectrum estimates during the summer months. The MAW/HTV coherence peak remained absent from the noon time block until the coherence spectrum estimated during August. The height of the estimated MAW/HTV coherence peaks steadily increased for the sunset, sunrise, and midnight time blocks as the year progressed from summer to winter. No noticeable difference in the rate of increase of the estimated MAW/HTV coherence was observed between the three time blocks. The MAW/HTV coherence peak estimated during the noon time block increased at a greater rate than the estimated MAW/HTV coherence peaks during the other three time blocks. The MAW/HTV coherence estimated during the noon time block increased at a slightly greater rate than the other three time blocks from August to October. A large jump in the MAW/HTV coherence peak estimated during the noon time block was observed from October to November. The MAW/HTV coherence peaks for all time periods returned to the winter coherence levels by the month of November. The pattern observed in the seasonal variation of the estimated MAW/HTV coherence peaks for the year 2006 was qualitatively similar.

A seasonal and diurnal variation in the microbaroms coherence peak was also observed in the coherence spectra estimated at the Fairbanks array. The estimates of the microbarom coherence were maximal during the winter months. The winter month did not display a diurnal variation in the estimated microbarom coherence peak. The estimated coherence of the microbarom signal recorded at the Fairbanks array began to decrease from the winter maximum for all four time blocks during the month of March. The decrease in the estimated microbarom coherence in March from the previous months was approximately equal between the diurnal time windows. The estimated microbarom coherence continued to decrease during the month of April, but the observed decrease in coherence was no longer independent of the time of day for which the coherence spectrum estimation was made. The midnight, sunset, and sunrise time blocks displayed a slight decrease of approximately 0.2 in the estimated coherence of the microbaroms. The decrease in the coherence of the microbaroms estimated during the noon time block was more pronounced, decreasing by approximately

0.6 from the coherence estimated during the winter months. A more pronounced decrease in the estimated microbarom coherence was seen during all estimated time blocks in May. The coherence drop observed during the month of May was most drastic for the estimated noon microbarom peak, which decreased from 0.8 to slightly less than 0.4. The decrease in the estimated microbarom coherence was no longer constant between the remaining three time blocks during the month of May. The decreases in the microbarom coherence were 0.12, 0.1, and 0.14 for the midnight, sunrise, and sunset time blocks respectively. The pattern in the slight differences in the decrease in the estimated coherence of the microbaroms was also observed during the month of May in 2006. The estimated coherence of the microbaroms reached a minimum during the month of June, shown in Figure 5.2, for all estimated time blocks. The microbarom coherence estimated during the noon time was much less than microbarom coherence estimated for the other times during the month of June. Due to the close temporal proximity of the midnight, sunrise, and sunset time blocks during the month of June, it was not surprising that the estimated coherence of the microbaroms during these three time blocks was comparable. The microbarom coherence peak estimated during the sunrise, sunset, and midnight time blocks began to increase in July. A slight coherence increase of 0.06 in the microbarom coherence estimated during the midnight and sunrise time blocks was observed in the July coherence spectra. The coherence increase seen during the July sunset time block was approximately 0.12. No discernible increase in the microbarom coherence estimated during the July noon time block was observed. For the remaining months of 2005, the microbarom coherence estimated during midnight, sunset, and sunrise time blocks continued to slowly increase. During the months following July the estimated noon time microbarom coherence peak began to rapidly increase. The microbarom coherence peaks estimated during all time blocks returned to their estimated winter coherence levels in November. The pattern in the estimated 2005 microbarom coherence data was repeated in 2006.

The observed seasonal and diurnal variations in the estimated MAW/HTV and microbarom coherence peaks have several possible sources. A seasonal variation in the detection of the mountain associated waves and high trace velocity events has been observed in a study of the infrasound data collected at the Fairbanks array for 2004-2006 (D. Lee, personal communication, March 2007). The data survey was conducted by bandpass filtering

the data recorded at the Fairbanks array with a passband between 0.015 and 0.1 Hz and recording data sets with mean value of the 28 estimated cross-correlation maximum greater than 0.6 as detections of a MAW/HTV signal. The least squares estimate of wave trace velocity was used to differentiate between the mountain associated and the high trace velocity events. The high trace velocity signals were defined to have trace velocity estimates greater than 0.780 km/s and less than 1.5 km/s. Detections with trace velocity estimates less than 0.585 km/s were defined as mountain associated waves. The detection of MAW/HTV signals at the Fairbanks array peaked during the winter months and was minimal during the summer months. The pattern of MAW/HTV detections at the Fairbanks array arrived at by this study agreed with the observed seasonal variation in MAW/HTV coherence peaks. It is unclear if the seasonal variation in the MAW/HTV detections was due to a decrease in the production of the acoustic waves or if the waves are produced but not correlated at the Fairbanks array. The question of detection or production will be addressed in Section 5.3.2.

The seasonal variation in the detection of microbarom signals has been observed at many infrasound arrays.^{2,3,54,53} The source of this variation has been attributed to a variation in the propagation path of the infrasonic signals due to atmospheric winds, the proximity of the source, and the size and extent of the ocean swells producing the infrasound.^{2,53} Garcés *et al.* demonstrated a correlation between the prevailing wind direction in the tropopause and the stratopause above an array and the microbarom azimuth of arrival.⁵³ The sound speed of a wave is a function of temperature and wind speed given by the formula,

$$c_s = \sqrt{\gamma RT} + \vec{k} \cdot \vec{W}, \quad (5.6)$$

where \vec{k} is a unit vector in the direction of sound wave propagation, \vec{W} is the wind velocity, T is the temperature, R is the gas constant, and γ is the ratio of specific heats.⁵⁴ A acoustic wave will reflect when there is a positive gradient in the local sound speed with respect to altitude. A favorable prevailing wind direction lowers the turning height of the wave by increasing the sound speed to speeds greater than the ground level sound speed at lower altitudes. A strong stratospheric duct was modeled by Garcés *et al.* during the winter months of 1989-1990 in the atmosphere above Eielson, Alaska.⁵⁶ Using the Naval Research Laboratory Ground to Space (G2S) model the prevailing wind direction in the tropopause and stratopause above the Fairbanks array was calculated for 2003. The model for 2003

was used as a proxy for 2005-2006 due to the lack of model data for that time period. The model results for the prevailing atmospheric winds are shown in Figure 5.5. The coordinate system in Figure 5.5 is the mathematical coordinate system where 0 degrees is due east and 90 degrees due north. The mathematical coordinate system has the desirable property that all winds arriving from the north of the array have positive angles and winds arriving from the south of the array have negative angles. The Fairbanks array is situated in such a manner that the majority of microbarom signals are generated to the south of the array in the Gulf of Alaska. Atmospheric winds blowing from the south would assist the propagation of these microbarom signals to the Fairbanks array. All such winds have negative angles in the mathematical coordinate system.

The prevailing wind direction in the stratopause, shown with + in Figure 5.5, during the winter months at the Fairbanks array was from the southeast to the northwest. The prevailing direction of the stratopause winds shifted to a direction out of the east during the summer months of May, June, and July. In August the direction of the stratopause winds began to shift back toward a prevailing direction out of the south. The winds in the tropopause, shown with ·, have a larger variance than those in the stratopause, and no clear seasonal shift in prevailing wind direction was visible in the G2S model data. These model results permit the formation of stratospheric ducts⁵⁷ that assist in the propagation of acoustic waves generated by sources to the south of Fairbanks during the winter months.

During the summer months at the Fairbanks array, when the winds in the stratosphere and troposphere do not support the propagation of the microbaroms, coherent microbaroms can reach the array through thermospheric reflections.⁵⁴ The microbaroms arriving at an array by the thermospheric path are attenuated more than microbaroms traveling through the stratosphere and troposphere due to the longer path length of the thermospheric returns.⁵⁴ The winds in the thermosphere are affected by the atmospheric solar tide.^{54,56,58} Diurnal and semi-diurnal variations in the wind direction can increase the power in the thermospheric traveling microbaroms by decreasing the altitude of the turning point of the acoustic wave. When the atmospheric winds shift in the direction of propagation from the source to the array, the altitude of the turning point of the wave is lowered and the path length of the wave is shortened.

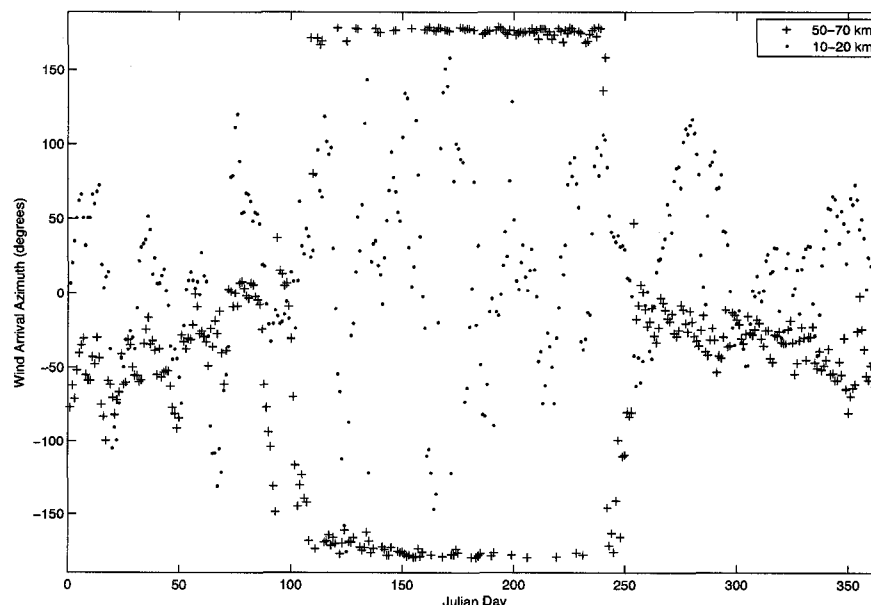


Figure 5.5. The direction of stratospheric and tropospheric wind arrival at the Fairbanks array during 2003. The stratospheric winds, 50 to 70 km, are shown with + and the tropospheric winds, 10 to 20 km, are plotted with -s. The Julian day number for 2003 is plotted along the x -axis. The direction of arrival is shown on the y -axis. The y -axis is oriented in the mathematic sense, with 0° pointing due east, 90° pointing due north, and -90° pointing due south.

The exact effect of the solar tide on the thermospheric winds and the altitude of the wave turning point is dependent on the latitude of measurement and the season of the year.⁵⁹ A theoretical study of the effects of the solar tide on the propagation of simulated infrasonic waves near the Fairbanks array was done by Garcés *et al.*⁵⁶ In this study, the increase in the northward meridional wind component caused by the atmospheric solar tide was found to be greatest at 9 a.m. and noon local time in the winter atmosphere near the Fairbanks array. The solar tide increase in the westward zonal wind was also greatest at 9 a.m. and noon, but the increase was less than the increase in the meridional wind component. Since the solar tide displays strong seasonal variations these results are valid only for the season at which they were calculated and cannot be extended to the other seasons at Fairbanks.

The atmospheric wind model presented by Garcés *et al.* was produced for the winter

months where no diurnal variation was observed in the microbarom coherence estimated at the Fairbanks array.⁵⁶ During the spring, summer, and fall months, where the diurnal variation was observed, the exact time of the maximum solar tide wind variation was not known. In Figure 5.2 the estimated microbarom coherence was noticeably less at noon than at the other times of the day. The pattern of the noon time coherence being less was also seen during the months of May and July. Due to the prevailing direction of the stratospheric and tropospheric winds during these months, the majority of the microbaroms arriving at the Fairbanks array during the summer months have traveled via thermospheric paths. Waves traveling via thermospheric paths have the potential to be affected by the atmospheric solar tide. In the periods where the stratospheric and tropospheric winds are shifting, fall and spring, the diurnal pattern is less pronounced. The less pronounced diurnal pattern could be a result of more microbarom signals traveling via stratospheric and tropospheric paths where the atmospheric tide does not affect the atmospheric winds. When the stratospheric and tropospheric winds have shifted to favorable prevailing directions during the winter months, the majority of the microbaroms travel via stratospheric and tropospheric paths and the diurnal cycle was no longer observed.

The diurnal cycle observed in microbarom coherence could also be the result of weaker microbarom signals arriving at the Fairbanks array during the summer, spring, and fall seasons. The lower power of the coherent microbarom signals traveling via the thermosphere makes the microbarom coherence estimated from these signals more sensitive to the random, wind driven pressure fluctuations at the array. The incoherent noise at the array will decrease the coherence of lower power microbarom signals more than higher power ones. The diurnal cycle observed at Fairbanks appeared to be the result of a diurnal cycle in the local wind turbulence noise and not a result of the atmospheric solar tide. The effects of the local wind speed on the coherence of the noise field is discussed in more detail in Section 5.3.2.

High Frequency Coherence and the Coherence Floor

The median estimated coherence of uncorrelated noise was found through numerical simulations to be 0.14. The noise model used to estimate the median coherence of uncorrelated noise had the same power spectral distribution as the empirical noise field estimated in

Chapter 4. The estimated coherence of the high frequency noise field where no clutter signals were present approached a coherence “floor” value that was greater than the predicted coherence value of uncorrelated random noise at both the Fairbanks and Windless Bight arrays. The higher coherence of the high frequency noise field coherence floor estimated at the arrays was due to residual coherence in the noise field. The residual coherence is a function of the spacing between the locations of data collection. If two identical sensors were spatially located at the same point in space, the coherence of the recorded data would be perfect, returning a value of 1 even from random turbulent pressure fluctuations. As the sensors are moved apart, the coherence of the recorded noise field data decreases, reaching an incoherent value within five or six wavelengths for all wavelengths.^{12,55} Local conditions, including terrain and wind speeds, affect the rate at which the estimated coherence of the turbulently fluctuating pressure field, the residual coherence, decreases.^{11,14} The estimated coherence floor was greater for the small separation ensemble than for the large separation ensemble at both array locations. The decrease in the magnitude of the estimated coherence floor between the small and large separation ensemble provided support for the theory that the residual coherence produces the coherence floor.

The 6 Hz coherence peak seen in the Fairbanks coherence data was the result of a known near-field source (K. Arnoult, personal communication, September 2006). Near-field sources are not affected by conditions in the upper atmosphere since they travel as surface waves.^{60,61} The variations in magnitude of the coherence peak of the 6 Hz signal are caused exclusively by the local conditions near the array. The other high frequency coherence peaks seen at the Fairbanks array were not persistent throughout the year like the 6 Hz coherence peak. Variations in these other high frequency coherence peaks could be caused by local conditions around the array or variations in the mechanism producing the coherent signals. The sources of these other high frequency coherence peaks must have been persistent during the time windows and months when they were observed, but not necessarily persistent throughout all time blocks and months. These other high frequency peaks were only observed in the estimated coherence spectrum of the small separation ensemble and were not coherent across the entire array. The sources of the other high frequency coherence peaks in the estimated Fairbanks noise field coherence spectrum were most likely human-activities from the nearby city of Fairbanks (fundamentally anthropogenic residual transient signals).

5.3 Effect of Local Wind Speed on the Coherence Spectrum

As indicated in Section 5.2.3, the local wind at an array has an effect on the estimated noise field coherence spectrum at that array. The most pronounced features of the coherence spectrum stem from the coherent signals from the microbaroms, MAW/HTV, and man-made sources. As the local wind speed increases the power contained in the turbulence pressure fluctuations increases at a frequency-dependent rate. The propagation of sound energy through a fluid with turbulent fluctuations has been the subject of many studies.^{62,63,64,65,66,67,68} It was determined in these studies that inhomogeneities caused by turbulence in media of propagation scattered coherent acoustic energy. The scattering of the acoustic energy causes an attenuation in the coherent power contained in the acoustic signal.

Acoustic energy with a wavelength approximately equal to the scale length of the turbulent eddy will be preferentially scattered by the turbulent eddy.⁶² Much effort has been put into the problem of determining the scale length of the turbulent eddies in the atmosphere using readily-made atmospheric measurements.^{13,50,51,68} The relations for the turbulent scale length produced from these studies were valid only for the atmospheric regions and conditions assumed in each study. All of the analytic turbulent scale length relations rely upon simplifying assumptions which limit the applicability of the relations to a general atmosphere. No analytic method for determining the turbulent scale length is available for the case of a generalized atmosphere. Without the analytic ability to predict the turbulent scale length from readily measured local variables, the effect of the turbulence created by the local winds on the coherence spectrum must be determined empirically.

5.3.1 Method

The effect of local wind speed on the estimated noise field coherence spectrum at an array was determined using statistical methods. The median local wind speed during each of the three minute time windows used to estimate coherence spectrum was calculated from the meteorological data recorded at that array. All of the estimated coherence spectra for a chosen time period were sorted into median local wind speed statistical ensembles based on wind speed bins of width equal to 0.1 m/s. The median coherence spectra for several of the measured wind speed ensembles were then compared to determine the effect of the

local wind speed on the estimated coherence of the noise field.

The principles of window closing³¹ were used to determine an appropriate duration of the time period used to make the wind speed coherence ensembles. At the Windless Bight array, no monthly or diurnal variation was observed in the estimated coherence spectrum of the noise field. Due to the lack of variation in the estimated noise field coherence spectrum at Windless Bight, it was possible to combine an entire season's worth of the noise field coherence spectrum estimates into the wind speed coherence ensembles. These large ensembles ensure the largest wind speed range possible at Windless Bight without compromising the fidelity of the resulting median coherence spectra.

Both a seasonal and diurnal variation in the estimated noise field coherence spectra were observed at the Fairbanks array. The diurnal and seasonal variations had to be taken into account when creating the local wind speed coherence spectra ensembles. Care was taken to ensure that any changes in the estimated coherence spectra with wind speed was due only to the changes in the local wind speed and not the observed seasonal or diurnal variations. The diurnal variations observed in the estimated noise field coherence spectra were confined to the spring, summer, and fall seasons at Fairbanks. The winter season at Fairbanks did not display any daily variation in the estimated coherence spectra. An ensemble of the coherence spectrum estimates for the winter months of November, December, and January was chosen to create the wind speed coherence ensembles in order to isolate the effect of the local wind speed on the noise field coherence spectrum. The seasonal stability of the estimated noise field coherence spectrum during the winter months at the Fairbanks array also provided a large local wind speed range without compromising the fidelity of the resulting coherence spectrum estimates. The other seasons observed at the Fairbanks array did not have a wind speed range large enough to meaningfully reflect the effects of local wind speed on the estimates of the coherence spectra.

5.3.2 Results

A decrease in the estimated coherence of the noise field was observed as the local wind speed increased at both the Fairbanks and the Windless Bight arrays. The decrease in the estimated coherence was most apparent in the clutter. The effect of the local wind speed was more pronounced in the small separation estimate of the noise field coherence spectrum than

in the large separation noise field coherence spectrum estimate. The effect of the local wind on the large separation noise field coherence was qualitatively consistent with the observed effect of the local wind speed on the small separation noise field coherence. For the sake of compactness, only the small separation noise field coherence spectrum estimates will be shown. The disadvantage of only showing the small separation coherence spectra was that the MAW/HTV coherence peaks were not distinct from the microbarom coherence peaks in the small separation coherence spectrum estimates. When a distinct MAW/HTV coherence peak was necessary for analysis of the effect of the local wind speed on the estimated coherence spectrum, the large separation coherence spectrum estimates are referenced, but not shown.

The effect of the local wind on the small separation noise field coherence spectrum estimated for the winter months of 2005 at Fairbanks is shown in Figure 5.6. The noise field coherence spectrum was estimated for four median local wind speeds measured at the Fairbanks array. To ensure a stable estimate of the coherence spectrum, only wind speed ensembles with at least 100 data sets were considered in the analysis. There were ensembles for each wind speed between 0.1 and 1.5 m/s in multiples of 0.1 m/s that met the stability criteria at the Fairbanks array during the winter of 2005. The extremal wind speeds of 0.1 m/s, shown in blue, and 1.5 m/s, shown in magenta, were plotted in Figure 5.6. There were instances of higher median local wind speeds recorded at the Fairbanks array during the winter months, but the ensembles of coherence spectrum estimates for these wind speeds did not have enough elements to provide a stable estimate of the coherence spectrum. Two intermediate wind speeds, 0.5 m/s, shown in red, and 1 m/s, shown in green, were chosen to fill in between the extremal wind speeds and provide additional information about the effect of the local wind speed on the coherence spectrum.

At Windless Bight, a greater range of wind speeds met the stability criterion than at Fairbanks. The wind speed sensor used at Windless Bight has the potential to return false wind speeds readings when the local wind speed is less than 1 m/s (D. Osborne, personal communication, October 2006), so to avoid any false wind speed readings the lowest wind speed considered in the analysis was 1 m/s. The highest wind speed at Windless Bight with at least 100 recorded realizations during the winter of 2006 was 6 m/s. To span the recorded wind speed range without cluttering the resulting plot, the noise field coherence

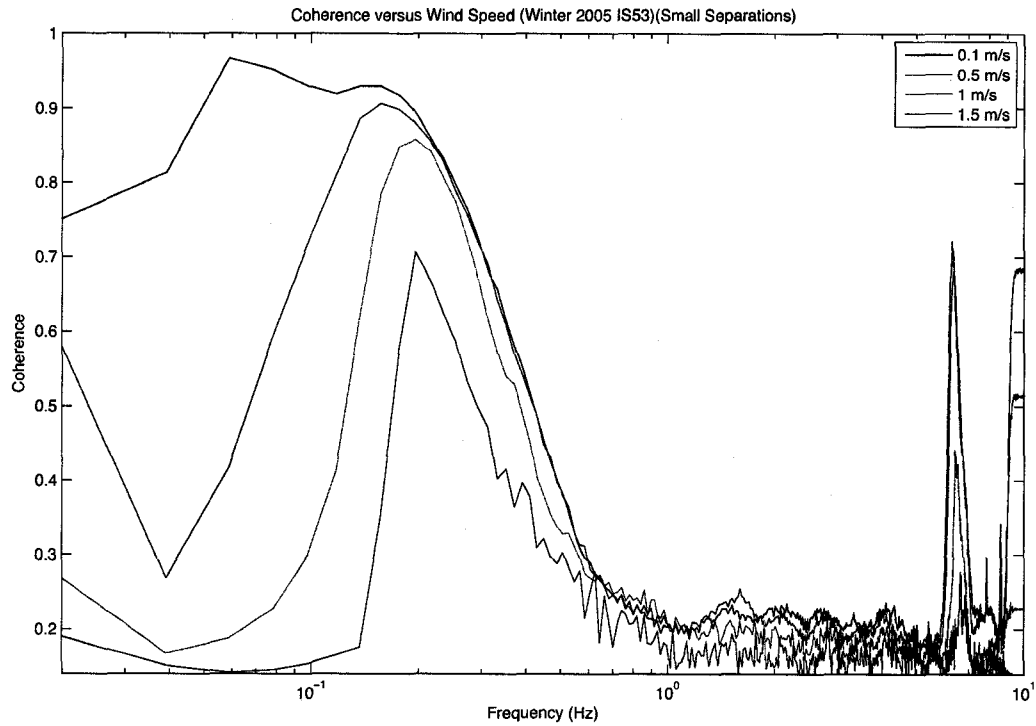


Figure 5.6. The median small separation noise field coherence spectrum estimated at the Fairbanks array versus the median local wind speed. The coherence spectra were estimated for the winter of 2005 at the Fairbanks array. The estimated coherence spectrum of the noise field for periods with local wind speeds of 0.1, 0.5, 1, and 1.5 m/s are shown in blue, red, green, and magenta, respectively. Notice that as the median local wind speed increases the estimated noise field coherence spectrum decreases across all estimated frequencies.

spectrum at 1 m/s intervals was estimated and plotted in Figure 5.7; note that the data is still grouped into 0.1 m/s wind speed bins. The median Windless Bight noise field coherence spectrum was calculated at 1, 2, 3, 4, 5, and 6 m/s. The resulting coherence spectra are shown in blue, red, green, magenta, cyan, and black respectively. The scales of Figure 5.7 and Figure 5.6 are identical.

The presence of the MAW/HTV coherence peak in the small separation estimate of coherence spectra at the Fairbanks and Windless Bight arrays was found to be dependent on the local wind speed during the period of data collection. In Figure 5.4 the MAW/HTV coherence peak was not seen in the small separation coherence spectrum for Windless Bight. An indistinct coherence peak in the Windless Bight coherence spectrum was observed in the 1 m/s coherence spectrum estimate, shown in Figure 5.7, at a frequency consistent with the MAW/HTV signals; it is indistinct because it overlaps the microbarom coherence peak. The small coherence peak in the estimated coherence spectrum disappeared for the 2 m/s coherence spectrum estimate. The median wind speed recorded during the winter of 2006 at the Windless Bight array was 2.5 m/s. According to the results displayed in Figure 5.7, the MAW/HTV coherence peak should not be visible in the estimated small separation noise field coherence spectrum for Windless Bight at a wind speed of 2.5 m/s.

In Figure 5.3, the small separation MAW/HTV peak coherence estimated at the Fairbanks array was less than the small separation coherence peak of the Fairbanks microbaroms. The median wind speed at the Fairbanks array during the month of December was found to be 0.4 m/s. For the lowest measurable wind speed at the Fairbanks array, the coherence of the MAW/HTV signal is greater than the coherence of the microbaroms. The coherence of the MAW/HTV decreases rapidly with wind speed, decreasing to a level well below the coherence of the microbaroms at a wind speed of 0.5 m/s. At the highest local wind speed of 1.5 m/s, the coherence peak of the MAW/HTV has completely vanished and the level of coherence has approached the expected incoherent value of 0.14 for truly random noise. These trends for the MAW/HTV coherence peak was also observed in the large separation estimate of the coherence spectrum, but the large separation MAW/HTV coherence peak was more resistant to an increase in the local wind speed.

A decrease in the estimated coherence of the microbaroms with an increase in the local wind speed was also observed at both arrays. The decrease in coherence observed for micro-

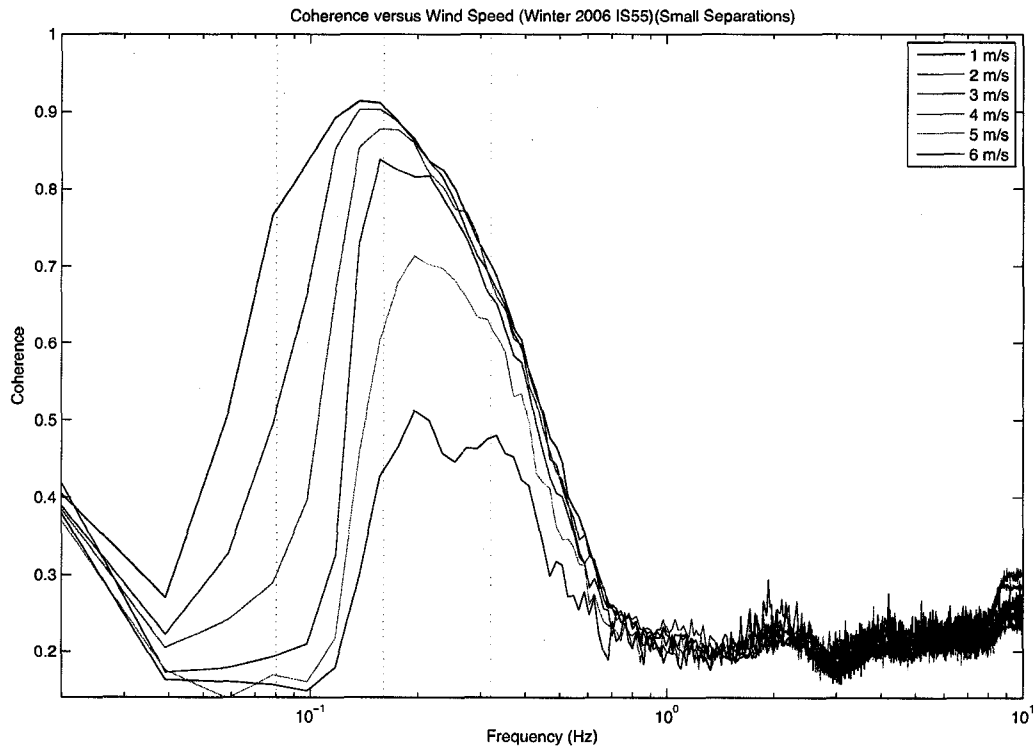


Figure 5.7. The median small separation noise field coherence spectrum estimated at the Windless Bight array versus the median local wind speed. The coherence spectra were estimated for the winter of 2006 at the Windless Bight array. The coherence spectrum of the noise field for local wind speeds of 1, 2, 3, 4, 5, and 6 m/s are shown in blue, red, green, magenta, cyan, and black, respectively. Notice that as the local wind speed increases, the estimated noise field coherence spectrum decreases across all estimated frequencies. At high local wind speeds the coherence floor at Windless Bight approaches the expected value of 0.14.

barom with respect to local wind speed was less rapid than the decrease of the MAW/HTV coherence. The coherence of the microbaroms began to decrease at lower local wind speeds in the coherence spectrum estimates for the Fairbanks array than the coherence spectrum estimates made at the Windless Bight array. The microbarom coherence estimated for the slowest local wind speed ensembles, 0.1 and 1 m/s at Fairbanks and Windless Bight, respectively, was found to be approximately 0.9 for both the Windless Bight and Fairbanks array. An increase of 0.5 m/s in the local wind speed at the Fairbanks array decreased the estimated microbarom coherence only slightly. For each positive increment in the wind speed, the decrease in the microbarom coherence increased in magnitude. For example, the largest decrease in microbarom coherence observed at the Fairbanks array was for the wind speed increase from 1 to 1.5 m/s. The pattern in the microbarom coherence decrease, seen at the Fairbanks array, was repeated at the Windless Bight array, but the magnitude of the wind speed increase need to effect the same decrease in coherence was greater than at the Fairbanks array. The initial increase in the local wind speed from 1 to 2 m/s had a negligible effect on the estimated coherence of the microbaroms. The width of the peak decreased for this initial wind speed increase due to the rapid decrease in the MAW/HTV coherence. As the median local wind speed continued to increase, the height as well as the width of the microbarom coherence peak began to decrease. Similar to the microbarom coherence at the Fairbanks array, the magnitude of the decrease of the estimated microbarom coherence peak increased as the wind speed increased. In addition to the decrease in the coherence of the microbaroms, the frequency of the microbarom peak appeared to move toward higher frequencies as the local wind speed increased at both Fairbanks and Windless Bight.

5.3.3 Discussion

As seen in Chapter 4, increasing local winds produce more energetic turbulent cells. It is possible that these turbulent cells are correlated across the length scales of the Fairbanks and Windless Bight arrays. Several papers have dealt with the correlation of the fluctuating pressures caused by the turbulent wind flow.^{11,12} The paper by Shields¹¹ dealt specifically with the low frequency wind noise correlation. Using the Taylor hypothesis,¹⁵ Shields put forth an expression for the cyclic frequency of the turbulent pressure fluctuations in terms

of the convection velocity, v , and the wavenumber in the direction of the bulk flow, k_1 ,

$$F = \frac{k_1 v}{2\pi}. \quad (5.7)$$

The decrease in the correlation of the pressure fluctuations in terms of the distance in wavelengths between the sensors was then experimentally determined. The relationship revealed that the intersensor separation must be less than 0.2λ for the correlation of the pressure fluctuations to increase to correlation values greater than 0.2. Combining the cyclic frequency of the turbulence pressure fluctuations equation with the spatial separation information, the wind speeds that are theoretically necessary to produce correlations can be found for the two arrays.

The inner three sensors are separated by approximately 200 m for both the Fairbanks and Windless Bight arrays. The estimated coherence of the small separation ensemble was about 0.2 for the lowest frequencies at higher local wind speeds. A sensor separation of less than 0.2λ is necessary to produce a coherence higher than the background coherence the low frequencies. For the lowest frequency estimate calculated, 0.02 Hz, the required wavelength is 1 km. Using the required wavelength and the lowest frequencies, the necessary wind speed to result in correlated turbulent pressure fluctuations was found to be 20 m/s. Sustained local wind speeds at or above 20 m/s are rare, even at Windless Bight, and the ensembles of coherence spectra at these wind speeds are too sparse to result in a stable estimation of the noise field coherence spectrum. In addition to the sparse statistics at the required wind speeds, the Taylor hypothesis is not valid at such high wind speeds.¹⁵ No increase in the estimated coherence spectra was observed as the local wind speeds increased. With a lack of empirical evidence to the contrary there is no reason to doubt the theoretic exclusion of coherent turbulent pressure fluctuations at the wind speeds observed for the Fairbanks and Windless Bight arrays.

The coherence of the clutter was observed to decrease with increasing local wind speeds. The apparent frequency shift observed in the estimated microbarom coherence peaks for both of the arrays can be explained by a frequency dependence in the rate of microbarom coherence decrease. The estimated coherence of the lower microbarom frequencies decreased at more rapidly with local wind speed than the coherence of the higher microbarom frequencies. As the local wind speed increased the coherence at the higher microbarom frequencies,

which started out at lower coherence levels than the lower microbarom frequencies, remained high, making the frequency of microbarom peak appear to shift as the wind speed increased.

The Windless Bight coherence estimates for frequencies in the neighborhood of the microbarom coherence peak were plotted against local wind speed in Figure 5.8. The coherence spectrum estimates were made using the coherence spectrum estimates for the winter of 2006. The right hand panel of Figure 5.8 contains the microbarom frequencies of 0.16 and 0.32 Hz, shown in red and green respectively, and the frequencies in the neighborhood of the microbaroms. Very low frequencies, less than 0.04 Hz shown in blue, responded only very slightly to increases in the local wind speed. The magenta and black dots in the right hand panel of Figure 5.8 represent the coherence of the frequencies 0.63 and 1.25 Hz, respectively. These frequencies, which are higher than the frequencies of the microbaroms, also displayed a very weak response to changes in the local wind speeds. The left hand panel of Figure 5.8 contains the wind response of the estimated coherence for the bulk of the microbarom frequency estimates. The coherence of the frequencies 0.06 Hz, blue dots, and 0.08 Hz, red dots, decreased as the local wind speed increased from 1 m/s. The estimated coherence at 0.1 Hz, green dots, did not immediately decrease as the local wind speed increased past 1 m/s. The first several wind speeds had no effect on the estimated coherence at 0.1 Hz. When the local wind speed increased past 1.2 m/s the microbarom coherence at 0.1 Hz began to rapidly decrease, in a manner similar to the lower frequency microbarom coherence estimates. The microbarom coherence estimated at 0.12 Hz, shown in magenta dots, did not respond to the local wind speed until it went past 1.6 m/s. In the left hand panel of Figure 5.8 the microbarom coherence at 0.14 Hz remained constant the longest as the wind speed increased, starting to respond to the wind at 2.5 m/s. The wind speeds required to decrease the estimated coherence of the microbaroms at the highest microbarom frequencies were the highest for all the estimated coherences. The persistence of the high frequency microbarom coherence estimates caused the observed shift in the microbarom coherence peak.

Scattering and Absorption

Local winds create turbulent fluctuations that can scatter coherent acoustic energy. One possible source of the frequency dependence of the decrease in the coherence of the mi-

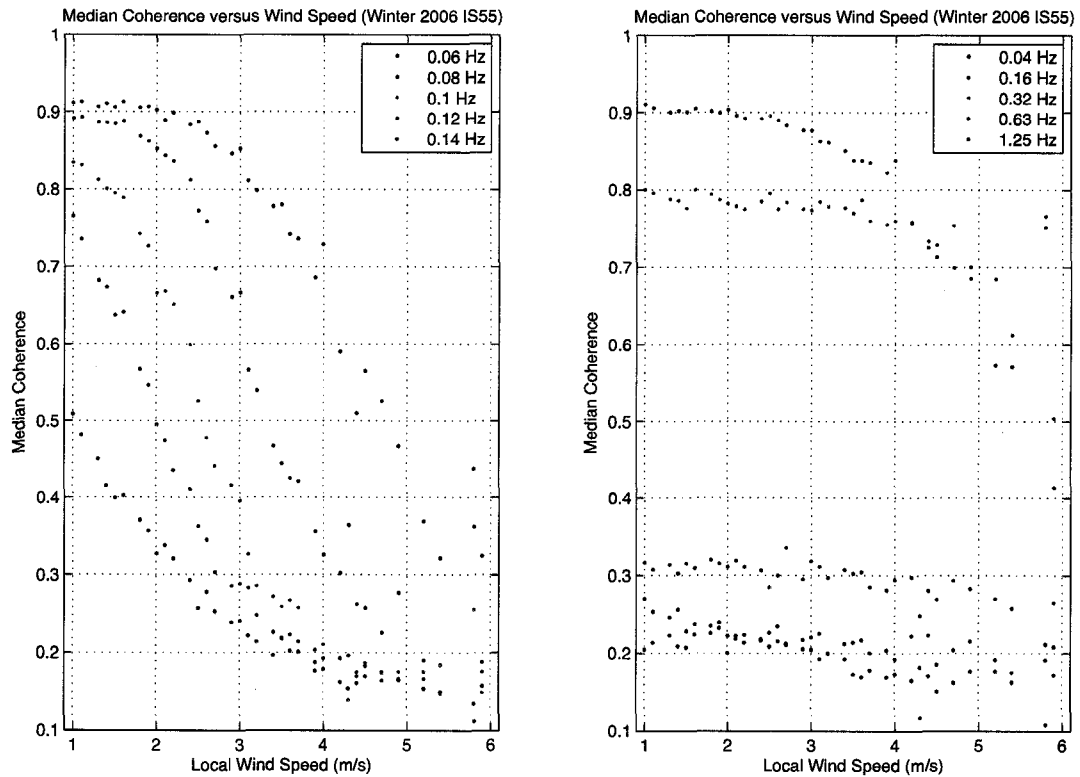


Figure 5.8. The wind response of the coherence estimates at the microbarom and neighboring frequencies. The frequencies most responsive to increases in the local wind speed are shown in the left hand panel. The right hand panel displays the frequencies less responsive to the local wind speed. In the left hand panel the coherence of the lower frequencies begin decreasing at lower wind speeds than the higher frequencies. Frequencies greater than or less than the microbaroms, 0.04, 0.63, and 1.25 Hz shown in the right hand panel, displayed a limited response to changes in the local wind speed.

microbaroms with local wind speed is the preferential scattering and absorption of coherent energy by the turbulent eddies.^{62,63} Acoustic energy with a wavelength approximately equal to the scale length of a turbulent eddy will be preferentially scattered or absorbed by that turbulent eddy.^{62,63} If more turbulent eddies were formed with scale lengths approximately equal to the longer wavelength microbarom components, the coherent acoustic energy of the lower microbarom frequencies would be attenuated more rapidly than the higher microbarom frequencies. In turn, that greater low frequency attenuation would cause the coherence of the low frequency microbarom components to decrease more rapidly with local wind speeds than that of the high frequency microbarom components.

Eddies are formed by extracting turbulence kinetic energy from the mean flow at the largest scales.^{69,13,14} The exact size of the large length scales is imposed by physical constraints on the flow geometry, such as terrain and the depth of the boundary layer. These largest scales are known as the energy-containing range since the turbulent energy is produced at these ranges. The smallest turbulent scales are set by the viscosity of the fluid, and the rate at which energy is supplied to the small scale eddies by the energy containing eddies. The turbulent energy is dissipated at the small scale eddies by conversion of the turbulent kinetic energy into heat via viscosity. Between the energy-containing and small scales are the inertial subrange turbulence scales. At the inertial subrange turbulence scales, the turbulence kinetic energy is neither generated nor destroyed, but is transferred from larger to smaller scales. The large-scale eddies are broken down into smaller-scale eddies through the process of vortex stretching. In general the energy is transferred from the largest eddies to the smallest ones on a timescale of the energy-containing eddies, typically on the order of 10 minutes.⁶⁸

The turbulence length scales for each of the eddy scale sizes is calculated by a characteristic formula. The scale length of the energy-containing eddies is found through the integral scale length. The integral scale length for the energy-containing eddies is given by⁶⁸

$$\mathcal{L} = \frac{1}{\sigma^2} \int_0^\infty R(r) dr, \quad (5.8)$$

where \mathcal{L} is the scale length of the eddies, $R(r)$ is the autocorrelation of a velocity component or temperature, r is the spatial displacement, and σ^2 is the variance of the velocity component or temperature. The scale length of the inertial subrange of turbulent eddies is

given by¹⁵

$$l = \frac{u^3}{\epsilon}, \quad (5.9)$$

where l is the scale length of the eddies, ϵ is the dissipation of turbulent energy per unit mass, and u is the velocity scale defined by

$$u^2 = \frac{1}{3} [\bar{u}_x^2 + \bar{u}_y^2 + \bar{u}_z^2], \quad (5.10)$$

where \bar{u}_i^2 is the mean squared wind velocity in the i^{th} direction. The final turbulence length scale is for the dissipative small scale eddies. The length scale of these eddies is given by Kolmogorov microscale.⁶⁸ The Kolmogorov microscale η is dependent on dissipation rate, ϵ , and the kinematic viscosity, ν and is given by

$$\eta = \left(\frac{\nu^3}{\epsilon} \right)^{\frac{1}{4}}. \quad (5.11)$$

The work done under the most general assumptions involves the inertial subrange.^{13,15}

The turbulent length scales provided by the above relations are meant to give the order of the eddy length scale, not an exact measurement of the turbulent length scale.^{13,15,68} Even with the required knowledge of the dissipation rate and kinematic viscosity, which is not available at either the Fairbanks or Windless Bight arrays, the prediction of the turbulent scale sizes generated by the local wind would not be exact enough to determine if the frequency dependence of the coherence decrease is a result of preferential scattering and absorption. The general progression of the turbulent scale length can nonetheless be determined from the scale length relationships. Turbulence is generated from the bulk flow at the largest possible scale lengths. These large scale lengths would preferentially scatter or absorb the lowest frequency signals present in the noise field. The large scale lengths break down into smaller scale lengths in an unpredictable manner. At the smaller scale lengths there is preferential scattering or absorption of progressively higher frequency signals as the scale length is reduced toward the Kolmogorov microscale. No analytic method exists to predict if certain turbulent scale lengths are preferentially created as the large scale eddies are broken down into smaller ones. With no information to the contrary, it must be assumed that all turbulent scale lengths are equally likely and the distribution of turbulent scale lengths generated as the eddies break down is uniform.⁴⁵ The initial

turbulent eddy scale length will be the largest possible, preferentially scattering signals with wavelengths comparable to the eddy scale length. As the turbulent eddy breaks down, it will preferentially scatter shorter and shorter wavelengths. Since there is no preferred inertial turbulent scale length and all smaller turbulent scale lengths are equally likely, the frequency dependence of the decrease of the microbarom coherence with wind speed cannot be caused by the preferred scattering and absorption of the acoustic energy by the turbulent eddies.

Signal-to-Noise Ratio and Loss of Coherence

The coherence of a signal can also be decreased by an increase in the incoherent noise power. A decrease in the signal-to-noise ratio will produce a decrease in the coherence of a signal without any scattering or absorption of the signal if the noise is uncorrelated.[†] It was shown in Section 4.3 that the rate of wind noise power increase was frequency dependent at both the Fairbanks and Windless Bight arrays. The result of the frequency dependence of the rate of increase of the noise power with local wind speed is a frequency dependent signal-to-noise ratio.

The frequency dependence of the rate of increase of the noise power with local wind speed was qualitatively similar at both the array sites. Magnitude of the rate of increase was initially small and increased as the frequency increased. At approximately 0.08 Hz, the rate of increase of the noise power with local wind speed reached a local maximum and began to rapidly decrease as the frequency continued to rise. The local minimum of the rate of increase occurred in the neighborhood of 0.63 Hz for both array sites. The rate of increase of the noise power with local wind speed for the winter of 2006 at Windless Bight is shown in Figure 5.9. The rate of increase of the noise power with local wind speed, b , was found by fitting an exponential curve of the form

$$P = ae^{bx} \quad (5.12)$$

to a plot of the median power, P , versus the wind speed, x . The details of the fitting process were discussed in Section 4.3.1. The red circle represents the frequency with the highest

[†]This is also seen in a numerical simulation where the physical affects of signal scattering and absorption cannot be occurring.

value of b , at 0.08 Hz. The upper frequency limit for the bulk of the coherence microbarom energy at Windless Bight is 0.32 Hz, shown with a cyan circle in Figure 5.9. The final highlighted rate of increase, at 0.16 Hz (shown in green), was flagged to assist in tracking the microbarom coherence peak as the local wind speed increased.

The highlighted rates of increase of the wind noise power in Figure 5.9 correspond to the vertical dashed lines of the same colors in Figure 5.7. The power contained in the wind noise increased at a lower rate for frequencies to the right and left of the red dashed line in Figure 5.7. The lower rate of increase in the wind noise power corresponded to a smaller decrease in the signal-to-noise ratio as the local wind speed increased at the higher microbarom frequencies. The smaller decrease in the signal-to-noise corresponded to a smaller decrease in the estimated coherence of the microbaroms at the higher frequencies. The movement of the microbarom coherence peak about the dashed green line in Figure 5.7 illustrated the effect of the frequency dependent decrease in the signal-to-noise ratio. At the lowest local wind speed of 1 m/s, the microbarom coherence peak appeared to be located slightly left of the 0.16 Hz line. Since b was greater at lower microbarom frequencies than at higher frequencies, the increase in the wind noise power with local wind speed decreased the coherence of the lower microbarom frequencies at a greater rate than the higher microbarom frequencies. As a result, the frequency location of the microbarom coherence peak slowly moved toward the higher frequencies on the right-hand side of the dashed green line as the local wind speed increased. The rate at which the frequency location of the microbarom coherence peak moved toward higher frequencies not only depended on the rate of increase of the noise power with local wind speed, but also on the estimated coherence of the microbaroms at each frequency. The coherence estimates of the higher microbarom frequencies were less than for the lower frequencies. Compared with the rapid decrease of the estimated coherence of the lower microbarom frequencies, the estimated coherence of the higher frequencies was more slowly decreasing. Due to the simultaneous coherence decrease, the migration of the microbarom coherence peak was slower than indicated by the rates of increase of the noise power with local wind speed shown in Figure 5.9.

The observed rate at which the coherence of the microbaroms decreased was not constant between the two arrays. Although the local wind speeds at the Windless Bight array generally had greater magnitudes than those recorded at the Fairbanks array, the coherence

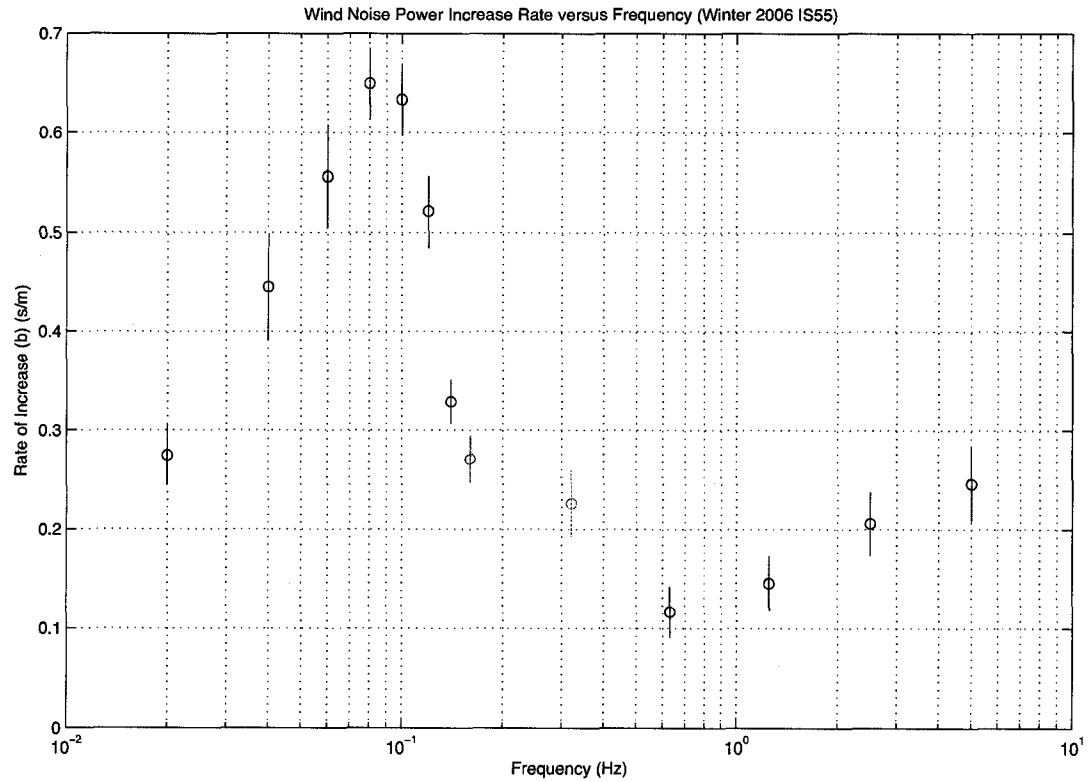


Figure 5.9. The frequency dependence of the rate of increase of the wind noise power for winter 2006 at Windless Bight, Antarctica. The b was found by fitting an exponential curve to the median power versus wind speed data. The red circle represents the point of maximum noise power increase with wind speed at 0.08 Hz. The green and cyan circles represent the rate of increase at 0.16 and 0.32 Hz, respectively. The bulk of the coherence microbarom energy at the Windless Bight array occurs between 0.08 and 0.32 Hz. The 5% and 95% confidence limits of the rates of increase are shown with vertical bars.

of the microbaroms at Fairbanks decreased much more rapidly than at Windless Bight. The rate of increase of the wind noise power at the two array locations can explain the difference in the microbarom coherence decrease rate. Recall that, while the pattern of the frequency dependence of the rates of increase was qualitatively similar between Fairbanks and Windless Bight, the magnitude of the rates of increase was greater at Fairbanks. The larger magnitudes of the rates of increase caused a greater frequency dependent decrease in the signal-to-noise ratio at the Fairbanks array. The accelerated decrease in the estimated microbarom coherence with increasing local wind speed observed at Fairbanks was due to the higher wind noise power growth rate at Fairbanks.

Atmospheric Solar Tide versus Local Wind Speed Noise

At this point it is tempting to argue that the observed daily variations in the monthly estimates of noise field coherence spectra were caused by the diurnal variation in the local wind speed at the Fairbanks array and not by the atmospheric solar tide. To attempt to provide support for observation of the atmospheric solar tide during the summer months at the Fairbanks array, the median local wind speed was determined for each time block during the year of 2005. The relative heights of the microbarom coherence peaks were then compared for comparable median monthly wind speeds. The median wind speed during midnight, sunrise, and sunset time blocks of June, shown in Figure 5.2, was 0.3 m/s. The median wind speed during the noon time block was 0.8 m/s for June 2005. To determine if the large loss of microbarom coherence during the noon time block observed in Figure 5.2 was caused principally by the atmospheric solar tide or the local wind speed, a month with comparable wind speeds in the four time blocks was found. The month of April 2005, shown in Figure 5.10, had median wind speeds of 0.8, 0.25, 0.3, and 0.4 m/s for the noon, midnight, sunrise, and sunset time blocks, respectively. The red curves in Figure 5.10 represent the median small separation coherence spectrum estimates for the four time blocks. The median large separation coherence spectrum estimates for the four times blocks are shown in blue.

A comparison of the coherence spectra for the months of April and June indicated that the power contained in the microbaroms during the month of June was less than the microbarom signal power during the month of April. The generally lower level of microbarom coherence observed during the month of June was a result of the longer path length of the

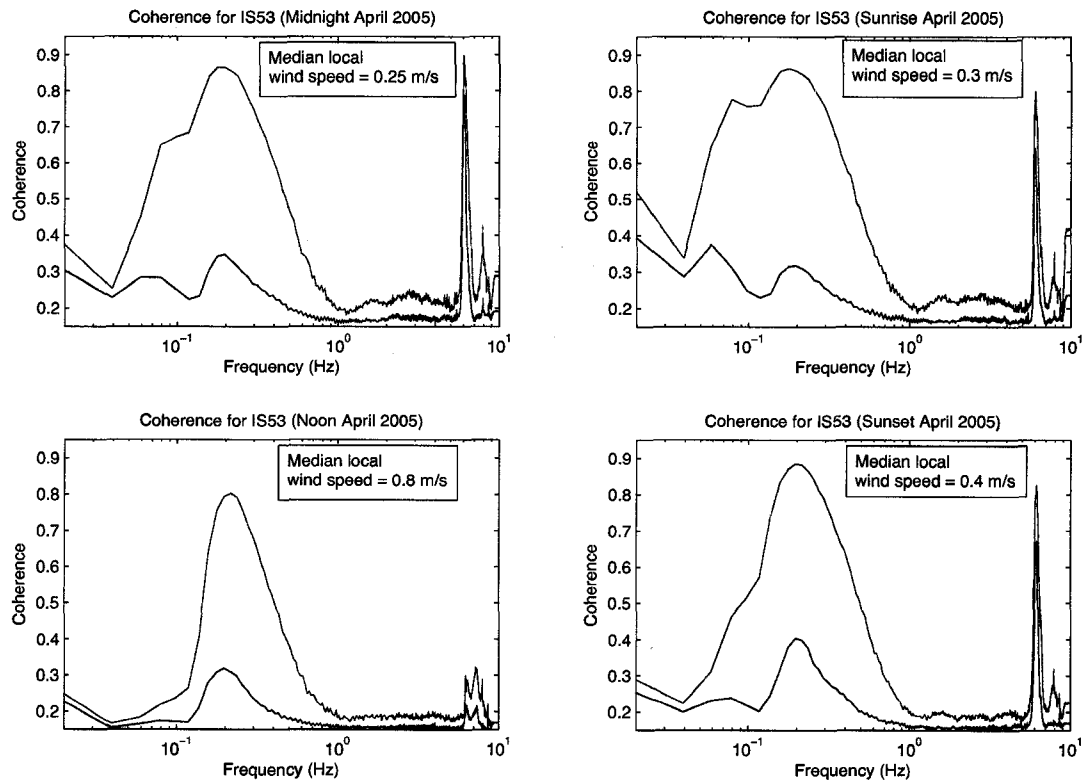


Figure 5.10. The estimated noise field coherence spectrum for April 2005 at the Fairbanks array. The red curves display the coherence spectra of the noise field for intersensor separations of approximately 200 m, the small separations. The blue curves are the coherence spectra for intersensor separations on the order of a kilometer, the large separations. The sample time windows of midnight, sunrise, noon, and sunset are shown in the top left, the top right, the bottom left, and the bottom right, respectively. The median monthly local wind speed for each time block is included with each coherence spectrum.

thermospheric reflected waves. The microbarom signal power was more attenuated traveling on the thermospheric path than on the shorter paths possible in April. The loss of microbarom signal power caused a decrease in the signal-to-noise ratio during the month of June. The lower signal-to-noise ratio resulted in a decrease in the estimates of the June microbarom coherence. The majority of the coherent microbarom signals arriving at the Fairbanks array during the month of April appear to have taken the lower stratospheric or tropospheric paths. The shorter path length resulted in more coherent microbarom energy arriving at the array in April. The larger signal power arriving at the array increased the signal-to-noise ratio of the microbaroms and resulted in a higher coherence of the microbaroms during the month of April.

If the observed decrease in the microbarom coherence estimated for the noon time block in June was due to the shifting winds caused by the atmospheric solar tides, a large decrease in the microbarom power arriving at the array should be visible in the estimated noise power spectra for June 2005. The noise field power spectral density estimates for June and April are shown in Figure 5.11. The four time block PSDs were made in the manner described in Section 4.2.1. The median PSDs for midnight, sunrise, sunset, and noon are shown in black, blue, red, and magenta respectively. The frequency range of the PSD has been focused on the microbarom frequencies between 0.1 and 1 Hz.

The diurnal variation in the estimated microbarom power received at the Fairbanks array during the four time blocks was slight during the month of June. The estimated microbarom power received during June 2005 at the Fairbanks array was least during the sunset time block, not the noon time block. It seems unlikely that the small variations observed in the estimated received microbarom power could cause the drastic decrease in coherence, even if the power received during the noon time block was least. In the bottom panel of Figure 5.11 the received microbarom power during the month of April was observed to have more diurnal variation than microbarom power received during the month of June. The changes in the estimated microbarom coherence during the month of April were less dramatic than the variations observed in June microbarom coherence. The fact that the received power varies more, but the coherence varies less, supports the assertion that the diurnal variations in the received microbarom power do not explain the coherence loss observed at the Fairbanks array during the summer months.

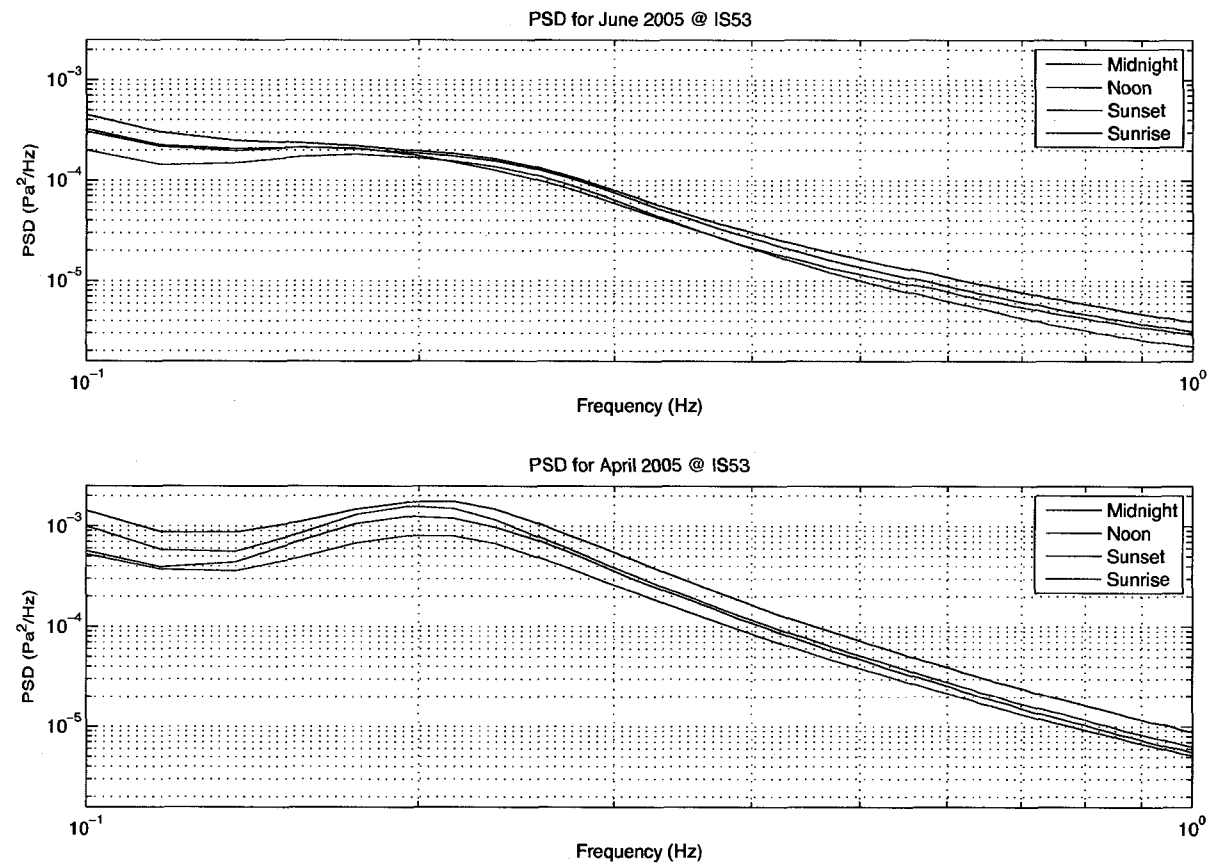


Figure 5.11. The PSD of the noise field at the Fairbanks array for the months of April and June. The median PSDs for midnight, sunrise, sunset, and noon are shown in black, blue, red, and magenta, respectively. The frequency range was chosen to focus attention on the microbarom frequencies. The top plot was made using the data collected during June 2005 and the bottom plot used the data collected during April 2005.

The small magnitude of the variations in received microbarom power point to variations in the local wind as the principle cause of the diurnal variations in the estimated microbarom coherence. The loss of coherence between the noon time coherence estimate and the other time block estimates was greater during the month of June than in April. The difference between the reaction to identical changes in the median local wind speeds can be explained by the difference in the microbarom power received at the array during the two months. The microbarom power received at the Fairbanks array in June was approximately a tenth of that received during April. The coherence of the less powerful microbarom signals received in June was more sensitive to increases in the wind noise power. Assuming the wind noise power increased at approximately the same rate with wind speed during both months, the signal-to-noise ratio during June would decrease approximately ten times as fast as in April. The accelerated decrease in the microbarom signal-to-noise ratio in June caused the greater decrease in the microbarom coherence during the noon time block. It should be explicitly stated that this explanation of the daily variation of the microbarom coherence does not preclude some effect due to the atmospheric solar tide. If the magnitude of any effect of the atmospheric solar tide is smaller than the effects of the local wind, then the atmospheric solar tide effects would be masked by the effects of the varying local wind speeds.

5.4 Effect of Correlated Noise on LSE of Azimuth and Trace Velocity

The accuracy of the least squares estimation of azimuth and trace velocity is critically dependent on the accuracy of the estimated lag vector. With uncorrelated noise, the lag that results in the cross-correlation maximum occurs when the signals recorded at spatially separated sensors are phase aligned. With correlated infrasonic noise, the lag calculated using the cross-correlation maximum is dependent on the relative strength of the signal of interest and the clutter. Clutter with amplitudes approximately equal to the amplitude of the signal of interest will result in an inaccurate lag vector. When the least squares estimates of azimuth and trace velocity are made with an inaccurate lag vector, the resulting estimates do not correspond to either the clutter or the signal of interest. The qualitative effects of the correlated noise on the least squares estimate of azimuth and trace velocity were determined by numerical simulation. The performance of the least squares estimates with correlated noise was then compared to uncorrelated noise.

5.4.1 Method

To investigate the effect of the correlated noise field on the least squares parameter estimate, a synthetic test signal was polluted with surrogate correlated noise. Synthetic correlated noise data was produced by corrupting a clutter signal with uncorrelated noise. The PSD frequency dependence of the additive noise did not affect the results of the simulation as long as the noise was uncorrelated. GWU noise was used to corrupt the synthetic clutter signal in an attempt to isolate the effects of the correlated clutter on the least squares estimate of azimuth and trace velocity. The exact waveform used as the clutter signal had quantitative effects on the results of the simulation, but results remain qualitatively similar for all waveforms used.

To limit the parameter space in the numerical simulation of the effects of the correlated noise on the least squares estimate, the correlated infrasonic noise field at Fairbanks was modeled as the 6 Hz clutter and the GWU noise. The 6 Hz clutter signal was modeled as a windowed sine wave with a duration of one minute. The sine wave was windowed with a Hanning window.²⁹ The azimuth and trace velocity of the clutter signal were held constant at 23 degrees and 0.330 km/s, respectively. The correlation level of the noise field was adjusted by altering the signal-to-noise ratio of the 6 Hz clutter signal and the uncorrelated noise. To compare the effect of various noise field correlation levels, noise sets with correlation levels of 0.7, 0.5, and 0.3 were produced.

The surrogate correlated noise was then used to corrupt the test signal of interest. A windowed sine was also used as the signal of interest. The windowed sine had a center frequency of 2 Hz, a duration of 5 seconds, and was centered within the clutter window. Similar to the clutter signal, altering the choice of the waveform used for the signal of interest resulted in small quantitative changes in the results, but the results remained qualitatively similar. The trace velocity of the signal of interest was held constant at 0.350 km/s throughout the simulation. The azimuth of the signal was varied to determine the dependence of the effect of the correlated noise on azimuth.

Since the noise field is non-deterministic, the effects of the correlated noise field on the parameter estimates were found using statistical methods. Four ensembles of corrupted signal data were produced, one for each of the correlation levels of the noise and one for uncorrelated noise. The data ensembles included 1000 realization of the azimuth and trace

velocity at a chosen signal-to-clutter ratio. The signal-to-clutter ratio was varied from -30 dB to 30 dB. A plot of median azimuth or median trace velocity estimate versus the signal-to-clutter ratio was then produced to illustrate the effects of the correlated noise on the least squares estimate of the parameters.

5.4.2 Results

The primary effect of correlated noise on the performance of the least squares parameter estimate was a higher required signal-to-noise ratio for accurate least squares parameter estimation. The effect was similar to the effect observed for the empirical noise power distribution discussed in Section 4.4, but more pronounced. Figure 5.12 shows the effect of the surrogate correlated noise on the least squares estimation of a windowed sine wave with an azimuth of 113 degrees, which is perpendicular to the clutter azimuth, and a trace velocity of 0.350 km/s. In Figure 5.12 the median estimate of the azimuth is shown in the top panel and the median trace velocity estimate is shown in the lower panel. At signal-to-clutter ratios from 10 to 30 dB the median estimate returned for both azimuth and trace velocity corresponded to the signal of interest. The azimuth estimate for the data corrupted with 0.7 correlated noise, shown with $+$, began to migrate away from the azimuth of the signal of interest at a signal-to-clutter-noise of 8 dB. The trace velocity estimate of the 0.7 correlated data had also drifted away from the desired trace velocity at this signal-to-clutter ratio. At a signal-to-clutter ratio of 6 dB both estimates for the data corrupted with the 0.5 correlated noise had drifted away from the azimuth and trace velocity of the signal of interest. The estimates of azimuth and trace velocity for the data corrupted with the 0.3 correlated noise data had migrated away from the desired values at a signal-to-clutter-noise ratio of 4 dB.

In Figure 5.12 the estimated trace velocity began to increase after the estimates had started to shift away from the signal of interest values. The azimuth estimates immediately began to migrate toward the clutter signal azimuth value of 23 degrees. As the signal-to-clutter-noise ratio continued to decrease, the estimated trace velocity stopped increasing and began to move back toward the clutter signal value of 0.330 km/s. The higher the correlation of the clutter signal, the faster the convergence of the parameter estimates on the clutter azimuth and trace velocity. The estimates consistently converged toward the

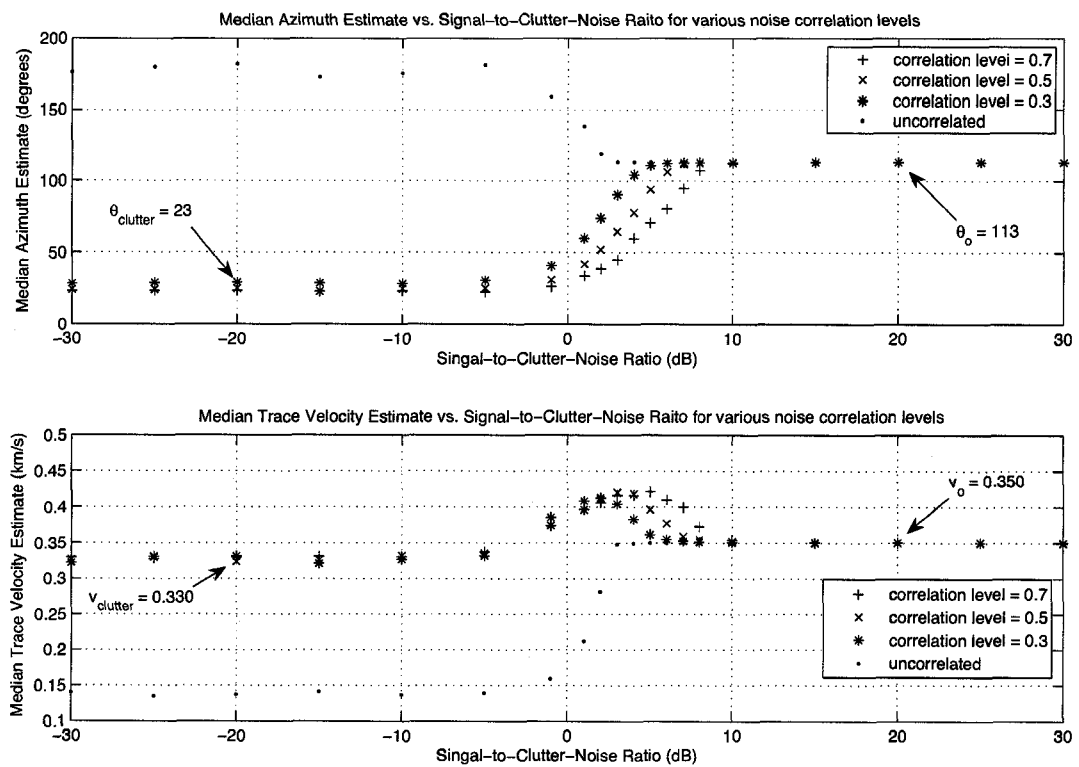


Figure 5.12. The effect of correlated noise on the least squares parameter estimates. The noise field correlation levels of 0.7, 0.5, 0.3, and uncorrelated are shown by +, x, *, and ·, respectively. The upper plot shows the median azimuth estimates and the lower plot shows the median trace velocity estimates. The azimuth of the signal of interest was 113 degrees and the azimuth of the clutter signal was 23 degrees. The clutter trace velocity was 0.330 km/s and the signal had a trace velocity of 0.350 km/s.

clutter signal values when the clutter was present, but the higher the correlation value of the clutter, the smaller the variance in the clutter signal parameter estimate distributions.

The behavior of the estimates in the region between the point where the least squares estimates no longer locked on the signal of interest and the point where the estimates locked on the clutter signal, the transition region, was unpredictable. When the parameters of either signal of interest or the clutter signal were altered, the behavior of the estimates in this region was altered. For example, if the azimuth of the signal of interest was set to a value nearly parallel to the azimuth of the clutter signal, 28° , the trace velocity estimates decreased in magnitude in the transition region instead of increasing in magnitude. The azimuth estimate in the transition region appeared not to suffer from this sensitivity to the wave parameters and generally smoothly moved from one value to the other. The transition region was also characterized by large variances in the distribution of the azimuth and trace velocity distributions making any estimate in the region suspect.

When the noise field corrupting the signal of interest is uncorrelated, the performance of the least squares estimate was superior to the performance with correlated noise. Notice that in Figure 5.12 the uncorrelated noise data, shown with \cdot , remained locked onto the signal of interest at lower signal-to-noise ratios than any of the correlated noise data sets. Unlike the correlated noise data, as the signal-to-noise ratio of the uncorrelated noise data set continued to decrease the azimuth estimates become random. The trace velocity estimate still converged toward a preferred trace velocity value as the signal-to-noise ratio decreased. The value that the trace velocity moves towards was dependent on the window length of the data. For small windows of uncorrelated data, the expectation of the lag maximizing the cross-correlation function is zero and the trace velocity converges toward infinity. For large windows the trace velocity converges towards slow velocities. The slow trace velocity estimates for large windows are caused by an increase in the variance of the lag estimate distribution for large data windows. The increase in the variance of the lag estimate distribution results in some of the estimated lags moving away from the correct value of zero for uncorrelated noise. With a few of the lags miscalculated, the estimate of the trace velocity converges toward low values instead of the infinite trace velocity expected when no signal is present.

5.5 Conclusion

The clutter signals observed in the infrasonic noise field at both the Fairbanks and Windless Bight arrays had the potential to be correlated. The estimated correlation of the clutter signals was dependent on the intersensor separation distance and the local wind speed. In addition, at the Fairbanks array the estimated correlation can also be dependent on the time of day and the season of the year. The degree to which the clutter correlation depended on these parameters was different between the two array locations. The observed microbarom and MAW/HTV clutter signals were coherent across both the Fairbanks and Windless Bight arrays. The coherence spectrum estimated at the Fairbanks array exhibited coherent high frequency clutter signals as well as the coherent MAW/HTV and microbarom signals.

The estimated coherence spectrum at the Windless Bight array was stable throughout the year, displaying no seasonal or diurnal variation in the estimated coherence spectrum. A seasonal dependence in the estimated microbarom and MAW/HTV coherence was observed at the Fairbanks array. During the winter months at Fairbanks the coherence of the microbarom and MAW/HTV signals estimated at small separations was approximately 0.9. The spring and summer microbarom and MAW/HTV coherence decreased from the coherences seen during the winter months, reaching a minimum during the month of June. The coherence of the clutter remained at the summer time minimum coherence level until September, where the microbarom and MAW/HTV coherence began to increase. The estimated microbarom and MAW/HTV coherence returned to the observed winter coherence levels during the month of November.

The seasonal variations in the microbarom and MAW/HTV coherence observed at the Fairbanks array were caused by a shift in the upper atmospheric winds during the summer months. The prevailing atmospheric wind direction during the summer months at the Fairbanks array did not support the creation of lower atmosphere wind ducts to assist in the propagation of the clutter signals to the Fairbanks array. The lack of low atmosphere propagation paths in the summer forced the microbarom and MAW/HTV signals to travel via thermospheric paths. These longer paths resulted in a larger attenuation of the clutter power. The local turbulent pressure fluctuations would thus more efficiently de-correlate the lower power clutter signals that arrived at the array by thermospheric paths causing the observed loss of coherence in the clutter signals during the summer months.

A diurnal variation in the estimated clutter coherence was observed during the spring, summer, and fall months at the Fairbanks array. The diurnal variation in the coherence of the microbarom and MAW/HTV signals was caused by diurnal variation in the local wind speeds. The turbulent pressure fluctuations produced by the local wind flow decreased the coherence of the clutter signals by introducing random noise into the clutter signal. An increase in the local wind speed resulted in an increase in the power contained in the turbulent pressure fluctuations. The increase in turbulent pressure fluctuation power decreased the coherence of the clutter signals by decreasing the signal-to-noise ratio of the data. The measured local wind speed was generally highest during the noon hour at the Fairbanks array. The estimated microbarom and MAW/HTV coherence was lowest during the noon time block. When the local wind speeds were lowest, near the midnight hour, the estimated clutter coherence was greatest. The local winds at the Windless Bight array did not exhibit a diurnal cycle. The coherence of the clutter signals estimated at the Windless Bight array did not vary between the daily time blocks. Thus the diurnal cycle in the coherence of the microbaroms observed at Fairbanks array was driven by a combination of atmospheric path and local wind speed.

It has been indicated that the solar atmospheric tide will produce a diurnal fluctuation in the coherence spectrum of thermospherically traveling acoustic signals.^{54,56} No data on the solar atmospheric tide during the summer months was available at the Fairbanks array, but a study⁵⁶ had been conducted on the structure of the atmospheric tide during the winter months at Fairbanks. The shift in the atmospheric winds produced by the solar atmospheric tide indicated in this study did not correspond to the diurnal cycle in the estimated clutter signal coherence observed at the Fairbanks array. The lack of correlation between the modeled solar atmospheric tide and the observed diurnal cycle in the coherence of the microbarom and MAW/HTV signals does not disprove that the solar atmospheric tide has an effect on the propagation of acoustic waves traveling through the lower thermosphere or upper mesosphere. It is possible that the diurnal variation in the local wind speed masked any effects of the solar atmospheric tide on the microbarom and MAW/HTV signals or that the structure of the solar atmospheric tide at the Fairbanks array changed between the winter and summer months.

The coherence spectrum estimated at the Fairbanks array also contained a highly co-

herent signal at 6 Hz. This high frequency coherent signal was a local signal generated by a building on the UAF campus (K. Arnoult, personal communication, September 2006). No seasonal dependence was observed in the estimated coherence of the 6 Hz local signal. The lack of a seasonal variation in the coherence level of the 6 Hz signal is consistent with the assertion that the observed seasonal variations in the microbarom and MAW/HTV coherence were produced by atmospheric path differences between the seasons. A diurnal variation in the coherence of the 6 Hz signal was observed during the summer, spring and fall seasons, further supporting the theory that the diurnal variations in coherence of the microbarom and MAW/HTV signals were caused by the diurnally fluctuating local winds and not by the solar atmospheric tides.

In addition to altering the coherence level of the infrasonic noise field, changes in the local wind also shifted the frequency of the estimated microbarom coherence peak. The shift in the frequency of the microbarom coherence peak was caused by the frequency dependence in the rate of increase of the wind noise power. As the local wind speed increased, the wind noise power contained in the different frequencies increased at different rates. At frequencies where the wind noise power increased at a faster than average rate, the coherence decreased more rapidly with local wind speed. The estimated microbarom coherence peak spanned a frequency range that included the frequencies with the largest rate of increase of the noise power with local wind speed. As the coherence of the lower microbarom frequencies decreased at a faster rate than the higher microbarom frequencies, the frequency location of the estimated microbarom coherence peak appeared to shift toward the higher frequencies. The shift in the frequency location of the estimated microbarom coherence peak was observed at both the Fairbanks and Windless Bight arrays.

Finally, the coherent noise field estimated at the array had an effect on the performance of the least squares estimate of signal azimuth and trace velocity. The coherent noise field degraded the performance of the least squares estimate, requiring higher signal-to-noise ratios for accurate estimation of the azimuth and trace velocity. The signal-to-noise ratio where the estimates migrated away from the desired values was dependent on the coherence level of the noise field. The more coherent the noise field, the higher the signal-to-noise ratio where the least squares estimate began to break down. At lower signal-to-noise ratios, the estimates of azimuth and trace velocity locked onto the clutter field values. The transition

region between the signal of interest and the clutter was characterized by high variances in the estimates and a sensitivity to the parameters of the signal of interest and the clutter.

Chapter 6

Conclusions

The purpose of this work was to characterize the infrasonic noise field present at the Fairbanks array (IS53) and Windless Bight array (IS55), and determine the effect of the infrasonic noise field on the accuracy of the least squares estimation of wave azimuth and trace velocity. The effect on the least squares azimuth and trace velocity estimates was investigated when the signal of interest was corrupted with the commonly assumed additive Gaussian, white, uncorrelated (GWU) noise field. A statistical picture of the infrasonic noise field was then estimated from data collected at the Windless Bight and Fairbanks arrays. The power spectral density and magnitude square coherence estimated from the data revealed that the infrasonic noise field present at both arrays violated the assumption of white, uncorrelated noise. In this final chapter, the character of the infrasonic noise field at the arrays will be summarized. The effect of the empirical noise field on the least squares estimate of azimuth and trace velocity will be summarized, and some general conclusions on the validity of the assumed GWU noise field will be presented.

6.1 Summary

While the least squares estimate of the vector slowness is an unbiased estimate under the assumption of a GWU noise field, the least squares estimates of azimuth and trace velocity were found to be biased estimates, even with the GWU noise field. The magnitude of the bias in the estimates was dependent on both array geometry and wave parameters. A circularly symmetric array was found to eliminate the azimuthal dependence of the bias in the estimate of trace velocity and completely eliminate the bias in the azimuth estimate. When the trace velocity of the wave approached zero, the least squares estimates of azimuth and trace velocity become unbiased estimates. The magnitude of the bias in each of the estimates was at least an order of magnitude less than the uncertainty in the estimated parameters for the ideal GWU noise field. Due to the comparatively large uncertainties, the systematic error represented by the bias in the least squares estimate of azimuth and trace velocity was masked by the uncertainty in the azimuth and trace velocity estimates and had no conspicuous effect on the accuracy of the source location in the presence of the ideal noise field.

The estimated monthly power spectral densities of the infrasonic noise field at Fairbanks and at Windless Bight were not smooth functions of frequency. Microbarom signals produced a prominent power spectral feature at both the Fairbanks and Windless Bight arrays. Power spectral densities estimated at the Fairbanks array displayed a noise floor greater than the expected instrumental electronic noise floor in all the estimated power spectra during 2005 and 2006. A noise floor greater than the expected instrument noise floor was also observed at Windless Bight during the summer months, but not during winter, spring, or fall months. In addition to power spectrum features produced by the microbarom signals, the infrasonic noise field power spectrum estimated at the Fairbanks array also contained high frequency peaks due to human activity in the vicinity of the nearby town of Fairbanks, Alaska. The noise field PSD estimated at Windless Bight did not display any man-made peaks in the high frequencies due to the remote geographic location of the array.

The PSD of the infrasonic noise field estimated at Fairbanks was not a stationary field. The prominent characteristics of the estimated PSD varied seasonally and diurnally at the Fairbanks array. It was suggested that the diurnal cycle in the estimated noise field power was due to the convective heating of the air due to insolation of the ground surrounding the array. The theory that this solar driven convective heating produced the observed diurnal variations was supported by the lack of an observed diurnal cycle during the winter in Fairbanks, when the ground was snow covered, and the absence of a diurnal cycle at Windless Bight, where the ice shelf was perpetually snow covered. Seasonal variations in the character of the estimated PSD were seen at Fairbanks, but not at the Windless Bight array. The proposed mechanism for the seasonal variations in the PSD estimated at Fairbanks was seasonal shifts in the atmospheric winds causing a lack of lower atmospheric waveguides in the summer months.

The turbulent pressure fluctuations caused by wind flow can change the shape of the noise power spectrum in a non-trivial manner. The rate at which power contained in the noise field increases with wind speed was dependent on the frequency of the pressure fluctuations. Both arrays displayed qualitatively similar frequency dependence in the rate of increase of the noise power with local wind speed. The noise power increased most rapidly at frequencies in the neighborhood of 0.08 Hz at both the Fairbanks and Windless Bight arrays. A local minimum was observed in the rate of increase at a frequency of

approximately 0.32 Hz for both arrays. The high frequency behavior of the rate of increase differed between the Fairbanks and Windless Bight arrays. The rate of increase of the noise power with local wind speed decreased for frequencies higher than 1 Hz for all seasons at Fairbanks and during the summer months at Windless Bight. The remaining three seasons at Windless Bight exhibited a continuing increase in magnitude of rate of increase with frequency for frequencies greater than 0.32 Hz. The magnitude of the rate of increase was influenced by the terrain at the location of the array. The rate of increase at Fairbanks was consistently greater than the rate of increase at Windless Bight. The difference in the rate of increase of the noise power with local wind speed suggests that the terrain in which the Fairbanks array is situated was more efficient at converting the wind flow into turbulent pressure fluctuations. The frequency dependence of the rate of increase proved to be an important feature of the infrasonic noise field, affecting not only the shape of the noise power spectrum at different wind speeds, but also shifted the frequency characteristics of the coherence spectrum of the infrasonic noise field.

The effect of the empirically derived noise field on the least squares estimation of azimuth and trace velocity was shown to be limited, if the data was first bandpass filtered to isolate the microbaroms. The infrasonic frequency band was divided into three frequency bands: a high frequency band from 1 to 10 Hz, a low-frequency band from 0.015 to 0.01 Hz, and a microbarom band from 0.01 to 1 Hz. When the data were bandpass filtered the performance of the least squares estimator with the empirical noise was comparable to the estimator performance with white noise at lower signal-to-noise ratios. The similar change in the performance of the least squares estimates between the GWU and modeled empirical noise fields was observed in all three frequency bands used in the study.

Several correlated clutter signals were present in the estimated infrasonic coherence spectra at Windless Bight and Fairbanks. The estimated correlation of the clutter signals was dependent on the intersensor separation distance, the local wind speed, and the season of the year. The degree to which the clutter correlation depended on these parameters was different between the two array locations. The observed microbarom and MAW/HTV clutter signals were coherent across both the Fairbanks and Windless Bight arrays. The coherence spectrum estimated at the Fairbanks array exhibited coherent high frequency clutter signals as well as the coherent MAW/HTV and microbarom signals.

The estimated coherence spectrum at the Windless Bight array was stable throughout the year, displaying no seasonal or diurnal variation in the estimated coherence spectrum. A seasonal dependence in the estimated microbarom and MAW/HTV coherence was observed at the Fairbanks array. During the winter months at Fairbanks, the coherence of the microbarom and MAW/HTV signals estimated at small separations was approximately 0.9. The spring and summer microbarom and MAW/HTV coherence decreased from the levels seen during the winter months, reaching a minimum during the month of June. The coherence of the clutter remained at the summer time minimum level until September, where the microbarom and MAW/HTV coherence began to increase. The estimated microbarom and MAW/HTV coherence returned to the observed winter levels during the month of November. The variations observed at Fairbanks were due to a combination of seasonally shifting winds in the troposphere and stratosphere, and a diurnal variation in local wind speeds. At IS53, some of the man-made clutter was also correlated across the array. Since the man-made clutter were near-field signals, the coherence of the signals varied with changes in the local wind speed, but were not affected by seasonal variations due to large scale atmospheric effects.

In addition to altering the coherence level of the infrasonic noise field, changes in the local wind also shifted the frequency of the estimated microbarom coherence peak. The shift in the frequency of the microbarom coherence peak was caused by the frequency dependence in the rate of increase of the noise power with local wind speed. As the local wind speed increased, the wind noise power contained in the different frequencies increased at different rates. At frequencies where the wind noise power increased at a faster than average rate, the coherence decreased more rapidly with local wind speed. The estimated microbarom coherence peak spanned a frequency range that included the frequencies with the largest wind noise power growth rates. As the coherence of the lower microbarom frequencies decreased at a faster rate with local wind speed than the higher microbarom frequencies, the frequency location of the estimated microbarom coherence peak appeared to shift toward the higher frequencies as the local wind speed increased. The shift in the frequency location of the estimated microbarom coherence peak was observed at both the Fairbanks and Windless Bight arrays.

The coherent elements of the infrasonic noise field estimated at IS55 and IS53 had an

effect on the performance of the least squares estimate of signal azimuth and trace velocity. The presence of correlated signals in the infrasonic noise field changed the assumed model of the sensor output from a signal of interest corrupted with uncorrelated noise to a signal of interest, clutter, and uncorrelated noise. The addition of clutter in the data degraded the performance of the least squares estimate, requiring higher signal-to-noise ratios to get the same accuracy in the estimation of azimuth and trace velocity. The signal-to-noise ratio where the estimates migrated away from the desired values was dependent on the coherence level of the noise field. The more correlated the clutter in the infrasonic noise field, the higher the signal-to-noise ratio where the least squares estimate began to break down. The typical signal-to-noise where this break down occurred was approximately 8 dB for clutter with a correlation coefficient of 0.7, which is a typical value for the microbarom clutter. At low signal-to-noise ratios, the estimates of azimuth and trace velocity locked onto the values of the clutter in the noise field. The transition region between the signal of interest and clutter was characterized by high variances in the estimates and a sensitivity to the parameters of the signal of interest and clutter.

6.2 Discussion

The least squares estimate of the slowness vector, and through the slowness vector the azimuth and trace velocity, is sensitive to the signal-to-noise ratio of the data used in the estimation. Figure 6.1 displays the results of a numerical simulation designed to determine the signal-to-noise ratio where the estimated slowness vector pdf can no longer be described as a Gaussian distribution. The slowness vector pdfs were produced by least squares estimation of the trace velocity and azimuth for 10,000 realizations of a synthetic signal corrupted with noise at each signal-to-noise ratio shown in Figure 6.1. The noise used to corrupt the synthetic signal was the ideal Gaussian, white, uncorrelated (GWU) noise. At each signal-to-noise ratio, 1,000 simulated slowness vector pdfs were produced to determine the percentage of distributions at each signal-to-noise ratio that were not Gaussian, in the following sentence. The percent of synthetic slowness vector pdfs that failed the chi-squared distribution test⁴⁷ with respect to an ideal Gaussian is shown on the y -axis. The signal-to-noise ratio of the data used during the estimation is shown along the x -axis. At high signal-to-noise ratios, nearly all the slowness vector pdfs pass the chi-squared test

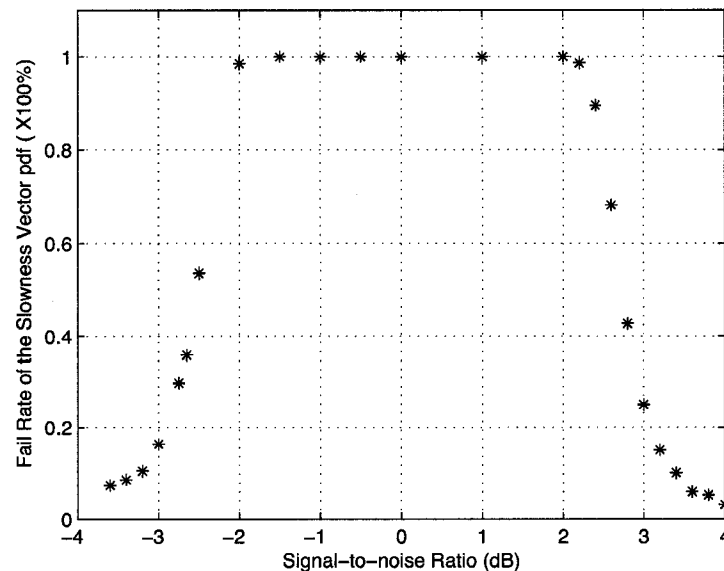


Figure 6.1. The percentage of synthetic slowness vector pdfs that fail a chi-squared distribution test as a function of the signal-to-noise ratio.

and the distributions of the slowness estimates are 2-D Gaussian distributions in slowness space. As the signal-to-noise ratio decreases, the variances of the 2-D Gaussian distributions begin to increase and a progressively larger percentage of the distributions fail the chi-squared test, reaching a 100% fail rate at a signal-to-noise ratio of approximately 2 dB. The non-Gaussian distribution of the slowness estimates indicates that the Gaussian, white, uncorrelated noise present in the synthetic data has effectively masked the signal of interest and reliable estimation of the parameters is no longer possible. At low enough signal-to-noise ratios, approximately -3.5 dB, the distribution of the slowness estimates returns to a 2-D Gaussian distribution, but is now centered on either the noise or clutter values.

Although the physical noise field present at the Fairbanks and Windless Bight arrays violated the assumptions of white, uncorrelated noise, the least squares estimate of azimuth and trace velocity showed only a small degradation of performance when the data was bandpass filtered prior to estimation. At high signal-to-noise ratios, greater than 10 dB, the performance of the estimator with an empirically derived infrasonic noise field showed

no deviation out to four significant figures from the estimator performance with the assumed noise field. At these high signal-to-noise ratios, the distribution of the slowness estimates was approximately a 2-D Gaussian. The main effect of the empirical noise field was to increase the signal-to-noise ratio where the estimate distribution began to deviate from a Gaussian distribution. The increase in the threshold signal-to-noise ratio was not large, less than 10 dB for the numerical simulations performed in this study. In light of the results of this study, it seems reasonable to assert that the assumption of Gaussian white noise does not result in any major deviations in the LSE estimations relative to the physical case at signal-to-noise ratios greater than 10 dB. At signal-to-noise ratios less than 10 dB, the noise model assumptions begin to noticeably deviate from the physical reality present at the Fairbanks and Windless Bight arrays, and the least squares estimates of azimuth and trace velocity begin to fail.

Bibliography

- [1] Complete information on the Preparatory Commission for the Comprehensive Nuclear-Test-Ban Treaty Organization (CTBTO) and the various monitoring technologies may be found at <<http://www.ctbto.org>> .
- [2] A. LePichon, V. Maurer, D. Raymond, and O. Hyvernaud, "Infrasound from ocean waves observed in Tahiti," *Geophys. Res. Lett.* **31**, L19103 (2004).
- [3] J. Olson and C. Szuberla, "Distribution of wave packet sizes in microbarom wave trains observed in Alaska," *J. Acoust. Soc. Am.* **117**, 1032–1037 (2005).
- [4] C. Wilson, "Infrasound observed at I53US from large Alaskan earthquakes in 2002," *Inframatics* **3**, 11–14 (2003).
- [5] C. Chyba, P. Thomas, and K. Zahnle, "The 1908 Tunguska explosion: atmospheric disruption of a stony asteroid," *Nature* **361** (1993).
- [6] F. Whipple, "The great Siberian meteor and the waves, seismic and aerial, which it produced," *Q. Jl R. met. Soc.* **56** (1930).
- [7] R. Strachey, "On the air waves and sounds caused by the eruption of Krakatoa in August, 1883," In Symons (1888).
- [8] L. Berkofsky, "Internal gravity-vorticity lee waves over mountains," *J. Geophys. Res.* **65**, 3685–3691 (1960).
- [9] C. Wilson and J. Olson, "Mountain Associated Waves at I53US and I55US in Alaska and Antarctica in the frequency passband from 0.015 to 0.10 Hz," *Inframatics* **2**, 6–10 (2003).
- [10] C. Wilson, "Infrasound from Auroral Electrojet motions at I53US," *Inframatics* **10**, 1–13 (2005).
- [11] F. Shields, "Low-frequency wind noise correlation in microphone arrays," *J. Acoust. Soc. Am.* **117**, 3489–3496 (2005).

- [12] J. McDonald and E. Herrin, "Properties of pressure fluctuations in an atmospheric boundary layer," *Boundary-Layer Meteorology* **8**, 419–436 (1975).
- [13] J. Mann, "The spatial structure of neutral atmospheric surface-layer turbulence," *J. Fluid Mech.* **273**, 141–168 (1994).
- [14] G. Katul, J. Albertson, C. Hsieh, P. Conklin, J. Sigmon, M. Parlange, and K. Knoerr, "The "inactive" eddy motion and the large-scale turbulent pressure fluctuations in the dynamic sublayer," *American Meteorological Society* **53 No. 17**, 2512–2524 (1996).
- [15] W. George, P. Beuther, and R. Arndt, "Pressure spectra in turbulent free shear flows," *J. Fluid Mech.* **148**, 155–191 (1984).
- [16] R. Strachey, "Notes on R.H. Scott's paper on barometrical disturbances of August, 1883," *Proceedings of the Royal Society of London* **36** (1884).
- [17] T. Simkin and R. Fiske, *Krakatau 1883: The Volcanic Eruption and Its Effects* (Smithsonian Institution Press, 1983).
- [18] M. Hedlin and R. Raspet, "Infrasound wind-noise reduction by barrier and spatial filters," *J. Acoust. Soc. Am.* **114**, 1379–1386 (2003).
- [19] S. Kay, *Fundamentals of Statistical Signal Processing, Volume I: Estimation Theory* (Prentice Hall, 1993).
- [20] J. Pedlosky, *Waves in the Ocean and Atmosphere* (Springer, 2003).
- [21] A. Gill, *Atmospheric-Ocean Dynamics* (Kluwer Academic, 1982).
- [22] L. Kinsler and A. Frey, *Fundamentals of Acoustics* (John Wiley & Sons, 1950).
- [23] L. E. Kinsler and A. R. Frey, *Fundamentals of Acoustics, 2nd edition* (John Wiley & Sons, 1962).
- [24] D. H. Johnson and D. E. Dudgeon, *Array Signal Processing: Concepts and Techniques* (Prentice Hall, 1993).

- [25] C. Szuberla, K. Arnoult, and J. Olson, "Discrimination of near-field infrasound sources based on time-difference of arrival information," *J. Acoust. Soc. Am.* **120**, EL23–EL28 (2006).
- [26] Wolfram's Mathworld website <<http://mathworld.wolfram.com/>> .
- [27] E. M. Salomons, *Computational Atmospheric Acoustics* (Kluwer Academic, 2001).
- [28] The International Reference Atmosphere can be found at <<http://modelweb.gsfc.nasa.gov/atmos/cospar2.html>> .
- [29] C. W. Therrien, *Discrete Random Signals and Statistical Signal Processing* (Prentice Hall, 1992).
- [30] M. Spiegel and L. Stephens, *Schaum's Outline of Theory and Problems of Statistics* (McGraw-Hill, 1999).
- [31] G. Jenkins and D. Watts, *Spectral Analysis and its Applications* (Holden-Day, 1968).
- [32] D. Johnson, "The application of spectral estimation methods to bearing estimation problems," *Proc. IEEE* **70**, 1018–1028 (1982).
- [33] M. Bartlett, "Periodogram analysis and continuous spectra," *Biometrika* **37**, 1–16 (1950).
- [34] R. Blackman and J. Tukey, *The Measurement of Power Spectra from the Point of View of Communications Engineering* (Dover Publications, 1958).
- [35] A. Oppenheim and R. Schaffer, *Digital Signal Processing* (Prentice Hall, 1975).
- [36] P. Welch, "The use of fast Fourier transform for the estimation of power spectra," *IEEE Transactions on Audio and Electroacoustics* **AU-15**, 70–73 (1970).
- [37] R. Bracewell, *The Fourier Transform and Its Applications* (McGraw-Hill Book Company, 1978).
- [38] Additional information about the array geometry and instrumentation of I53US and I55US can be found at <<http://www.gi.alaska.edu/infrasound/>> .

- [39] J. Olson and C. Szuberla, "Least-squares estimateion of the azimuth and velocity of plane waves using infrasound array data," *Inframatics* **6**, 8–12 (2004).
- [40] M. Boas, *Mathematical Methods in the Physical Sciences* (John Wiley & Sons, 1983).
- [41] B. Ferguson, L. Criswick, and K. Lo, "Locating far-field impulsive sound sources in air by triangulation," *J. Acoust. Soc. Am.* **111** (2002).
- [42] H. Liu and E. Milios, "Acoustic positioning using multiple microphone arrays," *J. Acoust. Soc. Am.* **117**, 2772–2781 (2005).
- [43] C. Szuberla and J. Olson, "Uncertainties associated with parameter estimation in atmospheric infrasound arrays," *J. Acoust. Soc. Am.* **115**, 253–258 (2004).
- [44] B. Song and J. Ritcey, "Angle of arrival estimation of plane waves propagating in random media," *J. Acoust. Soc. Am.* **99**, 1370–1379 (1996).
- [45] J. Kapur and H. Kesauan, *Entropy Optimization Principles with Applications* (Academic Press, 1992).
- [46] W. H. Press, S. A. Teukolsky, W. T. Vetterling, and B. P. Flannery, *Numerical Recipes in C, 2nd edition* (Cambridge University Press, 1992).
- [47] J. Taylor, *An Introduction to Error Analysis* (University Science Books, 1982).
- [48] J. Bowmann, G. Baker, and M. Bahavar, "Ambient infrasound noise," *Geophysical Research Letters* **32**, LO9803 (2005).
- [49] H. Benioff and B. Gutenberg, "Waves and currents recorded by electromagnetic barographs," *Bull. Am. Meteorol. Soc.* **20**, 421–429 (1939).
- [50] M. Raupach, R. Antonia, and S. Rajagopalan, "Rough-wall turbulent boundary layers," *Appl. Mech. Rev.* **44**, 1–25 (1991).
- [51] A. Townsend, "Equilibrium layers and wall turbulence," *J. Fluid Mech.* **11**, 97–120 (1961).
- [52] R. Stull, *An Introduction to Boundary Layer Meteorology* (Kluwer Academic Publishers, 1988).

- [53] M. Garcés, M. Willus, C. Hetzer, A. LePichon, and D. Drob, "On using ocean swells for continuous infrasonic measurements of winds and temperature in the lower, middle, and upper atmosphere," *Geophys. Res. Lett.* **31**, L19304 (2004).
- [54] D. Rind, "Investigation of the lower thermosphere results of ten years of continuous observations with natural infrasound," *J. atmos. terr. Phys.* **40**, 1199–1209 (1978).
- [55] E. Gossard and D. Sailors, "Dispersion bandwidth deduced from coherency of wave recordings from spatially separated sites," *J. Geophys. Res.* **75**, 1324–1327 (1970).
- [56] M. Garcès, D. Drob, and J. Picone, "A theoretical study of the effect of geomagnetic fluctuations and solar tides on the propagation of infrasonic waves in the upper atmosphere," *Geophys. J. Int.* **148**, 77–87 (2002).
- [57] A. Peirce, "Guided infrasonic modes in a temperature- and wind-stratified atmosphere," *J. Acoust. Soc. Am.* **41**, 597–611 (1967).
- [58] J. Forbes and F. Vail, "Monthly simulations of the solar semidiurnal tide in the mesosphere and lower thermosphere," *J. atmos. terr. Phys.* **51** (1989).
- [59] S. Chapman and R. Lindzen, *Atmospheric Tides* (D. Reidel Publishing Company, 1970).
- [60] T. Embleton, "Tutorial on sound propagation outdoors," *J. Acoust. Soc. Am.* **100**, 31–48 (1996).
- [61] J. Piercy, T. Embleton, and L. Sutherland, "Review of noise propagation in the atmosphere," *J. Acoust. Soc. Am.* **61**, 1403–1418 (1977).
- [62] M. Lighthill, "On the energy scattered from the interaction of turbulence with sound or shock waves," *Proc. Camb. Phil. Soc.* **49**, 531–551 (1953).
- [63] M. Howe, "On the absorption of sound by turbulence and other hydrodynamic flows," *IMA J. Appl. Math.* **32**, 187–210 (1984).
- [64] V. Ostashev, D. Wilson, and G. Goedecke, "Spherical wave propagation through inhomogeneous, anisotropic turbulence: Log-amplitude and phase correlations," *J. Acoust. Soc. Am.* **115**, 120–130 (2004).

- [65] V. Ostashev, "Sound propagation and scattering in media with random inhomogeneities of sound speed, density, and medium velocity," *Waves in Random Media* **4**, 403–428 (1994).
- [66] N. Pan, "Excess attenuation of an acoustic beam by turbulence," *J. Acoust. Soc. Am.* **114**, 3102–3111 (2003).
- [67] D. Wilson, J. Wyngaard, and D. Havelock, "The effect of turbulent intermittency on scattering into an acoustic shadow zone," *J. Acoust. Soc. Am.* **99**, 3393–3400 (1996).
- [68] D. Wilson, J. Brasseur, and K. Gilbert, "Acoustic scattering and the spectrum of atmospheric turbulence," *J. Acoust. Soc. Am.* **105**, 30–34 (1999).
- [69] D. Wilson, J. Brasseur, and K. Gilbert, "Acoustic scattering and the spectrum of atmospheric turbulence," *J. Acoust. Soc. Am.* **105**, 30–34 (1999).

Appendix A

Entropy Optimazation Derivation of the Slowness Vector pdf

†

In the derivation of the pdf of the slowness vector in Section 3.3.1, assumptions were made about the nature of the noise field at the points of data collection.⁴³ The assumption of a normally distributed noise pdf is a standard assumption in signal processing, but still force the use of information that is not known a priori from the data. An alternative derivation of the pdf of the slowness vector can be preformed by applying the principles of entropy optimization.⁴⁵ The principles of entropy optimization allows a derivation of the unknown probability density function that is based on the data collected and no additional assumptions.

The principles of entropy optimization are rules that standardize the criteria used when selecting a distribution function to represent empirical data. The general entropy optimization principle is:

Out of all probability distributions satisfying given moment constraints together with the natural constraint on the probabilities, choose the distribution that is closest to the given a priori probability distribution, Q , and in the case that Q is not specified, choose the distribution that is closest to the uniform distribution.⁴⁵

This principle is a common sense statement that only the information given should be used to choose a distribution to represent the emperical data.

The uniform distribution has the maximum uncertainty of all possible distributions. Choosing distributions that are closer to the distribution of maximum uncertainty may seem counter intuitive, but there is a reason for this rule. If a distribution other than the one with maximum uncertainty is chosen to represent the data, information not avaiable from the data must have been used to determine that the distribution with the smaller uncertainty better represent the data. If the extra information used to select the distribution of lower uncertainty was not part of the original constraints derived from the data, then the use of the extra information goes against scientific principles. Using only the information derived from the data when determining which distribution will represent the empirical data is at

†This appendix summarizes a derivation found in the book by Kapur and Kesauan.⁴⁵

the heart of the principles of entropy optimization.

In order to minimize the entropy, it is first necessary to define the entropy and standardize the measure of this entropy. When entropy is discussed in entropy optimization what is meant is the probabilistic uncertainty in the distribution.⁴⁵ The measurement of the entropy for a continuous-variate distribution with a pdf $f(x)$ is

$$-\int_a^b f(x) \ln[f(x)] dx. \quad (\text{A.1})$$

According to the principles of entropy optimization, to find the pdf A.1 must be maximized under the constraints on the moments and the “natural” constraint that the probabilities sum to unity. The natural constraint equation is

$$\int_a^b f(x) dx = 1, \quad (\text{A.2})$$

where the pdf must sum to unity over all space. The constraints on the moments can be compactly written as

$$\int_a^b f(x) g_r(x) dx = a_r, \quad (\text{A.3})$$

where $g_1 = x, g_2 = x^2, \dots$ and the moments are represented by a_r . If m moments are known from the empirical data, then the number of moment constraint equations in Equation A.3 is m and $r = 1, 2, 3, \dots, m$. To maximize the entropy, the Lagrangian of the entropy,

$$L \equiv -\int_a^b f(x) \ln[f(x)] dx - (\lambda_0 - 1) [\int_a^b f(x) dx - 1] - \sum_{r=1}^m \lambda_r [\int_a^b f(x) g_r(x) dx - a_r], \quad (\text{A.4})$$

must be minimized using the Euler-Lagrange equation. The Euler-Lagrange equation states that if J is defined by an integral of the form $J = \int f(x, y, y') dx$, then J has a stationary value if

$$\frac{df}{dy} - \frac{d}{dx} \left(\frac{\partial f}{\partial y_x} \right) = 0,$$

where

$$\partial y_x = \frac{\partial y}{\partial x}.$$

The Lagrangian of the entropy contains no $f'(x)$ terms, so $J = \int F(x, f(x))$ and the Euler-Lagrange equation becomes

$$\begin{aligned} \frac{\partial F}{\partial f(x)} - \frac{d}{dx} \left[\frac{\partial F}{\partial f'(x)} \right] &= 0 \\ \frac{\partial F}{\partial f(x)} &= 0, \end{aligned} \quad (\text{A.5})$$

where the term involving the derivative with respect to $f'(x)$ is equal to zero. It follows from Equation A.5 that the minimum of the entropy can be found by differentiating Equation A.4 with respect to $f(x)$ and setting the result to zero,

$$\begin{aligned} \frac{\partial}{\partial f(x)} [f(x) \ln[f(x)] + (\lambda_0 - 1)f(x) + 1 + \sum_{r=1}^m \lambda_r f(x) g_r(x) + a_r] &= 0 \\ \ln[f(x)] + 1 + (\lambda_0 - 1) + \sum_{r=1}^m \lambda_r g_r(x) &= 0 \\ -\lambda_0 - \sum_{r=1}^m \lambda_r &= \ln[f(x)] \\ e^{[-\lambda_0 - \sum_{r=1}^m \lambda_r g_r(x)]} &= f(x). \end{aligned} \quad (\text{A.6})$$

Equation A.6 is the general form of the pdf where the unidentified multipliers, $\lambda_0, \lambda_1, \dots, \lambda_m$, determine the exact form of the pdf and are found by substituting the general form into the constraint equations.

The normal distribution is the maximum entropy probability distribution (MEPD) for any random variate varying between $-\infty$ and $+\infty$ with a known mean and variance. With the first two moments known, Equation A.6 becomes

$$f(x) = e^{-\lambda_0 - \lambda_1 x - \lambda_2 x^2},$$

or rewriting the constants

$$f(x) = e^{-b(x-c)^2}. \quad (\text{A.7})$$

The constraint equations can now be employed to determine the constants a, b , and c . There are three constraint equations, one from the natural constraint and two from the constraints on the moments,

$$a \int_{-\infty}^{\infty} \exp^{-b(x-c)^2} dx = 1 \quad (\text{A.8})$$

$$a \int_{-\infty}^{\infty} x \exp^{-b(x-c)^2} dx = m \quad (\text{A.9})$$

$$a \int_{-\infty}^{\infty} x^2 \exp^{-b(x-c)^2} dx = \gamma. \quad (\text{A.10})$$

The integrands in Equation A.8 and Equation A.9 are both in the form of Gaussian integrals, resulting in

$$a \int_{-\infty}^{\infty} \exp^{-b(x-c)^2} dx = a \sqrt{\frac{\pi}{b}} \quad (\text{A.11})$$

and

$$a \int_{-\infty}^{\infty} x \exp^{-b(x-c)^2} dx = a c \sqrt{\frac{\pi}{b}}. \quad (\text{A.12})$$

The integrand of Equation A.10 is more involved and the integration requires the use of substitution of variables. Let

$$u = x - c$$

so

$$x^2 = u^2 + c^2 + 2uc$$

and the integrand becomes

$$\begin{aligned} a \int_{-\infty}^{\infty} x^2 e^{-b(x-c)^2} dx &= a \int_{-\infty}^{\infty} (u^2 + c^2 + 2uc) e^{-b u^2} du \\ &= a \int_{-\infty}^{\infty} u^2 \exp^{-b u^2} du + ac^2 \int_{-\infty}^{\infty} e^{-b u^2} du + 2ac \int_{-\infty}^{\infty} u \exp^{-b u^2} du \\ &= \frac{a}{2} \sqrt{\frac{\pi}{b^3}} + ac^2 \sqrt{\frac{\pi}{b}} + 2ac(0) \\ &= a \sqrt{\frac{\pi}{b}} \left[\frac{1}{2b} + c^2 \right]. \end{aligned} \quad (\text{A.13})$$

The system of equations to solve for the constants is

$$\begin{aligned} a \frac{\pi}{b} &= 1 \\ a c \sqrt{\frac{\pi}{b}} &= m \\ a \sqrt{\frac{\pi}{b}} \left[\frac{1}{2b} + c^2 \right] &= \gamma^2. \end{aligned} \quad (\text{A.14})$$

Upon solving the system of equations the constants are found to be

$$\begin{aligned} a &= \frac{1}{\sqrt{2\pi}\sigma} \\ b &= \frac{1}{2\sigma^2} \\ c &= m, \end{aligned} \quad (\text{A.15})$$

where $\gamma^2 - m^2$ has been replaced with the variance σ^2 . Substituting the constants into Equation A.7 produces a normal distribution,

$$f(x) = \frac{1}{\sqrt{2\pi}\sigma} e^{-\frac{(x-c)^2}{2\sigma^2}}, \quad (\text{A.16})$$

and the MEPD with two known moments is the normal distribution.

This result can be extended to multivariate distributions by using the multivariate entropy measure,

$$- \int \dots \int f(x_1, x_2, \dots, x_n) \ln[f(x_1, x_2, \dots, x_n)] dx_1 dx_2 \dots dx_n. \quad (\text{A.17})$$

If the means, variances, and co-variances are prescribed as

$$\begin{aligned} E[x_i] &= m_i \\ E[(x_i - m_i)^2] &= \sigma_i^2 \\ E[(x_i - m_i)(x_j - m_j)] &= \rho \sigma_i \sigma_j, \end{aligned} \quad (\text{A.18})$$

the maximum entropy probability distribution is

$$f(\vec{x}) = \frac{1}{(2\pi)^{\frac{n}{2}} |\Sigma|^{\frac{1}{2}}} e^{[-\frac{1}{2}(\vec{x} - \vec{m})^T \Sigma^{-1} (\vec{x} - \vec{m})]}, \quad (\text{A.19})$$

where

$$\vec{x} = \begin{pmatrix} x_1 \\ x_2 \\ \vdots \\ x_n \end{pmatrix}$$

$$\vec{m} = \begin{pmatrix} m_1 \\ m_2 \\ \vdots \\ m_n \end{pmatrix}$$

and

$$\Sigma = \begin{bmatrix} \sigma_1^2 & \rho_{12}\sigma_1\sigma_2 & \cdots & \rho_{1n}\sigma_1\sigma_n \\ \rho_{21}\sigma_2\sigma_1 & \sigma_2^2 & \cdots & \rho_{2n}\sigma_2\sigma_n \\ \vdots & \vdots & \ddots & \vdots \\ \rho_{n1}\sigma_n\sigma_1 & \cdots & \cdots & \sigma_n^2 \end{bmatrix}. \quad (\text{A.20})$$

For the specific case of 2-d estimation with uncorrelated components of the slowness vector, the same assumption made in the paper by Szuberla et al.⁴³, the variance matrix, Σ is

diagonal. The diagonal variance matrix allows the MEPD to be written as a sum to one dimensional Gaussian distributions,

$$f(\vec{s}) = \frac{1}{2\pi\sigma_{s_x}\sigma_{s_y}} e^{-\frac{(s_x-m_x)^2}{2\sigma_{s_x}^2}} e^{-\frac{(s_y-m_y)^2}{2\sigma_{s_y}^2}}. \quad (\text{A.21})$$

The MEPD in this form is identical to the slowness vector distribution found in Chapter 3. With only two moments of the distribution known the empirical slowness vector data must be represented by a normal distribution.